

Validation of fast reactor thermomechanical and thermohydraulic codes

*Final report of a co-ordinated research project
1996–1999*



INTERNATIONAL ATOMIC ENERGY AGENCY

IAEA

November 2002

The originating Section of this publication in the IAEA was:

Nuclear Power Technology Development Section
International Atomic Energy Agency
Wagramer Strasse 5
P.O. Box 100
A-1400 Vienna, Austria

VALIDATION OF FAST REACTOR THERMOMECHANICAL AND
THERMOHYDRAULIC CODES

IAEA, VIENNA, 2002
IAEA-TECDOC-1318
ISBN 92-0-118302-X
ISSN 1011-4289

© IAEA, 2002

Printed by the IAEA in Austria
November 2002

FOREWORD

This report is a summary of the work performed under a co-ordinated research project (CRP) entitled Harmonization and Validation of Fast Reactor Thermomechanical and Thermo-Hydraulic Codes and Relations using Experimental Data. The project was organized by the IAEA on the recommendation of the IAEA's Technical Working Group on Fast Reactors (TWGFR) and carried out from 1996 to 1999.

In certain conditions, temperature fluctuations in the coolant close to a structure caused by thermal striping can lead to thermomechanical damage to structures. Institutes from a number of Member States have an interest in improving engineering tools and prediction techniques concerning the characterization of the thermal striping effects, in which numerical models have a major role. Therefore, the IAEA through its advanced reactor technology development programme supports the activities of Member States in this area. Design analyses applied to thermal striping phenomena need to be firmly established, and the CRP provided a valuable tool in assessing their reliability.

Eleven institutes from France, India, Italy, Japan, the Republic of Korea, the Russian Federation and the United Kingdom co-operated in this CRP.

This report documents the CRP activities, provides the main results and recommendations and includes the work carried out by the research groups at the participating institutes within the CRP on harmonization and validation of fast reactor thermomechanical and thermohydraulic codes and relations.

The IAEA would like to express its appreciation to all who took part in the project and in the preparation of this report. Special thanks go to O. Gelineau and M. Sperandio of the FRAMATOME-NOVATOME (France) who served as Chairpersons throughout the Research Co-ordination Meetings (RCM). The IAEA officers responsible for this work were A. Rineiskii and A. Stanculescu of the Division of Nuclear Power.

EDITORIAL NOTE

This publication has been prepared from the original material as submitted by the authors. The views expressed do not necessarily reflect those of the IAEA, the governments of the nominating Member States or the nominating organizations.

The use of particular designations of countries or territories does not imply any judgement by the publisher, the IAEA, as to the legal status of such countries or territories, of their authorities and institutions or of the delimitation of their boundaries.

The mention of names of specific companies or products (whether or not indicated as registered) does not imply any intention to infringe proprietary rights, nor should it be construed as an endorsement or recommendation on the part of the IAEA.

The authors are responsible for having obtained the necessary permission for the IAEA to reproduce, translate or use material from sources already protected by copyrights.

CONTENTS

1. Technical background for the co-ordinated research project	1
2. Description of the benchmark	2
2.1. Presentation of the problem.....	2
2.1.1. Introduction.....	2
2.1.2. Temperature measurement.....	3
2.1.3. Observations of cracks	3
2.1.4. Metallurgical observations.....	3
2.2. Data provided	3
2.3. Thermohydraulic and thermal results required for comparison with experience	4
2.4. Scope of the benchmark	4
2.4.1. Objectives	4
3. Experimental activities on thermomechanics and fracture mechanics at the participating institutes	5
4. Summary of activities within the CRP on thermohydraulics, thermomechanics and fracture mechanics: Results from individual projects	8
5. Comparison of the analysis methods, codes and predictions	12
6. The CRP results and recommendations	12
6.1. The main results	12
6.1.1. Thermohydraulics modelling	12
6.1.2. Comparison with Phénix measurements and between thermohydraulics computations.....	12
6.1.3. Thermomechanical assessments	13
6.2. Recommendations	13
6.2.1. Range of frequencies, sampling	13
6.2.2. Domain and boundary conditions	13
6.2.3. Thermohydraulic simulation.....	14
6.2.4. Thermomechanical calculations.....	14
Appendix	16

ANNEX: WORK PERFORMED BY THE RESEARCH GROUPS AT THE PARTICIPATING INSTITUTES WITHIN THE CRP

Thermomechanical and thermohydraulic analyses of a T-junction using experimental data.....	31
<i>O. Gelineau, M. Sperandio, J.P. Simoneau, J.M. Hamy, P.H.L. Roubin</i>	
Thermal hydraulics and thermomechanical analysis of thermal striping in a mixing tee-junction of secondary sodium circuit of Phénix reactor	63
<i>P. Chellapandi, K. Velusamy, A. Biswas, R. Rama, S.B. Bhoje, G. Vaidyanathan, S. C. Chetal</i>	
Thermomechanical and fracture mechanics analysis on a tee junction of LMFR secondary circuit due to thermal striping phenomena	89
<i>N. Kasahara</i>	

Thermohydraulics computer code system and computational results on thermal striping phenomena at a tee junction of LMFR secondary circuit with the system	117
<i>T. Muramatsu</i>	
Recent activities related to thermo-mechanical fatigue, creep and fracture mechanics in Korea nuclear fields.....	145
<i>H.-Y. Lee, J.-B. Kim, B. Y.Y.-W. Park</i>	
Tee-junction of LMFR secondary circuit involving thermal thermomechanical and fracture mechanics assessment on a striping phenomenon.....	153
<i>H.-Y. Lee, J.-B. Kim, B. Yoo</i>	
Results of the thermomechanical and fracture mechanical analysis of pipeline tee-junction break under conditions of interaction between hot sodium jet and main cold sodium flow	168
<i>P.N. Birbryer, A.I. Kiryushin, V.V. Zhukov, V.A. Sobolev, S.A. Soloviev</i>	
Computational investigation of thermohydraulic aspects of two convergent flows at different temperatures mixed in the tee junction area	186
<i>S.I. Scherbakov</i>	
Thermal striping benchmark exercise: Thermal hydraulic analysis of the Phénix fast reactor secondary pipework t-junction.....	206
<i>R. Stainsby, D. Martin</i>	
Benchmark on tee junction: Fatigue damage analysis.....	227
<i>M.W.J. Lewis</i>	
List of Participants.....	255

1. TECHNICAL BACKGROUND FOR THE CO-ORDINATED RESEARCH PROJECT

During operation of a reactor, temperature fluctuations in the coolant close to a structure may occur in many areas such as core outlet zone, lower part of hot pool, free surface of pool, secondary circuit, and water/steam interface in steam generators. In certain conditions, these temperature fluctuations can lead to thermomechanical damage to structures. In 1992 extensive cracking was found in a control rod guide tube that had been removed from the core of the UK Prototype Fast Reactor (PFR). High-cycle thermal fatigue was found to be the cause of the cracks in the connecting pipe and the middle-stage heat exchange (HE) shell at the Tsuruga-2 PWR (Japan) in 1999: two coolant flows — lower temperature main flow inside the inner cylinder of the HE and higher temperature bypass flow outside the inner cylinder — were mixed. Repair of the damage interrupted the reactor operating programme. Consequently, knowledge of temperature fluctuations and induced thermomechanical damage to structures is essential to properly support operation and maintenance of a nuclear reactor during the plant life-time. In a LMFR (liquid metal cooled reactor), several areas of the reactor are subject to this problem. There are often difficulties in calculations, because of the complexity of the phenomena involved. This issue has been encountered in the Phenix LMFR in the secondary loop, where initial crack in a tee-junction zone was detected during a campaign of inspections.

The Technical Working Group on Fast Reactors (TWGFR) recommended to the IAEA to organize a specialists meeting on "Correlations between material properties and thermohydraulics conditions, fluid temperature fluctuations and induced thermomechanical damage in LMFR", to identify common trends in the interpretation of experimental and analytical work and the influence on design features. The IAEA's specialists meeting, which was held in Aix-en-Provence, France, in November 1994 noted that various computer codes for thermomechanical analyses had been and were being developed in some countries. Significant progress has been made in substantiating the phenomenological basis of the material design codes available to reactor designers, but some problems still remain to be harmonized. Great advances have been made in the last few years to improve calculation methods for predicting fluid temperature fluctuation amplitudes and frequencies, involving large-eddy simulation and direct solution of the Navier-Stokes equation. Within a short time, when improved computing capacity which at present is being implemented, has become available, it should be possible to provide information on fluid temperature at all times and at all important locations. When this level of detail in thermohydraulic calculations has been reached, all the requirements for calculating stresses in structural materials will have been met.

Two problems need subsequent development and harmonization, however. Firstly, the question of appropriate boundary conditions between more approximate fluid mechanic codes used to predict overall flow properties and codes to predict the fine detail of thermal fluctuations in critical regions has to be harmonized. Secondly, adequate experimental validation including measurements of suitable detail and precision has to be provided. The above mentioned specialists meeting also stressed that the best way to improve and validate calculation codes and methods would be organize benchmark calculation comparison in the frame of the TWGFR. The TWGFR following the recommendation of Member States, at its 28th Annual Meeting in May 1995, proposed to perform benchmark analyses in order to verify and validate the thermohydraulic and thermomechanical codes and analytical methods using experimental data.

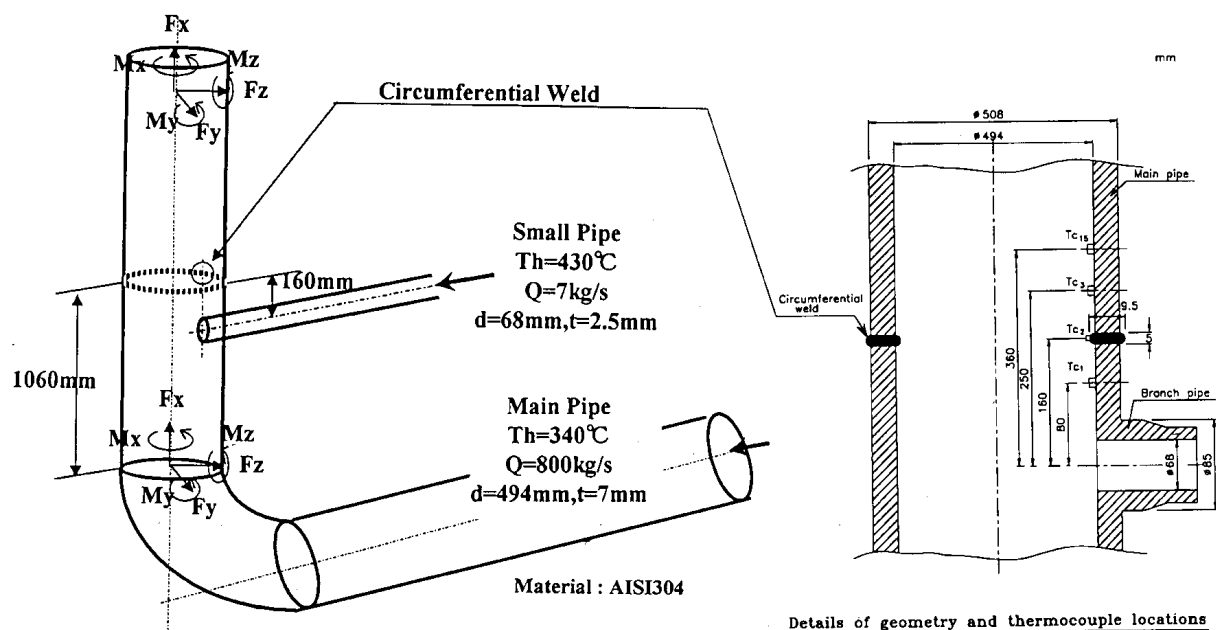


FIG. 1. Geometrical characteristics of the Phenix secondary piping system.

Two possible benchmark problems were discussed at the Specialists Meeting in Aix-en-Provence to verify and validate the thermomechanical codes using experimental and analytical data: the square channel with transverse jet, and the T-junction of the LMFR secondary circuit. The former would test thermohydraulic calculations and experiments while the latter would test thermohydraulic and mechanical calculations.

A benchmark exercise on “T-junction of LMFR secondary circuit” was approved by the IAEA in 1996 in the scope of the subject co-ordinated research project (CRP). The physical phenomenon chosen here deals with the mixture of two flows of different temperatures (which induced temperature fluctuations that resulted in fatigue damage of the pipe wall).

2. DESCRIPTION OF THE BENCHMARK

2.1. Presentation of the problem

2.1.1. Introduction

The problem considered deals with the mixing of two flows at different temperatures in the secondary circuit of the LMFR (Fig. 1). During normal operation, sodium at low temperature flows into the main pipe of the secondary circuit. A small pipe, connected with a tee-junction to the main pipe, discharges sodium into the main pipe at a temperature, which is higher than in the main pipe. Work has been done at FRAMATOME-NOVATOME (France) to provide the participants with experimental data to harmonise and validate codes and methods by comparison of predictions with test results.

A set of French experimental data was made available to all the institutes, participating in the CRP, and these countries applied their codes and methods to analyse these data. The input data provided come consequently from the actual operation of the reactor. Necessarily, because of the complexity of these data, some have been simplified where possible (i.e. when it was certain that this simplification would not influence the results). Also, the comparison

of thermohydraulic results with the actual phenomenon was possible, owing to an instrumentation installed on site during the campaign of inspection.

It was agreed that each participant may concentrate his efforts to one or several benchmark problem areas.

This benchmark provided the opportunity to test numerical approaches on a real problem, not idealized but industrial, involving a number of parameters and different aspects of the phenomenon (thermohydraulic, thermomechanical, fracture mechanics). It allowed to compare the results of numerical approaches with some actual phenomena observed on site, in order to validate and to verify the adequacy of these approaches to simulate an actual phenomenon.

2.1.2. Temperature measurement

Temperatures were measured on the outer skin at 15 locations; 4 thermocouples (TC 1–3–15–6) along the meridian line on the down stream junction of the hotter side, 2 at the junctions (TC 10–11), 4 on the circumferential direction away from the meridional line and 2 thermocouples on 180° opposite to the meridional line. Acquisition periods are 1 ms for short record and 1.5 s for long record. Temperature records showed a slight skew symmetry of the temperature distribution, indicating that the jet from the branch pipe is directed side ways. The maximum linearised temperature difference across the wall is about 12 K with a non-linear peak component of 2 K. These values have been obtained after reconstituting the temperatures on the inner wall surface from the measured values and associated frequencies. Maximum reachable frequency by this is about 0.25 Hz; higher than this are not observable. The fatigue damage corresponding to the measured temperature fluctuations was assessed to be negligible.

2.1.3. Observations of cracks

Through cracks of about 100 mm length were observed on the circumferential weld (160 mm from the centre line of the branch, Fig. 1) at almost symmetrical locations on either side of the meridional line. These cracks were noticed after grinding of the external weld bead. The pipe was cut in air to observe the nature of cracks on the inner surface. An immediate appearance of a white spot around the tee (1st plume) was also noticed. While the white spot was due to the constant wetting of hot sodium, the black spot may be due to oxidation due to contact of air in the zone where hot and cold sodium mixing takes place. The cracks appeared on the black spot in the weld adjacent to heat the affected zone originated from the inner surface.

2.1.4. Metallurgical observations

The cross section of the weld and with crack was examined metallurgically. The cracks were transgranular and appeared as numerous thin striations. The characteristics of the crack clearly indicate that these cracks are due to high cycle fatigue.

2.2. Data provided

Time of operation of the circuit was approximately 90 000 hours. Information was provided on the mass flowrates, pressures and membrane stresses. Under the operating conditions temperatures of the sodium in main pipe were 320°C with flow rate of 2 850 m³/h and the

corresponding values for sodium in branch pipe are 410°C and 25 m³/h. Additionally, 15 thermocouples, mounted upon the external diameter of the main pipe, have given both mean and fluctuating temperatures for relevant positions. In addition to these measurements, a lot of visual inspections and metallurgical examinations have been performed and were available. They made possible to make comparisons with thermomechanical evaluations.

Geometrical characteristics:

- main pipe: $D = 494 \text{ mm}$, $t = 7 \text{ mm}$
- small pipe: $D = 68 \text{ mm}$, $t = 8.5 \text{ mm}$

Circumferential weld located 160 mm downstream from the tee junction (Fig. 1).

Operating conditions:

- no transient to be considered (only nominal steady state);
- total duration: 90 000 hours

External forces:

- forces and moments in the pipes due to weight and thermal expansion

Sodium characteristics (ρ , λ , C_p , α , ν) vs. temperature have been provided.

Material:

- base material: AISI 304;
- weld material: 16Cr-8Ni-2Mo

Main material characteristics (ρ , λ , C_p , α , S_y , stress-strain curve, cyclic curve, fatigue curve) have been provided.

2.3. Thermalhydraulic and thermal results required for comparison with experience

After the completion of thermalhydraulic and thermal calculations, each participant to the benchmark was required:

- characterize the mixing area, which means locate, define the dimensions of the mixing area, define the parts of the pipe subjected to the mixing phenomenon. Figures were to be given;
- provide isothermal lines (mean temperatures) on the parts of the pipe as defined previously;
- provide the temperature signals (temperature variations as a function of time) on inner and outer skins of the pipe at points significant, as well as the points noted a on Fig. 1 on inner and outer skins; (the points noted a on Fig. 1 locate thermocouples, which are fixed on outer skin of pipes);
- provide the results of a spectral analysis of the metal temperatures at the points defined above.

2.4. Scope of the benchmark

2.4.1. Objectives

Harmonization and validation of fast reactor thermo-mechanical and thermo-hydraulic codes and relations using experimental data aimed to investigate the capabilities of today's available industrial procedures and numerical methods to estimate the thermal loads on structures in contact with mixing flows at different temperature, as in case of thermal striping phenomena, in order to predict the damage induced on the structures.

The work of each participant was:

- to evaluate the thermalhydraulic behaviour of the phenomenon;
- to foresee the thermomechanical consequences on the main pipe of the secondary circuit (it had been operating for 90 000 hours).

The final objectives were to:

- compare the procedures used by the participants and to harmonize them;
- compare the results with the actual phenomena observed on site.

3. EXPERIMENTAL ACTIVITIES ON THERMOMECHANICS AND FRACTURE MECHANICS AT THE PARTICIPATING INSTITUTES

Indira Gandhi Center for Atomic Research, IGCAR (India)

Test facilities have been constructed recently in the domain of assessment of creep-fatigue damage under steady as well as transient conditions, thermal ratchetting and thermal striping on the LMFR component models and preliminary results are being obtained. Most of the results obtained have been effectuated during a commissioning stage, except for the tests on control plug mock-ups where cracks have been initiated after about 90 thermals shocks each with 24 hours hold period, the theoretical prediction of which based on viscoplastic analysis is about 70. Thus results have shown satisfactory comparison. Tests are in progress to study the crack propagation behaviour in the welds with and without initial defects. Relaxation tests conducted using 15 t high temperature component facility on circular plates having all the component features, viz. multi axially, weldments and stress concentrations have been discussed. Regarding thermal ratchetting simulations, the salient features of the test facilities constructed using hot air and cold water have been brought out.

The new features of the tests facilities is the use of air and water to simulate the thermal transients instead of sodium. In parallel, test facilities using the combination of electric heater coil and water is also being constructed. The thermal striping simulation is done in 3 stages. First, using water to derive the temperatures spectrum on 3 situations in FBR viz. bottom portion of control plug, expansion tanks and mixing T- junctions using water tests (hot water is about 85°C and cold water 10°C). Next to simulate the damage using hot gas (~650°C) and air at room temperature jets which impinge on the flat plates. Finally the results will be qualified by the tests in sodium in the facility called “INSOT” which is being constructed at the centre. A systematic programme has also been established to carry out the fracture assessment studies on secondary sodium piping as well as primary pump discharge ducts.

Power Reactor and Nuclear Fuel Development Corporation, PNC (Japan)

The activities covered the R&D for the development of design methods for LMFR components. Three sodium test facilities: thermal transient test facility for large structures, medium, and small size components are in operation. Results on 304 SS materials, with reference to MONJU reactor, obtained from test facilities. Tests on reactor vessel model and tube sheet to generate experimental data to validate the structural creep-fatigue failure criteria and confirm the inherent design margins in the design code (BDS for MONJU and DDS for future LMFR (DFBR). Recent models also include SS 316 FR partially. Tests are also planned for SS 316 FR which is the candidate material for DFBR.

Acoustic emission monitoring and ultrasonic testing methods are used to measure the crack propagation under thermal transients (about ± 40 K/s). Analysis is done with FINAS code and damage as well as crack growth are assessed. All the cracks data observed are stored as data base "STAR". The "STAR" data base provides input information for the damage calculation code, called PARTS-DS. It also helps to establish the design procedures for the creep fatigue design based on length and depth of crack at various elevations. Very sophisticated tests on tube sheets have indicated that the cracks appeared in the ligaments both on surface and through wall, indicating that thin ligaments are more dangerous. The transient temperature evaluation and striation due to crack propagation were used for validation of theoretical predictions by INFAS and CANIS codes.

Korea Atomic Energy Research Institute, KAERI, Korea Institute of Nuclear Safety, Republic of Korea, (Republic of Korea)

For the structural integrity tests on LMFR specific, the structural test facilities are under planning. The plant lifetime extension programme using fatigue and fracture mechanics technologies is in progress. A fatigue monitoring programme called K-FAMS (KAERI-fatigue monitoring system) that has the capability of computing the real time transient fatigue usage factor, has been developed to provide important information for structural reliability, the safe operation and the optimal time of inspection maintenance of the nuclear power plant components. The YGN unit 3 is the first NPP in Korea in which leak before break (LBB) concept was applied from the design stage. Towards structural integrity at high temperature guidelines for creep crack growth test at elevated temperatures were set up in the collaborative work at the Korea Standards Research Institute (KSRI) and the National Research Institute of Metals (NRI), Japan. Creep fatigue damage evaluation method using new damage function and viscoplasticity finite element programme, development of improved methods for calculating stress intensity factors for thermal loading and development of new creep crack growth parameter C_t developed and used.

OKB Mechanical Engineering, OKBM (Russian Federation)

The low cycle fatigue and fracture investigations done on tube-tubesheet joint intermediate heat exchanger (IHX) nozzle model of BN 600 reactor and IHX to IHX support shell joint. For the tube-tubesheet joint, two models with 19 and 37 tubes respectively were discussed. The test results for heating rate 50-70 K/h hold period of 3 h at 550°C and cooling rate with of 5-6.5 K/s had not indicated any fatigue damage. The tests on BN 600 nozzle model with the heat rate 60-90 K/h up to 600°C hold at 580-600°C for 3 h and cooling in time 30-40 s up to 400°C revealed no crack initiations in the all surfaces of 2 test models. The calculated peak to

peak strain values was 0.62% which can permit up to 3 000 cycles. The last aspect is on the creep fatigue damage on IHX support shell joint. The calculations showed that the margin on number of load cycles is less than the permissible value. Hence tests were conducted on the flat model, with 12Cr18 Ni material. The test temperature is 490°C. The calculation and experiments' comparison showed a good coincide. Accordingly crack initiation in the weld bead zone was observed after 1100 cycles by acoustic emission method for the clearance of 0.5 mm between the shells. If this width is increased to 2 mm, cracks were seen only after 2000 cycles.

AEA Technology, National Nuclear Corporation, NNC (UK)

To assess the influence of residual stresses on fracture behaviour with reference to CEGB-R6 procedure, tests were done in 2 phases. In phase 1, ductile tearing tests were done on aluminium alloy model material (AL 2024 and AL 5083) using 25 mm and 6.25 mm plate specimens. Residual stress field present in the through-thickness cracks is studied using 5 pairs; each pair consisting of plates with and without residual stresses. Under phase 2, fracture tests were done on surface cracks situated in a through-thickness self balancing residual stress field on welded A433-B steel material of 70 mm thick plate. Fracture resistance curves are drawn in the form δa vs P . Subsequently the experimental data points were placed in the Failure Assessment Diagrams (FAD). The data indicated that the points lie in the unstable region of FAD. Conclusions have not yet been drawn. The interesting aspect of tests is the measurement of residual stress field across the thickness and validate with the theoretical predictions as well as the trace of the surface crack profile. The investigation also covered the integrated research capability of NNC in terms of R&D expertise, special test rigs and facilities, rig manufacture, instrumentation, knowledge of reactor design, design engineering and safety case expertise. The main area of present works of NNC is on gas reactors. Some specific thermomechanical tests regarding creep/fatigue tests of stainless steel at elevated temperature, slat baths test rig tests on welded structures and oxidation structural tests on mild steel fillet welds at 300 to 500°C were done. Thermal shock tests in heat treatment, salt bath test facility have offered many interesting results on structural features involving cast to cast variations, surface finish, weldments, strain range, hold time and test geometries. The results have been used to support the experimental programme of the fast reactor in the UK and for EFR. The results have also been supplied to the EC Working Group on Codes and Standards (WGCS) for benchmark activities associated with elastic and inelastic analysis for comparison of rules and procedures. The presentation covers some of the important test rigs viz. VSR which is a full size pressurised CO₂ loop built in the 1960s to examine the vibration stability of gas cooled reactor core components, 1/8 and 1/4 scale boiler models which reproduce the complete AGR gas flow circuit, boiler stress corrosion cracking (SCC) rigs which permit the direct measurement of SCC in boiler steel exposit to austenitic water chemistries up to 350 °C and 17 MPa and CO₂ oxidation facility.

Cadarache Centre (CEA - France)

R&D in support of LMFR in the domain of high temperature fracture mechanics, LBB demonstrations, thermal stripping, ratchetting and behaviour of cracks on welded structures at high temperature were carried out. Apart from this, supporting R&D work carried out towards life extension of PHENIX reactor are continued. The objectives of most of the studies are to develop and validate the finite element method (FEM) in compliance with RCC-MR code and

A16 procedures. The important test facilities are: AMORFIS and PROFIS for the initiation and propagation studies on CR specimen, TUBFIS for the tubes under reverse bending, TERFIS for studying tubes under combined tension and thermal loads. In the domain of LBB demonstration, interaction of LBB and corrosion, development of an axisymmetric crack under complex loadings (CHARFIS programme) specific studies on vessels and pipes (SHELL and CHARLIE-FAR), validity of leak rate/leak creep correlation, crack shape evolution before and after through wall cracking and effect of seismic loadings on detectable through wall crack are highlighted. In order to improve the design rules against fatigue initiation in thermal stripping conditions, FAENA test facilities has yielded many interesting results on the effects of surface, environment weld and biaxial thermal strains etc. The results confirm the RCC-MR fatigue curve for high cycle fatigue damage assessment. The integrity fracture of FAENA tests is that it can depict the various cracks starting from initiation level to a complete penetration in a single test on a tube. A systematic experimental programme on feature tests using SOUFLE (plates under reverse bending) and SOFA (axisymmetric specimens under repeated thermal shocks and primary bending) has been conducted to improve the weld joint efficiencies recommended in RCC-MR for creep fatigue damage assessment. Some of the supporting R&D towards life extension of PHENIX are establishing crack initiation criteria for partial penetration welds by means of creep fatigue tests under mechanical or thermal shock conditions, crack initiation in the weldments the straight pipes in creep at around 650 °C and intergranular cracking near weld for 304, 316 and 321 steels based on mock-up tests and use of local approach used in conjunction with metallurgical observations.

4. SUMMARY OF ACTIVITIES WITHIN THE CRP ON THERMOHYDRAULICS, THERMOMECHANICS AND FRACTURE MECHANICS: RESULTS FROM INDIVIDUAL PROJECTS

Indira Gandhi Center for Atomic Research, IGCAR (India)

For the thermal hydraulic analysis, the PHOENICS code was used. A steady state analysis was performed and the pipe bend was seen to induce swirl into the main flow. The results showed the jet to follow the pipe wall. For the temperature and velocity investigation in the fluid, only the straight pipe section near the branch pipe was used. Thermal analysis was also conducted for the branch pipe junction and the main pipe. For the thermomechanical analysis, only the main pipe temperatures were necessary. A comparison of mean temperature profiles was performed and an idealised result close the AEA and PNC solutions was used for the subsequent thermomechanical analysis. The thermomechanical analysis was performed using 2D and 3D models. The 3D model was used for the stresses due to mean temperature distribution. The axisymmetric analysis was done using the CONE programme and calculations were done for the part through cracks. A fine mesh was used at the crack tip. Two models were used, one without the weld bead geometry and another with the weld bead profile. The thermal fluctuation loads were applied as a sinusoidal response. For the validation of results by FEM, case without bead and a temperature amplitude of 20 K was considered. The crack depths were investigated from 0.5 mm to 5 mm. The loading was applied at 0.065 Hz, 1 Hz and 2.25 Hz and stress intensity factors were compared. For the analysis mixing tee junction, weld bead is realistically modelled and analysed for temperature amplitude of 45 K. Subsequently, damage summations were performed. The code procedure of RCC-MR called σ_d - approach was used to calculate the time to initiate a crack (σ_d approach is a design approach of RCC-MR code to estimate the fatigue life of structures with crack like defects). The A16 procedure was used for the assessment of crack propagation

applied to 0.25 and 0.5 Hz frequencies and RCC-MR Paris law. Random fluctuating response was also assessed using the model without the head profile for studying effect of different frequencies which could be put together to assess the signal damage. Overall the crack initiation time was found to be 30-40 h and time to propagate a crack up to 5 mm is around 1000 h.

National Agency for New Technology, ENEA (Italy)

ENEA has several years experience in computational fluid dynamic both in CFD analyses and CFD numerical model development. The activities are mainly carried out in support of programs related to nuclear plant analysis and severe accident analysis. Analyses have been carried out on the thermalhydraulics of nuclear reactor containment (hydrogen stratification, hydrogen detonation, spring systems, aim steam leakage through concrete cracks), on the core-catcher and on the molten corium relocated in the reactor pressure vessel lower head. ENEA uses the TRIO E.F and CASTEM 2000 numerical tools both developed at CEA. They are finite element based codes for incompressible viscous flows. They allow the analysis of natural and forced convective flows both in laminar and turbulent conditions. .

Coupled thermal-hydraulic calculations of the tee-junction was performed based upon a finite element technique. A model of the tee-junction was set up including the fluid and the pipe walls and the model was extended down-stream till to contain the mixing area. The velocity field was computed by means of a numerical solution of momentum and mass conservation equations for a viscous and incompressible fluid. Floating effects (if relevant) was accounted in the limit of the Boussineq approximation. Turbulence was described by means of a $k-\epsilon$ model. Wall functions used to describe the turbulent-laminar transition near the wall. The temperature field predicted by means of a coupled analysis of the convection-diffusion in the fluid and diffusion in the wall. Established velocity profile, as well as uniform temperature in each of the two fluids, was assumed as upstream boundary conditions. The mass, momentum and energy conservation equations solved in coupled form and in transient conditions. The analysis was carried out by means of the TRIO E.F./CASTEM2000 finite element numerical codes. The results of the above described analyses (see attachment) are: (1) characterization of the flow mixing region and the mean temperature distribution in the sodium and in the pipe wall, (2) investigation the capability of $k-\epsilon$ based numerical models to predict low frequency oscillation in the velocity and in the temperature fields.

Power Reactor and Nuclear Fuel Development Corporation, PNC (Japan)

A DINUS-3 programme was used for a numerical simulation with a straight position of the pipe and the tee-junction modelled with 3D elements. The boundary element BEMSET thermal conduction code was used for the pipe itself. The pipe temperatures were computed at time steps and were linked to the thermal hydraulic computations. The jet trajectory was away from the wall, the jet direction was influenced by the secondary flows. A good comparison achieved when compared with measurements and it was possible to evaluate the sodium mixing mechanics in the different regions around the jet. For the thermomechanical calculations FINAS (thermomechanic) and CANIS (fracture) codes were used. The maximum stress amplitude is investigated by a simplified sinusoidal temperature fluctuation of 90 K and a computerised random signal analysis. Stress concentration factors at the welded joint ($K_{ave} = 2-3$) was obtained and mean stresses were determined using 3D model. A large number of possible crack initiation cases were checked and most possible cases were chosen for

assessment against fatigue. For crack propagation, the effect of mean stress was studied and showed to be important. Detailed FE calculations based on random temperature/stress fluctuations. The most dangerous frequency, was found to be 0.085 Hz for both crack initiation and propagation. Life time was predicted by using detailed finite element calculation base on random signal obtained by thermalhydraulic calculation.

Korea Atomic Energy Research Institute, KAERI (Republic of Korea)

The thermalhydraulic analysis using FLUENT codes was ceased in the middle of benchmark study. Therefore, two cases of thermalhydraulic loading based on the computation of AEA (UK) were used for thermomechanical evaluation. One is the simplified sinusoidal load cases with the alternating temperature differences of 90K and 70K with thermal striping frequencies of 0.1 Hz, 0.5 Hz and 1.0 Hz. The other is the random type thermal fluctuation load computed by AEA. The thermomechanical and fracture assessment for the random type load was carried out using the Green's function methods. A fatigue evaluation was performed against ASME subsection NH. The striping frequency of 0.5 Hz was the most severe however all evaluations showed unacceptable damage assessments. The assessment of random load was the least damaging. A fracture mechanics assessment was carried out for the sinusoidal and random thermal loadings. The sinusoidal cases were more severe than the random case. Results might be higher if mean stress effect is fully considered in determination of stress intensity factors. Cracks can initiate for both 90 K and 70 K cases and again 0.5 Hz is most critical. For crack propagation assessment the time to grow a crack to 5 mm length was 940 h for sinusoidal load and 42 200 h for random load. It is estimated that cracks would not penetrate the wall in 90 000 h because the level of primary stress is low.

OKB Mechanical Engineering, OKBM (Russian Federation)

For the thermomechanical calculations both 3D and 2D FE models were considered, the latter including the weld bead geometry. No random analysis were performed and stresses were determined for frequency range from 0.1 Hz to 5 Hz based on thermal and pressure conditions using the Russian code procedure and allowable number of cycles calculated from material fatigue curves for base metal and weld metal. Maximum damage was attributed to a frequency of 0.66 Hz. Time for which the cyclic strength requirement is reached is 9 h for welded joint and 730 h for the parent plate. A fracture assessment was performed using the ANKORT code and crack propagation (Stress controlled) through thickness determined. For the weld metal 750 h and parent metal 2 430 h is needed to propagate through thickness. These calculations assume linear stress distribution through thickness. When allowing for non linear distribution for stress the crack propagation is less severe.

Institute of Physics and Power Engineering, IPPE (Russian Federation)

A two-dimensional thermohydraulic model of the t-junction, allowing to perform numerous alternative calculations in a short time and to study consequences of design variations, has been developed and explanations of low-frequency pulsations of velocity and temperature appearance, in a mixing streams area located near a wall, have been done. Calculations on non-stationary periodic flow and temperature fields in fluids and on a pipe wall for the t-junction of a LMFR secondary circuit were carried out. The frequencies of oscillations of fluid in a mixing area were 8.1 and 7.45 Hz for radial and azimuthal oscillations respectively. The combinative frequencies were 7.77 and 0.325 Hz. At a frequency of 7.77 Hz the peak-to-peak temperature difference of a inner pipe skin was 28 K at thermocouple 2 position, at a

frequency of 0.325 Hz is 35 K at the same place. At a depth of 2 mm in a wall, the peak-to-peak temperature difference decrease down to 5 K at a frequency of 0.325 Hz. High-frequency oscillations did not penetrate at this distance. It is necessary to notice, that the lowest frequencies are being calculated as a difference of the highest frequencies. Therefore, the value accuracy of frequency is rough in a calculation, and the lowest frequencies may have no fixed value during an experiment. For thermomechanical calculations, it is necessary to use the most dangerous predicted frequencies.

AEA Technology, National Nuclear Corporation, NNC (UK)

Results of a thermal hydraulic assessment performed by the AEA were obtained using CF4X code. A steady state solution was performed and from this, the temperature fluctuations and synthesised time temperature histories for 32 s duration was derived. The calculations enabled results to be obtained in the pipe wall allowing that boundary layer attenuation using a 1D transient model. The presence of secondary flow arising from the pipe bend contributed to lifting the jet from the pipe wall. The presence of swirl from the fittings in the system should also be studied. The AEA calculations considered fatigue evaluations from a design assessment and failure assessment point of view. The approach was to consider avoidance δT , fluid δT and pipe wall δT and consider in addition the Minor summation approach. The effect of parent plate and weld behaviour was also investigated and fatigue strength reduction factors introduced to represent probably variations due to cast, flush weld, etc. Also effect of boundary layer attenuation is included and mean stresses from a 3D FE model. Results showed that crack initiation is not predicted due to the wall temperature differences that is predicted for parent plate and weld using fluid fluctuations from thermal hydraulic analyses. The effect of weld bead geometry is not included and may have additional effect and should be investigated. The NNC calculations considered fatigue assessment using UK method which suggested loading was possible in the weld. Fracture calculations which considered selected likelihood of initiation and propagation using the random traces from the AEA thermal hydraulic and measured traces. Studies were performed based on stress intensity factor variations. The calculations consider mean loads and effect of residual stresses in the weld and stress intensity factors were determined and added to the values for the random traces calculated using stress controlled and strain controlled stress intensities. A crack propagation analysis was performed using an upper bound Paris law. Crack initiation and propagation is possible for thermal hydraulic traces but not measured traces. Crack propagation analysis shows that the growth using stress controlled formulations is rapid. Result using strain controlled factors indicate that 2.8×10^4 - 18×10^4 hours are needed to grow through thickness. Thermal calculations performed by Leicester University examine the attenuation effects of wall thickness on the measured temperature signals.

FRAMATOME-NOVATOME (France)

Results for the CEA study were obtained using the TRIO-VF code and considered three models each with a successive level of refinement, the last one focusing the detailed area in the vicinity of the jet. The study involved a Large Eddy Simulation (LES). The jet followed the pipe wall. A spectral analysis with white noise was performed and a time duration of about 30 s was used. The diffusion coefficient is modified near the wall to get an improved solution. However, attenuation factor is such that thermal fluctuations would show no damage. The AEA results were selected as the worst case.

Thermal hydraulic analysis was performed by FRAMATOME using the Star-CD code. This computation included the effect of swirl and a sensitivity study was performed with and without this effect and it was shown that the swirl modified the jet trajectory such that it follows the pipe wall rather than lift away from it. It was considered that the bend would be insufficient to cover a swirl flow behaviour. The FRAMATOME-NOVATOME thermomechanical and fracture calculations covered assessment of sinusoidal fluctuations at 0.5 Hz and 1 Hz and random fluctuations from AEA results. A 3D study of mean stresses was performed using SYSTUS code and actual mean temperatures. Fatigue assessments using the sinusoidal fluctuation temperature at 0.5 Hz against RCC-MR showed negligible damage in the parent plate and unacceptable damage in the weld. Using the calculated AEA histories and flow, the fatigue damage was found to be again negligible in the parent plate and unacceptable in the weld. For the weld a fatigue strength reduction factor of 1.25 was used with a stress concentration factor of 1.7 for the weld bead. Fracture mechanics assessments using the sinusoidal fluctuation temperature showed rapid growth from 0.5 mm to 5 mm in 150 h assuming stress intensity variation and upper bound growth law. The effect of mean stress was shown to be important in calculating the time of propagation (between 160 and 2 200 h). It was also concluded that the crack would stop before nearing the wall because of low primary stresses.

5. COMPARISON OF THE ANALYSIS METHODS, CODES AND PREDICTIONS

A comparison was prepared of the Partners' results obtained from the thermohydraulic analysis and the fatigue and fracture studies. The comparison was done in tabular form (see attachment) and important differences highlighted. This tabular form was a starting point for a formulation of the main CRP results and recommendations.

6. THE CRP RESULTS AND RECOMMENDATIONS

6.1. The main results

6.1.1. Thermohydraulics modelling

- The models used in this benchmark show that the pseudo direct Navier-Stokes simulation is an alternative way in case of no subgrid scale model available, and is possible with standard codes.
- The steady - state approaches need a priori assumptions on the frequencies which are therefore not a result of the calculations. Moreover, the finite volume (or finite difference) implementation with precise discretization schemes are the most used.
- The boundary conditions prescribed are mainly steady - state, with spatial distributions in some cases and particular care is taken for the treatment of the wall attenuation.
- The domain size depends on the kind of grid. Non-structured meshes allow to model larger domains and a part of the hot pipe. Local refining is also useful for large domains. The number of computational cells varies significantly, but one can retain the order of 100 000 cells. The physical duration of the simulation remains short and insufficient as regard to the damaging low frequencies.

6.1.2. Comparison with Phénix measurements and between thermohydraulics computations

- Different types of flow behaviours are obtained: computation giving flattened jets provide temperatures close to the Phénix ones for location just behind the tee-junction. For further locations, mean temperature results are sparse. The closest results to experiments correspond to computational domains covering the whole pipe and made of fine meshes.
- An important dispersion is observed for the fluid peak to peak values. The low values are due to too diffusive calculations (k- ϵ run or finite element run with 1st order in space).
- The longer runs (as regard to the physical time) provide the lower frequencies (this means that the results depends strongly on this time). In all the cases, low frequencies measured on the Phénix are not found, which implies a too high attenuation by the metal wall. The maximum of fluctuation is found further downstream from the tee for the cases where steady boundary conditions are the closest to the tee junction.
- A reasonably good matching with measurements but on the meridian line is obtained for some cases, but the maximum measured peak to peak value of 19°K is not found by any calculation.

6.1.3. Thermomechanical assessments

- In spite of the different codes used, the maximum stress range values obtained are consistent. The prediction of cracking is strongly dependent on the fatigue strength reduction factor applied in the method. It appears that if this coefficient is too severe, the parent metal is found cracked which is not observed in reality.
- The geometrical discontinuity formed by the weld bead has to be considered. However, the actual value in a sharp discontinuity is not easily assessable by classical FEM (finite elements method). In that case a σ_d approach could be a good alternative. The crack propagation results are diverging due to the different formulations used for the stress intensity factor variation and due to the presence or not of a mean stress effect.

6.2. Recommendations

6.2.1. Range of frequencies, sampling

The range of the damaging frequencies from the wall thickness should be determined firstly:

- frequencies lower than this band do not produce sufficient ΔT across the wall,
- frequencies higher than this band cannot penetrate the wall.

-The physical time of computation is deduced from the lower bound of the range, considering that this physical time must cover at least 10 periods of this low frequency. The time step of the computation must also be able to catch the higher bound of frequency. (There can be other and more severe constraints (numeric) for the time step).

6.2.2. Domain and boundary conditions

The main objective is to provide realistic boundary conditions. Some phenomena cannot be modelled by a local thermal hydraulic domain. Hence, the boundary conditions should include:

- secondary flows (e.g. swirl flow)
- low frequency variations of temperature and/or velocity.

A parametric study can be a good way to state on the necessity of modelling those phenomena.

- The following recommendations are proposed for elaborating the thermohydraulic model:
 - a) use of an extended domain (mainly upstream) plus prescription of low frequency phenomena at boundary conditions. Mesh must remain very fine in the region of temperature fluctuations : non structured grids and local refinement are therefore very useful;
 - b) an alternative way is the use of realistic boundary conditions from experiments or other computations which can allow the use of a smaller domain;
 - c) if the physical time required (by the range of frequencies of interest) is too long and not compatible with the CPU time, catch high frequencies on the small domain and during a relatively short physical time by assuming to disconnect high and low frequencies, add low variations of temperature to the computed signal of temperature for the thermomechanical analysis. The low frequencies (if in the range of interest) may appear in the computation as a combination of two neighbouring frequencies in case of fluctuating flow near the wall. But, if they depend on a global behaviour (loop scale or plant itself), should be got from measurements (e.g. correlation with flow rate signals). In case of a pipe, the domain must include the full pipe (not half or part of it).

6.2.3. Thermohydraulic simulation

- Transient simulation using a Large Eddy Simulation model (or as a pseudo direct Navier-Stokes simulation if no subgrid model is available) is recommended. The discretization schemes must be at least of order 2 in space. Order 2 in time is also better but not completely needed.
- Care must be given to the transient behaviour of the first computational mesh (mesh adjacent to the wall) in association with transient heat transfer coefficient with induced filtering of high frequencies. The effect of small geometrical singularities may not be negligible, but this problem is of secondary priority and cannot be solved before the problem of attenuation on a flat plate.

6.2.4. Thermomechanical calculations

Mean stresses shall be considered in the fatigue damage assessment. The mean stresses influence also the crack propagation. A parametric study is recommended to quantify this influence and the manufacturing residual stresses have to be included in the analysis.

A weld can be characterized by 3 parameters: a) the weld bead which is a geometrical discontinuity; b) a different material from the parent metal; and c) the presence of residual stresses. These parameters influence the time to initiate and propagate a crack and must be defined precisely. In particular, the factor 1.25 applied on the fatigue rupture curve to represent a material effect is too low to cover all the consequences induced by the «as-welded» weld. It is therefore recommended to take care to the representation of the weld in thermomechanical assessments.

Combination of major cycles with thermal striping cycles is necessary to get the total fatigue damage.

The time to propagate a crack is sensitive to formulation chosen for the stress intensity variation. The strain controlled formulation is preferred to the stress controlled one for this problem.

A 3D crack could be assessed in relation to the size of the mixing zone involved (here the size of the hot spot).

The sensitivity of the defect depth on the threshold of the stress intensity factor should be taken into account. The σ_d approach using the random signal if possible could be a good alternative.

Beyond 70% of the thickness, an analysis of the instability of the remaining ligament shall be performed.

Appendix

COMPARISON OF THE ANALYSIS METHODS, CODES AND PREDICTIONS

1. THERMOHYDRAULIC METHODS

1.1 Model – Numerics:

	AEA (UK)	ENEA (Italy)	CEA (France)	FRAMATOME (France)	IGCAR (India)	PNC (Japan)	KAERI (Korea)	IPPE (Russia)	OKBM (Russia)
Code	CFX4	Castem 2000	Trio-VF	Star-cd	Phoenix	Dinus-3	Fluent	Turbo-flow	TUPT
Type	FV	FE	FV	FV	FV	FD	FV	FV (2 models 2D)	FV
Fluctuations calculated from	$k-\epsilon-\theta^2$ + spectrum assumptions	ps. DNS	LES	ps. DNS	k- ϵ -RSM (cylind. part) + DNS on smaller domain	ps. DNS	k- ϵ -RNG	transient transport equations no turb model	steady NS equations no turb model
Steady/ transient	steady	transient	transient	transient	steady + transient	transient	transient	transient	steady
Spatial scheme (order)	High upwind (2)	1	QUICK (3)	Ui: central diff (2) T : blend (central diff. + upwind) (1-2)	Hybrid (1) (SIMPLE algorithm)	convection high upwind (3) diffusion: central diff (2) leap frog (2)	QUICK (3)	implicit	
Time scheme (order)		1	1	1	1		1	1	

RNG: k- ϵ - variant (Renormalization group)

RSM: Reynolds stress model

All models 3D except Turbo-flow.

- The pseudo Direct Navier-Stokes simulation is an alternate way in case of no subgrid scale model (LES) available, and is possible with standard codes;
- The steady approaches need a priori assumptions on the frequencies which are therefore not a result of the calculations;
- The finite volume (or finite difference) implementation with precise discretization schemes are the most used.

1.2. Boundaries

	AEA	ENEA	CEA	FRAMATOME	IGCAR	PNC	KAERI	IPPE	OKBM
Boundary conditions	pipe profiles steady	constant steady	constant steady + 5% white noise	constant steady	steady for steady k-ε run random for DNS run	steady spatial distribution from experiments	steady constant	steady	steady
Wall treatment (thermics)	damping function in laminar sublayer	laminar (cond.)	wall function in laminar sublayer	laminar (cond.)	standard (wall function)	1st mesh attenuation by transient heat coeff.	standard (wall function)	heat transfer coeff.	heat transfer coeff.

- For PNC CEA and Framatome: discretization includes viscous sublayer
- The boundary conditions prescribed are mainly steady, with spatial distributions in some cases
- Care is taken for the treatment of the wall attenuation.

1.3. Domain and grid

	AEA	ENEA	CEA	NOVATOME	IGCAR	PNC	KAERI	IPPE	OKBM
Domain size: Grid	non structured	non structured	structured	non structured + local refinement	structured BFC	structured	structured BFC	structured 2 domains 2D	structured
Main pipe: upstream T (m)	2.5	0.1 part of pipe	0.39	4.5	steady run: cylinder + bend half pipe	0.085	cylinder + bend	cylindrical part	cylindrical part
downstream T (m)	0.6	0.5	0.64	1.8	DNS: $10 \times 10 \times 1 \text{ mm}^3$	0.620			
Hot pipe (from junction) (m)	0.3	0.1	0.17	0.65		2 cells			
Grid (total of cells)	102 984	50 000	167 854 ~130 000 used	96 727 (whose 1456 solid cells)	steady run: 16 600 DNS:1250	180 000		2000	45 000
Physic duration of simulation (s)	(steady)	1	27.4	85	DNS: 0.35	10		45	
CPU time (h)	20	-	1000	350					

BFC: boundary fitted co-ordinates (curvilinear)

- The domain size depends on the kind of grid. Non-structured meshes allows to model larger domain and a part of the hot pipe. Local refining is also useful for large domains;
- The number of computational cells varies in great proportions, but one can retain the order of 100 000 cells for LES or DNS calculations;
- The physical duration of the simulation remains short and insufficient as regard to the damageable low frequencies

1.4. Results of calculations

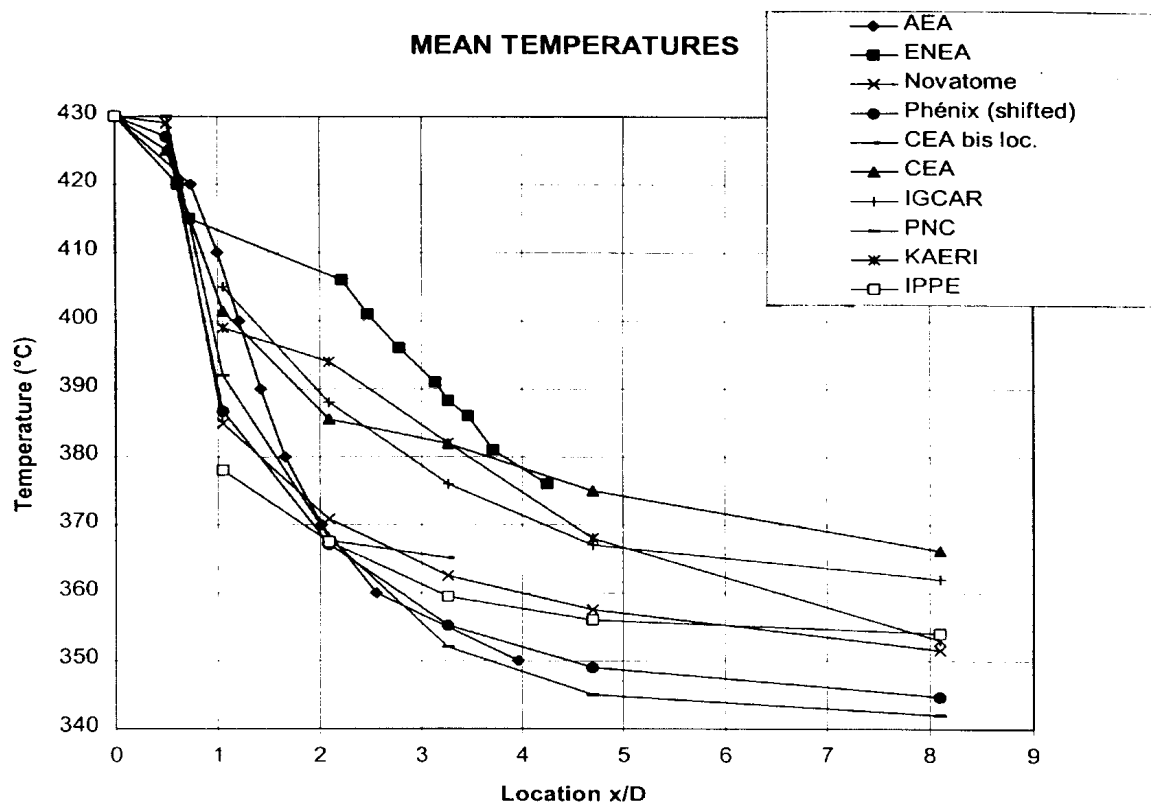
1.4.1. Hot-jet in the main pipe, mean temperatures along the meridian line (hot spot side)

Behaviour of the hot-jet in the main pipe:

AEA	CEA	Framatome	ENEA	IGCAR	PNC
rised	flattened	flattened (with swirl)	flattened	rised	flattened

flattened: the hot jet is turned down along the main pipe wall, behind the tee-junction;
 rised: the hot jet is directed towards the centre of the main pipe.

1.4.2. Mean temperature profiles - along the meridian line (hot spot side):



- Different types of curves are observed : The flattened jets curves are close to the Phenix measured one for x/D less than 1.5 (CEA, PNC, Framatome);
- For higher values of x/D curves are sparse and are mainly parallel to the Phenix one. The closest results correspond to domains covering the whole pipe, and made of fine meshes.

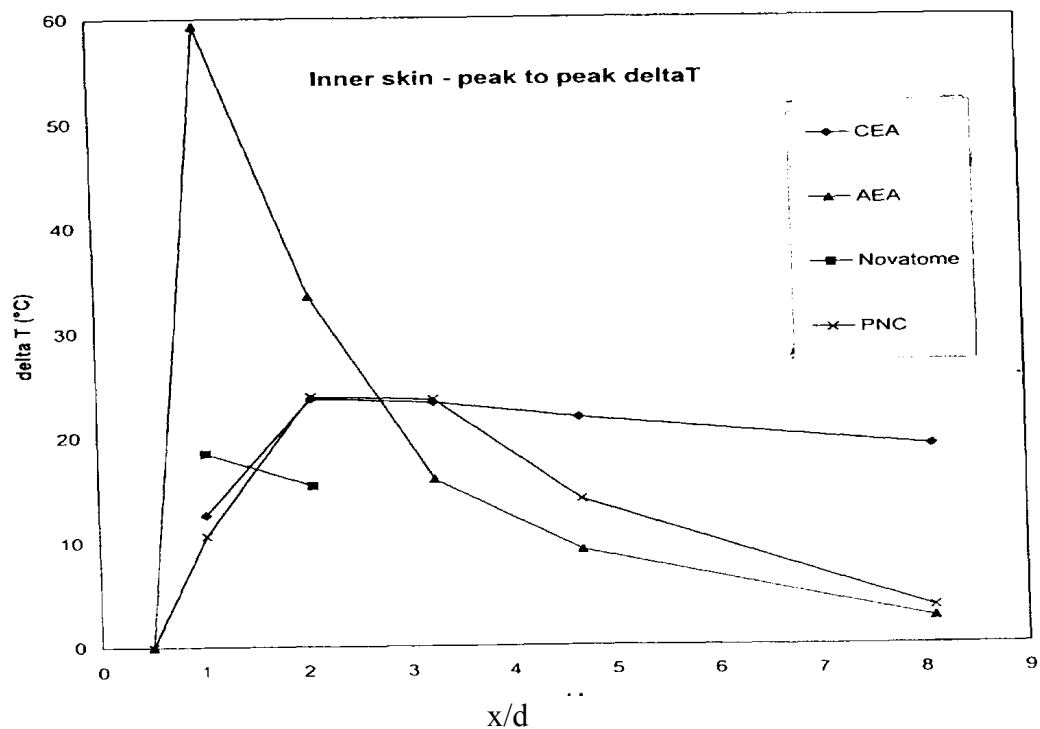
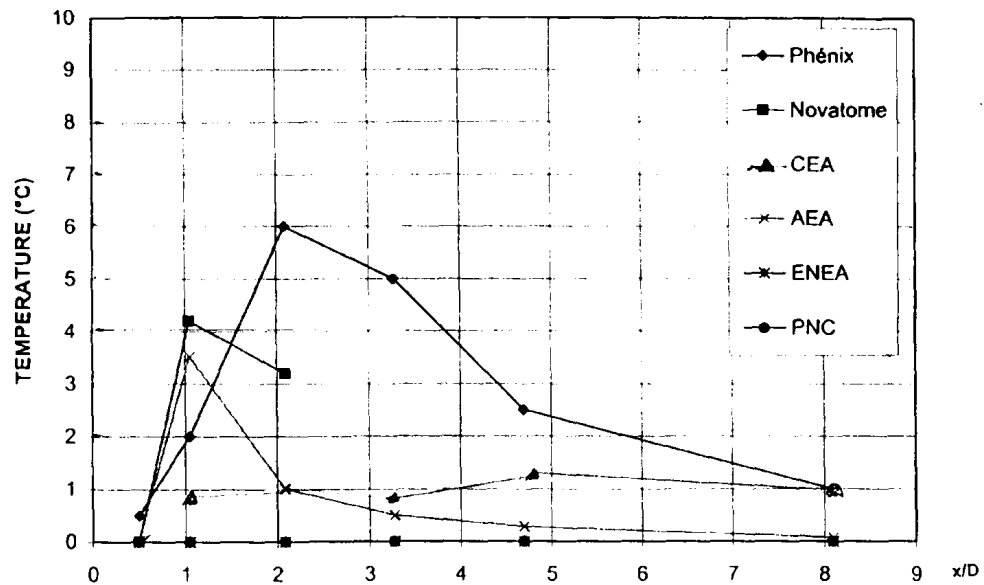
1.4.3. Temperature fluctuations

Maximum ΔT (potential: 90°C)	AEA	ENEA	CEA	FRAMATOME	IGCAR	PNC	KAERI	IPPE	OKBM
in fluid	75 (TC1)	4 (TC4)	68 (TC3)	73 (TC1)	40	35 (TC2)	10	63	60
at inner skin	60 (TC1)	-	24 (TC2)	18 (TC1)	-	24 (TC2)	-	28 for 8 Hz 38 for 0.325 Hz	59 for 0.01 Hz 38.5 for 2 Hz
at outer skin	3.5 (TC1)	~0	1.2 (TC15)	4.2 (TC1)	-	-	-	-	-
frequencies range	prescribed	-	5 to 30 Hz	0.1 to 10 Hz	1.95 Hz	1 Hz shedding	3.8 Hz	7.45, 8.1 Hz	0.01, 2 Hz
major peaks	spectrum	6 Hz	6.6 and 11 Hz	1 Hz		8 Hz Karman vortex			
secondary peaks		12 Hz		0.7, 8 Hz		Karman vortex			

- An important dispersion is observed for the fluid peak to peak values. The very low values are due to too diffusive calculations (k - ϵ run or finite element run with 1st order in space);
- The longer runs (as regard to the physical time) provide the lower frequencies, this means that the results depends strongly on this time;
- In all the cases, low frequencies measured on Phenix are not found, which implies a too high attenuation by the metal wall;
- The maximum of fluctuation is found further downstream for the cases where steady boundary conditions are the closest to the tee junction.

1.4.4. Peak to peak temperature at pipe outer and inner skins

PEAK TO PEAK TEMP. PIPE OUTER SKIN



- The Framatome and AEA curves provide a reasonably good matching with measures but on the meridian line. The signals of temperature computed by PNC do not cross the wall (not enough low frequencies).
- CEA and PNC results are similar at outer skin but differ about the frequencies, which imply greater outer skin fluctuations for CEA case.
- The maximum measured peak to peak value of 19°C is not found by any calculation.

2. FATIGUE DAMAGE ANALYSIS

2.1. Fluctuating stress evaluation

	$\Delta\sigma$
AEA	Not calculated
NNC TC01A	386 MPa analytic.
FRA TC01A	340 MPa analytic.
PNC TC5	373 MPa 2D FEM
KAERI TC01A	292 MPa 2D FEM
IGCAR TC2	360 MPa (480 MPa) 2D FEM (σ_d approach)
OKBM TC01A	360 MPa 2D FEM

- It can be noted that the maximum stress used in the thermomechanical assessment is similar from one participant to another.

2.2. Stationary stress evaluation

Axial mean stress	due to the forces and moments	due to the hot spot
AEA and NNC	< 10 MPa	-70 MPa < < 5 MPa
FRA	< 10 MPa	-40 MPa < < 40 MPa
PNC	< 10 MPa	-73 MPa < < 0 MPa
KAERI	< 10 MPa	-89 MPa < < 5 MPa
IGCAR	< 10 MPa	-80 MPa < < 3.5 MPa
OKBM	< 10 MPa	-30 MPa

- The stresses due to the forces and moments in the pipe are found low by all the participants.
- The stresses due to the hot spot are defined using a 3D finite element model. The values depend on the spot extension, and are therefore different according to the participants.

2.3. Fatigue assessment methods

	PNC	KAERI	IGCAR	OKBM	AEA	NNC	FRAMATOME
Loading	ΔT	ΔT	ΔT	ΔT	$\Delta\theta_{\text{peak max}}$ [or Rainflow: $N = f(\Delta\theta_{\text{peak}})]$	$\Delta\theta_{\text{peak max}}$	$\Delta T1, \Delta T2 = f(\text{time})$
$\Delta\sigma$	FEM $\Delta\sigma = f(\Delta T, \text{time})$	FEM	FEM + σ_d approach	FEM	-	-	$\sigma = f(\text{time})$ analytically or by FEM Rainflow $\sigma = f(N)$
$\Delta\varepsilon$	$= \Delta\sigma^*/E$ (not design)	ASME-NH with von Mises	RCC-MR procedure	Russian norms	-	$\Delta\varepsilon = \alpha \Delta\theta_{\text{peak}}/(1-\nu)$	$\Delta\varepsilon = 2K(1+\nu)/(3E)\Delta\sigma$ (RCC-MR)
Fatigue curve	Specified curve turn into Japanese eq.	Specified curve	Specified curve	Specified curve	Specified fatigue curve divided by FSRF	UK curve using a crack based model	Specified fatigue curve
Damage criterion	$V = N/N_{\text{adm}}$	$V = N/N_{\text{adm}}$	$V = N/N_{\text{adm}}$	$V = N/N_{\text{adm}}$	$\Delta\theta_{\text{peak all}}$ $= 3/2\Delta\varepsilon_{\text{all}}(1-\nu)/$ $((1+\nu)\alpha)$ $\Delta\theta_p < \Delta\theta_{p \text{ all}}$ (or $V = N/N_{\text{all}} < 1$)	$\Delta\varepsilon < \Delta\varepsilon_{\text{all}}$	$V = N/N_{\text{all}} < 1$

- Each participant used their own procedure. All the participants but NNC used the given fatigue curve including particular specification according to their procedure.
- A sinusoidal signal has been used in the case when the thermohydraulic calculation fails to provide an adequate predicted signal.

2.4. Fatigue data

Cumulated coefficient, C, applied to the parent metal fatigue curve and corresponding allowable strain range at 10^8 cycles :

	parent metal	weld
AEA	C = 1.6 (average) $\Delta\epsilon_{all} = 0.163\%$	C = 2 (average) $\Delta\epsilon_{all} = 0.13\%$
NNC	C = 1 $\Delta\epsilon_{all} = 0.266\%$	C = 1.25 $\Delta\epsilon_{all} = 0.213\%$
FRA	C = 1 $\Delta\epsilon_{all} = 0.261\%$	C = 2.5 $\Delta\epsilon_{all} = 0.105\%$
PNC	C = 1.2 $\Delta\epsilon_{all} = 0.192\%$	C = 1.5 (+ geom. coeff.) $\Delta\epsilon_{all} = 0.153\%$
KAERI	C = 1	C = 1.25 (+ geom. coeff.) $\Delta\epsilon_{all} = 0.213\%$
IGCAR	C = 1	C = 1.25 $\Delta\epsilon_{all} = 0.213\%$
OKBM	C = 1	C = 1.9

- AEA provides the most pessimistic coefficient for the parent metal as it considers that the material is affected by different parameters which are :
 - * surface finish, proposed reduction factor : 1.2
 - * ageing, proposed reduction factor : 1.2
 - * environmental effects, proposed reduction factor : 1.1
 - * cast-to-cast variation, proposed reduction factors : 0.83, 1, 1.2

Considering these parameters leads to decrease the specified base metal curve by a factor ranging from 1.3 to 1.9, the "mean" curve being affected by a factor 1.6 in comparison with the specified one.

- For the weld, the most penalising curve is also provided by AEA, but no geometrical coefficient is used to take into account the weld bead.

2.5. Mean stress effects on fatigue assessment

AEA	no
NNC	no
FRA	no
PNC	yes but not sensitive
KAERI	no
IGCAR	no
OKBM	yes

- all the participants but OKBM found that the mean stress effects are negligible and do not take them into account. For OKBM, this mean stress effect is introduced directly in the Russian procedure.

2.6. Plasticity effects

AEA	no
NNC	no
FRA	yes
PNC	no because very limited zone
KAERI	yes
IGCAR	yes
OKBM	no

- The plasticity effects are included in several analyses. PNC and KAERI have defined the plasticity amount using finite element modelisation. A limited zone of plasticity was found.

2.7. Weld coefficients

Applied	On the fatigue curve	On the stress range
AEA	1.25	-
NNC	1.25	-
FRA	1.25	1.7
PNC	1.25	2.3 (included in the FE model)
KAERI	1.25	1.48 (included in the FE model)
IGCAR	1.25	-(σ_d approach)
OKBM	1	1.9

- Considering both the reduction of the fatigue curve and the geometrical coefficient due to the weld, the most severe assessment is performed by PNC.

2.8. Fatigue assessment results

parent metal			weld	
AEA	TC01A	yes	TC01A	yes
NNC	TC01A	no	TC01A	yes
FRA	TC01A	no	TC01A	yes
PNC		no	TC5	yes
KAERI		no	TC01A	yes
IGCAR		no	TC2	yes
OKBM	TC01A	yes	TC01A	yes

Results turned into strain ranges $\Delta\epsilon$, and associated margin as regards the failure (margin = $1 - \Delta\epsilon/\Delta\epsilon_{all}$):

		parent metal		weld
AEA	TC01A	$\Delta\epsilon = 0.18\%$ $m = -10$	TC2	$\Delta\epsilon = 0.14\%$ $m = -4$
NNC	TC01A	$\Delta\epsilon = 0.21\%$ $m = +22$	TC01A	$\Delta\epsilon = 0.21\%$ $m \approx 0$
FRA	TC01A	$\Delta\epsilon = 0.21\%$ $m = +20$	TC01A	$\Delta\epsilon = 0.4\%$ $m = -91$
PNC	-	$\Delta\epsilon = 0.1\%$ $m = +48$	TC01A	$\Delta\epsilon = 0.23\%$ $m = -50$
IGCAR	-	-	TC01A	$\Delta\epsilon = 0.41\%$ $m = -1$

- The parent metal is predicted cracked for AEA and OKBM (this is not observed in reality) showing that these assessments are too conservative. For AEA, this tends to show that the FSRF chosen is too large for the present material.
- All the participants prove that the weld has cracked but the margins obtained are very different. It appears that the NNC results are just sufficient to demonstrate the failure. This suggests that the influence of the weld is probably greater than the coefficient 1.25 considered. This is also the case of the AEA analysis.
- The others have considered a geometrical effect to take into account the weld bead and display a larger margin regarding the limit.

3. CRACK PROPAGATION ANALYSIS

3.1. Fracture assessment methods

Paris law: $da/dN = C \Delta K^n$	PNC $da/dN = C \Delta J^n$	KAERI	IGCAR	OKBM	NNC	FRAMATOME
C (m/cycle)	9.43×10^{-17}	-	1.8×10^{-8}	4.2×10^{-8}	2.66×10^{-12}	7.5×10^{-13}
n	1.816	-	4	2.9	4.17	4
ΔK	$\Delta J = (1 - \nu^2)/E^* \Delta K^2$ $\Delta K = K_{\max} (1-R)^n$ $n = 0.5$ stress controlled	Same as Framatome	FEM + A16 procedure strain controlled	$\Delta K = K_{\max} (1-R)^n$ stress controlled	function (K) K for edge crack in a rectangular plate strain and stress controlled formulations	function (K, R, plasticity) K for plate formulated by Newman and Raju stress controlled formulation
$\Delta K_{\text{threshold}} (\text{MPa.m}^{1/2})$	none			$(10^{-8}/C_0)^{1/n}$	2.8	$-4R+6.5$

- The Paris law is used with different coefficients and hypotheses according to the reference temperature, the lower or upper bound hypothesis chosen. Also two kinds of formulations are used : strain or stress controlled.

3.2. Residual stress values

	Membrane σ_m	Bending σ_b
NNC	0	$\sigma_{1\%}$ average
FRA	0	$\sigma_{0.2\%}$ mini
PNC	0	$\sigma_{0.2\%}$ average
KAERI	0	0
IGCAR	0	0
OKBM	0	0

- Half participants takes them into account as mean stresses.

3.3. Mean stress effect

Mean stress considered on:

	Threshold	Crack growth
NNC	yes	no
FRA	yes	yes
PNC	no	yes
KAERI	no	no
IGCAR	no	yes
OKBM	no	yes

- The mean stresses are not always considered in the crack growth assessment or in the threshold formulation

3.4. Crack propagation results

	Time to failure at a 5 mm depth
NNC	~ 25 000 h
FRA	160 h < < 2200 h
PNC	112 000 h < 13 000 < 3300 h
KAERI	42700 h < < 941 h
IGCAR	1094 h < < 148 h
OKBM	~ 750 h weld < 2430 h parent metal

- All the fracture assessment results suggest a crack propagation through the thickness within 90000 hours (the threshold value is always lower than the stress). However, the results are spread out. The factors of dispersion are mainly due to the mean stress value, the formulation for the stress intensity factor and the different coefficients taken for the Paris law.

Annex

WORK PERFORMED BY THE RESEARCH GROUPS AT THE PARTICIPATING INSTITUTES WITHIN THE CRP

THERMOMECHANICAL AND THERMOHYDRAULIC ANALYSES OF A T-JUNCTION USING EXPERIMENTAL DATA

O. GELINEAU, M. SPERANDIO, J.P. SIMONEAU, J.M. HAMY
FRAMATOME - NOVATOME, Lyon, France

P.H.L. ROUBIN
CEA DRN SERA, Saint Paul lez Durance, France

Abstract. The objectives of the benchmark are to examine the ability of the assessment methods to explain the actual phenomena observed in order to determine whether the design methodologies without being too severe could successfully avoid any damage on the component. The paper represents the French contribution to this benchmark. After a description of the numerical codes used in the thermal-hydraulic and thermomechanical domains, the application of French methodologies is performed on the benchmark.

1. INTRODUCTION

For this benchmark, a flow mixing problem downstream a T-junction of the Phénix reactor has been chosen, because temperature measurements (on the pipe external wall only) and a post mortem mechanical expertise are available: cracks have been detected in a circumferential weld located 160 mm downstream the small branch axis (Fig. 1). This study gives an opportunity to perform a coupled thermalhydraulics-thermomechanics analysis methodology in an actual industrial context. The thermalhydraulic contribution to the benchmark has to provide the temperature field in the pipe wall, prior to the mechanical study. To capture the fluctuations of temperature in the flow, two thermal-hydraulic analyses are carried out: one using Large Eddy Simulation (LES) with TRIO-VF code (used in CEA), another using a pseudo Direct Navier-Stokes formulation with STAR-CD code (used in FRAMATOME).

In the FRAMATOME contribution, the STAR-CD DNS was performed on a global model extending several diameters before the main pipe elbow. It also includes parts of solid walls in order to compute at the same time the conduction effects. The computation shows the hot jet turned down along the main pipe wall, and slightly deviated by the swirl flow prescribed at the cold inlet. The temperature fluctuations in the sodium reach 73°C. The range of frequencies extends from about 0.1 Hz to 10 Hz with a major peak at 1 Hz. But those fluctuations do not produce enough temperature variations on the outer skin of the wall because the very low frequencies observed on the experimental signals are not found numerically (those frequencies can be explained by a slow deviation of the hot spot).

In the CEA contribution, because of the time and memory size requirements inherent to this technique, the problem has to be split into several independent steps. Each step provided the boundary conditions for the following step, the latter being solved on a sub-domain of the former. The TRIO-VF LES shows that, because of its low momentum compared to that of the main duct flow, the small branch flow is pushed down onto the pipe wall, resulting in a narrow mixing zone with steep circumferential temperature gradient on the wall. Maximum fluctuations in the fluid reach 68°C on the edges of this mixing zone close to the cracked weld, but the high frequencies of these fluctuations are efficiently damped by the sodium boundary layer and almost no amplitude can be predicted on the outer side of the pipe, unlike experimentally observed.

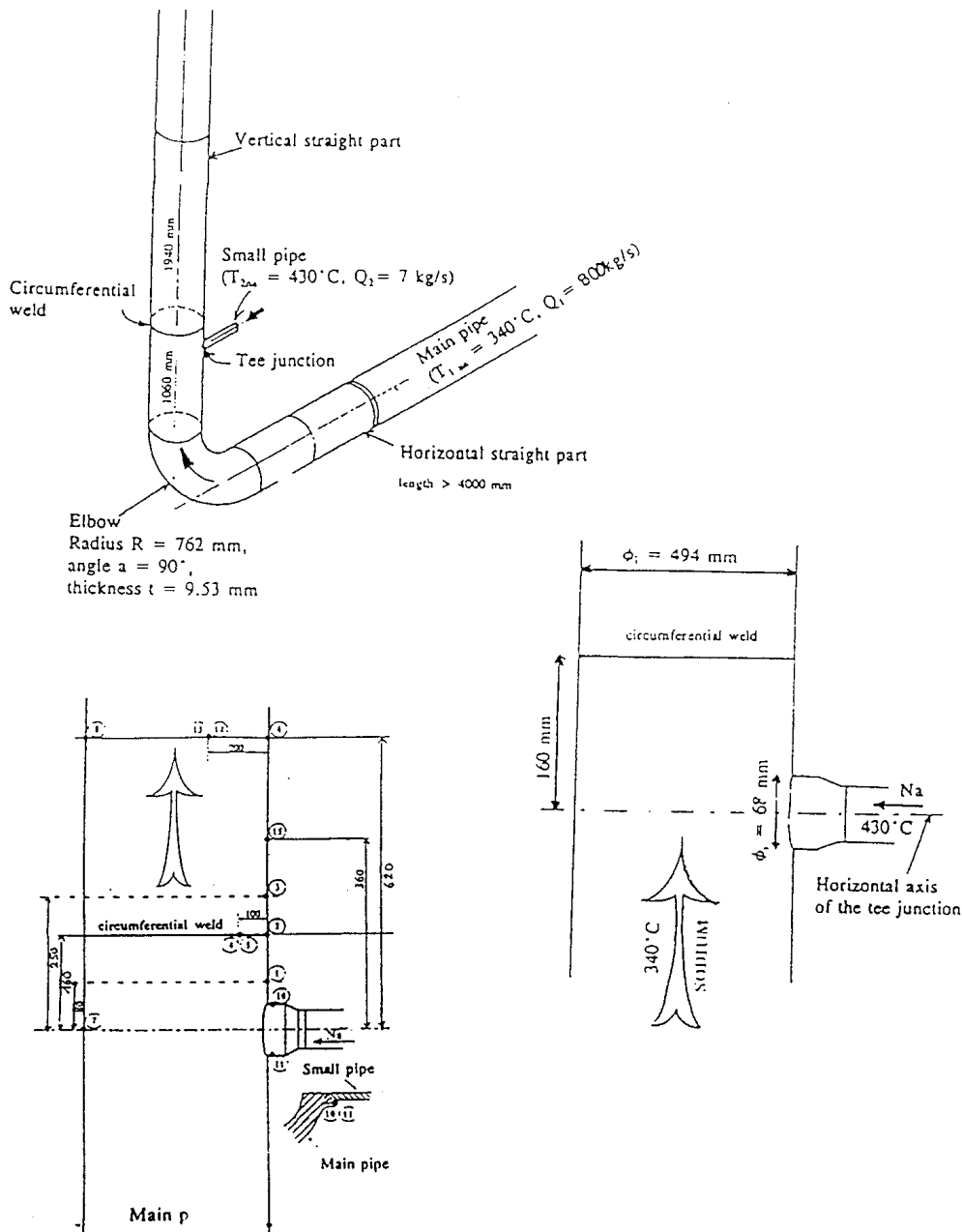


FIG. 1. Presentation of the benchmark geometry.

Finally, it appears that the prediction of fluctuations is difficult, and to obtain practically usable results (exploitable time history signals of temperature), a fast powerful code is necessary (fine mesh, extended domain, unsteady run over a long physical time, low diffusive solver). Furthermore, very low frequencies which have influences on the medium frequencies and then on the damage on the component, are not predicted by the present computations. A thermomechanical analysis is then performed (by FRAMATOME) using two kinds of thermalhydraulic loadings:

- predicted random temperature fluctuations,
- simplified sinusoidal temperature fluctuations.

The fatigue damage is estimated. It is found that cracks may be initiated in a few hours in the circumferential weld (inner side) of the main pipe for both loadings. On the contrary, no

initiation of crack can occur in the base metal during 90 000 hours. A fracture mechanics assessment shows that the cracks propagate rapidly through the wall and stop at about 1 mm from the outer side of the wall due to the lack of significant solicitation able to break the remaining ligament.

1.1. State of art

Problems referred to as thermal striping problems or high cycle number thermal fatigue may be created since it exists a transition zone between a "hot" fluid and a "cold" fluid. For instance:

- a mixing zone between two flows at different temperatures,
- a stratification zone able to fluctuate during operation.

The quantification of these phenomena is not easy due to the random feature of the fluctuations, but it appears essential as important damages may be generated. Several problems were identified in the past. They involved thermal fluctuations and material cracking was observed.

Up to now, the prediction of such fluctuations was performed by means of a simplified approach where the fluctuations were modelled by a monofrequent sinusoidal signal. This approach is not satisfactory because it does not represent the random behaviour of the actual loading and may be overconservative if the frequency is not well chosen.

This simplified approach constitutes an alternative approach to eliminate a certain number of problems from the design stage of a project. However, a finer prediction of the fluctuating aspect of the thermal loading is required by engineers to solve the most difficult cases and to save expensive design modifications. This is now allowed by recent thermalhydraulic techniques.

The most employed CFD models rely on the Reynolds Averaged Navier Stokes equations modelling (RANS), which now benefits from a long and successful experience but also requires much empirical adjustment and can only provide limited statistical quantities of the fluctuations, mainly second order correlations such as the temperature variance.

Thanks to the continuous progress in computing power, LES or DNS is no longer limited to «academic» simple flow problems but now emerges as an acknowledged technique for industrial flows. Its disadvantage of requiring heavy computations is compensated, when appropriately used, by the quality of the predictions, less sensitivity to model parameter adjustment and its unique capability to provide the full time history of the flow variables.

2. DESCRIPTION AND VALIDATION OF COMPUTER CODES

2.1. Thermalhydraulic codes

2.1.1. TRIO-VF code

The TRIO-VF code, developed by CEA/DRN [1], solves the 3D Navier-Stokes and energy equations for a non compressible fluid, buoyancy being accounted for by the Boussinesq hypothesis.

Spatial discretisation is a finite volume method applied to a staggered cartesian or cylindrical grid. Convective terms are modelled with the second order «Quick-Sharp» [2] scheme and time discretisation can be a first (Euler) or a second order (Runge-Kutta) scheme.

The solving algorithm is derived from the semi-implicit SOLA method [3].

The subgrid-scale model used for turbulence modelling in the LES uses a classical eddy viscosity concept formulated by the «selective structure function» model [4].

TRIO-VF has been validated both through International Benchmark exercises [5] and on more specific experiments carried out in the field of nuclear engineering [6-8].

Concerning LES, the validation domain must still be extended, but already successful comparison with experiment were obtained for flows such as the «downward facing step» with or without buoyancy, single or multiple jet mixing problems, impinging jets and more recently unsteady coupled wakes behind cylinders [9-14].

2.1.2. STAR-CD code

STAR-CD is a general purpose code for fluid mechanics and thermics issued from Imperial College of London [15]. Here, the time marching uses the PISO method for pressure solving. This algorithm is derived from the standard well-known SIMPLE one. It is semi-implicit which permits larger time steps than a fully explicit one.

The discretisation is of first order in time and on second order in space via the low diffusive central differencing scheme.

The absence of any Large Eddy Simulation model lead to perform unsteady computation with a pseudo Direct Navier-Stokes method, i.e. by running a laminar case. The large eddies are explicitly calculated and no additional turbulent viscosity is added. At the walls, laminar friction and conduction are assumed.

The great benefit of STAR-CD is the capability of employing unstructured and embedded meshes.

2.2. Thermomechanical code

SYSTUS code [16] is a general finite element code. It is used in many domains where the latest numerical techniques are required: civil work, mechanical construction, nuclear, offshore, SYSTUS is issued from TITUS, born in 1962. It has been the property of FRAMATOME SA during 20 years, and is now developed by ESI group under the name "SYSTUS International". SYSTUS+ has replaced SYSTUS since 1997.

SYSTUS and SYSTUS+ can take into account 3 types of non-linearity:

- geometrical non-linearity including contact,
- non-linearity of the physical properties (temperature dependence),
- plasticity, creep, viscoelasticity, viscoplasticity.

Also, the critical load and associated buckling mode can be obtained using a linear or non-linear analysis.

Several possibilities are offered to study the dynamic behaviour of structures:

- calculation of eigen values and eigen modes,
- response to harmonic solicitations,
- response to any solicitations using modal analysis or direct integration,
- spectral analysis (seismic studies),
- modal synthesis.

SYSTUS and SYSTUS+ have a large finite element library, with isoparametric elements in 1, 2, 3 dimensions, shell elements, beam elements and bar elements. Specific elements to deal with contacts, fluid-structure interaction are also available.

The possibility for using the super-elements method allows SYSTUS to calculate structures with a large number of degrees of freedom.

Also, pre- and post-processors are developed in order to facilitate the input/output of the study.

3. SUMMARY OF THE WORK DONE IN 1996-1998

3.1. Introduction

The present work represents the French contribution to the thermal striping benchmark study of a tee junction of Phénix plant secondary circuit, and is a part of the final report issued by the International Atomic Energy Agency. The technical specification relative to this benchmark is provided at the beginning of this final report.

First, the thermalhydraulic analyses are carried out. Two different codes (TRIO-VF and STAR-CD) are used allowing for two types of results.

Then, a thermomechanical evaluation and a fatigue assessment of the tee junction are performed showing the ability of the structure to initiate a crack. A fracture mechanics assessment is done using the above thermomechanical results. At last, a conclusion is made on the final state of the structure.

French practices are applied for all these analyses.

3.2. Thermalhydraulic analyses

3.2.1. *TRIO-VF simulation (CEA application)*

3.2.1.1. Model

Because of the time and memory size requirements inherent to LES, the thermalhydraulic study had to be split into *four* independent steps. Each step provided the boundary conditions for the following step, the latter being solved on a more finely discretised sub-domain of the former, as illustrated on Fig. 2 and detailed below:

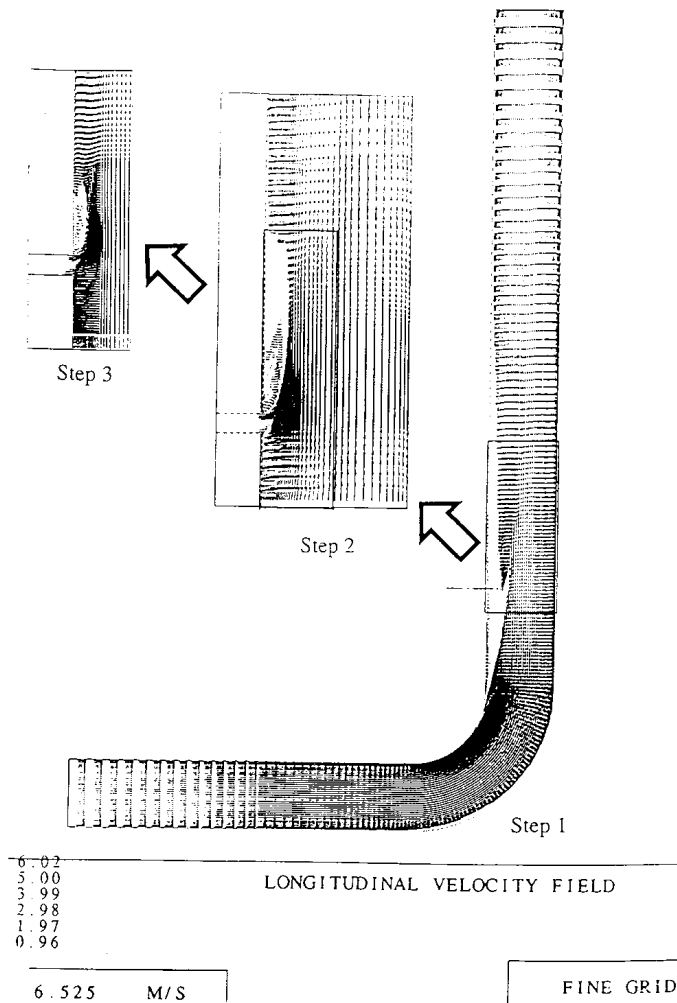


FIG. 2. CEA (TRIO-VF) longitudinal velocity fields.

(k, ϵ) computation of the mean flow in a large section of the only main pipe including the elbow.

(k, ϵ) computation of the mean flow in a short section of the main pipe and of the small branch.

LES of the flow in a limited domain around the mixing zone.

Ultimately, in a 4th step, unsteady thermal computations in the wall were made at some of the thermocouple locations.

Note that doing so implies that phenomena in a sub-domain have no feedback effect on the larger domain conditions, consequently all steps are decoupled. In particular, the pipe thermal inertia cannot affect the boundary layer temperature, which is not strictly true.

3.2.1.2. Mean temperatures

For step 1, the domain extends 5 pipe diameters upstream the elbow and 10 diameters downstream, total length being 17.4 diameters with the elbow. Computations were undertaken on five grids of different mesh size, ranging from 6200 to 426 300 cells until results were practically grid independent. A uniform and steady velocity profile, and a constant pressure

are imposed on the upstream and downstream boundaries respectively. The classical logarithmic wall functions are applied to the pipe wall.

The main flow feature in the cold pipe is the secondary flow (Dean cells) that forms in the elbow and propagates far downstream (Fig. 3).

In step 2, the length of the main section is reduced to 2.7 diameters (0.5 upstream and 2.2 downstream the branch axis), the small branch is represented on its last 2.5 diameters with uniform inlet conditions. The grid then comprised 283 000 cells. The velocity profiles of step one were introduced as upstream boundary conditions for this domain.

Figure 4 shows that the mixing zone has a low and narrow extent in the main pipe cross section, because the branch jet, whose velocity is half that in the main pipe, is strongly deflected and turned down onto the wall as soon as it enters the main pipe. The width of the mixing zone intersection with the pipe is only about 2 branch diameters and almost constant in the downstream direction.

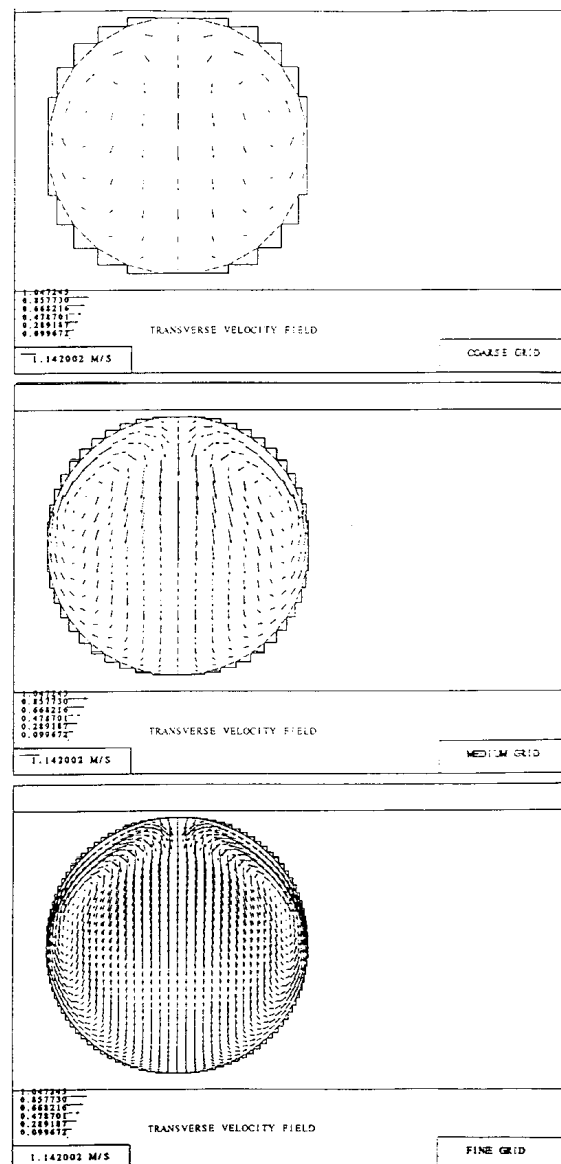
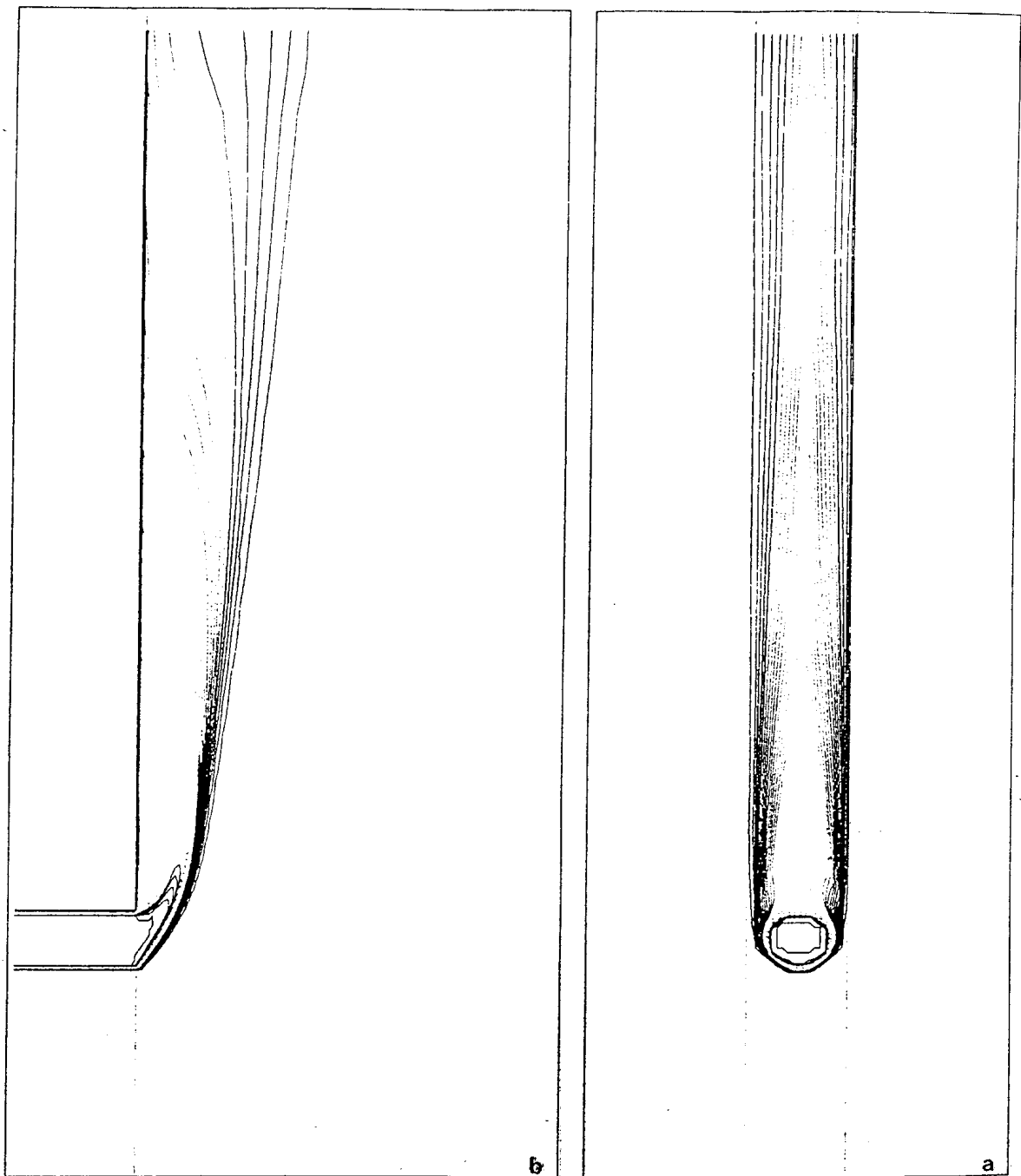


FIG. 3. CEA (TRIO-VF) transverse velocity fields.



340.00- 355.00
 358.00- 370.00
 373.00- 385.00
 388.00- 400.00
 403.00- 415.00
 418.00- 430.00

a)PLAN Y/Z X= -0.240
 b)PLAN R/Z Y= 0.00E+00

CARTE DES ISOTHERMES

VAL MINI: 340.0
 VAL MAXI: 430.0

TRIO-VF / VIVIANE

FIG. 4. CEA (TRIO-VF) mixing zone extent.

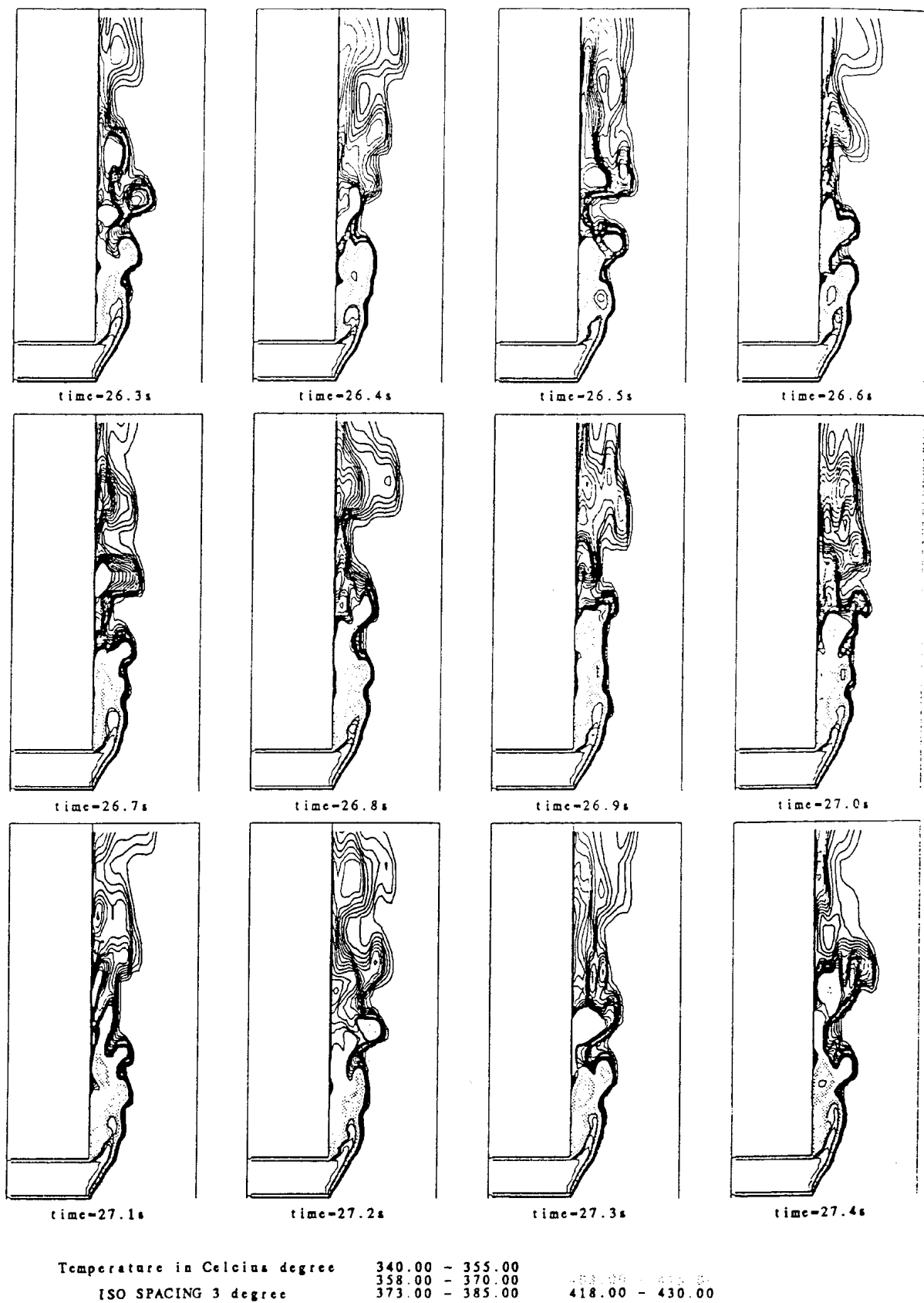
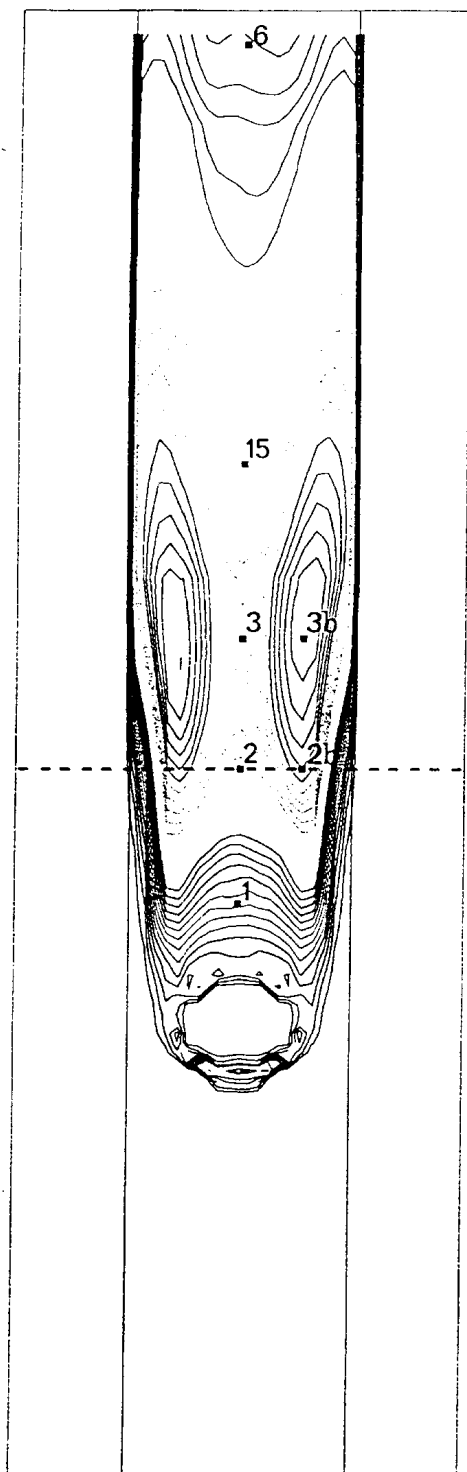


FIG. 5. CEA (TRIO-VF) isothermal lines time history.



—VMIN	3.815E-06	TEMPS=	10.400	SECONDES
—	3.5480- 5.3220	PLAN Y/Z X=	-0.240	
—	5.9133- 8.2787			
---	8.87- 11.24	CARTE DES TECT		
---	11.83- 14.19	VAL MINI:	3.8150E-06	
—	14.78- 17.74	VAL MAXI:	17.74	TRIO-VF /

FIG. 6. CEA (TRIO-VF) temperature variance.

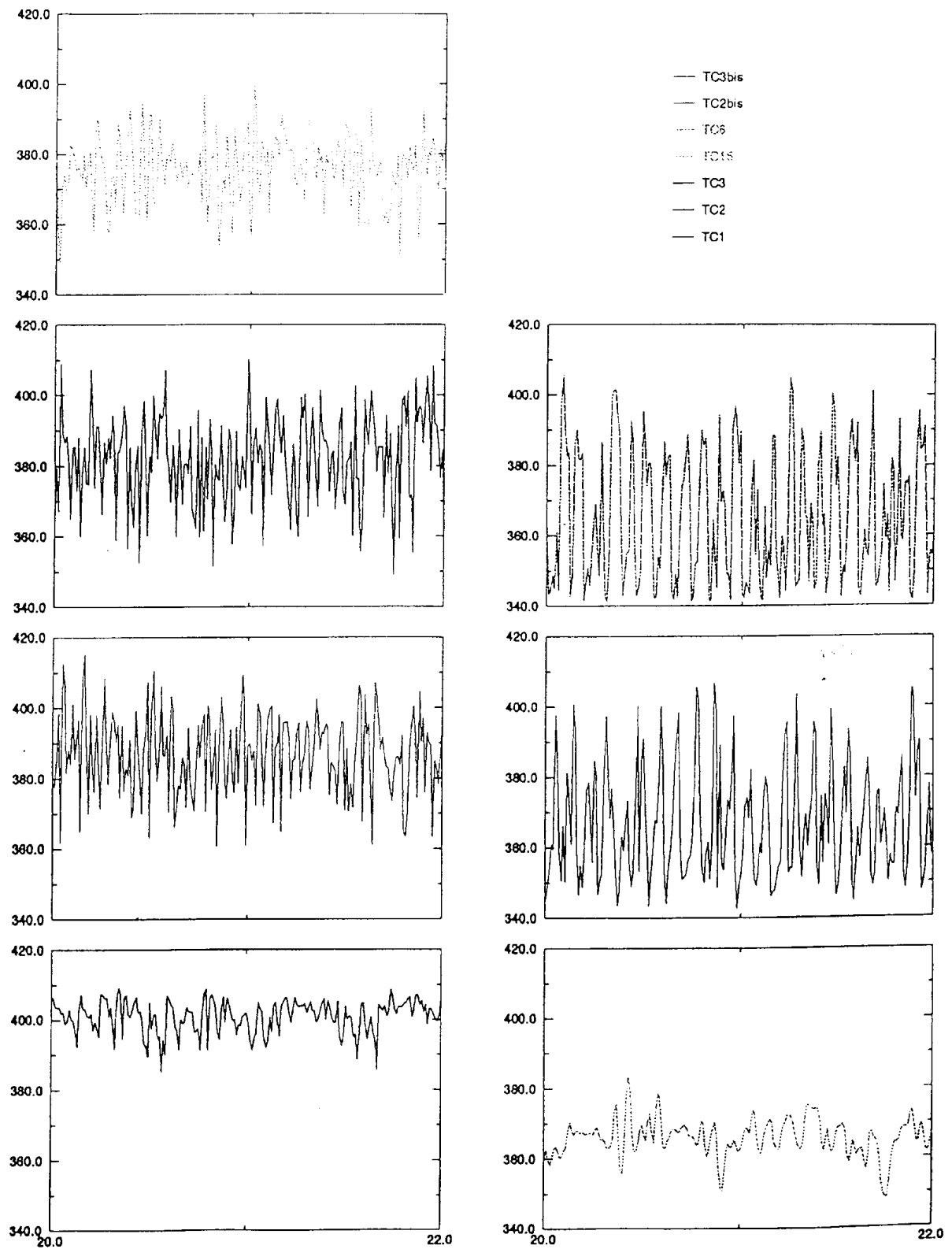


FIG. 7. CEA (TRIO-VF) temperature fluctuations at thermocouple locations.

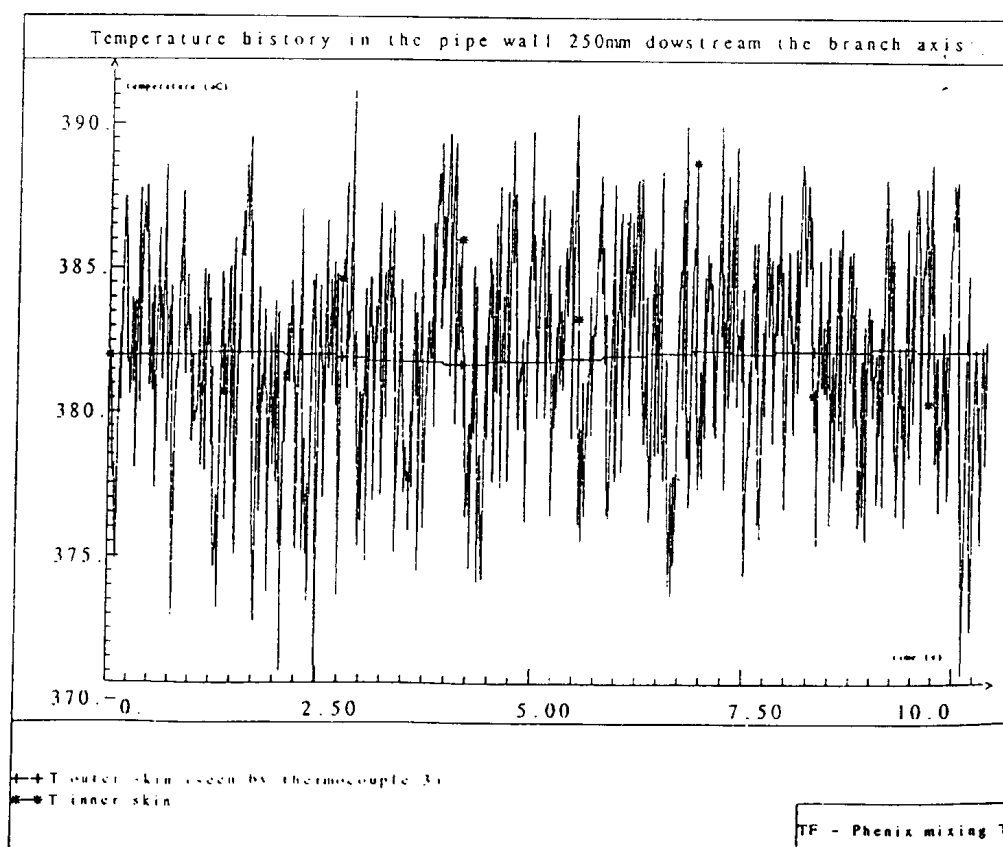
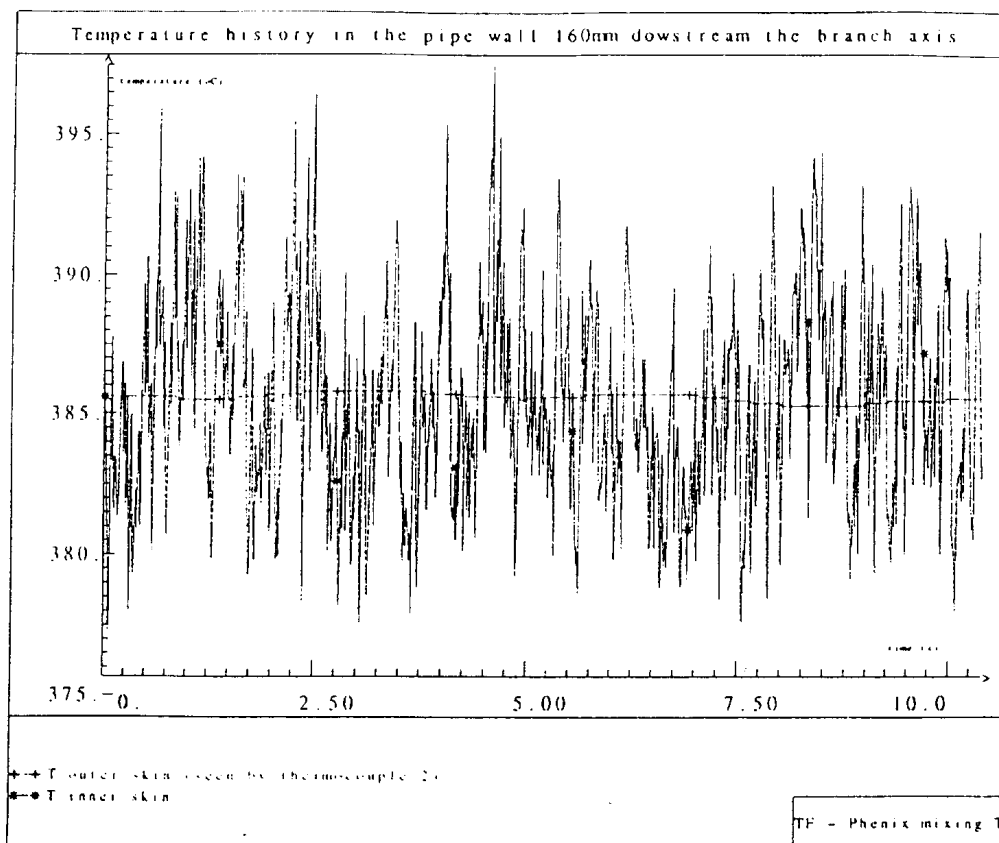


FIG. 8. CEA (TRIO-VF) inner and outer skins fluctuations at thermocouple 2.

3.2.1.3. Temperature fluctuations

The features described above invited to carry out a L.E.S, but to afford this, it was necessary to reduce again the domain size, in order to focus on the narrow mixing zone near the weld where the fluctuations occur. A grid finer and more regular than in the (k,ε) case had to be redefined, constituted by 168 000 cells, whose smallest size was 4 mm. It was also assumed, due to the small extent of the mixing zone, that the influence of the main pipe secondary flow was not dominant on the fluctuations characteristics, thus the secondary flow was neglected to simplify the boundary conditions of the LES, and a 5% white noise was added on the upstream main pipe boundary.

Figure 5 illustrates a sequence of instantaneous isothermal lines in the longitudinal median cross section, which shows pockets of hot fluid, vanishing as they are convected downstream. The temperature variance nearby the wall is presented on Fig. 6. Maximum fluctuations are observed in two symmetrical spots, precisely in the region where the weld was cracked. The maximum temperature variance is 18°C and peak to peak amplitude reached 68°C during the 27.4 seconds that could be simulated.

The final step consisted in using the temperature fluctuations predicted in fluid cells adjacent to the wall (i.e. boundary layer cells) as an input boundary condition for one dimensional heat conduction computations through the pipe wall. Such 1D thermal computations were made for each thermocouple location shown on Fig. 7.

The treatment included a sodium layer with an empirical effective thermal diffusivity α' defined in [14] by:

$$\frac{\alpha' - \alpha}{\alpha} = 1 + 0.5Pe^*$$

with

$$Pe^* = \frac{U^* \times y}{\alpha};$$

U^* = friction velocity;

y = distance to the wall;

α = thermal diffusivity.

The computed longitudinal profile of mean temperature presented on Fig. 15 shows a too hot spot of sodium downstream the tee, probably due to a lack of lateral moving of the hot jet.

With this model, it was found that because of their high frequency content around 10Hz, the large temperature fluctuations predicted by TRIO-VF outside the boundary layer were strongly damped in the sodium sublayer and moreover in the wall, leaving almost no signal on its external side, as shown by Fig. 8. See also this effect on Fig. 16 (compared peak to peak temperatures fluctuations).

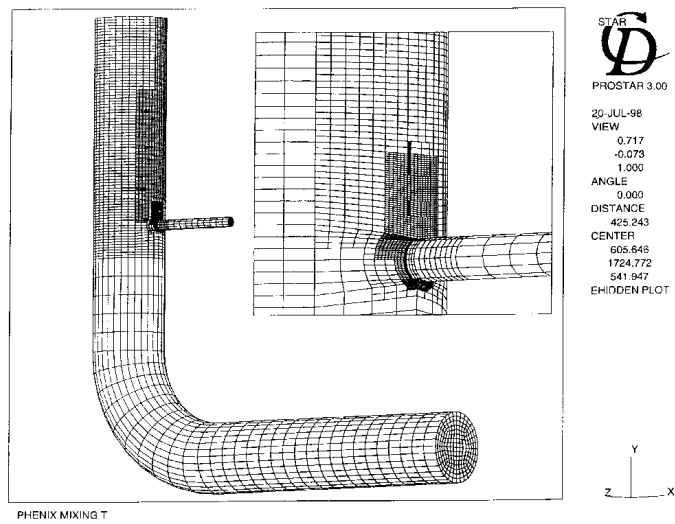


FIG. 9. Novatome (STAR-CD) model.

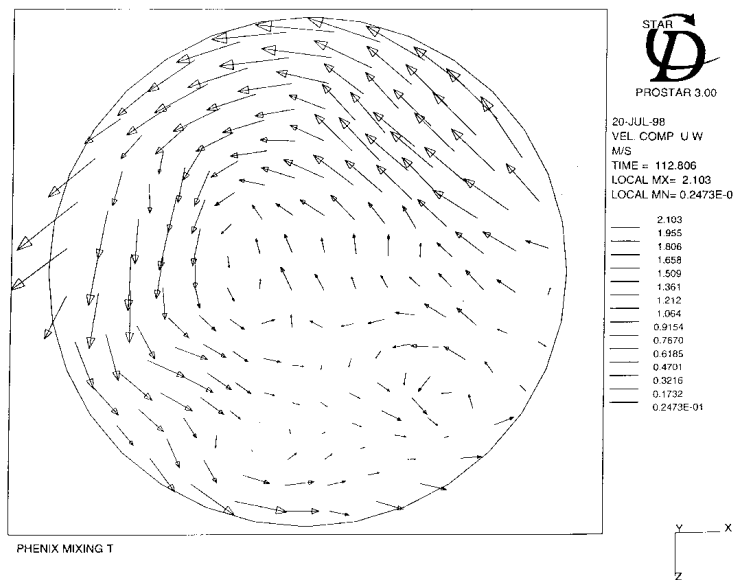


FIG. 10. Novatome (STAR-CD) velocity field: cross section upstream tee junction.

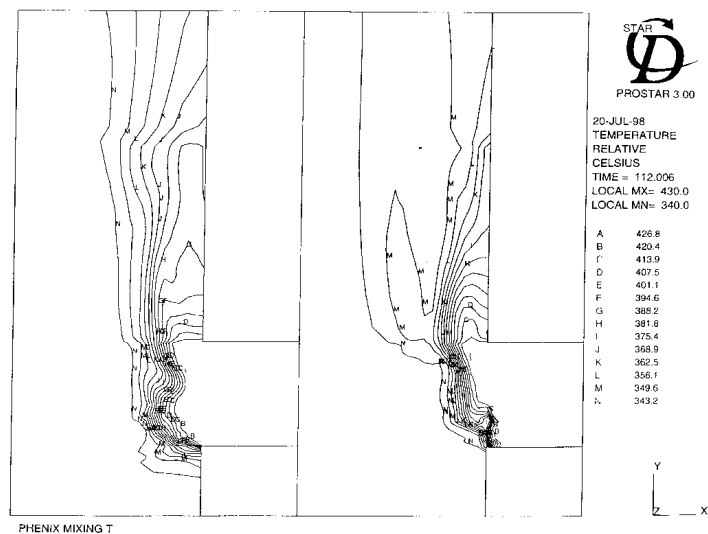


FIG. 11. Novatome (STAR-CD) instant isothermal lines, longitudinal section.

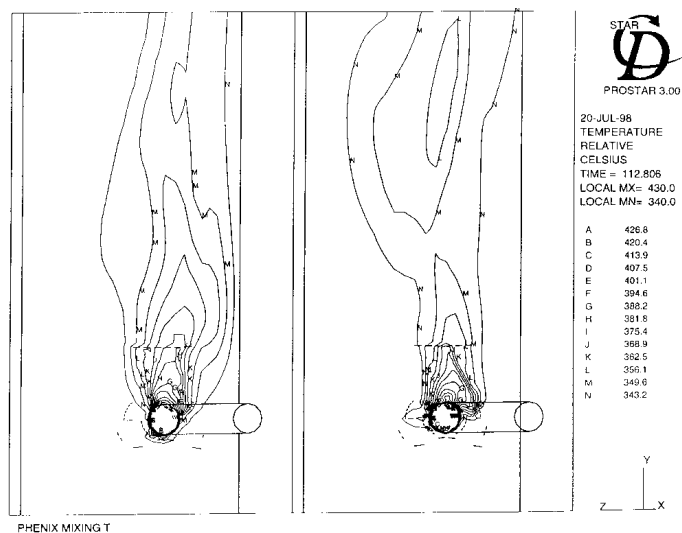


FIG. 12. Novatome (STAR-CD) instant isothermal lines, view of tee.

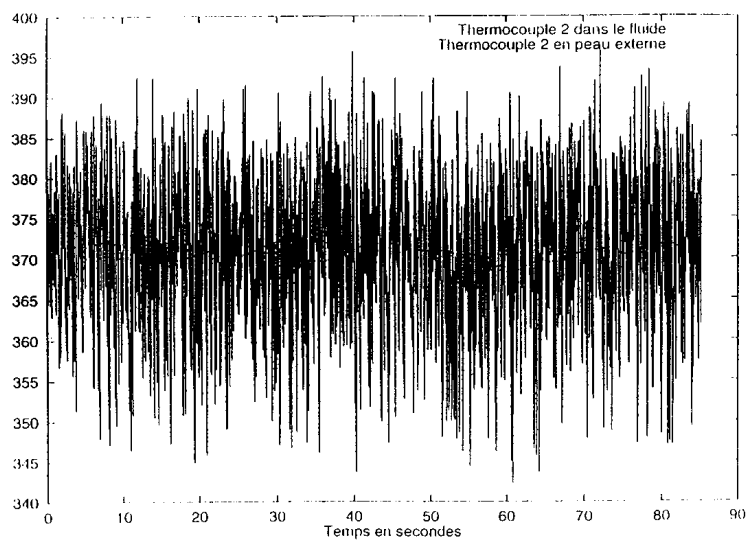


FIG. 13. Time history computed for thermocouple 2.

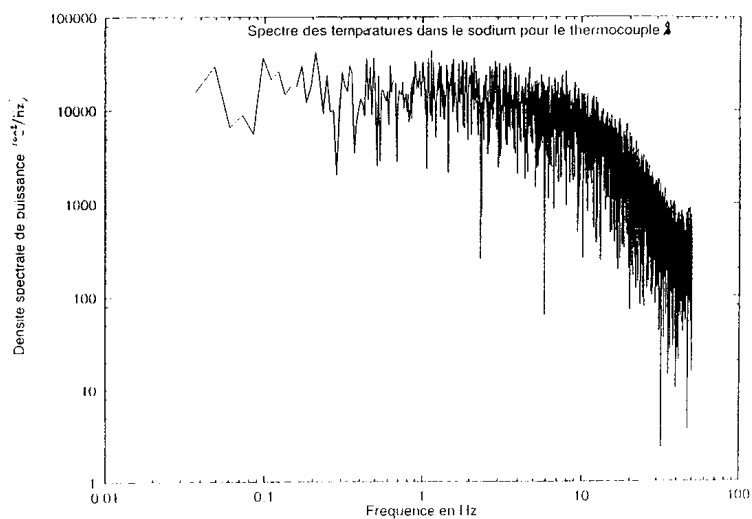


FIG. 14. Spectrum of computer signal of thermocouple 2.

3.2.2. STAR-CD simulation (FRAMATOME application).

Calculations were performed using STAR-CD code with a pseudo Direct Navier-Stokes approach.

3.2.2.1. Model

The prediction of fluctuations is obtained by setting steady conditions far upstream the tee. The domain can extend far upstream thanks to the capabilities of grid refinement of STAR-CD. The fluctuations are developing themselves in the two pipes. The swirl movement, observed experimentally, has also been implemented. This is necessary to obtain the hot jet turned down along the main pipe wall. Without this swirl flow, the hot jet will be found to be directed toward the centre of the pipe.

The boundary layer has been modelled by a full laminar treatment, i.e. the conduction has been considered between the first computation point and the wall.

The grid used is presented on Fig. 9; one can notice the large use of local refinement.

3.2.2.2. Mean temperature

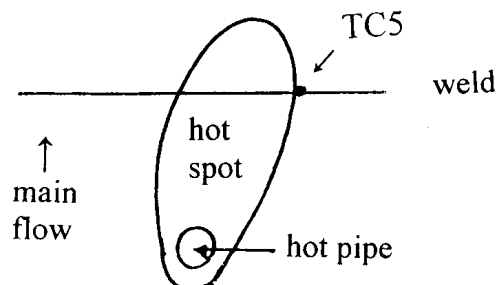
The profile of mean temperature along meridian line of the main pipe, behind the junction is plotted on Fig. 15.

The profile computed is close to the measured one. The computed temperatures are slightly higher than measurements for $x/d > 2$. The difference with the TRIO-VF profile is explained by the swirl flow and the deviation of the hot jet induced.

The plot of transversal velocity vectors of the cross section after the bend shows one rotating cell (Fig. 10), which is the consequence of the implementation of a swirl flow at inlet. Note that the same run but without swirl flow leads to two opposite rotating cells (as for TRIO-VF calculation).

3.2.2.3. Temperature fluctuations

The calculation is performed over a long physical time (~ 85 s), which allows catching low frequencies. Two instant temperature fields are shown on Fig. 11 (cross section) and Fig. 12 (view of domain). The amplitudes obtained at the outer skin are underestimated (see Fig. 16 showing the peak to peak fluctuation amplitude along meridian line behind the junction), but in a rather good agreement with the measurements. The major difference between experiments and computation is about the thermocouple 5 located on the "edge" of the hot spot on the outer wall:



An amplitude of 19°C is experimentally recorded. The STAR-CD analysis gives 73°C for the amplitude in the sodium but the computation is not performed for the outer wall. In order to obtain 19°C as amplitude for the outer wall, very low frequencies are necessary in the temperature signal. This would require a longer time of analysis (> 100 s).

Spectral analyses of the temperature signals have been carried out using a Fast Fourier Transform. For thermocouple 2: the spectrum shows a large band of energetic frequencies from 0.02 to 10 Hz with some peaks at 0.1, 0.7, 1, and 8 Hz. The maximum peak is found at 1 Hz. The corresponding time history signal is plotted on Fig. 13 and the spectrum is presented on Fig. 14.

The spectrum of thermocouple 11 shows a smaller bound of high values from 0.05 to 3 Hz with two major peaks at 0.7, 1, and 3 Hz. The experimental signal on the wall outer skin for thermocouple 5 has been extrapolated to the sodium. It leads to peaks at 0.025 and 0.045 Hz.

Those very low frequencies are not only turbulence effects but are pulsation at the scale of the sodium loop or even the plant itself. There are therefore not predictable by the present computations, this explains the differences on the TC5 results. That phenomenon may also have influences on the medium frequencies, which are interesting. They should be prescribed in the boundary conditions of the model but they are rather difficult to assess a priori.

3.2.3. Conclusions on thermalhydraulics section

In Phénix, low frequency fluctuations were detected outside the wall, they were likely to be caused by instability involving long pipe lengths and even the whole secondary loop system.

The TRIO-VF LES results are qualitatively consistent with the crack location and circumferential distribution, unfortunately they do not allow a direct comparison with the Phénix measurements because the bulk swirl in the main pipe and its unsteadiness were not included in the model. Additionally, the high frequency turbulent mixing depicted by the local TRIO-VF L.E.S would need fast response time thermocouples installed inside the pipe to be validated.

The STAR-CD DNS, whose domain included a long pipe length, also accounted for the swirl and fluid-structure coupling, these realistic features result in the good global comparison with the Phénix measurements. The range of frequency obtained shows a lack in low frequencies due to a too short physical time computed (85 s) but certainly also to other low frequencies present in the Phénix loop. Those low variations of temperature should be modelled through the boundary conditions.

3.3. Thermomechanical and fracture mechanics analysis (FRAMATOME application)

3.3.1. Loadings

3.3.1.1. Fluctuating loadings

Two different approaches are considered:

The thermal fluctuations are assumed being in the form of a sinusoidal signal with a constant amplitude equal to the maximum temperature variation in the fluid.

The random feature of the fluctuations is not taken into account in such approach.

The frequency of the sinusoidal signal must be taken within the range (0,1 Hz; 5 Hz), which is characteristic of turbulent movements inside the fluid [17].

For the tee junction area, the frequencies 0.5 Hz and 1 Hz are retained because they induce the maximum stresses in the wall.

The thermal fluctuations are provided by thermalhydraulic calculations, which attempt to reproduce the physical phenomenon.

The results of the AEA thermalhydraulic evaluation are considered here. In particular, the temperature history calculated at TC01A location (80 mm downstream of the tee junction) is considered which displays the maximum amplitude (calculation duration: 32.5 s). This loading history is applied everywhere in the tee area, in the circumferential weld and in the base metal.

Note 1:

At upper altitudes than 80 mm, the amplitudes near the wall decrease, due to the feature of the hot jet, which goes toward the centre of the pipe in the calculation.

No boundary layer attenuation is taken into account, it is considered that:

$$\Delta T_{\text{inner wall}} = \Delta T_{\text{fluid}}.$$

Note 2:

The AEA calculations provide a temperature history with significant temperature amplitudes over a workable duration and whose results were available sufficiently early in order to perform thermomechanical assessments within the due time. This is not the case of the two other calculations performed by FRAMATOME and CEA (presented in § 3.2. above).

3.3.1.2. Stationary loadings

Two kinds of "stationary" loadings are to be considered:

- (1) Hot spot induced by the impact of the jet on the pipe.
- (2) Forces and moments in the pipe.

3.3.2. *Thermomechanical analysis*

3.3.2.1. Stationary loadings

Model description:

- Hot spot: a 3D mesh with shell elements is built; a half pipe is represented assuming the hot spot is symmetric relatively to the tee junction. Symmetry conditions are applied on each side, at 0° and 180°. Shell continuity conditions are applied on both upper and lower ends. The size of the spot considered is shown in Fig. 17 together with details of the finite element mesh.
- Forces and moments: stresses are calculated using the RCC-MR formulae [18].

Stress fields:

- Hot spot: the membrane axial stresses vary from 30 Pa to 40 Pa along the circumferential weld. Bending stresses are lower. Figure 18 presents the axial stresses.
- Forces and moments: they induce very low stresses. In the tee junction area: 10 Mpa.

3.3.2.2. Fluctuating loadings using sinusoidal fluctuating temperature

Model description:

A 2D axisymmetric model of the pipe is built. The model contains 5 elements through the thickness in order to represent properly the through-wall gradient. The axial displacement is forbidden at one point.

Stress fields:

The two most severe instants of each signal are applied as loading on the model. The maximum equivalent stress range obtained is:

- $\Delta\sigma = 310$ MPa for 0.5 Hz;
- $\Delta\sigma = 320$ MPa for 1 Hz.

Damage:

The fatigue analysis is done only for the 0.5 Hz case (the conclusions will be true also for the 1 Hz case).

The methodology used is that of the RCC-MR Code: plasticity effects are taken into account by means of K_v and K_ϵ factors (respectively, triaxiality and sharp effects). A stress concentration factor of 1.7 is applied to take into account the geometrical discontinuity due to the weld bead (this value, provided by RCC-MR code, is usually applied for such a weld). The table hereafter summarises the analysis:

	in the weld 1HI	in the base metal
$\Delta\sigma_{TOT}$	$= 310 \times 1.7$ $\Delta\sigma_{TOT} = \Delta\sigma \times K_\epsilon$ $= 527$ MPa	$\Delta\sigma_{TOT} = \Delta\sigma = 310$ MPa
$\Delta\epsilon_{el}$	$\Delta\epsilon_{el} = 2 (1 + \nu)/3 E \Delta\sigma_{TOT}$	$\Delta\epsilon_{el} = 2 (1 + \nu)/3 E \Delta\sigma_{TOT}$
$\Delta\epsilon_{TOT}$	$= \Delta\epsilon_{el} (K_v + K_\epsilon - 1)$ $\Delta\epsilon_{TOT} = 0.45\%$	$= \Delta\epsilon_{el} (K_v + K_\epsilon - 1)$ $\Delta\epsilon_{TOT} = 0.22\%$
Fatigue curve	Fig. 19 decreased by a factor 1.25	Fig. 19
$N_{admissible}$	3×10^4	$\sim 10^{10}$
V over 90 000 h	$1.6 \times 10^8 / 3 \times 10^4 = 5300$	$1.6 \times 10^8 / 10^{10} = 0.016$

TABLE 1. FATIGUE ASSESSMENT USING SINUSOIDAL FLUCTUATING TEMPERATURE

in base metal		
Axial, circumferential and von Mises stress variation as a function of time (fluctuating part of stress)	Maximum value of stress variation	PSD and Variance of stress (fluctuating part of stress)
Sinusoidal variation	$\Delta\sigma_{\theta} = \Delta\sigma_{\text{axial}}$ $= \Delta\sigma_{\text{v.Mises}}$ $= 310 \text{ MPa}$	Frequency: 0.5 Hz
Axial, circumferential and von Mises mean stress (not fluctuating part)	Fatigue usage fraction defined as $\Sigma ni/N_{i_{\text{allowable}}}$ (see Note)	
$\sigma_{\text{axial min}} = -52 \text{ MPa}$ operation (membrane + bending)	0.016	
<p>Note: ni = cycle number corresponding to 90 000hours. $N_{i_{\text{allowable}}}$ = allowable cycle number according to the fatigue curves.</p>		
in weld		
Axial, circumferential and von Mises stress variation as a function of time (fluctuating part of stress)	Maximum value of stress variation	PSD and Variance of stress (fluctuating part of stress)
Sinusoidal variation	$\Delta\sigma_{\theta} = \Delta\sigma_{\text{axial}}$ $= \Delta\sigma_{\text{v. Mises}}$ $= 527 \text{ Mpa}$	Frequency: 0.5 Hz
Axial, circumferential and von Mises mean stress (not fluctuating part)	Fatigue usage fraction, defined as $\Sigma ni/N_{i_{\text{allowable}}}$ (see Note)	
$\sigma_{\text{axial}} = 125 \text{ MPa}$ residual (bending)	5 300	
$\sigma_{\text{axial min}} = -99 \text{ MPa}$ operation (membrane + bending)		

Note: ni = cycle number corresponding to 90 000 hours.

$N_{i_{\text{allowable}}}$ = allowable cycle number according to the fatigue curves.

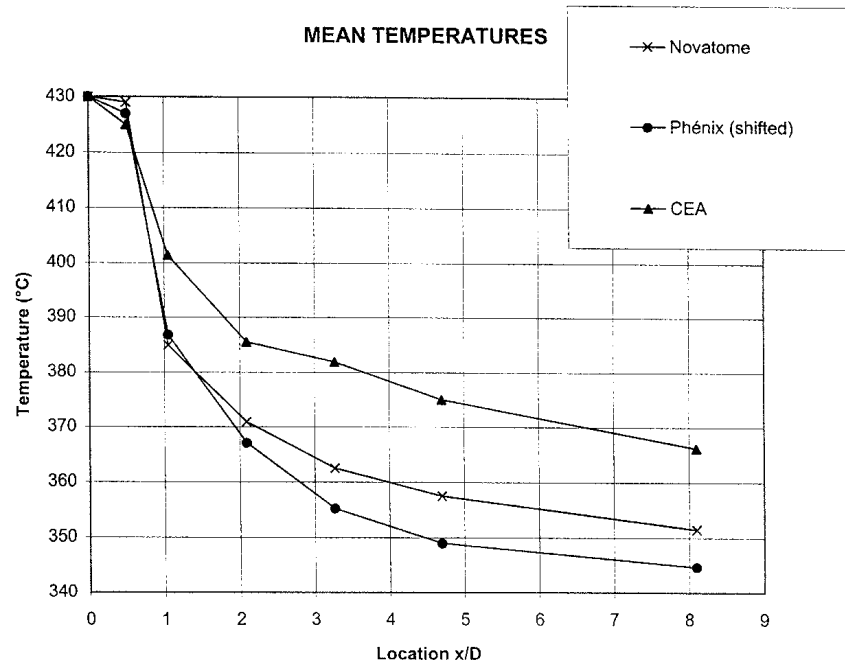


FIG. 15. Mean temperature profile comparison.

Note 1:

The cumulative factors 1.7 (on $\Delta\sigma$) and 1.25 (on fatigue curve) applied for the weld analyses appear realistic regarding the shape of the weld bead. However, it can be noted that factors equal to about 1.3 on $\Delta\sigma$ and 1 on fatigue curve, would also show that crack initiation is probable.

Note 2:

The factor 1.7 applied on the stress range corresponds to a factor 2 applied on the fatigue curve.

Conclusion:

The analysis performed shows that there is initiation of crack inside the circumferential weld. The initiation is predicted after a few hours (10 or 20 hours). Conversely, outside the weld, no risk of crack initiation is foreseen. Table 1 summarises the fatigue assessment for both weld and base metal.

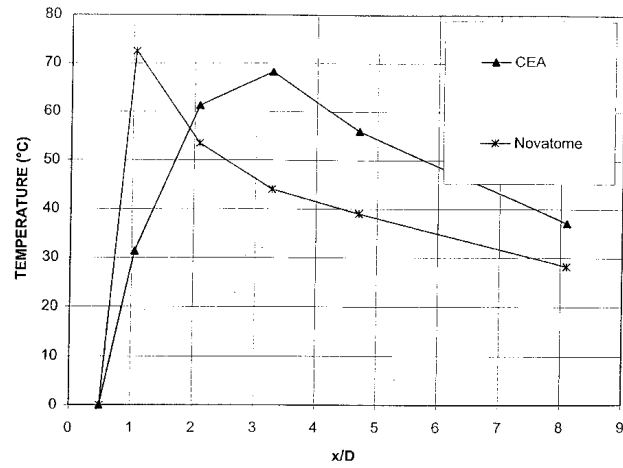
3.3.2.3. Fluctuating loadings using calculated temperature histories

Model description:

The calculation is performed through the thickness of the wall (1D approach). Analytical formulas for long cylinders are used.

The temperature history at each point of the wall is calculated by a 1D conduction approach. The corresponding stresses are defined considering the through-wall thermal gradients. The discrete Fourier transform is used for these calculation steps. The temperature history obtained on both sides of the pipe wall is presented in Fig. 20 on the whole calculated period (32.5 s). The corresponding Power Spectral Density is shown on Fig. 21.

PEAK TO PEAK TEMPERATURE - SODIUM VALUES



PEAK TO PEAK TEMP. PIPE OUTER SKIN

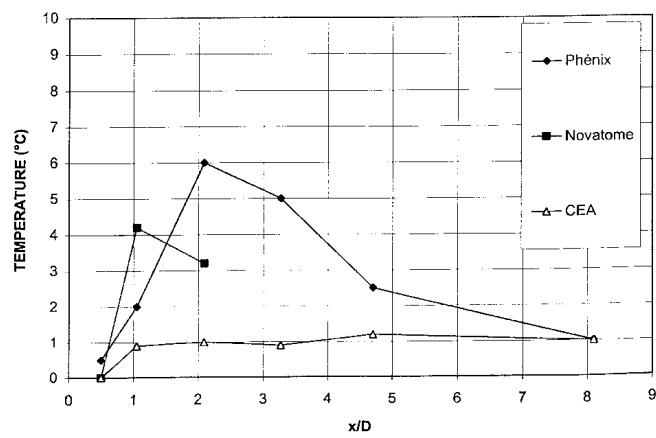


FIG. 16. Peak to peak fluctuations amplitude comparison.

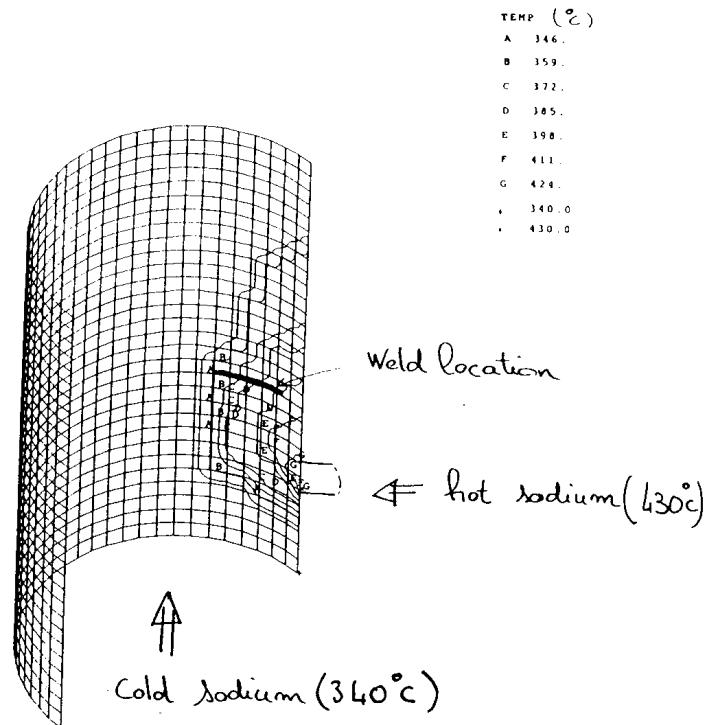


FIG. 17. Hot thermal spot on 3D.

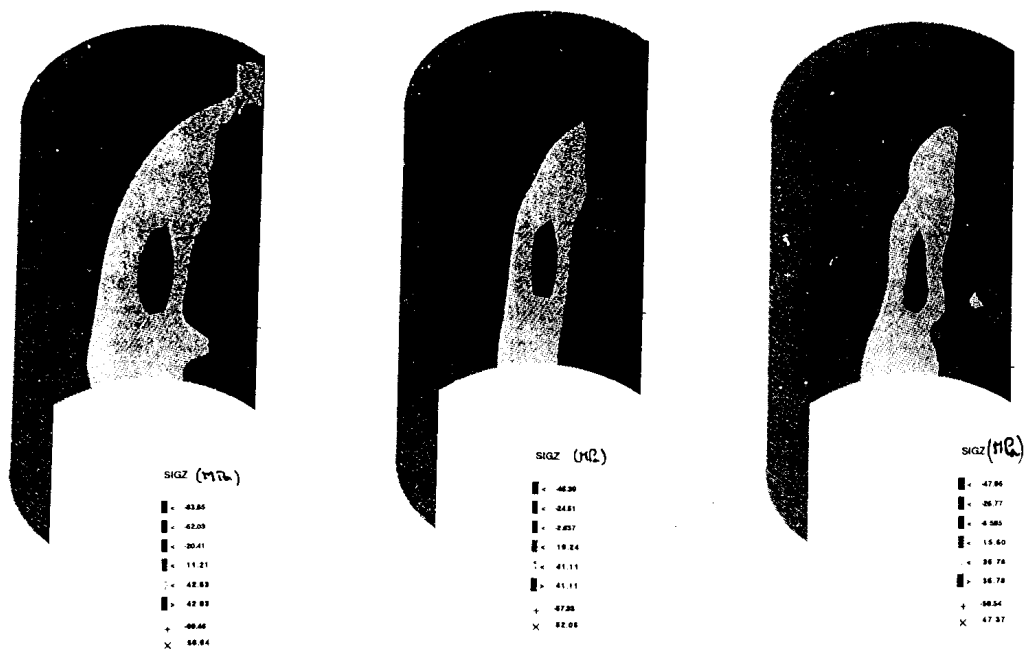


FIG. 18. Hot thermal spot - axial stresses.

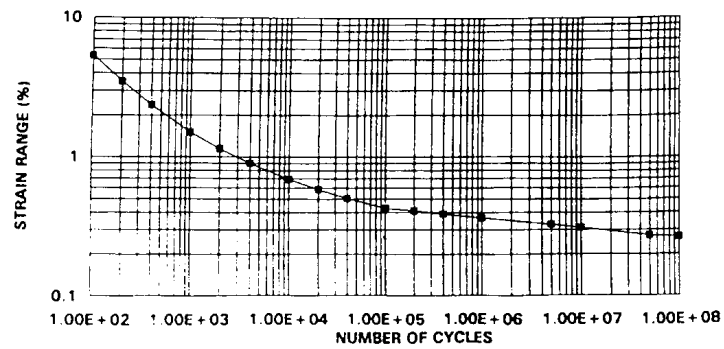


FIG. 19. Best fit fatigue curve.

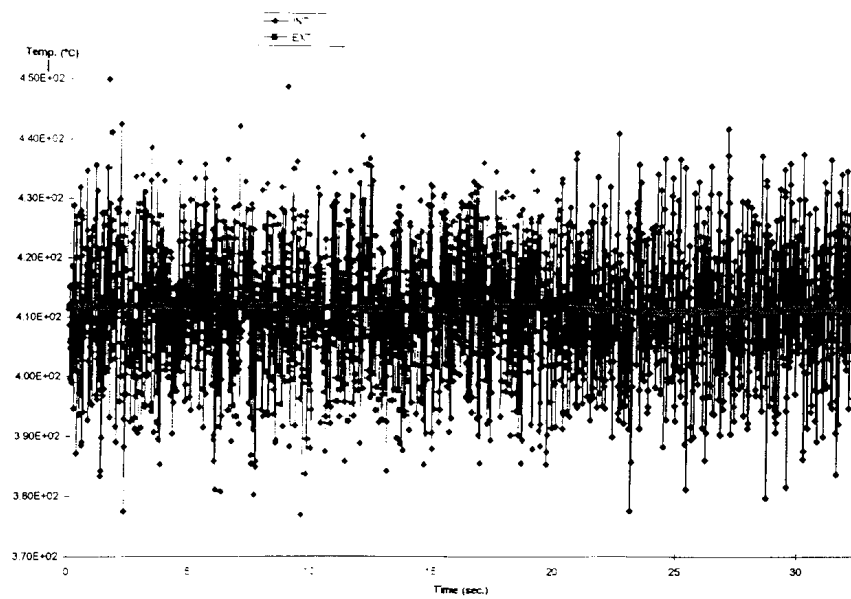


FIG. 20. Temperature history – AEA calculation.

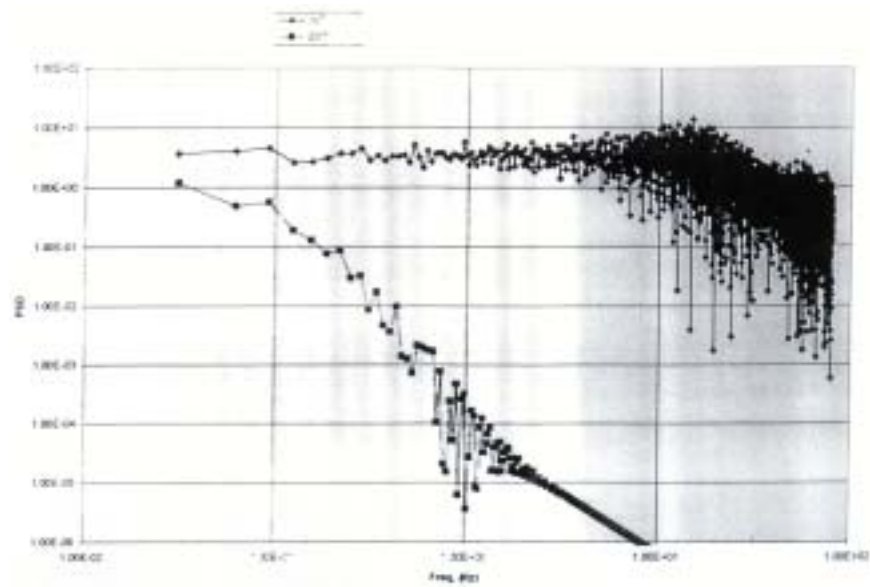


FIG. 21. Temperature power spectral density.

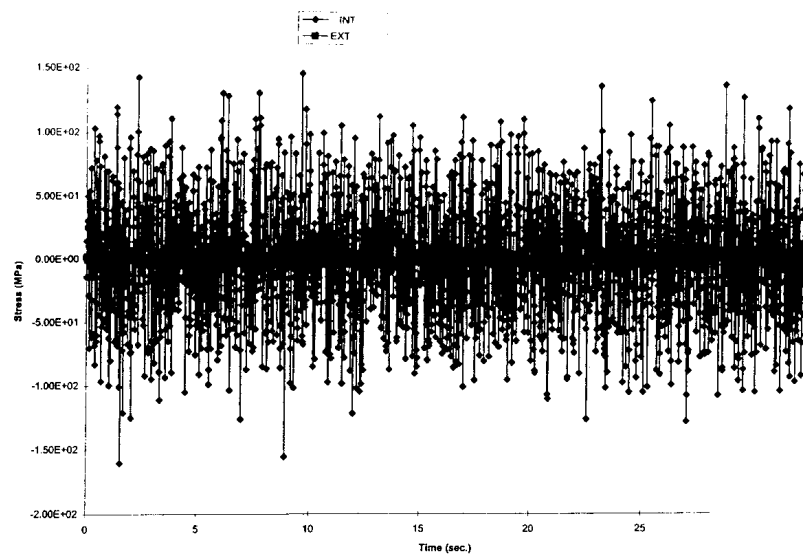


FIG. 22. Axial stress history.

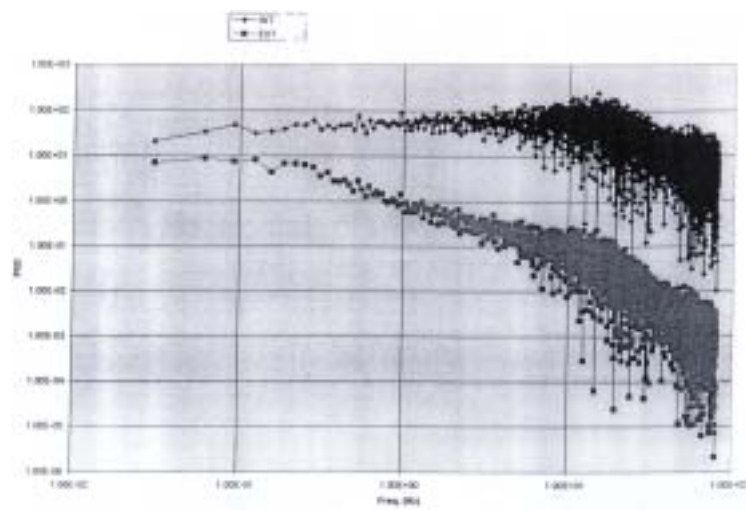


FIG. 23. Von Mises stress power spectral density.

Stress fields:

The axial stress history is shown on Fig. 22. The Power Spectral Density (PSD) is presented on Fig. 23. The maximum energy is reached around 10 Hz (see Note). The peak to peak stress variation (equivalent Von Mises) reaches a maximum of 340 MPa.

Note:

This high value of frequency is the consequence of the way the thermalhydraulic calculation is done: indeed, a spectrum with high frequencies contents (0 to ~10 Hz) is introduced as data into the calculation. Such spectrum is probably conservative, as regards the phenomenon occurred in which less high frequencies should be involved.

Damage:

The Rainflow method [19] allows a cycle counting associating each value of stress range with the counted cycle number (see Table 4).

The fatigue analysis is then performed as for the sinusoidal signal, using RCC-MR code factors (K_v and K_e) and a 1.7 stress concentration factor and a reduced fatigue curve for the weld. The fatigue usage fraction estimated on the 32.5 s is equal to:

- 4.06×10^{-9} in the base metal;
- 3.49×10^{-4} in the weld.

i.e. for the 90 000 hours of the life duration:

- 0.046 in the base metal;
- 3 500 in the weld.

Conclusion:

As for the previous analysis with sinusoidal signal, there is initiation of crack in the weld after a few hours. No crack is foreseen in the base metal. Table 2 summarizes the fatigue assessment.

3.3.3. Fracture mechanics results

A fatigue crack growth is performed for the sinusoidal temperature history. The stress range values are similar in both fatigue assessments performed so the same conclusion is also expected for the calculated temperature history.

3.3.3.1. Method description

The Paris law is used for the crack propagation:

$$\frac{da}{dN} = C \times (\Delta K_{eff})^n, \text{ with:}$$

$$\frac{da}{dN} = \text{propagation velocity;}$$

TABLE 2. FATIGUE ASSESSMENT USING CALCULATED TEMPERATURE HISTORIES

in base metal		
Axial, circumferential and von Mises stress variation as a function of time (fluctuating part of stress)	Maximum value of stress variation	PSD and Variance of stress (fluctuating part of stress)
See Fig. 18 (axial stress, circumferential stress and von Mises stress are identical)	$\Delta\sigma_{\max} = 340 \text{ MPa}$	See the PSD on Fig. 21
Axial, circumferential and von Mises mean stress (not fluctuating part)	Fatigue usage fraction defined as $\Sigma n_i/N_{i\text{allowable}}$ (see Note)	
$\sigma_{\text{axial min}} = -52 \text{ MPa}$ operation (membrane + bending)	0.046	
in weld		
Axial, circumferential and von Mises stress variation as a function of time (fluctuating part of stress)	Maximum value of stress variation	PSD and Variance of stress (fluctuating part of stress)
Stress variation in base metal $\times 1.7$	$\Delta\sigma_{\max} = 580 \text{ MPa}$	
Axial, circumferential and von Mises mean stress (not fluctuating part)	Fatigue usage fraction defined as $\Sigma n_i/N_{i\text{allowable}}$ (see Note)	
$\sigma_{\text{axial}} = 125 \text{ MPa}$ residual	3 500	
$\sigma_{\text{axial min}} = -99 \text{ MPa}$ operation (membrane + bending)		

Note: n_i = cycle number corresponding to 90 000 hours.

$N_{i\text{allowable}}$ = allowable cycle number according to the fatigue curves.

TABLE 3. FRACTURE MECHANICS ASSESSMENT USING SINUSOIDAL FLUCTUATING TEMPERATURE

Time to initiate a crack	Cycle number and associated time needed to have a crack depth of:			Crack depth at 90 000 hours
	1 mm	3 mm	5 mm	
~20 h	$>2.8 \times 10^4$ >35 h	$>1.4 \times 10^5$ >100 h	$>2.5 \times 10^5$ (*) >150 h	about 6 mm

(*) estimation using mean stresses for which propagation is maximum.

TABLE 4. CYCLE COUNTING AT INNER WALL

Stress range interval	Cycle number on 32.5 s in base metal	Cycle number on 32.5 s in weld
[0 – 200]	3336	2935
[200 - 220]	27	/
[220 - 240]	23	169
[240 – 260]	10	/
[260 – 280]	3	105
[280 – 300]	1	/
[300– 320]	1	79
[320 – 340]	2	48
[340 – 380]		27
[380 - 410]		23
[410 - 440]		10
[440 - 480]		3
[480 - 510]		1
[510 - 540]		1
[540 - 580]		2

C, n = envelope coefficients characteristic of the material in sodium environment taken at 320°C: $C = 7.5 \times 10^{-13}$, $n = 4$;

ΔK_{eff} = stress intensity factor variation (in MPa $\sqrt{\text{m}}$) defined using [20] for plates. Plasticity effects and mean stress influence are taken into account, according to RCC-M, Appendix ZG [21].

3.3.3.2. Hypothesis

- The stress intensity factor takes into account the non-linear distribution through the wall. Each frequency is examined separately;
- The propagation threshold considered (no propagation exists below this value) is:
 $K_{th} = -4R + 6.5$, with $R = (K_{th} \text{ in MPa}\sqrt{m})$;
- The crack is assumed initiated over a depth of 0.5 mm;
- Bending residual stresses are taken into account in the weld. They are added to the operating mean stresses defined in § 3.3.2.1. The residual stresses are assumed to be equal to the minimum yield stress at 340°C. The sensitivity of taking into account a mean stress in tension or in compression on the crack growth is estimated.

3.3.3.3. Propagation analysis results

The results of the assessment are presented in the following table, in term of cycle number necessary to propagate a crack from $a_0 = 0.5$ mm to $a = 5$ mm:

without mean stress	with mean stress
	increasing the propagation decreasing the propagation
$N_1 = 8 \times 10^5$	$0.3 N_1 < N_2 < 5 N_1$

The values obtained show that the crack propagates rapidly through the wall (in the weld), within an average of 150 hours.

The sensitivity study shows that the cycle number necessary to propagate a defect could vary in a ratio of about 15 whether the residual mean stresses are in tension or in compression, and in a ratio of about 5 whether the mean stresses are considered or not.

Note:

Using best estimate crack growth law instead of envelope law would approximately multiply by 2 the duration expressed above.

3.3.4. Conclusion about damage of the component

Beyond 5 mm of crack growth (representing 70% of the thickness), the validity of the Paris law is uncertain. So engineer judgement is expressed to estimate the behaviour of the crack beyond 5 mm:

- The remaining ligament is probably plastified;
- The cyclic stresses at the crack tip are low (about 15 MPa near the outer skin);
- The primary stresses (10 MPa) are not large enough to break the remaining ligament.

Such behaviour can be observed on strain controlled fatigue tests.

As a conclusion, the most probable behaviour is a rapid propagation of the crack through the thickness of the wall followed by a stop of the crack at about 1 mm from the outer skin of the pipe. Table 3 summarises the fatigue crack growth assessment in the circumferential weld.

4. RECOMMENDATIONS

The analyses performed on the benchmark lead to propose the following recommendations for the treatment of thermal striping phenomena:

Domain for thermal-hydraulic analysis:

- The domain must extend sufficiently upstream the region investigated, in order to let perturbations develop (5 to 10 diameters for a pipe), which is much more efficient than fluctuating boundary conditions.
- The geometry must be precisely modelled around the region of interest.

Thermal-hydraulic simulation:

From a formal point of view, a large Eddy Simulation is certainly better than a pseudo Direct Navier-Stokes approach, but its effect is of second order with regard to the influence of the secondary flow in the main pipe. The space discretisation scheme must be at least of 2nd order, while the time discretisation scheme can be of first order only.

Concerning the LES tentative computations of the thermalhydraulic study, it is obvious that today the method requirements are not easily affordable for any industrial flow configuration. Having split the resolution in successive steps to work on overlapped domains is also a heavy procedure and removes the possibility of coupled phenomena involving different scales between the domains.

For the present case, the ideal solution would have been to include in one single LES computation a long pipe length and a part of the pipe wall, as was done in FRAMATOME's simulation, but with a correct sub-grid turbulence modelling on a very fine grid.

To work on an affordable grid, such a complete model would need to develop a multi-grid compatible turbulence model able to resolve the pipe flow on a «coarser» grid in the main pipe and at the same time to resolve the small mixing zone on a «finer» grid near the branch, for instance.

If done so, still better predictions could be expected, putting together the qualities of the two approaches and suppressing much of their drawbacks: large scale turbulent structures that develop in the pipe and thermal coupling between fluid and structure would be taken into account with a correct turbulence modelling.

Boundary conditions of thermal-hydraulic model:

- A white noise or other unsteady boundary conditions are not necessarily required to obtain a fluctuating solution if they are prescribed sufficiently far upstream, but they can improve the development of instabilities;
- The effect of secondary flows due to the upstream circuit, such as a swirl flow, is not negligible on the main flow, and hence on the fluctuations. Those secondary flows can be the consequence of a pump or a valve located far upstream the tee.

Wall attenuation:

For thermal hydraulic simulation, it is recommended to increase the conduction transfer within the conductive sub-layer, with an empirical function such as the one used in the TRIO-VF computation. The small amount of turbulent heat transfer near the wall is then accounted for.

The quantification of the attenuation to the wall is of great importance. According to the thermomechanical analyses performed, it appears that in that case if a damping ratio greater than 15-20% is considered no crack initiation can be proved. The weld bead which stands into the fluid could disturb the flow inside the boundary layer and as a consequence reduce the attenuation. Consideration shall be given to this point in further thermal hydraulic analysis.

Sampling of time history signal:

The computation must provide the range of frequencies of interest. For a given thickness of wall, there is a band of frequencies which are potentially damageable. Frequencies lower than this band do not cause significant temperature differences between inner and outer skins of the wall, because the temperature variation is too slow.

Also the frequencies higher than this band do not permit the penetration of temperature variations into the wall.

Hence:

- The numerical simulation must be carried out over a sufficiently long physical time (condition for low frequencies). Thicker the wall is longer the physical time of calculation must be.
- The time step must be sufficiently small (condition for high frequencies).
- Moreover, low frequencies have been observed on PHENIX instrumentation. Those phenomena cannot be modelled via a thermal-hydraulic computation because they are not due to local hydraulics, but to the general fluid domain behaviour (loop, plant). Even if very low frequencies do not produce damages by themselves, because they imply weak temperature differences within the wall and their occurrences are few (but other low frequencies may be more damageable), it would be better to try to model them via boundary conditions because they may have influence on the flow and on fluctuations in the range of frequencies of interest.
- At the present time, if thermal hydraulic calculations fail to give the complete range of frequencies it appears that a sinusoidal signal (which was examined by FRAMATOME), even if unrealistic because not random, provides results which are consistent with the experimental observations and is very simple to use. Working with such a signal could be a good alternative (if the frequency of the signal is correctly chosen in order to avoid an excessive conservatism) to assess the thermal striping risks.

Mean stress effect on mechanical assessment:

- The mean stresses have a sensitive effect on the crack propagation assessment. A parametric study is recommended to quantify this influence on the crack propagation which can be reduced or enhanced as a function of stress value. Manufacturing residual stresses shall be included in the analysis.

- No effect of mean stress has been introduced in the fatigue damage assessment, which is correct as the major fluctuating stresses are in the plastic domain. However, this should be considered for lower stresses.

Weld influence:

1. The experimental observations highlight the important influence of the weld. The weld can be characterised by 3 parameters:
 - the weld bead generating a geometrical discontinuity. This is due to the "as-welded" condition of the weld inducing stress concentrations which have an influence on the time to initiate a crack,
 - the weld material different from the parent metal,
 - residual stresses existing in the weld which act as mean stresses (see above).
2. The weld bead must be taken into account as geometrical discontinuity in the fatigue assessment. The analyses performed shows that the factor 1.25 applied on the fatigue rupture curve to represent a material effect is too low to cover all the consequences induced by the «as-welded» weld. So it is recommended to take care to the representation of the weld in thermomechanical assessments.

5. CONCLUSION

The prediction of thermal striping phenomena needs first the knowledge of time history signals of temperature in the structure of interest. It requires fine unsteady thermal-hydraulic simulations, which are time and memory heavy consumers. The present synthesis shows noticeable differences between the results obtain from one analysis to another, which are of great influence on further thermomechanical evaluations.

From the thermomechanical and fracture mechanics point of view, the actual observations prove that the weld bead is likely to have an important influence on both thermalhydraulics and thermomechanics and shows the difficulties of the numerical approaches to be close to the reality (prediction of the boundary layer attenuation, influence of the weld bead on the crack initiation). Design procedures recommend to remove the weldments from the thermal striping zones. However, if such a risk cannot be avoided it appears essential to represent adequately the weld in the analysis.

Some recommendations are expressed on both thermalhydraulic and mechanical aspects, on computation domain, thermalhydraulic boundary conditions, weld bead representation, in order to improve the prediction of thermal striping problems and to prevent them in the component design phase.

REFERENCES

- [1] MAGNAUD, J.P, ROUZAUD, P., TRIO: a general computer code for reactor 3D flow analysis. Application to a LMFBR hot plenum, International Meeting on Advances in Nuclear Reactor Computation Methods, Knoxville, USA, (1985).

- [2] LEONARD, B.P., Simple High Accuracy Resolution Program for Convective Modelling of Discontinuities, Int. Journal for Numerical Methods in fluids, vol. 8, pp. 1291-1318, (1988).
- [3] HIRT, W., et alii, SOLA-A numerical algorithm for transient fluid flows, LASL report no. LA 5852, (1975).
- [4] LESIEUR, M., METAIS, O., New trends in LES of turbulence, Annual Review of Fluid Mechanics, vol. 28, pp. 45-82 (1996).
- [5] BOYLE, D.R., GOLAY, M.W., Measurement of a recirculating two-dimensional, turbulent flow and comparison to turbulence model predictions, J. of Fluid Engineering, vol. 105 (1983).
- [6] GRAND, D., et alii, Three dimensional computations of thermal hydraulic phenomena in reactor vessels, Int. Topical meeting in advances in mathematics, computations and reactor physics, Pittsburgh, (1991).
- [7] CHEREL, J.M., et alii, Advanced 3D thermalhydraulic modelling in the EFR hot plenum; comparison with experiment, NURETH, 6 vol. 3, Kyoto (1993).
- [8] SURLE, F. et alii., Comparison between sodium stratification tests on the Cormoran model and Trio-VF computations, NURETH, 6 paper 141, Grenoble (1993).
- [9] SILVERA NETO, A., Simulation des grandes échelles d'un écoulement turbulent décollé en aval d'une marche, Thèse de Doctorat INPG, Grenoble (1991).
- [10] FALLON, B., Simulation des grandes échelles d'écoulements turbulents stratifiés en densité, Thèse de Doctorat INPG, Grenoble (1994).
- [11] URBIN, G., METAIS, D., Large eddy simulation of three dimensional spatially developing round jets, paper presented in the 2nd ERCOFTAC Workshop on D.N.S. and LES, Grenoble, 16-19 September 1996 (1996).
- [12] URBIN, G., Etude numérique par simulation des grandes échelles de la transition à la turbulence dans les jets, Thèse de Doctorat INPG, Grenoble (1998).
- [13] BRUN, D., Etude expérimentale et numérique de l'interaction entre sillages d'obstacles cylindriques, Thèse de Doctorat INPG, Grenoble (1998).
- [14] BUFFET, J.C., Etude des fluctuations de température dans des écoulements de métal liquide au voisinage d'une paroi, Thèse de Doctorat ECL, Lyon (1984).
- [15] STAR-CD manuals, version 2.300a. Computational Dynamics Ltd, London.
- [16] SYSTUS Code - Release 233 VAX VMS.
- [17] SIMONEAU, J.P. , NOE, H., MENANT B., Large Eddy Simulation - Sodium flow in a tee function - comparison of temperature fluctuations with experiments, Proceeding of the ICONS 5, paper 2145, Nice, France (1997).
- [18] RCC-MR Code, Edition (1993).
- [19] WIRSHING, Ph., MOSHEN SHERRATA, A., Fatigue under wide band random stresses using the Rainflow method, Journal of engineering materials and technology, pp. 205-211, (1977).
- [20] NEWMAN, J.C., RAJU, I.S. A empirical stress intensity factor equation for the surface crack, Engineering Fracture Mechanics, vol. 115, No. 1-2, pp 185-192, (1981).
- [21] RCC-M Code - Edition (1988).

THERMAL HYDRAULICS AND THERMOMECHANICAL ANALYSIS OF THERMAL STRIPING IN A MIXING TEE-JUNCTION OF SECONDARY SODIUM CIRCUIT OF PHÉNIX REACTOR

P. CHELLAPANDI, K. VELUSAMY, A. BISWAS, R. RAMA, S.B. BHOJE,
G. VAIDYANATHAN, S.C. CHETAL
Indira Gandhi Centre for Atomic Research (IGCAR),
India

Abstract. The investigation of thermal striping risks calls for determination of (i) temperature fluctuations which can be in the form of random response or a set of sinusoidal functions, (ii) associated thermal stress oscillations to estimate the life cycles for initiating cracks, and (iii) crack propagation details. This report deals with the results of thermal hydraulics and thermomechanical investigations carried out by IGCAR.

1. INTRODUCTION

Thermal striping problems have been observed in the secondary circuit of PHÉNIX reactor in the vicinity of a mixing tee (Fig. 1) as per Ref. [1]. The structural damage caused by thermal striping starts with a crack initiation and subsequently crack propagation to the extent of sodium leak. The temperature difference between the hot sodium flowing in the branch pipe (7 kg/s and 713 K) and the sodium flowing in the main pipe (800 Kg/s and 623 K) is about 90 K. This difference in the sodium produces temperature fluctuations on the adjacent metal wall surface, causing cracks after a specified operating life of the plant.

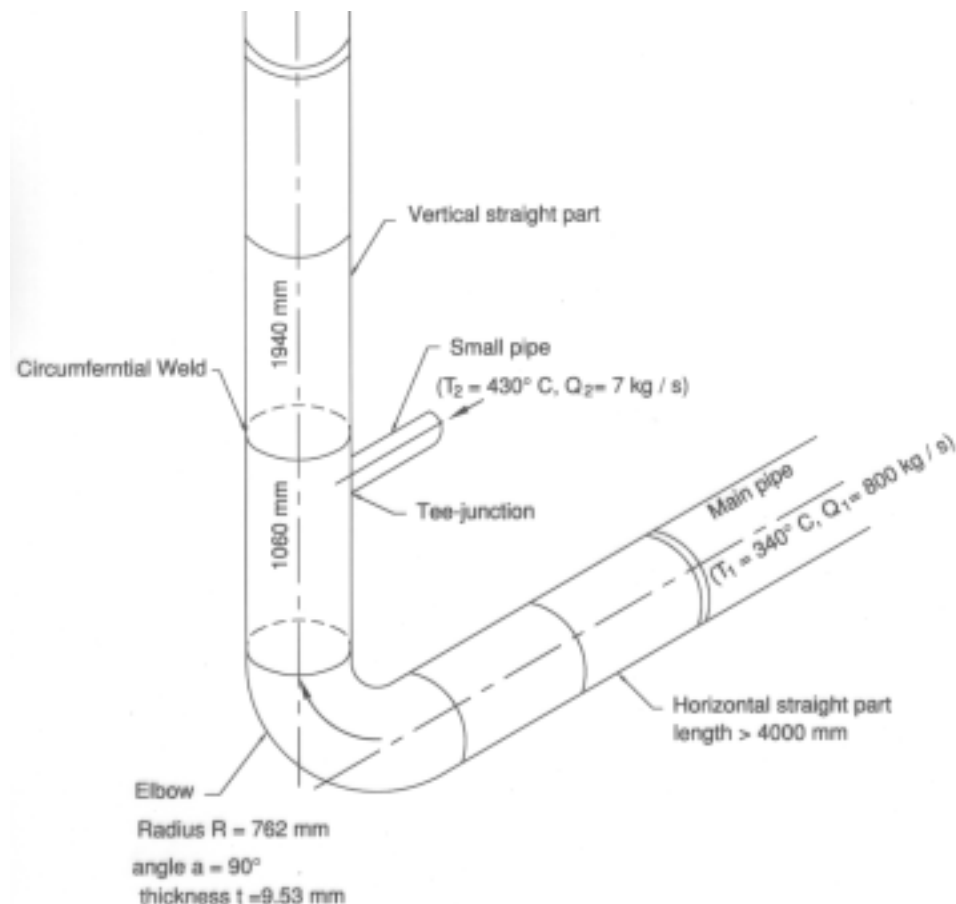


FIG. 1. Geometrical characteristics.

2. THERMAL HYDRAULIC ANALYSIS

2.1. Computer code

The turbulent flow conservation equations are solved using the general purpose, finite volume based, thermal hydraulic code PHOENICS [2]. The code has options of the standard K-epsilon as well as the Reynolds stress (employing transport equations for all the 6 components of Reynolds stress and 3 components of turbulent heat flux) models of turbulence. It has the non-orthogonal Boundary Fitted Co-ordinate (BFC) system, which is essential to simulate the bend pipe. It has the provision for conjugate heat transfer analysis wherein the heat conduction within a solid and convection in the surrounding fluid could be considered simultaneously, without the use of any external heat transfer coefficient. But it may be mentioned that in the version available at this centre, the code does not support the Reynolds stress turbulence model (RSTM) in the presence of BFC and conjugate heat transfer options. The code has the option that the user can insert his own conservation equations. This option has been utilised to insert the transport equation for the 'fluctuating intensity of temperature'. This equation is solved along with the other transport equations for Reynolds stress/flux, to find out the distribution of temperature fluctuating intensity. Another method of evaluating the fluctuating intensity is to use the local equilibrium model [3]. This model is also introduced in the code. The buoyancy effect is considered using Boussinesq approximation. The details of the governing equations solved can be had from Ref. [4].

In PHOENICS, the pressure-velocity coupling in the incompressible flow is resolved through the SIMPLEST algorithm that is a variant of the well known SIMPLE algorithm of Patankar and Spalding [4]. The convective and diffusive fluxes are combined by the HYBRID scheme, employing a staggered grid. The volume integrated algebraic equations of velocity components are solved by Jacobi-Point by Point method, whereas those of other variables are solved by the whole-field solution procedure. The whole-field solution procedure is an extension of Thomas algorithm to 3-D equations. For the smooth convergence of the coupled non-linear equations, a false transient method of under relaxation is employed.

2.2. Analysis methods

The steady state analysis is carried out in various steps viz. (1) including the horizontal bend portion of the main pipe in the analysis, (2) considering only the straight portion of the pipe with T-junction, (3) considering the presence of main pipe wall in the analysis and (4) localized analysis for the mixing zone including the branch and main pipe walls. The transient analysis is attempted over a restricted domain, using the Direct Numerical Simulation without any turbulence model.

2.3. Steady state results

2.3.1. Effect of bend in the main pipe

The bend portion of the main pipe was seen to induce a swirl on the main flow as the flow traverses the bend. The temperature distribution of sodium is shown in Fig. 2. It is evident that the influence of swirl on the temperature distribution is not significant. The influence of hot sodium on the upstream is also nil. The zone where the sodium mix, radially extends to $\sim 1/2$ the main radius and circumferentially it extends to a distance of ~ 125 mm.

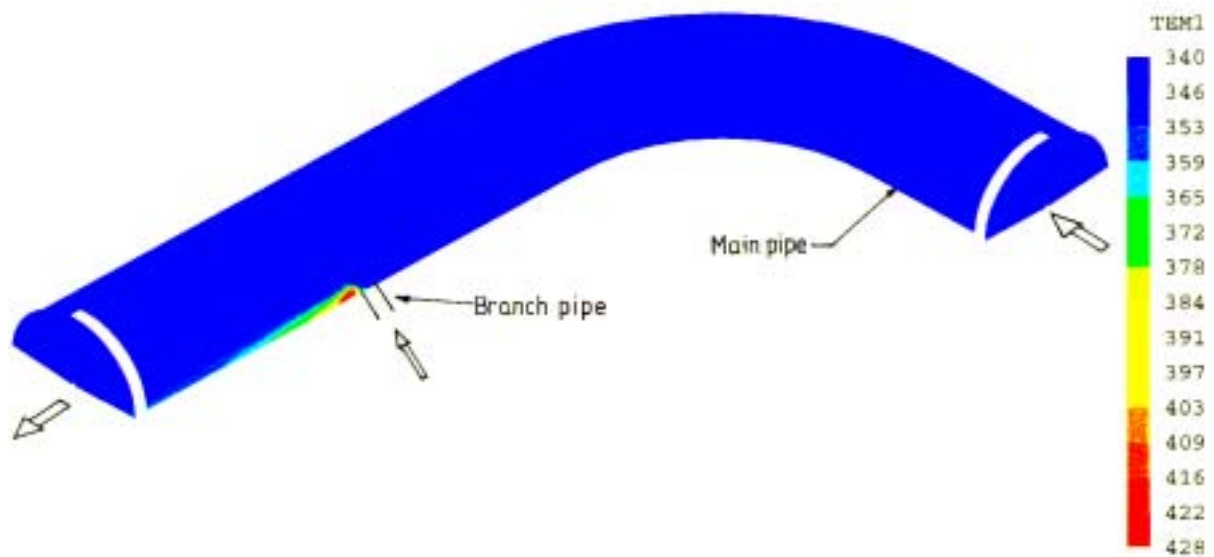


FIG. 2. Temperature distribution in the elbow.

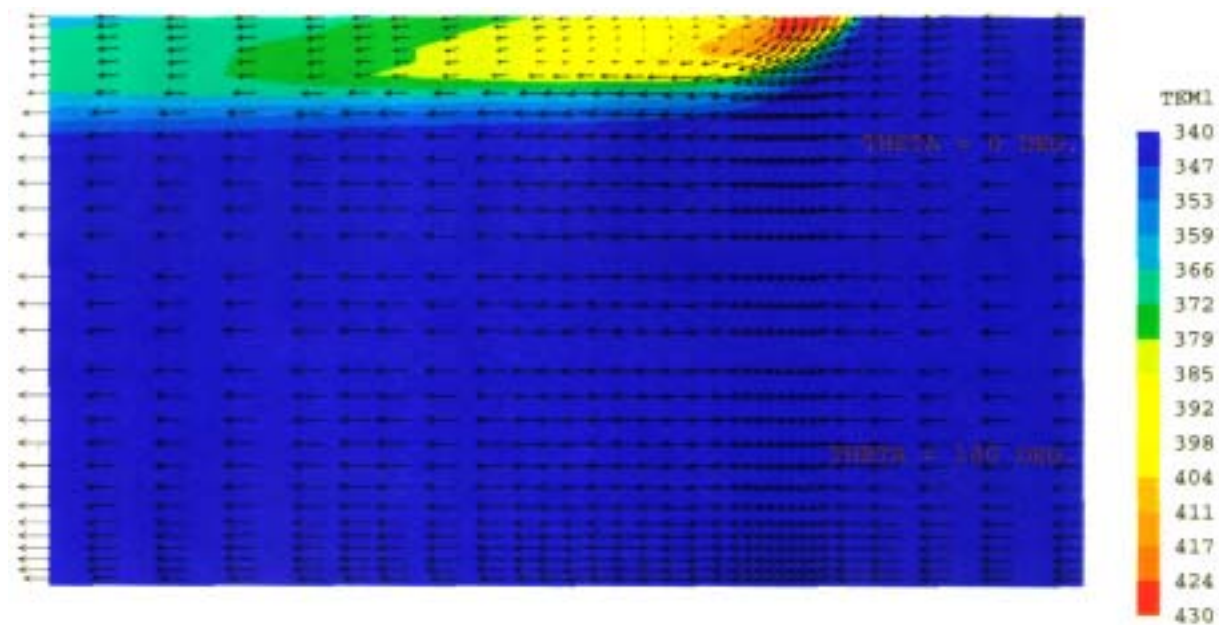


FIG. 3. Flow and temperature fields in the symmetry planes.

2.3.2. Effect of pipe wall

Since the bend induced swirl is found to be weak compared to the main flow, only the straight portion of the pipe is considered for subsequent analyses. This analysis is carried out to see whether the pipe walls need to be considered in the analysis. It was seen that the temperature change across the thickness of the wall is less than 4 K at any cross section.

This establishes that wall need not be considered in conjugation with the convection of the fluid.

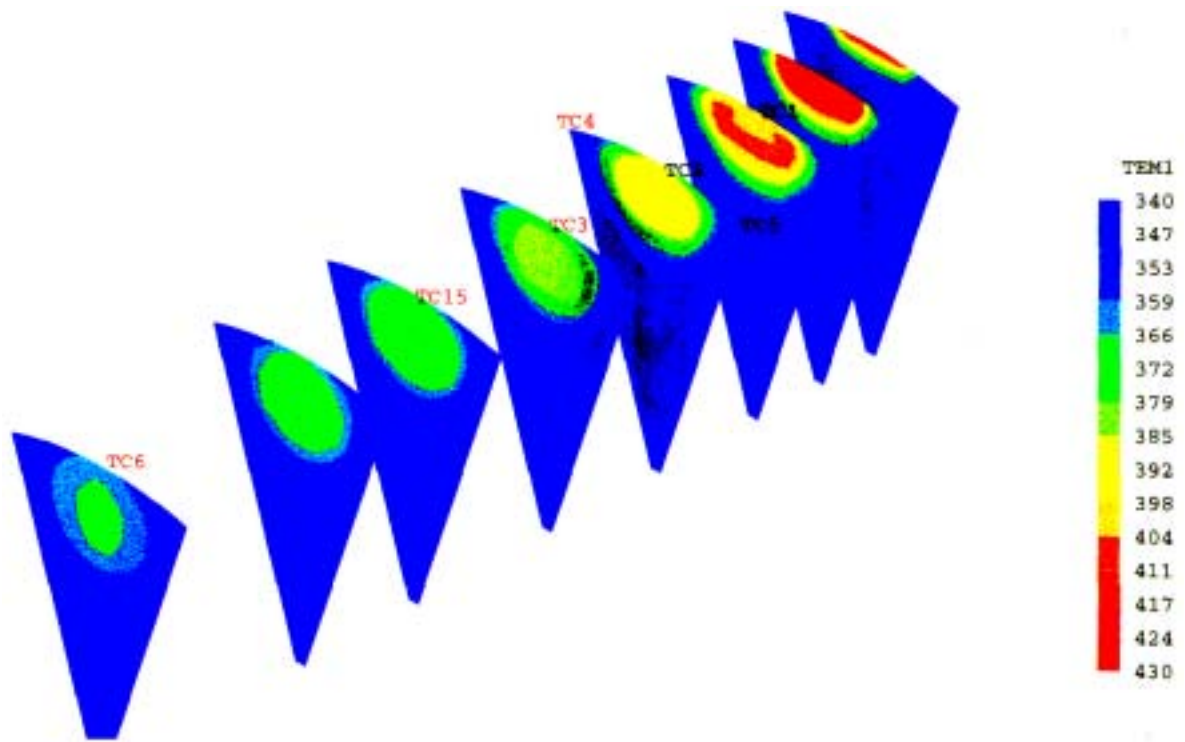


FIG. 4. Temperature distribution at various TC planes (RSTM; FINE GRIDS; AC1).

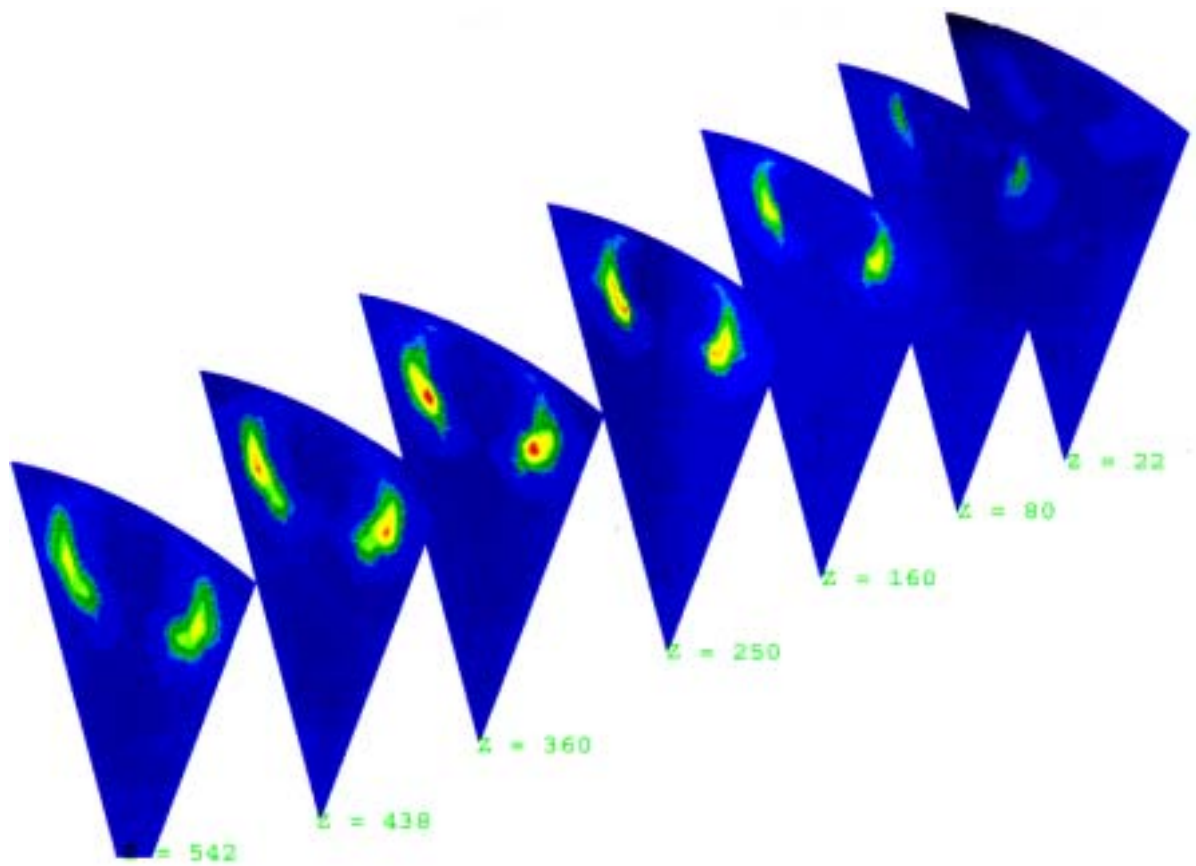


FIG. 5. Intensity of temperature fluctuation at various planes (RSTM; fine grids; AC1).

2.3.3. Flow and temperature distribution in the main pipe

The distribution of velocity and temperature in the symmetry plane, as predicted by the RSTM, are shown in Fig. 3. The radial injection of jet induces a small low pressure recirculation zone, just downstream of the jet junction. The temperature distribution at various axial positions is shown in Fig. 4. Marked in Fig. 4 are the various thermocouple positions. It is evident that the mixing area confines to almost 125 mm in radial direction and about two jet diameters in the circumferential direction. The intensity of temperature fluctuation evaluated from the local equilibrium model is shown in Fig. 5, where z is the axial distance measured from the center-line of the branch pipe. The maximum intensity is 1580 K² and the normalized RMS value is 44%. The maximum intensity occurs downstream of the jet in the parallel flow path and not at the junction between the jet and the main flow. Comparing with the temperature contours it can be seen that the intensity is maximum where the temperature gradient is maximum, as expected. Also the intensity is nearly zero adjacent to most of the thermocouples, placed in the symmetry plane (TC1, TC2, TC3, TC15, TC6). It may be mentioned that the maximum non dimensional RMS value as evaluated by differential transport model is low at 10% as against 44% predicted by the local equilibrium model. However the position of the maximum intensity is nearly the same for both the models. Also when the analysis was repeated with the standard K-epsilon model of turbulence, no significant changes in the flow and temperature distributions were seen.

2.3.4. Thermal analysis of the branch pipe

Since the grids of a boundary fitted mesh comprising of main pipe wall and jet pipe wall became highly skewed, a localized zone around the jet pipe including the walls of both the pipes was considered. The turbulent flow equations are solved with K-epsilon model invoking conjugate heat transfer option. The predicted temperature distribution on the outer surface of the pipe is shown in Fig. 6. It can be seen from this figure that there exists a sharp temperature gradient at the bottom part of the branch-main pipes junction. However the temperature gradient on the top part of the junction is not considerable as it is masked by the upward flowing high temperature sodium.

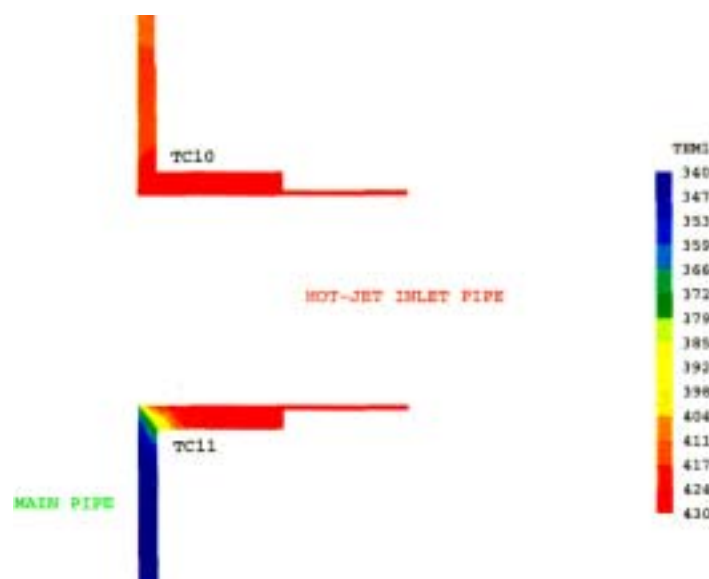


FIG. 6. Temperature in the metal walls at the junction.

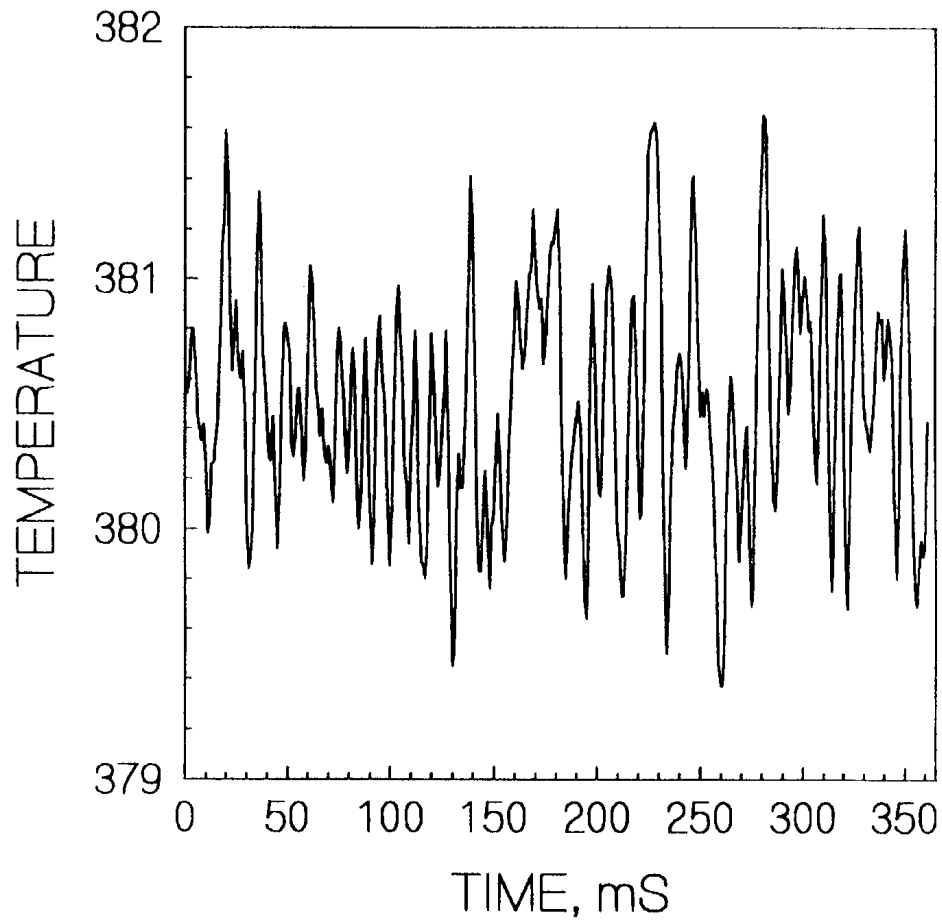


FIG. 7. Temperature vs. time plot (direct numerical simulation) at weld location.

TABLE 1. COMPARISON OF PREDICTED MEAN TEMPERATURE (K) AGAINST PLANT DATA

Location	IGCAR	PNC	KAERI	IPPE	AEA	Measured
TC – 1	678	665	672	656	674	-
TC – 2	661	641	667	653	635	635
TC – 3	649	625	655	647	623	628
TC – 4	613	613	613	614	613	615
TC – 5	613	613	613	614	613	631
TC – 6	635	615	626	634	615	618
TC – 7	613	613	613	613	613	-
TC – 8	613	613	613	613	613	613
TC – 9	613	613	613	613	613	613
TC – 10	700	-	-	-	700	-
TC – 11	694	-	-		694	-
TC – 12	700	-	700	-	700	-
TC – 13	613	613	613	613	613	619
TC – 14	613	613	613	613	613	613
TC – 15	640	618	641	641	618	621

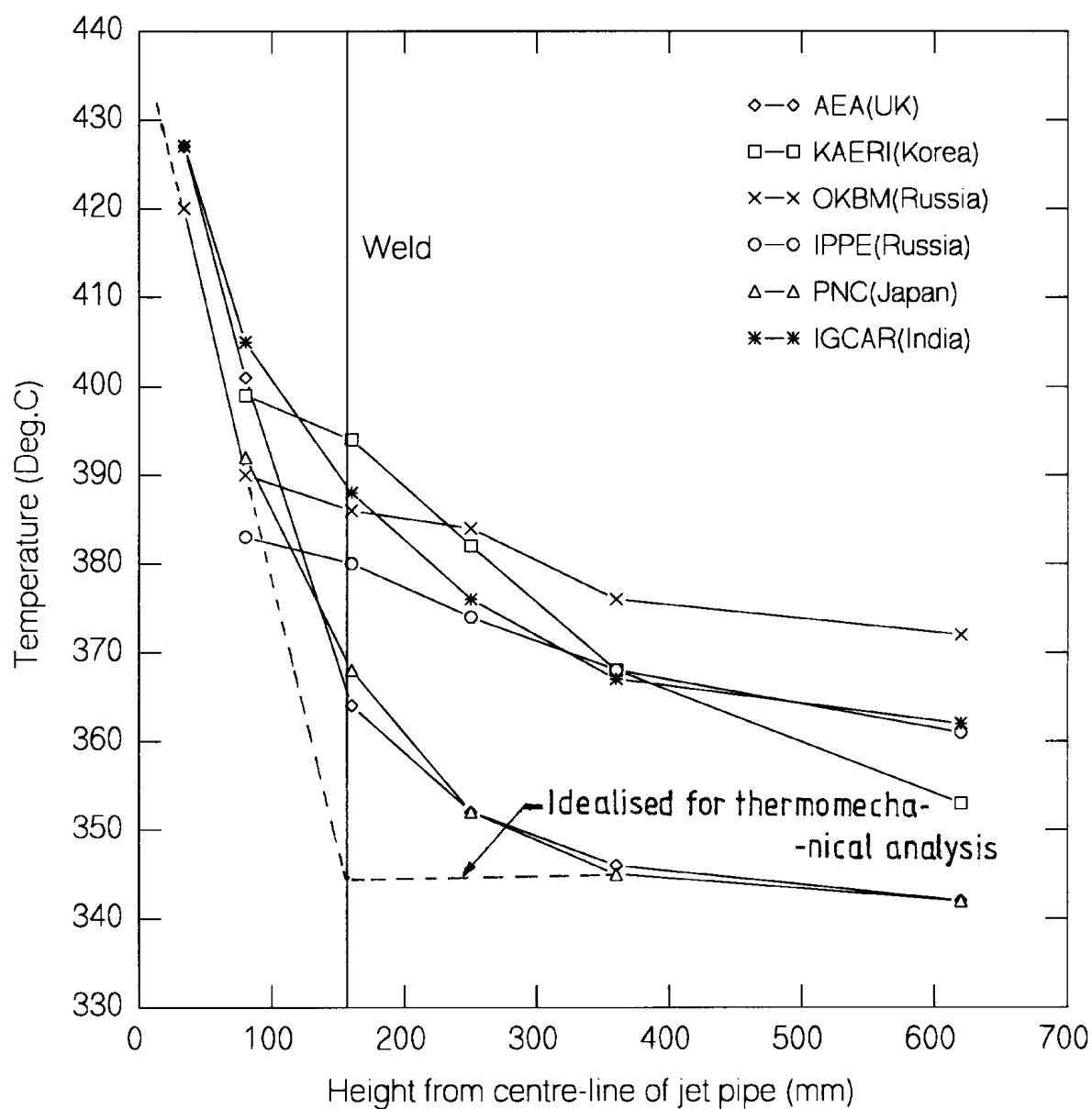


FIG. 8. Mean temperature of main-pipe along a vertical plane thro'jet-centre.

TABLE 2. PEAK-TO PEAK TEMPERATURE FLUCTUATIONS AND FREQUENCIES

Participants of the meeting	DT °C	Frequency, Hz
Great Britain (AEA)	86.48	0,01-10
India (IGCAR)	40	1.95
Korea (KAERI)	10	3.8
Russia (OKBM)	60	0.01-2
Russia (IPPI)	42	6.7-8.0
Japan (PNC)	~30	-

2.4. Transient results

For this purpose a restricted computational domain having 10 mm x 10 mm x 1 mm is considered. Two parallel sodium streams with a temperature difference of 90 K flow through this. The domain is split into 12500 (= 50x50x5) uniform sized cubes. The time step for the transient calculation is 1 ms. Calculations are carried out for a duration of 350 ms. The total CPU time required for this is 90 hours on a PC-486 machine. The inlet velocity to the domain is given random fluctuation generated out of pseudo random numbers. The temperature history at a monitoring point downstream of the domain is given Fig. 7. The frequency spectrum of the data evaluated by FFT analysis indicated that the frequency of temperature oscillations is 1.95 Hz. While the predicted frequency of oscillation is judged to be reasonable the amplitude appears too small.

2.5. Inter-comparison of the results

The predicted values of time averaged temperature at various thermocouple locations are presented in Table 1. Also presented in the Table are the values predicted by other participating countries and the plant measurement [5]. It should be mentioned, that the temperature values of the plant are available for an operating condition different from the one specified in the CRP specification i.e. the temperature of hot fluid is 680 K and that of cold fluid is 593 K (as against 703 K and 613 K respectively, specified in CRP). Hence the measured plant data are increased by 20 K and presented in Table 1. From the plant data, it may be seen that the temperature of the pipe wall is not symmetric as predicted by the calculations. This may be due to the presence of other bends or flow disturbances on the upstream side of the main and jet pipes, which are not specified/considered in any of the analysis. The temperature of the main pipe above the junction, in a vertical plane passing through the branch-pipe centre line is shown in Fig. 8. Also shown in the figure are the results of other participating countries. It is evident that the trend of all the results are identical and the present results match very well with that of Russia and Republic of Korea. It can be seen that due to the localized zone of mixing, only the thermocouples above the T-junction, on the downstream side (TC1, TC2, TC3, TC15, TC6) read temperatures different from that of main flow. The thermocouples on the upstream side of the junction (TC9) as well as those on the opposite side of the junction (TC7, TC8), and others far from the mixing zone (TC4, TC5, TC17, TC18), read the main flow temperature (613 K).

The peak-to-peak temperature difference and the frequency estimated by the participants are presented in Table 2. The results indicate that the data on frequency and temperature-difference differ significantly. The data of AEA contain the largest temperature-difference and a uniform spectral density of fluctuations in the range 0.01 to 10 Hz. Others obtained discrete spectral density.

2.6. Summary

The mixing region of hot and cold sodium has been found to extend about twice the jet diameter on all the directions. The predicted wall temperature values match reasonably with the plant data and well with the predicted values of other participating countries. In the present analysis the bend induced swirl is found not to affect the mixing region considerably. The temperature difference between the sodium and the wall is found to be less than 4 K. The results of RSTM and K-epsilon models were found to be very close. From the distribution of intensity of temperature fluctuation, it has been found that the thermocouples are positioned at

locations where the intensity is less and hence they are unlikely to indicate any signal. An attempt on Direct Numerical Simulation indicates that this option to predict the amplitude and frequency is not suitable and efforts should be directed towards other methods such as Large Eddy Simulation. Based on a small time simulation, the frequency is estimated to be ~2 Hz which is also in line with the predictions of other countries.

3. THERMOMECHANICAL ANALYSIS

3.1. Analysis methodology

The solution is sought basically in the time domain. Accordingly the transient temperature distribution in the metal wall is determined corresponding to the temperature history predicted by the thermal hydraulic analysis or idealized temperature assumed based on engineering judgement. Subsequently stress fluctuations are computed. Analysis is done with an assumption of a presence of a part-through crack of 0.5 mm deep at the junction of the circumferential weld in the main pipe located at a distance of 160 mm. from the central line of the branch pipe.

The following thermomechanical analyses are carried out:

- 3D thermal stress analysis corresponding to the time averaged temperature distribution using the general purpose code CASTEM 2000 with 4-noded shell elements.
- Axisymmetric analysis with and without considering the actual weld profile: Here the analysis is done for the temperatures, stresses and $J_{integral}$ values at the crack tip for the various crack depths in the range of 0.5 mm in the main wall thickness of 7 mm. Analysis is carried out for the frequency range, 0.01-10 Hz as predicted in the thermal hydraulic analysis.
- Random response of stress and $J_{integral}$ in the axisymmetric model corresponding to the random temperature distribution on the inner metal surface predicted by AEA, UK.
- Crack analysis to estimate the propagation of crack depth on the inner surface as per A16: Guide for defect assessment and leak before break analysis [6].

The ultimate objective is to estimate the time (no. of thermal fluctuations) to cause crack initiation as well as crack propagation after crack initiation. Crack initiation life is estimated based on (Td procedure recommended in RCC-MR (93) for the structures having geometrical singularity.

All the axisymmetric analyses are performed using the in-house code 'CONE'.

3.2. Details of the computer code 'CONE'

- Determination of transient temperature distribution, stress analysis and $J_{integral}$ computations by FEM;
- 8-noded axisymmetric elements;
- Heat transfer coefficient on the surface and associated surface temperature at various location have to be defined for the transient temperature calculation;

- Transient temperature is determined by 'Convolution Integral Algorithm' developed by 'Gurtin';
- Pressure, concentrated nodal forces and nodal displacements can be specified as input apart from thermal loading for stress analysis;
- Elasto-plastic-creep or viscoplastic analysis with ORNL and Chaboche models;
- Uses a special solution algorithm for mechanical calculations which is based on Non iterative Self correcting Solution (NONSS) algorithm. It generates tangential stiffness matrix for viscoplastic problems. About 7-10 times CPU timesaving is demonstrated compared to improved Euler's schemes;
- $J_{integral}$ is computed for both mechanical and thermal loadings;
- Continuum damage analysis capability using Lemaître-Chaboche continuum damage model;
- Validated thoroughly using many international benchmark problems in the domain of creep-fatigue, ratcheting and fracture mechanics.

3.3. Validation of 'CONE'

Prediction capability of 'CONE' for the stress intensity factor under thermal striping situations is demonstrated by solving 2 benchmark problems. The first one is a circular cylindrical shell with a part-through crack subjected to sinusoidal temperature variations on the inner surface. The problem is completely defined in Fig. 9. FEM meshes have been generated automatically in the code for the cracks at various depths that are illustrated in Fig. 10. The minimum element size in the vicinity of crack is 0.01 mm. From the computed $J_{integral}$ value stress intensity factor (K) is derived using the formula:

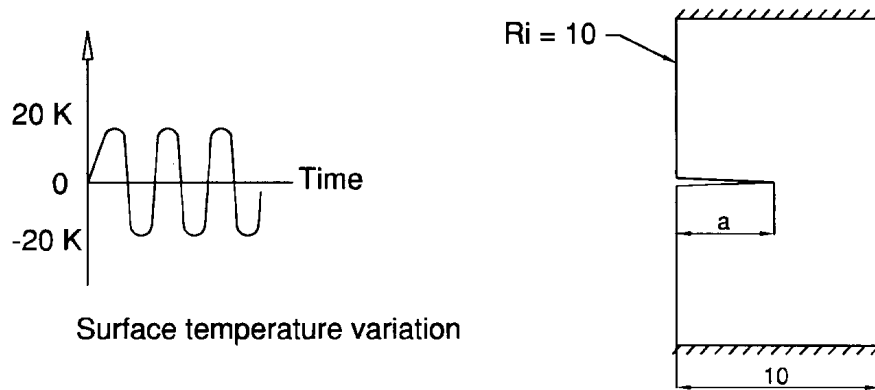
$$K = (J_{integral})^{1/2} E / (1 - \nu^2)$$

where E is Young's Modulus and ν is Poisson's ratio.

The fluctuations of K values at 3 discrete frequencies (0.0625, 1, and 6.25 Hz) are shown in Figs 11-13 for the crack depth varying from 0.5 to 5 mm respectively. FEM values predicted by CONE are compared in Fig. 14 with the analytical solutions given in Ref. [7] for various crack depths (0.5-5 mm) and frequencies 0.0625, 1, and 6.25 Hz. In the reference, K values are derived analytically using the stresses that are computed for the uncracked cylinder. This can be a satisfactory assumption for the higher frequency oscillations, for which the diffusion of temperatures is not penetrated deep into the thickness. However, for the lower frequency temperature oscillations, it is expected that the thermal stresses penetrate deep through the thickness. Hence the presence of a deep crack affects the stress distribution in the vicinity of the crack tip. Accordingly, the analytically computed stress intensity values do not match with the realistic values computed by FEM. For higher crack depths and lower frequency cycling, the analytical values computed without end restraint tend to match with the FEM solutions. These aspects are clearly seen in Fig. 14.

In order to validate the CONE for the situation involving random temperature fluctuations, a plate of 10 mm thickness with a part-through crack of varying depths from 0.5 mm to 5 mm is analyzed. The problem is defined completely in Fig. 15. The FEM mesh used for the problem no. 1 is employed for this problem also. $H(a, \omega)$, i.e. the maximum stress intensity factor per unit temperature amplitude and crack depth a, are calculated for the different crack depths and frequencies, the values of which are shown in Fig. 16.

Geometry : A part through crack on the inner surface of cylindrical shell



Crack length : 0.5 - 5 mm

Material data :

Material	= Type 321 SS
Temperature	= 773 K
Thermal conductivity	= 20.3 W / m / K
Specific heat	= 570 J / kg / K
Young's modules	= 1.63×10^5 MPa
Co - efficient of thermal expansion	= 20×10^{-6} mm / mm / K
Poisson's ratio	= 0.3
Mass density	= 7760 kg / m ³

Thermal loading :

Sinusoidal (0.0625 , 1 and 2.25 Hz) with amplitude of 20 K

Results to be compared :

Crack depth vs stress intensity factor at 3 discrete frequencies

FIG. 9. Definition of benchmark Problem No – 1.

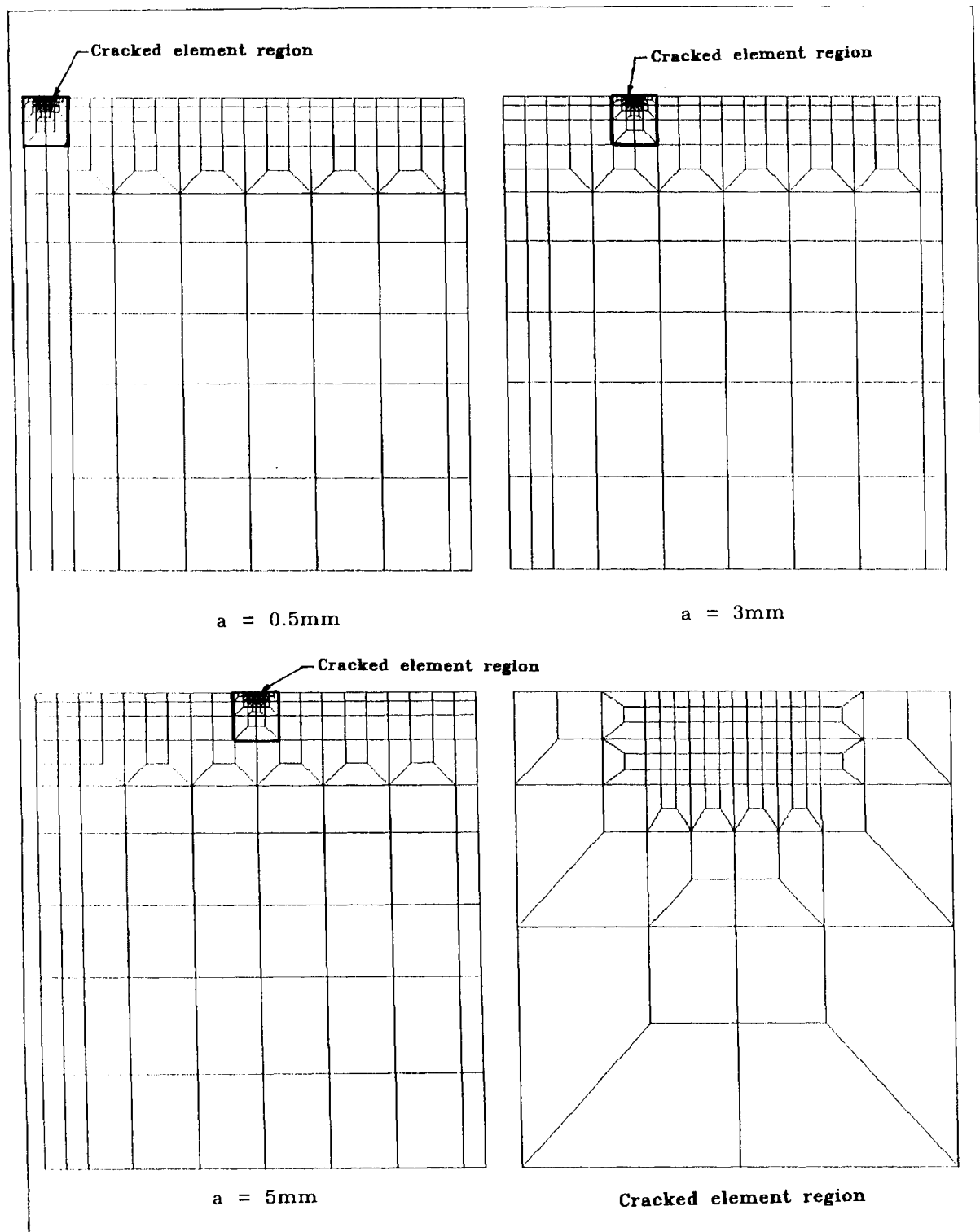


FIG. 10. Finite elements mesh for benchmark problem No: 1&2.

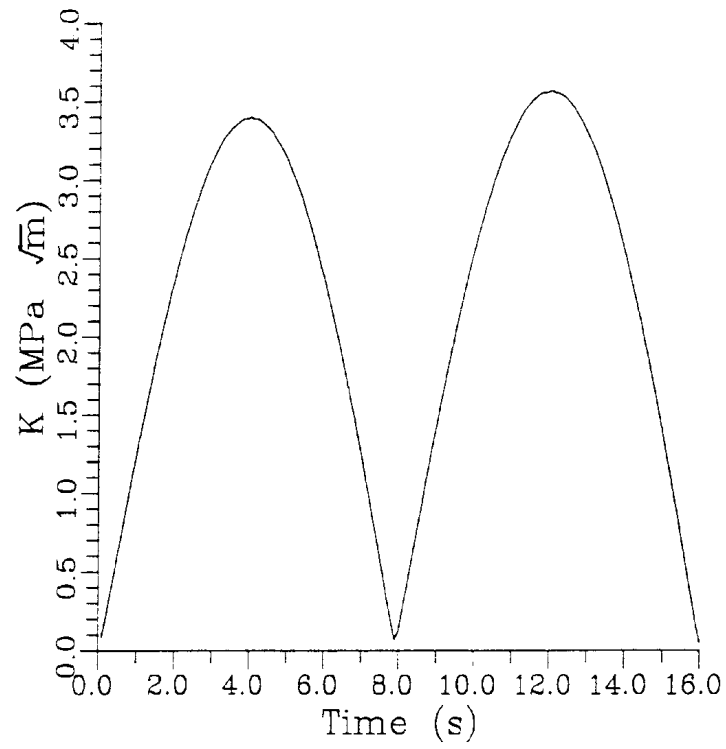


FIG. 11. Stress intensity factor fluctuation for 0.0625 Hz.

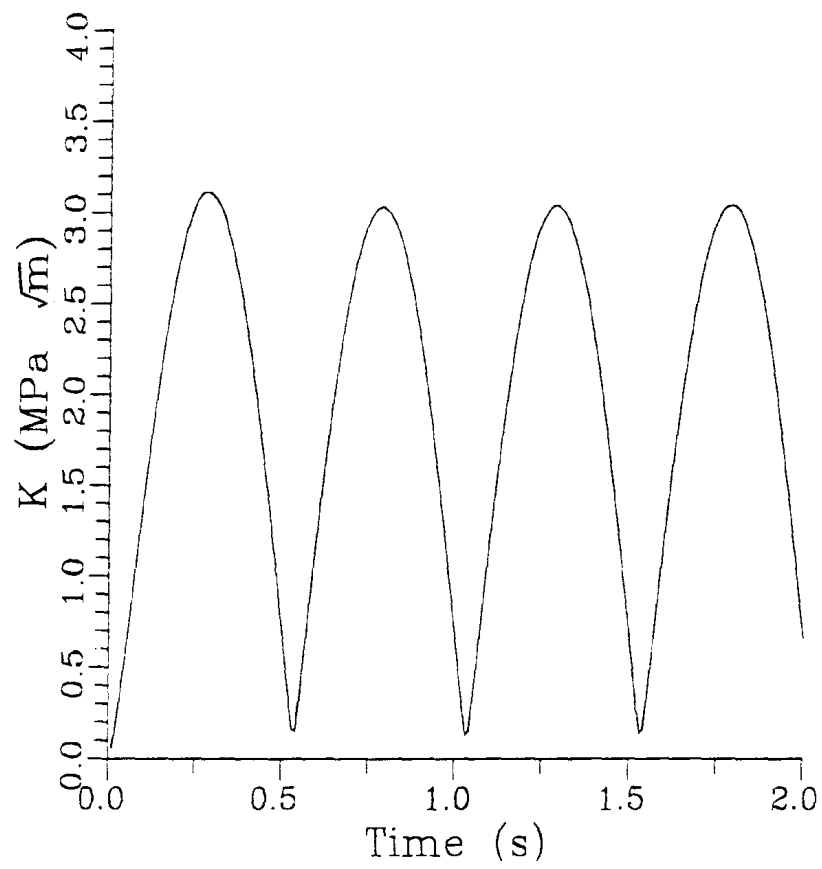


FIG. 12. Stress intensity factor fluctuation for 1 Hz.

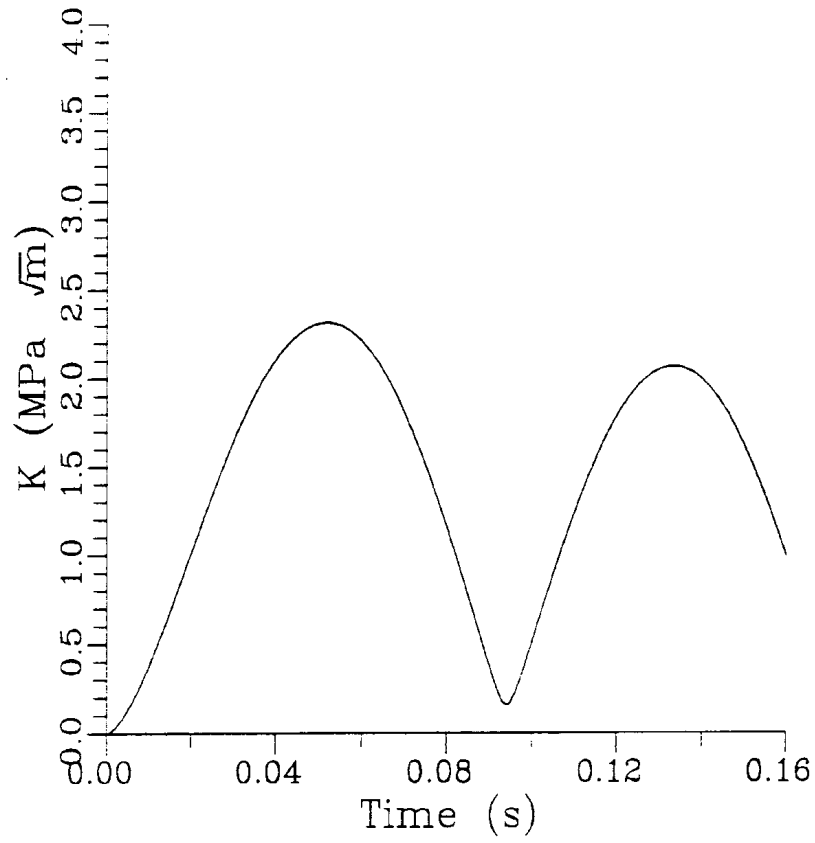


FIG. 13. Stress intensity factor fluctuation for 6.25 Hz.

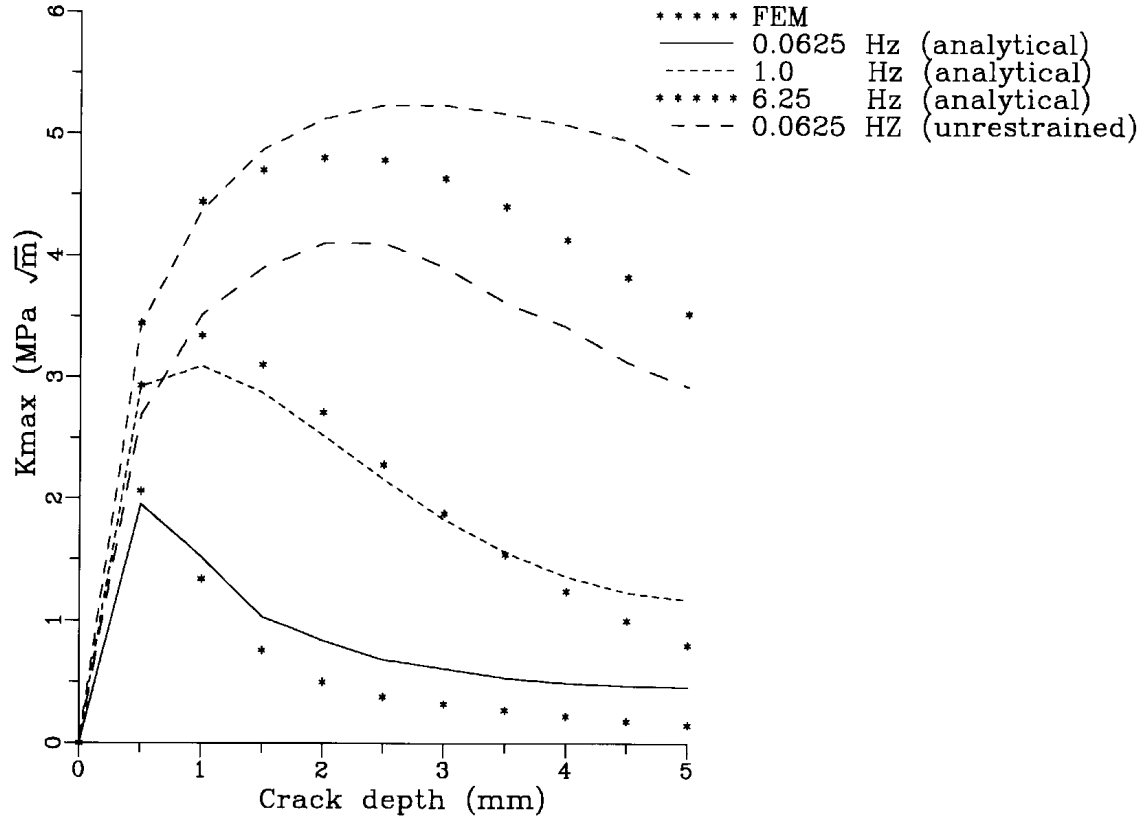
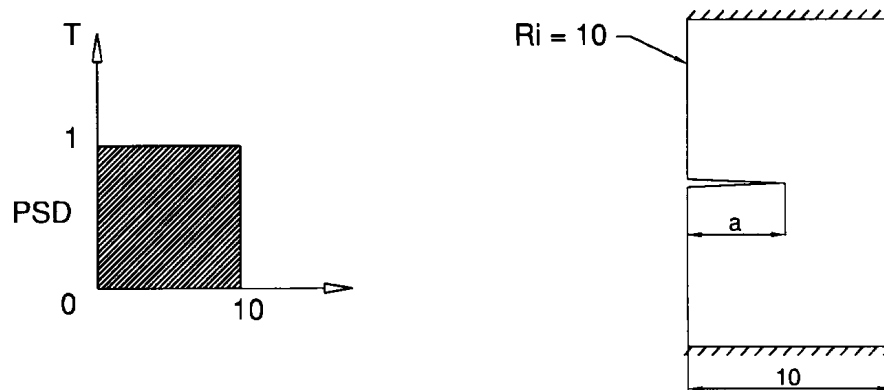


FIG. 14. Maximum stress intensity fluctuation (crack at the inner surface of cylinder).

Geometry : Plate with a part through crack



Crack length : 0.5 - 5 mm

Material data :

Material	= Type 316 SS
Temperature	= 823 K
Thermal conductivity	= 21.54 W / m / K
Specific heat	= 581 J / kg / K
Young's modules	= 1.585×10^5 MPa
Co - efficient of thermal expansion	= 19.91×10^{-6} mm / mm / K
Poisson's ratio	= 0.29

Thermal loading :

Random temperature signal with constant spectrum up to a frequency of 10 Hz

Results to be compared :

Crack depth vs Peak stress intensity factor

FIG. 15. Definition of benchmark Problem No – 2.

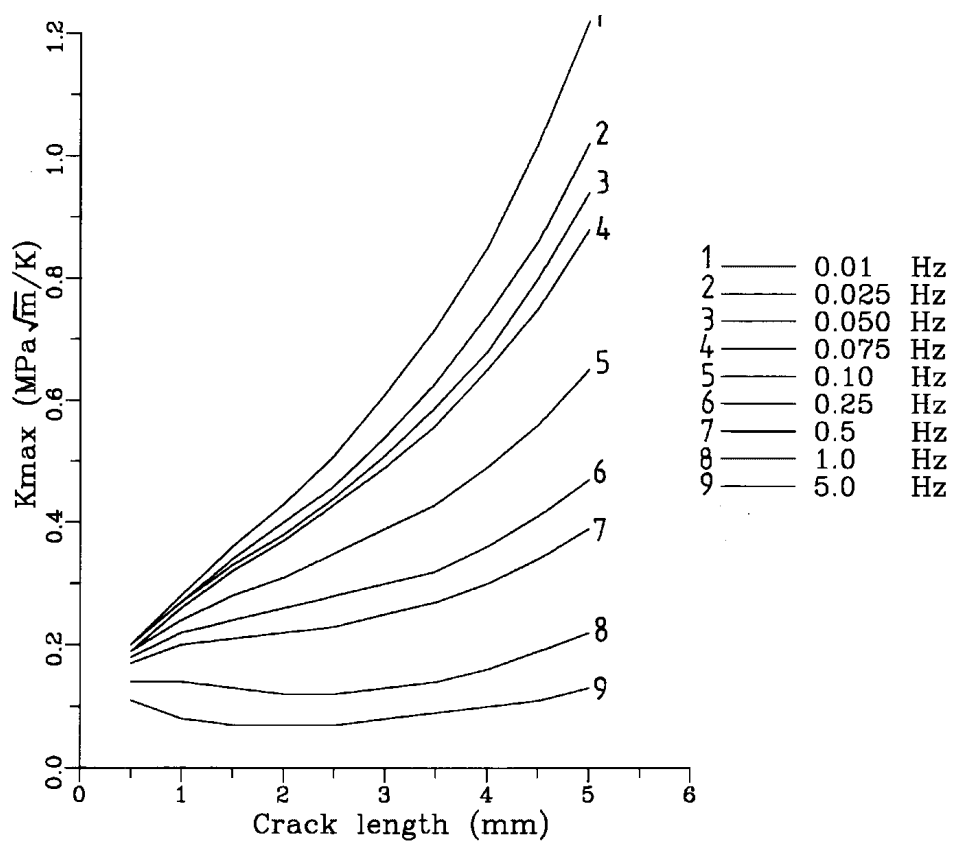


FIG. 16. Maximum stress intensity factor fluctuation (Plate assumption).

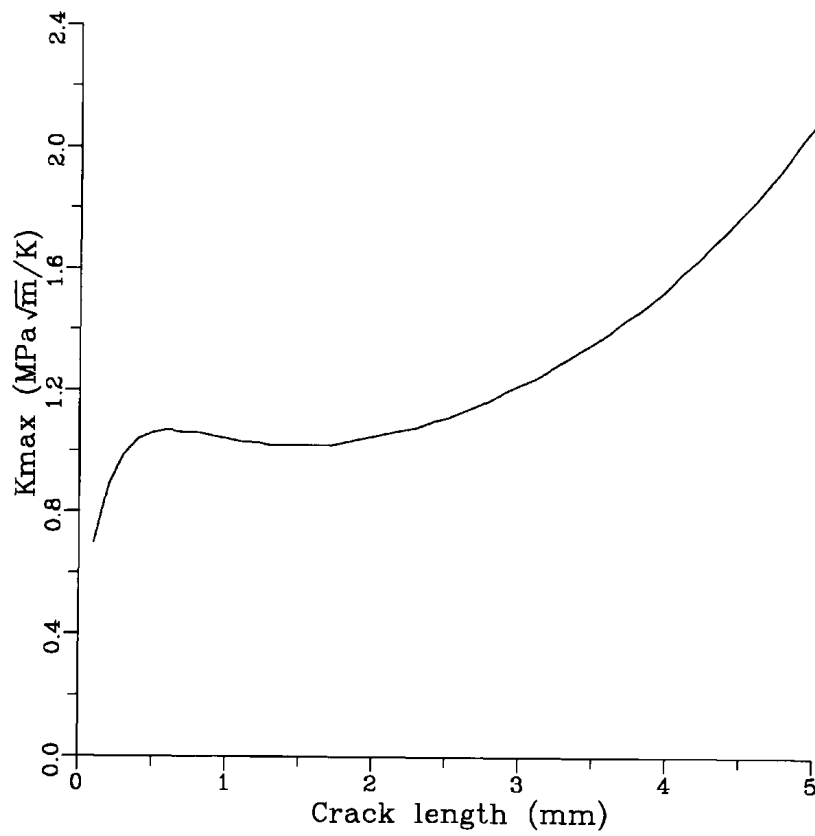


FIG. 17. Maximum stress intensity factor fluctuation.

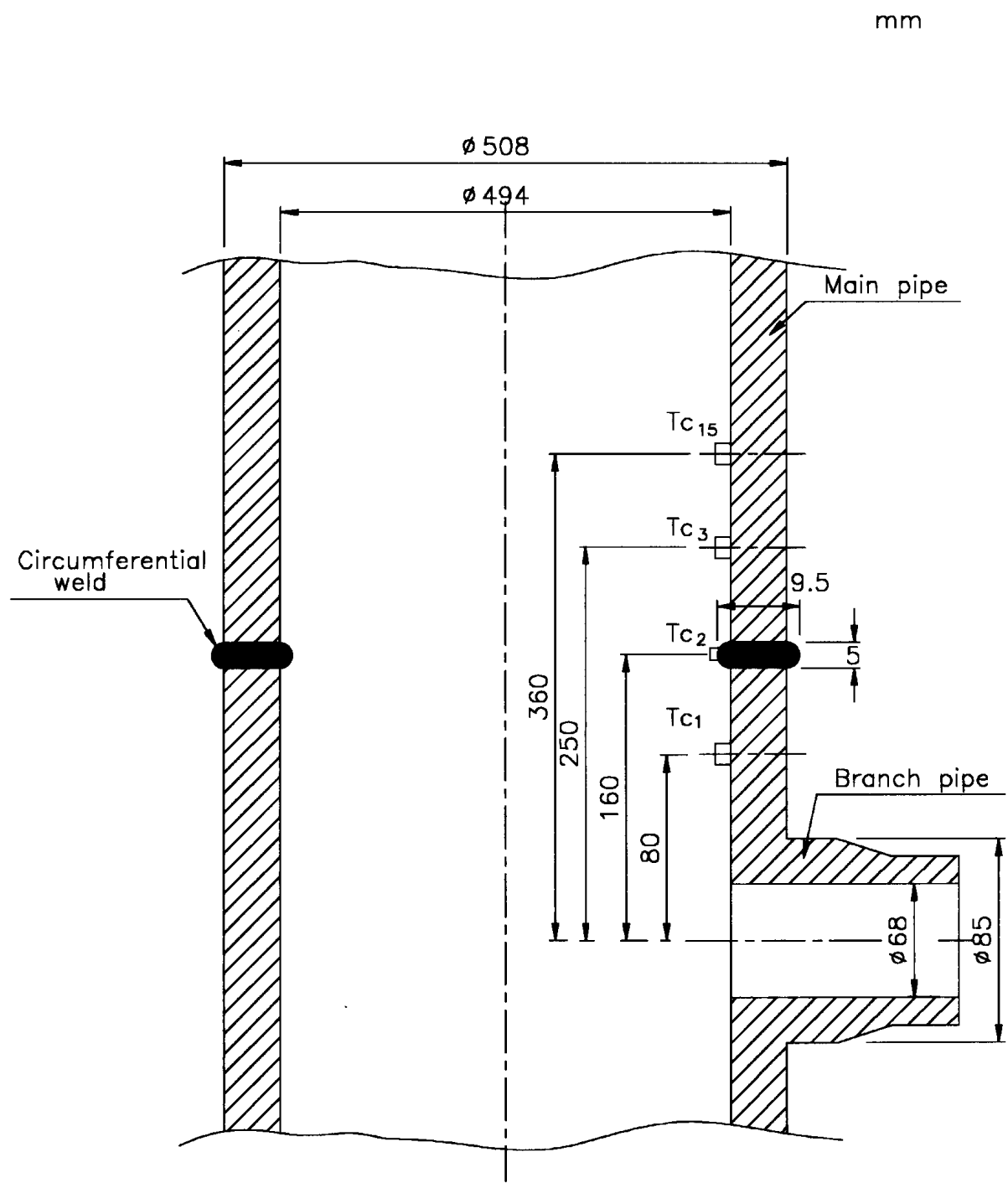


FIG .18. Details of geometry and thermocouple locations.

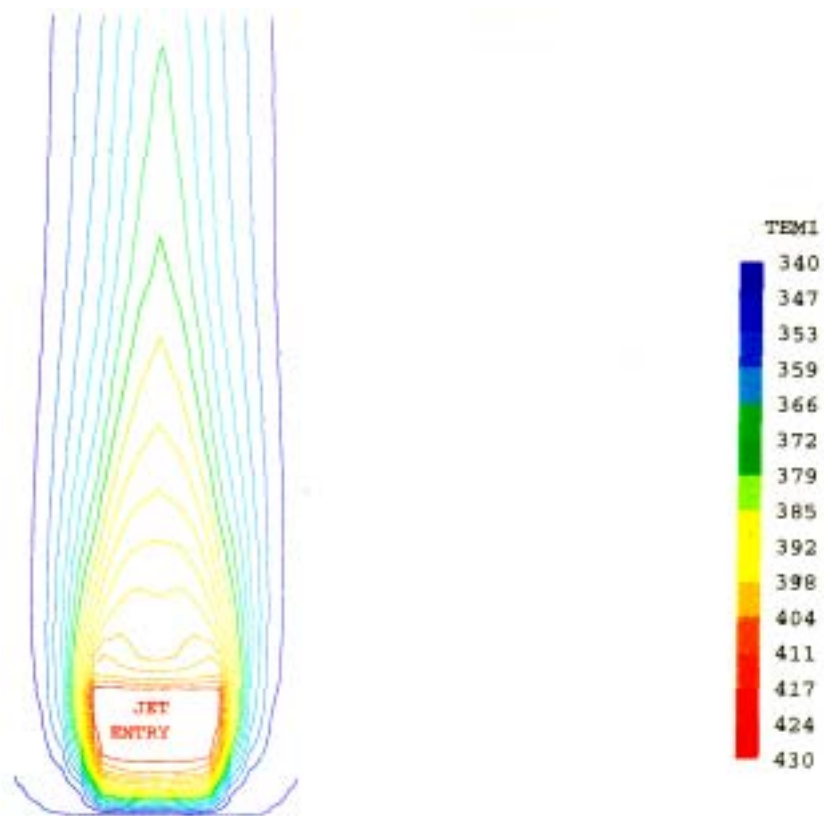


FIG. 19. Temperature on the main-pipe wall.

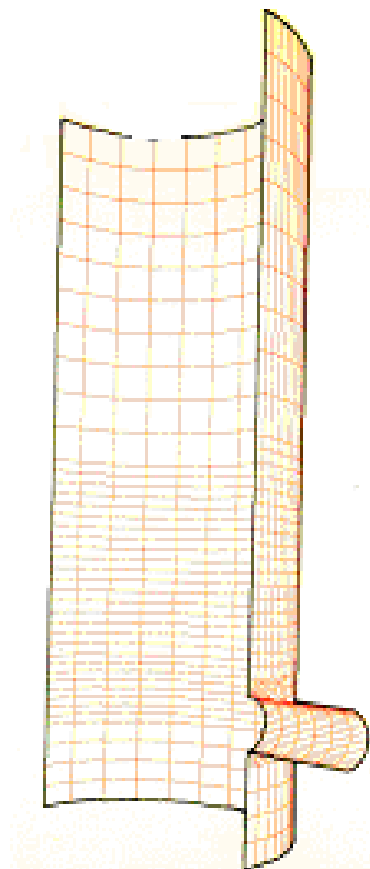


FIG. 20. FEM mesh..

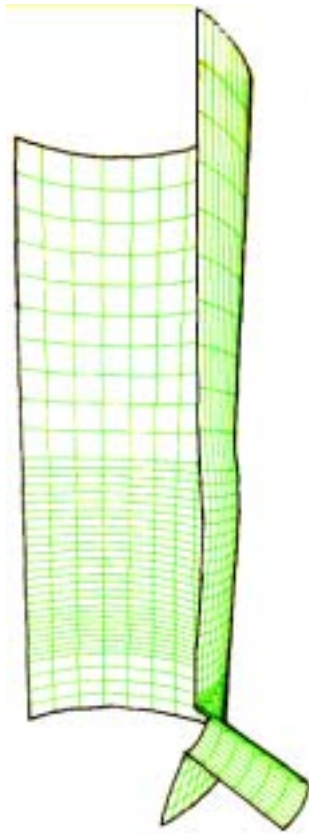


FIG. 21. Deformed FEM mesh.

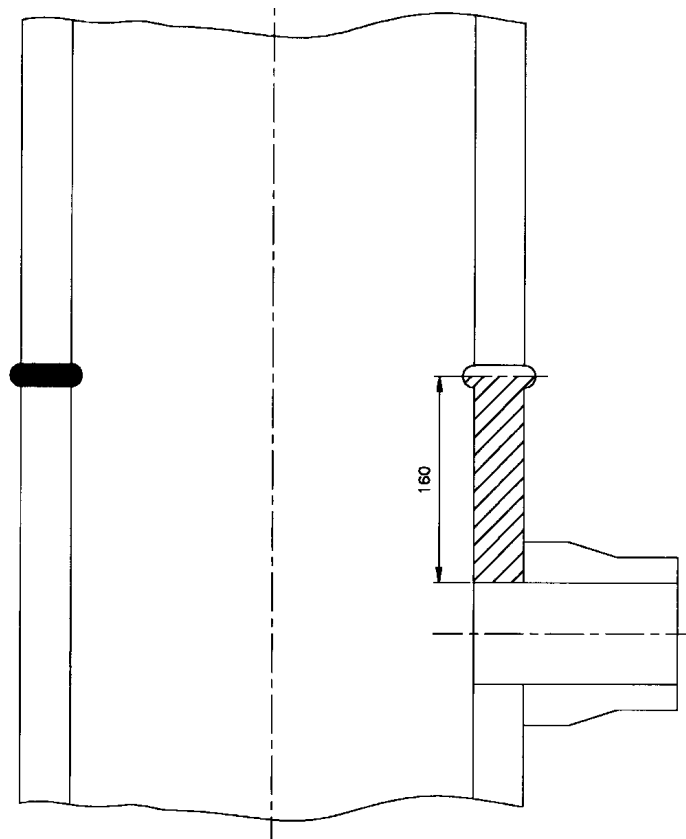
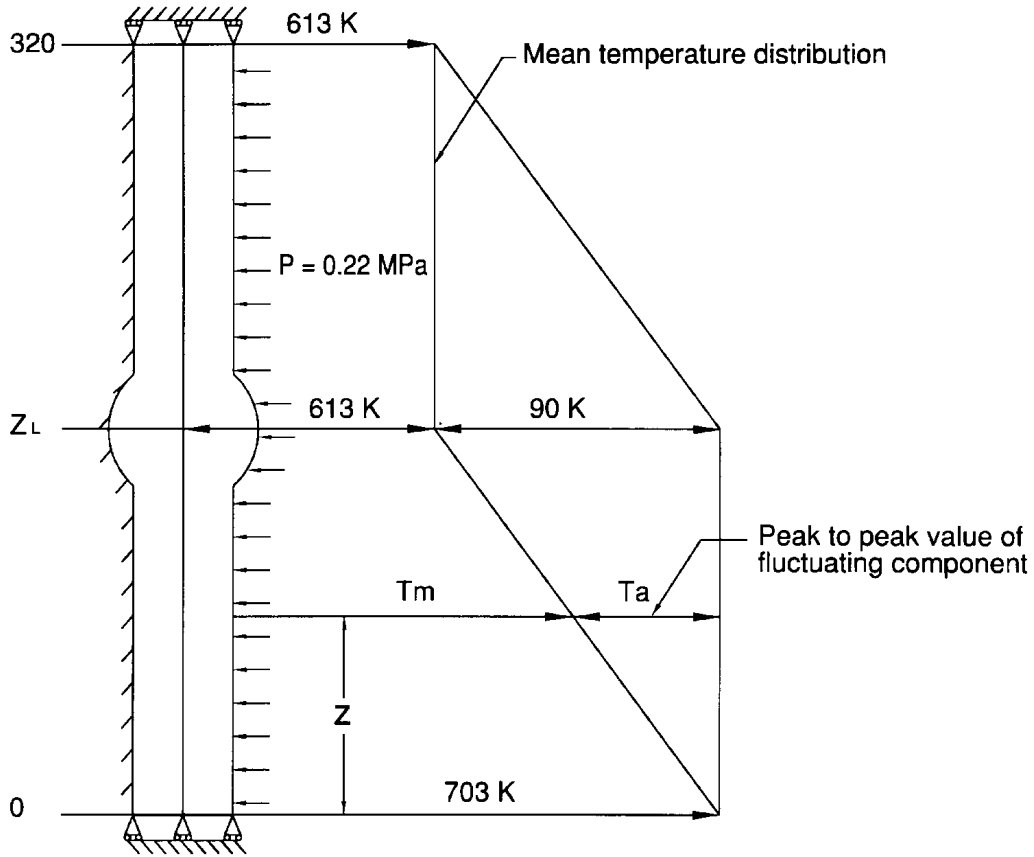


FIG. 22. Axisymmetric region considered for analysis.



$$T_m = (703 - 90 z / Z_L) \text{ (K)}$$

$$T_a = 45 z / Z_L (1 - \cos \omega t) \text{ (K)}$$

FIG. 23. Idealised temperature distribution assumed on the inner surface of the main pipe.

Using the PSD of surface temperature $S_T(\omega)$, which is assumed as a constant spectrum up to ω_0 (10 Hz), $S_K(a, \omega)$, the PSD values of K are calculated as:

$$S_K(a, \omega) = |H(a, \omega)|^2 S_T(\omega)$$

The rms value of K is given by: $K_{rms} = \int S_K(a, \omega) d\omega$.

As indicated in Ref. [8] that the stress intensity factor crest values at the surface does not increase significantly with depth. Hence $\Delta K_{max} / K_{rms}$ for any crack depth is assumed to be equal $\Delta K_{max} / K_{rms}$ for very small crack confined to the surface. Accordingly, $\Delta K_{max} / K_{rms}$ is equal to $\Delta T_{max} / T_{rms}$ which is the crest factor used to derive the ΔK_{max} from K_{rms} values. Fig. 17 shows the variation of ΔK_{max} , as a function of crack depth. The increasing dominance of the crack depth in relation to the temperature and thermal stress attenuation effects can also be seen in Fig. 17 as mentioned in the Ref. [8].

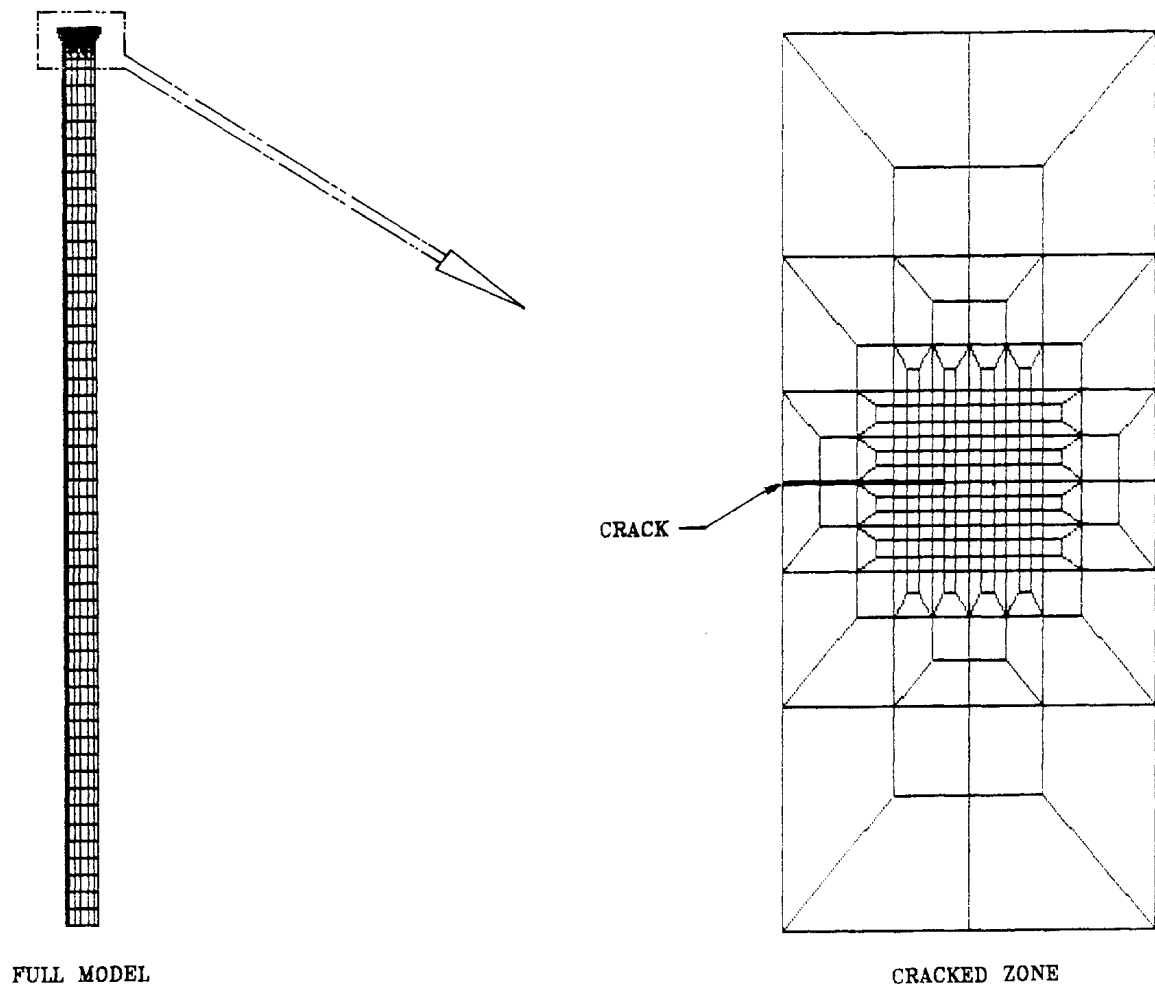


FIG. 24. FEM mesh used in the analysis.

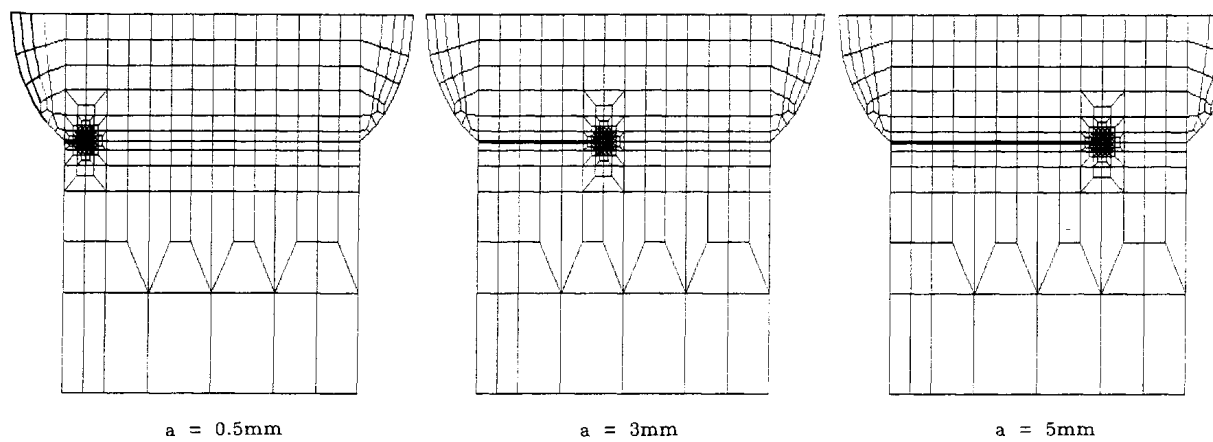


FIG. 25. FEM mesh for various crack depths.

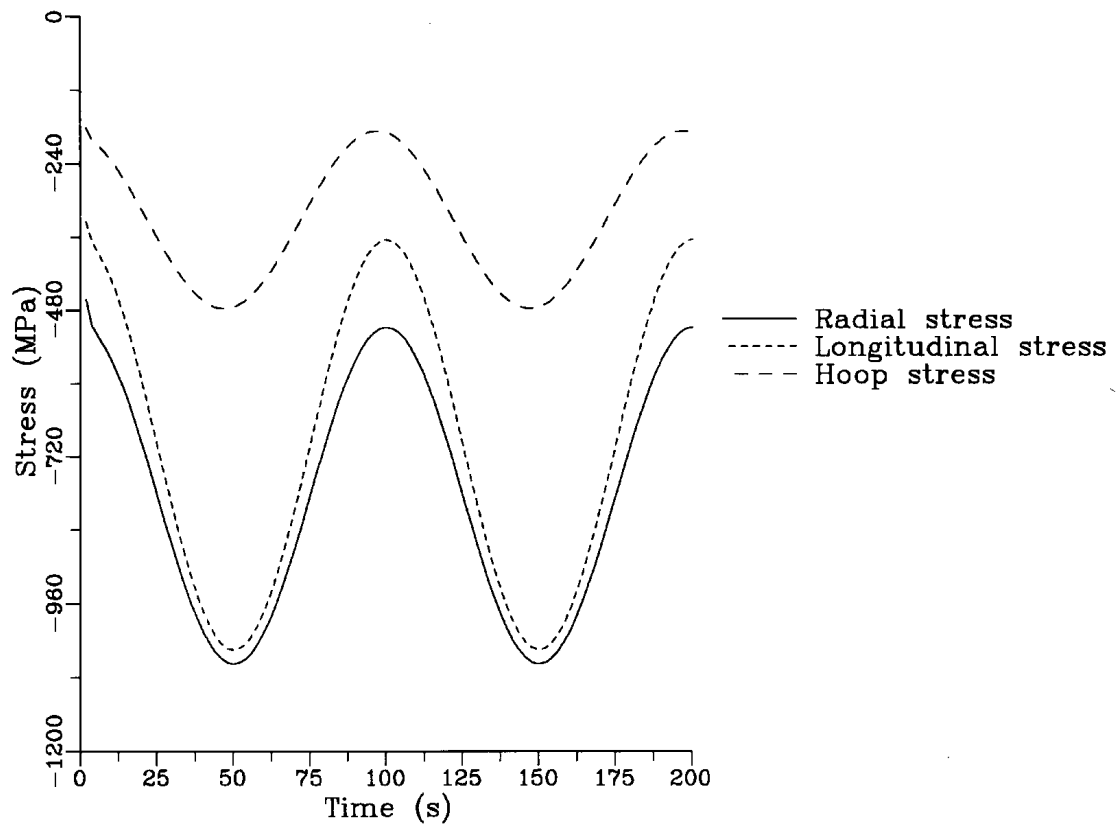


FIG. 26. Fluctuation of stresses at 0.05 mm from crack tip. $f = 0.01$ Hz, $a = 0.5$ mm.

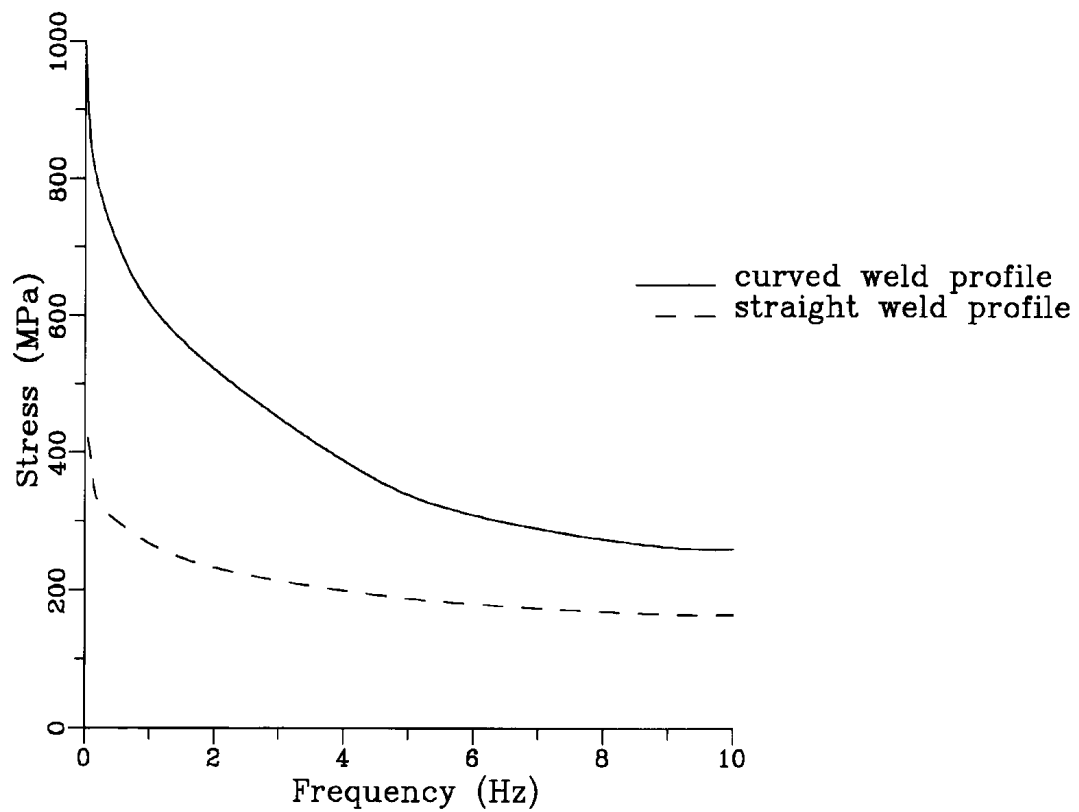


FIG. 27. Stress range at a distance of 0.05 mm from crack tip (defect size is 0.5 mm).

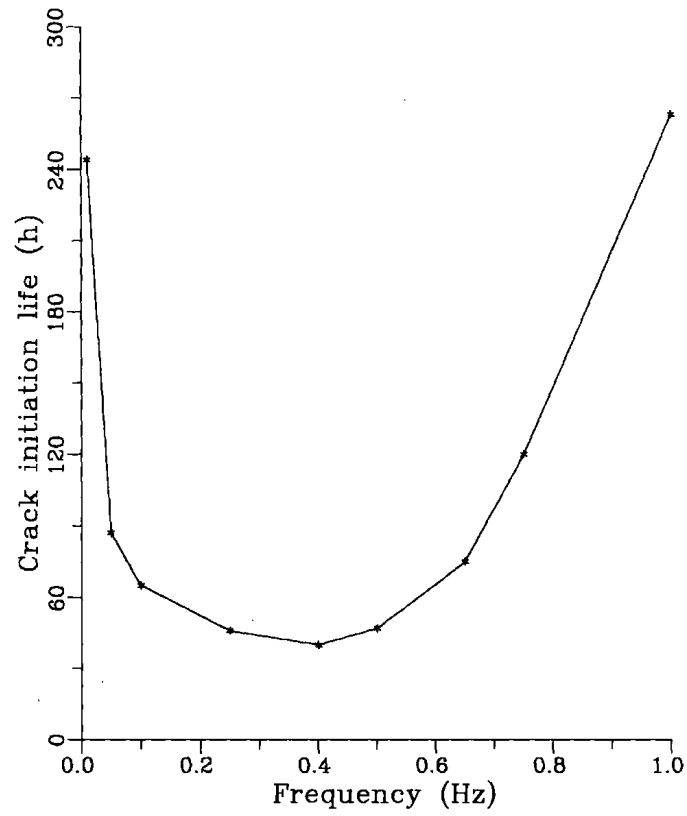


FIG. 28. Prediction of crack initiation life (as per RCC-MR with 0.5 mm defect).

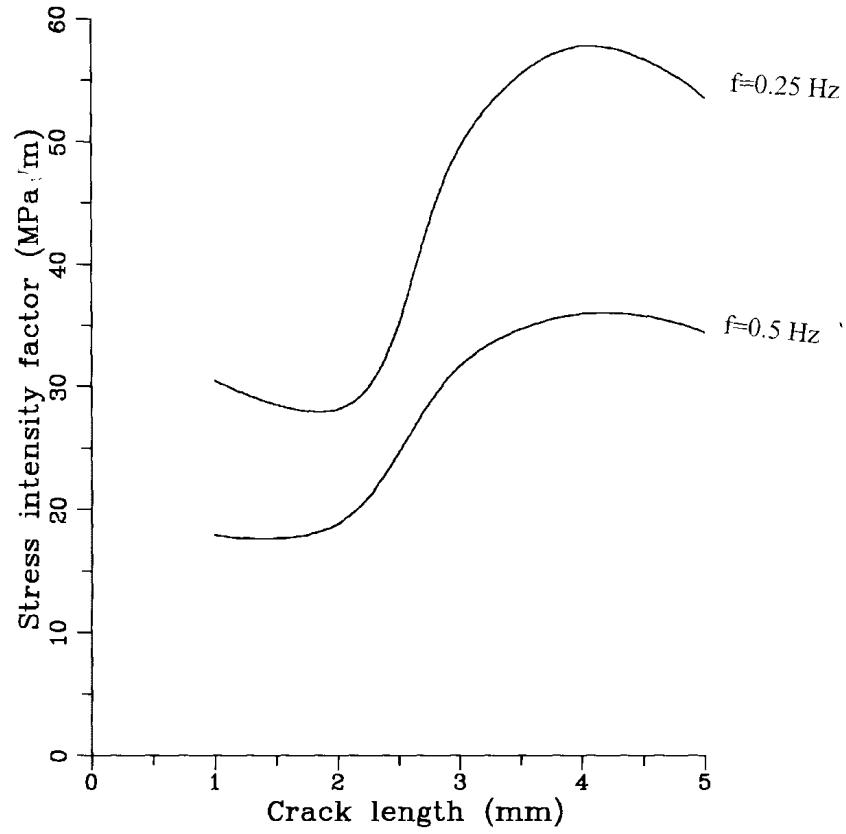


FIG. 29. Stress intensity factor range.

TABLE 3. RESULTS OF CRACK PROPAGATION ANALYSES

Crack depth (mm)	Number of cycles		Time (hours)	
	0.25 Hz	0.5 Hz	0.25 Hz	0.5 Hz
0.5	144600	1207129	80.3333	0670.62
1.0	175563	1443356	97.5350	0901.96
1.5	210922	1657401	117.179	0920.77
2.0	241706	1816789	134.291	1009.33
2.5	252574	1977572	140.319	1043.10
3.0	257166	1905114	142.970	1058.40
3.5	260301	1925044	144.612	1069.47
4.0	262708	1941114	145.949	1078.40
4.5	265153	1956996	147.307	1087.22
5.0	267963	1974161	149.969	1096.76

3.4. Analysis of mixing T-junction

3.4.1. Thermal stress analysis for time averaged temperatures

The input data is the time averaged temperature distribution as shown in Fig. 19, which have been predicted through thermal hydraulic analysis. 180° symmetric structure of the main pipe along with branch pipe is modelled by 4 noded isoparametric thin shell elements using CASTEM 2000. FEM mesh is shown in Fig. 20. The deformed pattern of the structure in the vicinity of the branch pipe and circumferential weld location are depicted in Fig. 21.

The following information are derived from the 3D analysis:

- The maximum Von Mises stresses at the junction of circumferential weld is about 3-4 MPa.
- Deformation and stress distributions in the main pipe wall along the axial length starting from the junction of the branch pipe to the distance of about 320 mm can be simulated by an axisymmetric analysis involving the regions indicated in the Fig. 22. Hence subsequently all the mechanical analysis can be done using axisymmetric model.

3.4.2. Analysis for crack initiation life

A preliminary conservative calculation indicates that no crack initiation is possible in the straight main pipe without any geometrical discontinuity, if subjected to the thermal striping corresponding to 90 K temperature difference. Presence of weld also does not cause crack initiation provided that there is no high stress concentration or any metallurgical notch in the weld discontinuity zone. Hence in order to explain the failure, it is necessary to assume either a high stress concentration region or a small crack like defect in the weld. Since RCC-MR code provides robust design procedure for estimating the fatigue life of the structures with a geometrical singularity, it is decided to assume a small defect of 0.5 mm deep at the highly stressed region at the interface of weld and parent metal based on engineering judgement. With this, the curved weld profile is also assumed which extends over the length of 5 mm in

the form of a circular arc with the maximum thickness of 1.25 mm on the either surfaces of main pipe. Thus, the maximum thickness along the weld centre line is 9.5 mm against the main wall thickness of 7 mm. The extra material deposited in the welds adds significant thermal inertia to the main pipe that is very important for the damage assessment under thermal cyclic fluctuations. Hence an FEM model involving both main pipe and curved weld profile is developed for the thermomechanical analysis.

Based on the predictions of time averaged temperatures as well as the fluctuating components of temperatures by various participants (Fig. 8 and Table 2), an idealized temperature distribution is assumed as indicated in the Fig. 23 for all the thermomechanical analysis. The frequency range considered is 0.01-10 Hz. FEM mesh is shown in Fig. 24 along with very fine meshes (minimum size is 0.01 mm) around crack tip. The fine mesh zone around the crack tip can be placed anywhere depending upon the orientation of crack tip. The automatic mesh generated at three typical crack lengths (0.5 mm, 1, and 5 mm) are illustrated in Fig. 25.

As per RCC-MR procedure, it is required to calculate the variation of stresses at a distance of 0.05 mm from the defect (0.5 mm in the present problem). The radial, longitudinal and hoop stress fluctuations at this specified location corresponding to the frequency of 0.01 Hz is indicated in Fig. 26. The Von Mises stress ranges computed over the frequency range, 0.01-10 Hz, for the case with curved weld profile and also for the straight weld profile are shown in Fig. 27. Using $K\epsilon$ and $K\sigma$ values (for SS 316 LN-1 for 304 LN values are not yet included) given in RCC-MR (1993) code, the elastoplastic strain ranges corresponding to the given stress range are estimated. The strain ranges are further divided by a factor of 1.5 as per the code before entering in to fatigue curve for welds given in the Ref. [1] to estimate the number for permissible cycles (N_p) for crack initiation for the given frequency (f). The time to cause crack initiation is then equal to (N_p/f)/3600 h. The values thus computed are shown in Fig. 28. It is seen in the figure that there exists a critical frequency range 0.3-0.5 Hz) for which time required to cause crack initiation minimum (about 40 h). This value is compared with the values (20-30 h) predicted by Novatome [9], The critical frequency value is reported as 0.2 as per Ref. [10].

3.4.3. Crack propagation analysis

The objective of the crack propagation analysis is to estimate the time vs. crack length as a function of frequency of thermal striping. Since it is noted from crack initiation studies that the critical frequency domain is 0.25-0.5 Hz, analysis is restricted to these 2 frequencies. Analysis is done both for straight weld profile (fully flushed weld) and the actual weld profile. The range of stress intensity values (ΔK) are derived from the range of $J_{integral}(\Delta J_{el})$ computed by FEM, using the formula:

$$\Delta K = (\Delta J_{el})^{1/2} E / (1 - \nu^2)$$

However for the crack propagation calculations, the ΔK values are derived from the corrected ΔJ based on A16 method. As per this, two correction factors, (i) for the use of real nominal stress rather than the elastically computed nominal value and (ii) for accounting for the plastic deformation, are used. The computed ΔJ values are also shown in the Fig. 29. Using this, crack length vs. number of cycles, derived by integration with the following Paris law is given in Table 3.

$$da/dn = 1.8 \times 10^{-10}, (\Delta K)^4$$

4. CONCLUSION

Thermomechanical and fracture analysis predicts satisfactorily the crack initiation and propagation times. Crack initiation time is 30-40 h. Time needed to propagate up to 5 mm is about 1000 h.

REFERENCES

- [1] INTERNATIONAL ATOMIC ENERGY AGENCY Benchmark on a T-Junction of LMFR Secondary circuit involving thermal striping phenomenon, Technical specifications (1996).
- [2] CHAM Development Team, The PHOENICS reference manual, CHAM Ref CHAM/TR 200a, CHAM Ltd., Wimbledon, London (1991).
- [3] RODI, W., Turbulence models and their application in Hydraulics, IAHR Report (1979).
- [4] PATANKAR, S.V., Numerical heat transfer and fluid flow, McGraw-Hill (1980).
- [5] BIRBRAER, P.N., KIRYUSHIN, A.T, KUZAVKOV, N.G., SOBOLEV, V.A., Thermohydraulic and Thermal Analysis of coolant pipes of T-junction- Generalization of calculation results performed by participants, paper presented in the Research Coordination Meeting on Harmonization and Validation of Fast Reactor Thermomechanical and Thermohydraulic Codes and Relations using Experimental Data, 6-10 October 1997, Obninsk, Russian Federation.

THERMOMECHANICAL AND FRACTURE MECHANICS ANALYSIS ON A TEE JUNCTION OF LMFR SECONDARY CIRCUIT DUE TO THERMAL STRIPING PHENOMENA

N. KASAHARA

O-arai Engineering Center,
Japan

Abstract. Structural analysis has been conducted concerning a tee junction of the PHÉNIX secondary circuit due to thermal striping phenomenon, in the IAEA coordinated research programme on "Harmonization and validation of fast reactor thermomechanical and thermohydraulic codes and relations using experimental data". Under the boundary condition provided from thermohydraulic analysis with DINUS-3, BEMSET, and AQUA codes, possibility of crack initiation and propagation was assessed, by two different approaches. One is a simplified analysis approach based on the Structural Response Diagram proposed in this study. The other is a detailed analysis method with the Finite Element structural analysis code FIN AS and the Fracture Mechanics analysis code CANIS.

When taking into account of attenuation factors of temperature fluctuation, calculated results indicate that cracks hardly initiate at base metal portions. On the other hand, strength of welded joint is reduced mainly by peak stress concentration at penetration beads, so that there is possibility of crack initiation within several thousands hours at the welded joint. According to fracture mechanics analysis, crack propagation rate is sensitive to mean stress and low frequency fluctuation. If there exist sufficient mean stress and low frequency components of temperature fluctuation, cracks will pass through the secondary circuit pipe wall.

1. INTRODUCTION

It is called thermal striping, that high cycle fatigue failure induced by random temperature fluctuation at mixing region of hot and cold fluid, which becomes sometimes a critical problem in LMFR plants. Since thermal striping phenomenon is characterized by the thermohydraulic and thermomechanical coupled problem, conventional evaluation procedures are conservative from unknown factors, and are required to be rationalized for construction of reliable and economical plants.

The present benchmark deals with an industrial thermal striping problem at a tee junction of the PHÉNIX secondary circuit, where though wall cracks have been observed during the course of a campaign of inspection, after an operation of 90 000 hours. Under nominal operation, sodium at 340°C flows into the main pipe of the secondary circuit. A small pipe, connected with a tee junction to the main pipe, discharges sodium at 4300°C into the main pipe. The two convergent flows at different temperatures ($\Delta T = 90\text{K}$) are therefore mixed at the tee junction area. The main features of the circuit in the tee junction area are shown in Fig. 1 [1]. Materials are AISI 304 stainless steel for base metal and 16Cr-8Ni-2Mo for weld metal. Such information was also provided in the benchmark, as a profile of the circumferential weld, forces and moments in the pipes (Table 1), material properties of base and weld metal.

This Co-ordinated Research Program (CRP) of IAEA was cooperative work between thermomechanical and thermohydraulic specialists, therefore, author adopted thermohydraulic analysis results with CFD codes [2] as thermal boundary conditions and paid attention to investigation of boundary area between both fields such as wall attenuation. From viewpoint of failure assessment, detailed analysis method was applied to confirm accuracy of them with sensitive study of many factors in thermomechanical and thermohydraulic area. In order to propose a rational design assessment procedure, simplified methods for screening rules are proposed and are validated to be conservative though this benchmark problem.

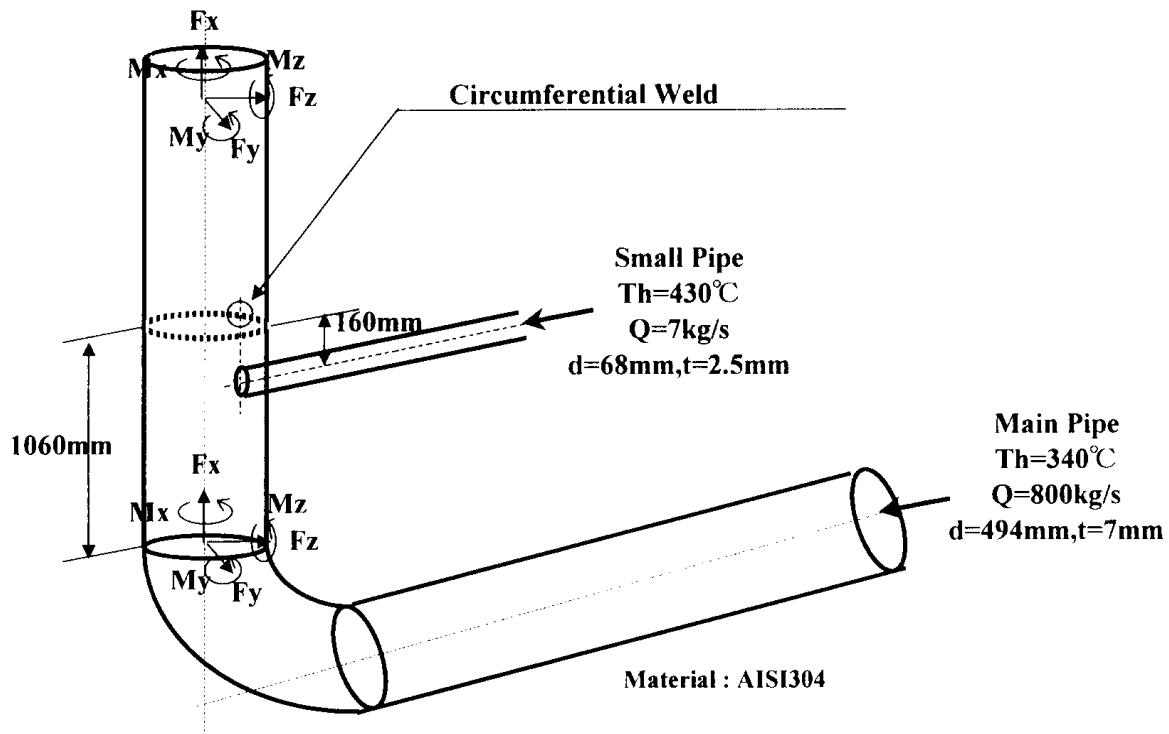


FIG. 1. Geometrical characteristics of the Phénix secondary piping system.

TABLE 1. FORCES AND MOMENTS OF MAIN PIPE AT 600 MM DOWNSTREAM FROM SMALL PIPE

$M_x = -1.1 \text{ E}+06$	N mm
$F_y = 2.5 \text{ E}+03$	N
$M_y = -2.1 \text{ E}+06$	N mm
$F_z = 9.1 \text{ E}+02$	N
$M_z = 8.7 \text{ E}+05$	N mm
$P_1 = 2.2$	bar

2. PROBLEM DEFINITION AND EVALUATION PROCEDURE

2.1. Thermal striping problem and factors to be considered

In order to analyze complex thermal striping problem, which covers both thermohydraulic and thermomechanical area, author has divided this phenomenon into the following steps (Fig. 2) and applied step by step procedure.

1. Temperature fluctuation in main flow;
2. Temperature fluctuation of boundary layer;
3. Temperature fluctuation on structural surface;
4. Temperature fluctuation inside structure;
5. High cycle fatigue crack initiation;
6. High cycle fatigue crack propagation.

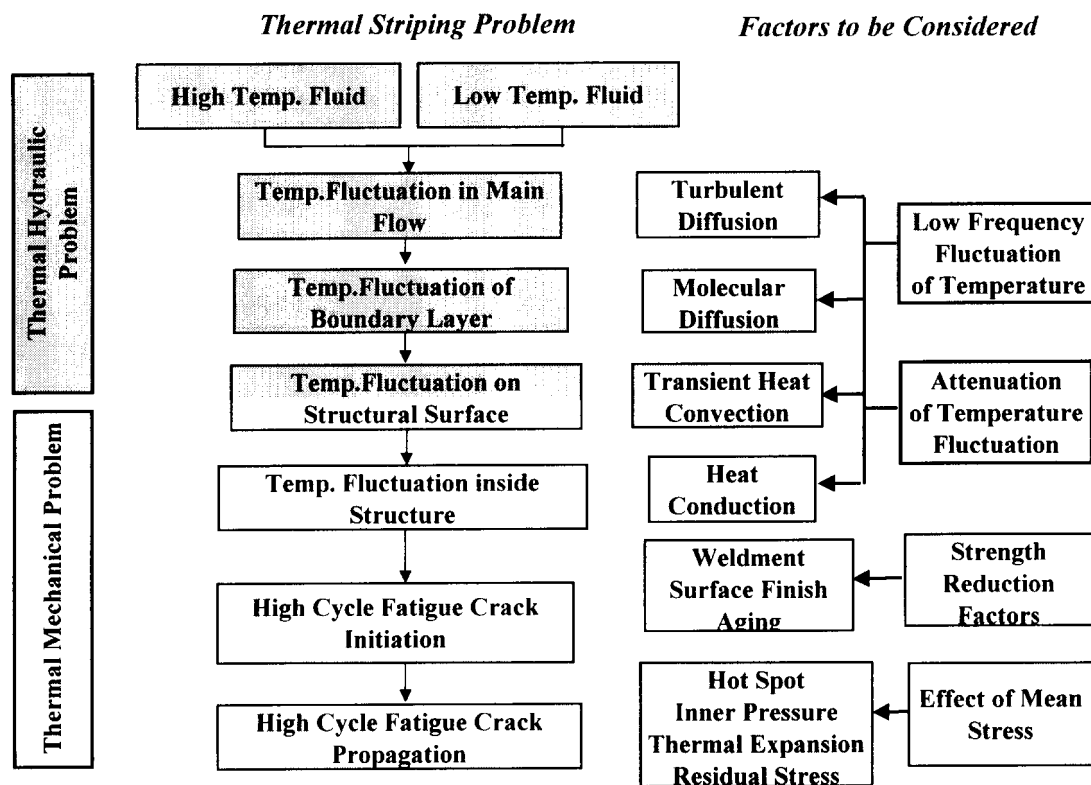


FIG. 2. Mechanism of thermal stripping phenomenon and sensitive factors.

Trough the discussion in IAEA CRP meeting on 'Harmonization and Validation of Fast Reactor Thermomechanical and Thermohydraulic Codes and Relations Using Experimental Data', several sensitive factors, which caused the scatter of evaluation results of participants, were found. Among them, this study took into account of the following factors.

- a. Attenuation of temperature fluctuation
This factor is sensitive to step (1) - (4) and consists of the following sub-factors.
 - Turbulent diffusion,
 - Molecular diffusion,
 - Unsteady heat convection,
 - Heat conduction.
- b. Strength reduction factors
This factor is sensitive to step (5) and consists of the following sub-factors.
 - Weldment,
 - Surface finish,
 - Aging.
- c. Effect of mean stress
This factor is sensitive to step (5) - (6) and consists of the following sub-factors.
 - Hot spot,
 - Inner pressure,
 - Thermal expansion,
 - Weld residual stress.

2.2. Evaluation procedure of thermal striping problem

Evaluation procedure of thermal striping problem with computer codes was explained in Fig. 3.

For evaluation of steps (1-4), three kinds of approaches were applied to couple fluid and structure, from different points of view. One is conventional simplified approach based on 1D theoretical analysis. Both source temperature difference and temperature fluctuation amplitude obtained from DINUS-3 code [3] were applied. DINUS-3 code can simulate temperature fluctuation in main flow and inside boundary layer, and can consider the attenuation of temperature fluctuation from turbulent and molecular diffusion. The second approach is a simplified analysis with assumption of sinusoidal fluctuation, for considering attenuation factors of unsteady heat convection and heat conduction. Last one is the detailed analysis by using DINUS-3 code for fluid temperature, BEMSET code for structural temperature [3], and FINAS code [4] for thermal stress, and can take account of all attenuation factors. DINUS-3 and BEMSET codes can couple based on heat flux at the structural surface, without heat transfer coefficient. Temperature distributions inside structure obtained by BEMSET codes are directly input to the FINAS code.

As for Step (5)-(6), 2D solid element calculation is carried by using FINAS code to evaluate strength reduction factors at circumferential weld. For consideration of mean stress induced by hot spot, 3D shell analysis is also adopted under thermal loads obtained by coupled calculation by AQUA [3] and BEMSET codes.

In order to predict crack propagation in Step (6), fracture mechanics analysis was conducted by the CANIS code [4].

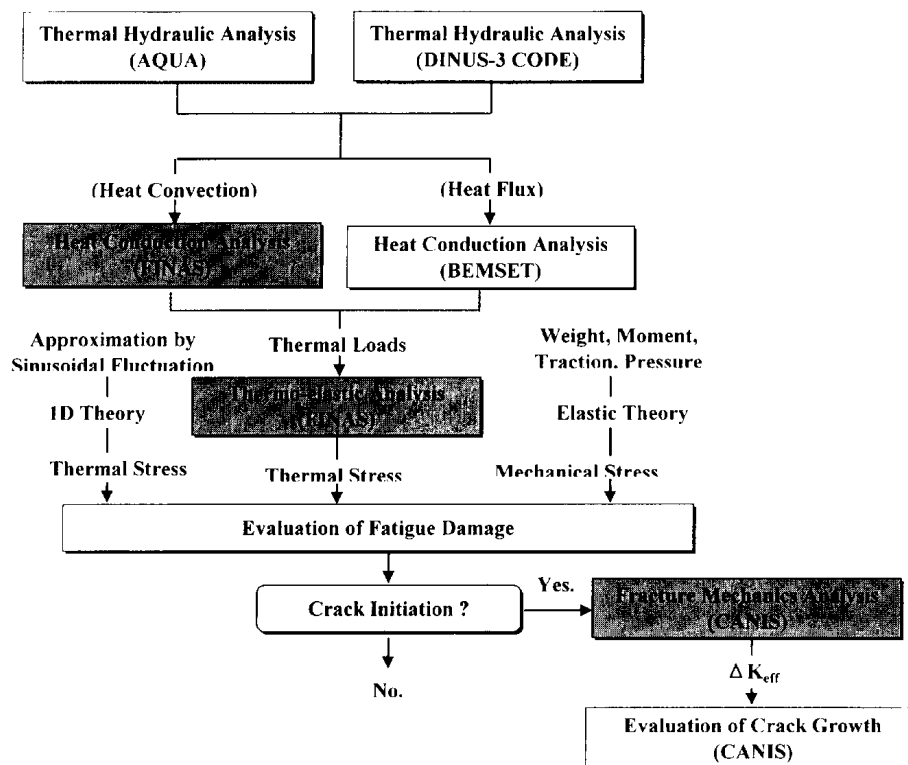


FIG. 3. Evaluation procedure of thermal striping problem with computer codes.

3. ANALYSIS OF THERMAL STRESS FLUCTUATION

3.1. 1D Theoretical analysis from temperature

Difference of source fluid temperature is $\Delta t = 90$ K, and the maximum local fluid temperature amplitude in close vicinity to structural surface was obtained as $\Delta t = 35$ K by the DINUS-3 code.

Thermal stress can be estimated directly from 1D thermal elastic equation (1).

$$\Delta \sigma = \frac{E\alpha}{1-\nu} \Delta T, \quad (1)$$

where E is Young's modulus, α is thermal expansion ratio, and ν is Poisson's ratio.

3.2. Simplified analysis with approximation by sinusoidal fluctuation

Structural Response Diagram Approach was proposed in this study (ref. Appendix) and was applied to estimate stress amplitude at the Phénix secondary pipe. This approach can find the frequency, which cause the maximum stress amplitude, and the corresponding amplitude, from Biot number and non-dimensional frequency.

Fig. 3 is an assumed model of the Phénix secondary pipe, where heat-transfer coefficient was determined to be $h = 14\,500 \text{ kcal/m}^2 \cdot \text{h} \cdot ^\circ\text{C}$ by turbulent heat convection equation for liquid metal [6].

$$Nu = 5 + 0.025Pe^{0.8} \quad (2)$$

Corresponding Biot number is

$$Bi = \frac{hL}{\lambda} = 6.7, \quad (3)$$

where L is wall thickness and λ , is heat conductivity.

According to the Structural Response Diagram shown in Fig. 3 and Table 2, the frequency, which cause the maximum stress amplitude, and the corresponding amplitude is:

$$f = \frac{a}{L^2} = 0.085 \text{ Hz}, \quad (4)$$

where a is thermal diffusivity, and

$$\Delta \sigma = \Delta \sigma^*(f = 0.085 \text{ Hz}) \frac{E\alpha}{1-\nu} \Delta T_f = 243 \text{ MPa}. \quad (5)$$

TABLE 2. RESULTS OF STRUCTURAL RESPONSE DIAGRAM APPROACH

f (Hz)	f*	$\Delta\sigma$ (MPa)
0.01	0.12	95.90
0.03	0.35	197.41
0.7	0.83	240.94
0.083	1.00	243.25
0.1	1.18	242.97
1	11.81	178.79
10	118.14	82.36

0. 01Hz, 0. 03Hz, 0. 07Hz, 0. 0846Hz, 0. 1Hz , 1Hz, 10Hz
CL

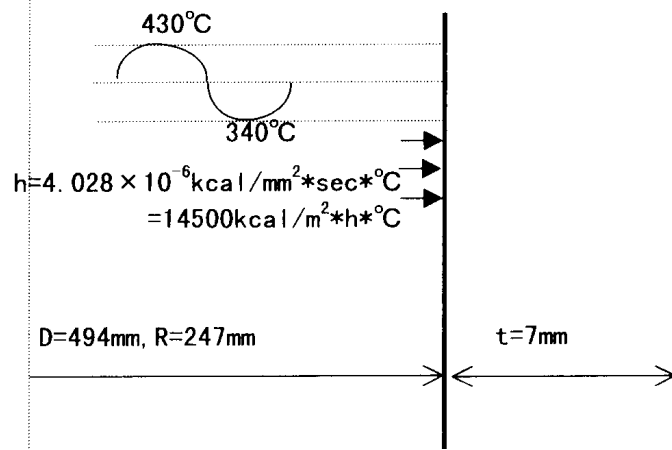


FIG. 4. Thermal stripping of Phénix secondary circuit.

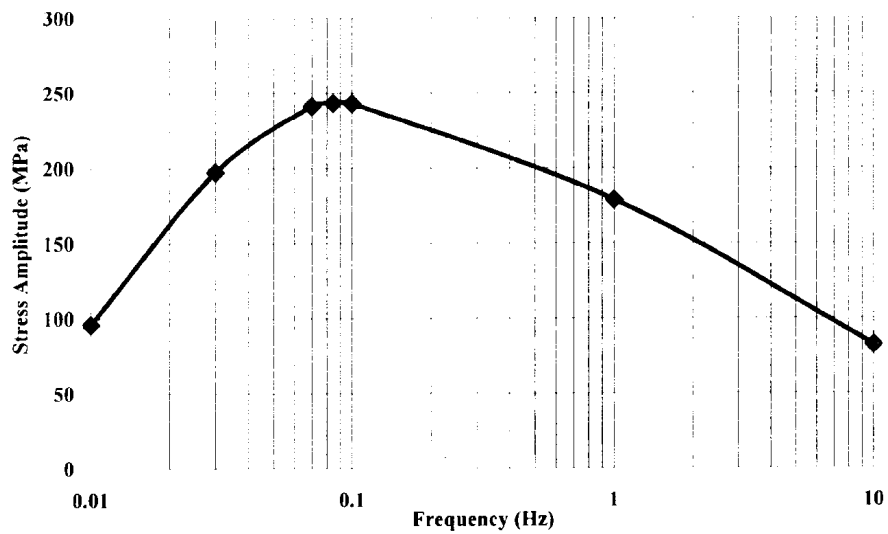


FIG. 5. Stress amplitude induced by sinusoidal temperature fluctuation with constant.

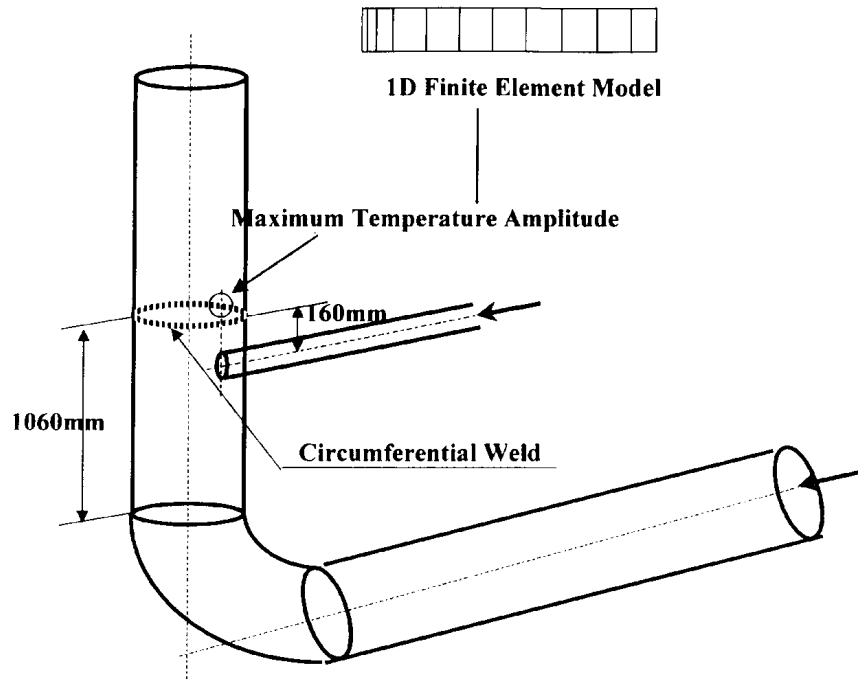


FIG. 6. 1D Finite element model of Phénix secondary pipe.

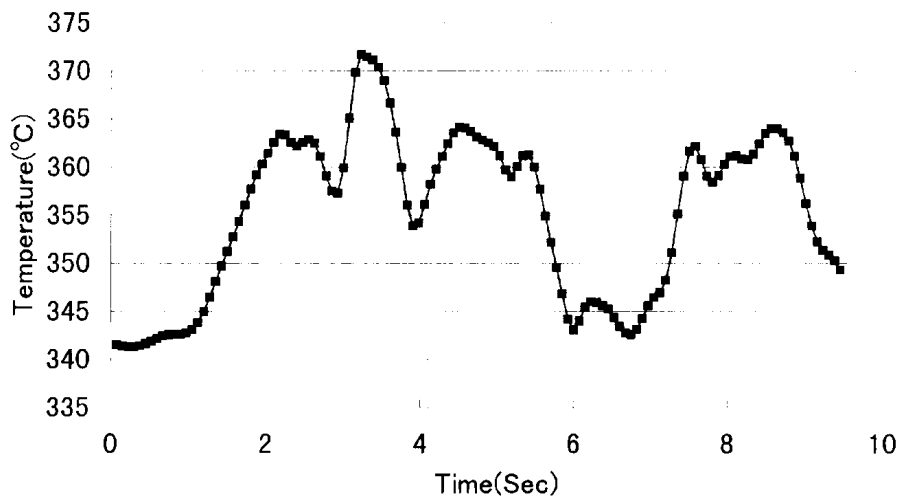


FIG. 7. Calculated temperature history at the inner surface of circumferential weld by DINUS-3 code.

3.3. Finite element analysis by FINAS code

Finite element calculation with a 1D model of Fig. 6 was carried out under thermal boundary conditions obtained by DINUS-3 code and BEMSET codes. 8-Nodes quadrilateral axisymmetric element QAX8 of the FINAS code was utilized for this calculation. Fig. 7 is calculated temperature history by the DINUS-3 Code at the inner surface of circumferential weld, where the maximum local fluid temperature amplitude was observed. Figure 8 is peak stress history at the inner surface of circumferential weld calculated by the FINAS code. This result dose not have periodical characteristics, therefore longer calculation is desirable. A ten second calculation indicates stress amplitude 113 MPa and the maximum absolute stress 81 MPa. From above results, this study assumed stress amplitude of 162 MPa, however it is planed to correct this value by longer thermal hydraulic calculation.

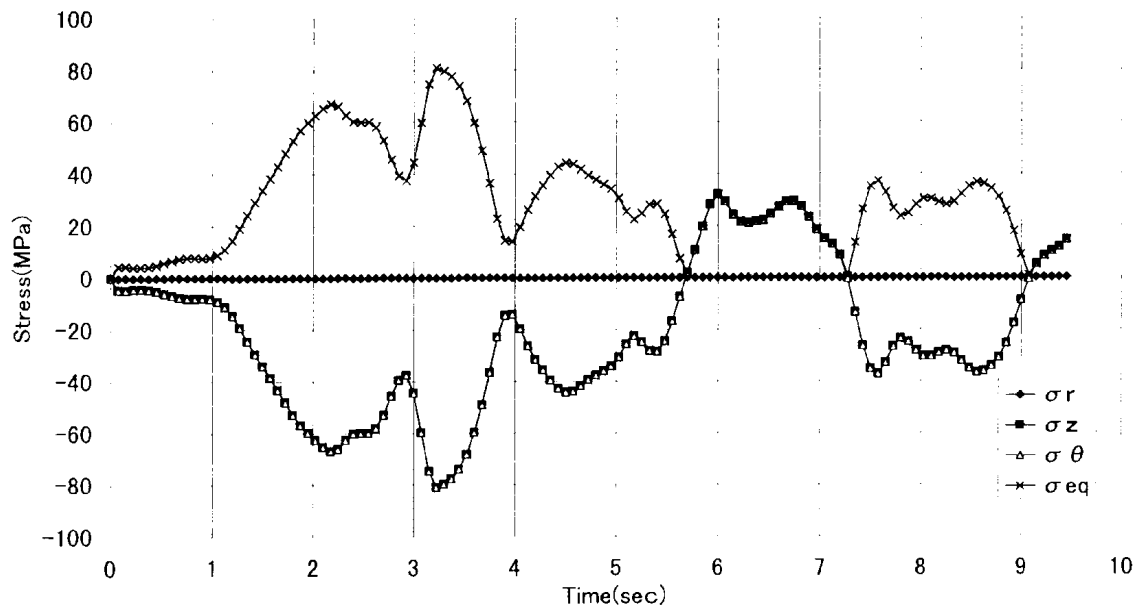


FIG. 8. Peak stress history at the inner surface of circumferential weld (1D analysis).

4. ASSESSMENT OF CRACK INITIATION

4.1. Strength reduction factors

Strength reduction factors at welded joints were considered according to a PNC's developed method, which takes into account of metallurgical discontinuity between base and weld metal, geometrical discontinuity at penetration beads, and degradation of weld metal [7]. Among these strength reduction factors, geometrical discontinuity is dominant in the case of as-welded joints subjected to high cycle fatigue. In order to evaluate stress concentration factors at welded joint, a detailed 2D finite element model shown in Fig. 9 was utilized. Geometry of the model is exactly same as a profile of the circumferential weld, and mesh subdivision was determined from sensitive analysis of stress to mesh size. 8-Nodes quadrilateral axisymmetric elements QAX8/HQAX8 of the FINAS code were adopted. This model has the different configuration from a model of BEMSET code; therefore, heat conduction analysis was performed by the FINAS code, under the heat convection boundary with temperature history obtained from the DINUS code.

Fig. 10 is a calculated stress contour and it clarifies that peak stress area is very restricted and plastic strain concentration might not occur since constraint by surrounded elastic part is strong. Fig. 11 shows a calculated peak stress history at the inner surface of the circumferential weld. By comparison with the 1D calculation result shown in Fig. 8, an average stress concentration factor at the inner surface of the circumferential weld was determined to be

$$K=2.3. \quad (6)$$

As for other factors, reduction factor 1.2 was assumed for considering each of surface finish and aging.

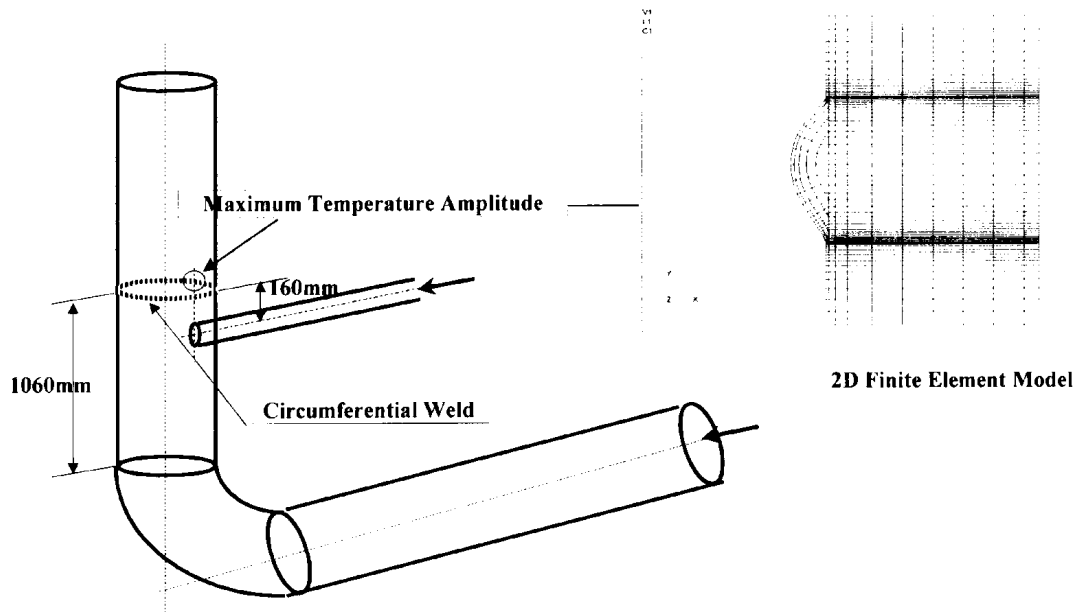


FIG. 9. 2D Finite element model of Phénix secondary pipe.

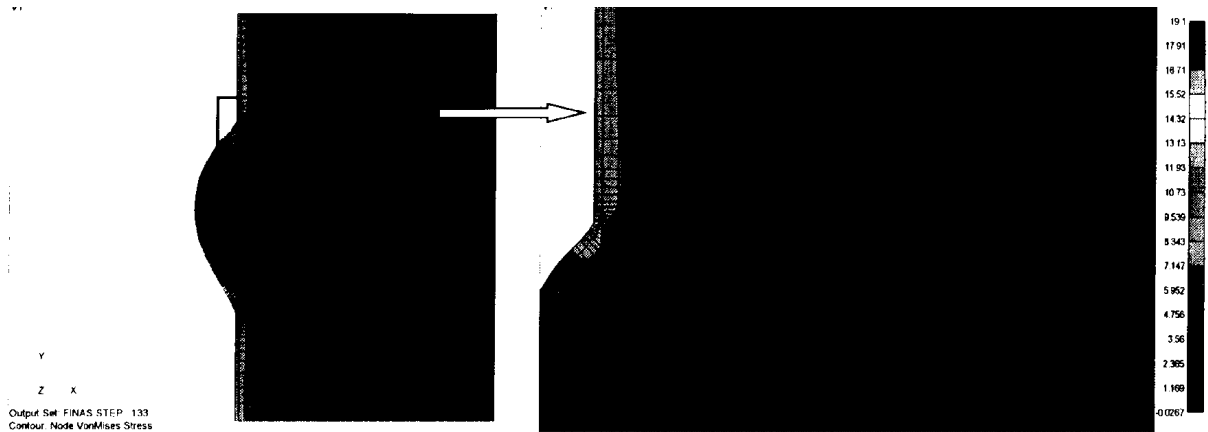


FIG. 10. Von Mises stress contour of circumferential weld (3.3 sec).

4.2. Mean stress

Mean stress component in transverse direction of the circumferential weld induced by forces and moments was calculated by the following formulae provided by Japanese MITI notice 501 [8].

$$\sigma_x = \frac{\sqrt{M_{yw}^2 + M_{zw}^2}}{I} \cdot \frac{D_1}{2} = 6.65 \text{ MPa}. \quad (7)$$

In order to estimate mean stress caused by hot spot, a 3D shell model shown in Fig. 12 was utilized. Element is QFLA4RT of the FINAS code, which has 9 integral points in wall thickness and can consider peak stress on the surface.

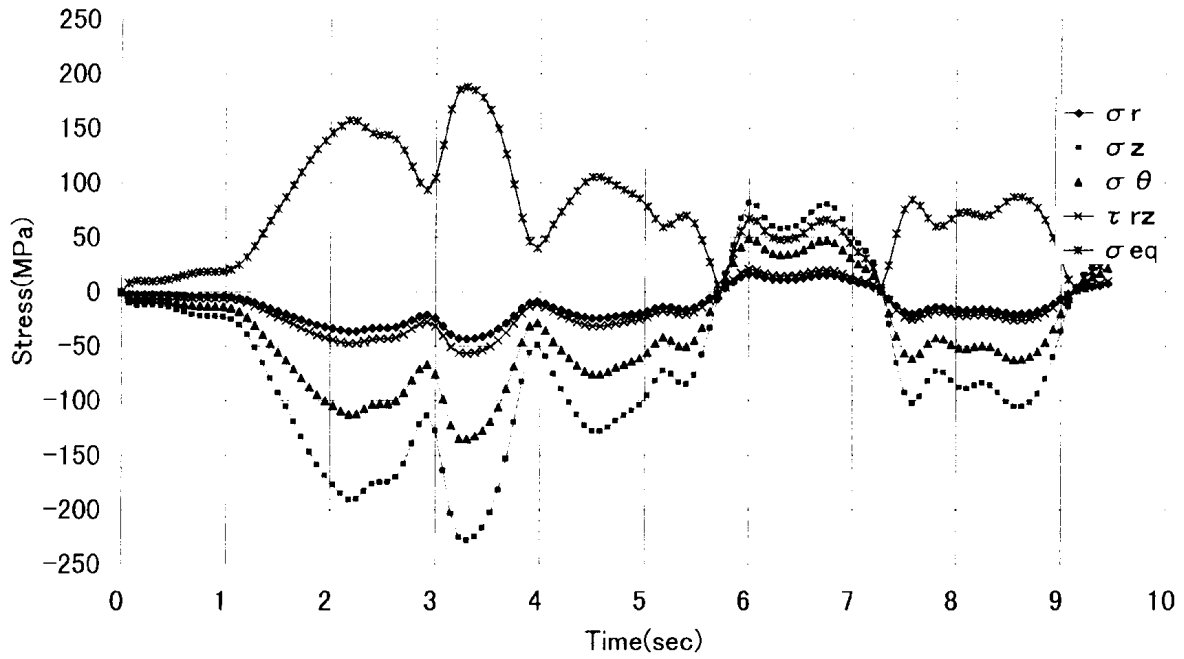


FIG. 11. Peak stress history at the inner surface of circumferential weld (2D analysis).

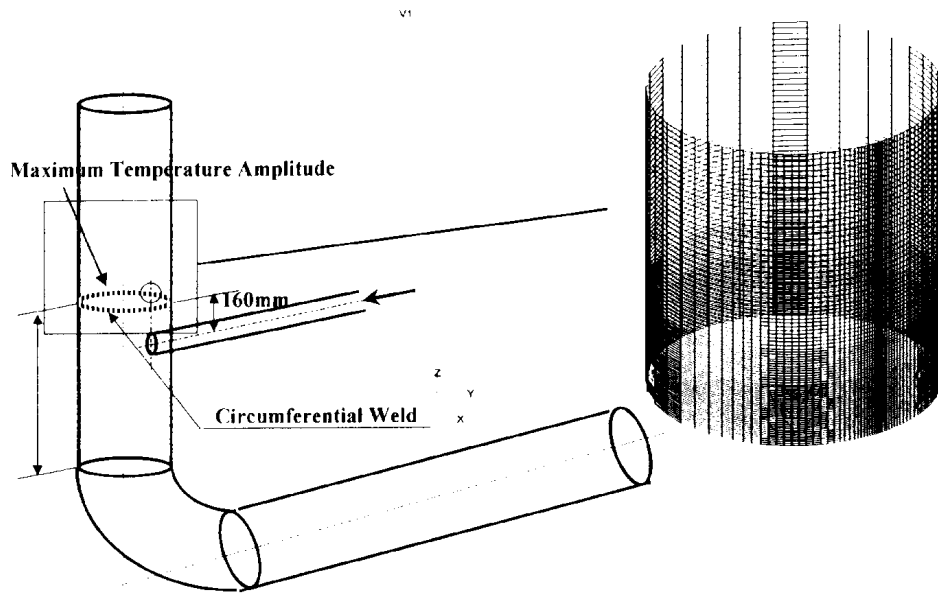


FIG. 12. 3-D Finite element model of Phénix secondary pipe.

Average temperature distribution on the inner surface of Phénix secondary pipe calculated by AQUA code was input to each integral point of QFLA4RT element. Figure 13 is calculated Von Mises stress distribution on the inner surface of Phénix Secondary Pipe. Figure 14 is stress distribution along the inner surface of the circumferential weld, where 75 MPa of compression stress is generated in transverse direction of the circumferential weld. At welded joints, residual stress was also considered, stress value of which was assumed to be a yield stress of material 124 MPa.

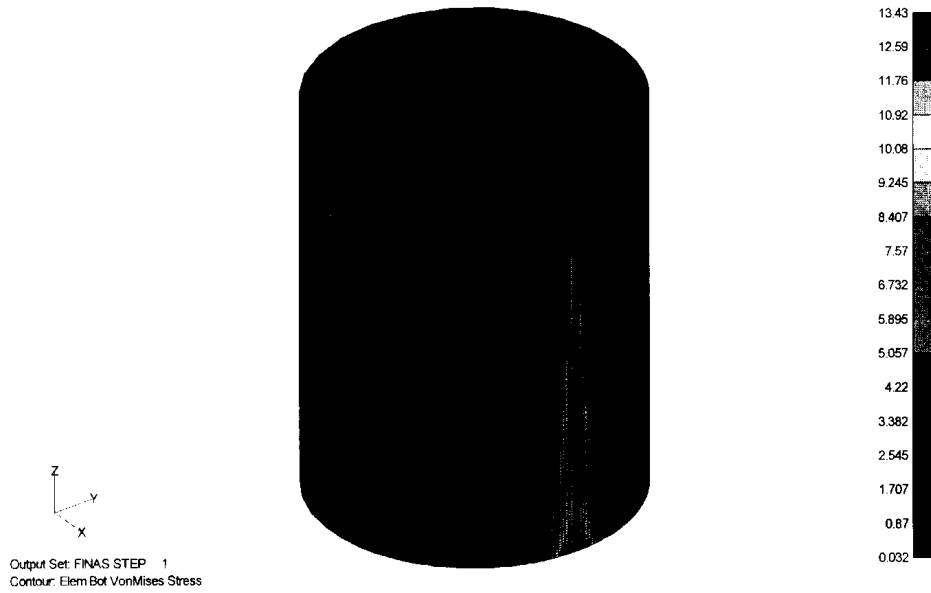


FIG. 13. Average Von Mises stress distribution on the inner surface of Phénix secondary pipe.

4.3. Fatigue damage evaluation

Stress ranges were compared with endurance limit (assume strain range for 10^8 cycle), taking account of attenuation factors, reduction factors, and mean stresses as in Fig. 5.

From Fig. 5, a possibility of crack initiation can be judged to exist at only at the welded joint.

No.24 in the Fig. 5 is the most possible result obtained by detailed finite element calculation considering all attenuation factors, where fatigue damage was calculated to be $D_f = 25.08$ for 90 000 hours from rain-flow counting and Miner's rule [9] with 4th order polynomial fitting fatigue curve for the weld joint at 425°C, which was approximation of provided data in benchmark problem.

$$\log_0(N_f)^{-1/2} = -1.5715 + 1.134 \log_0 \Delta \varepsilon_f - 1.308 (\log_0 \Delta \varepsilon_f)^2 + 2.391 (\log_0 \Delta \varepsilon_f)^3 - 1.354 (\log_0 \Delta \varepsilon_f)^4 \quad (8)$$

Compared with detailed finite element analysis, conventional simplified approach based on an ID Theoretical Analysis and simplified sinusoidal analyses based with the Structural Response Diagram were confirmed to be conservative.

5. CRACK PROPAGATION ANALYSIS

5.1. Fracture mechanics analysis with CANIS code

CANIS code evaluates stress intensity factor K from weight function method [10]. Effective range of stress intensity factor K_{eff} for fatigue crack propagation was evaluated from the next equations by using the CANIS code.

$$K_{eff} = K_{max} (1 - R)^n, R = K_{min}/K_{max}, n = 0.5 \quad (9)$$

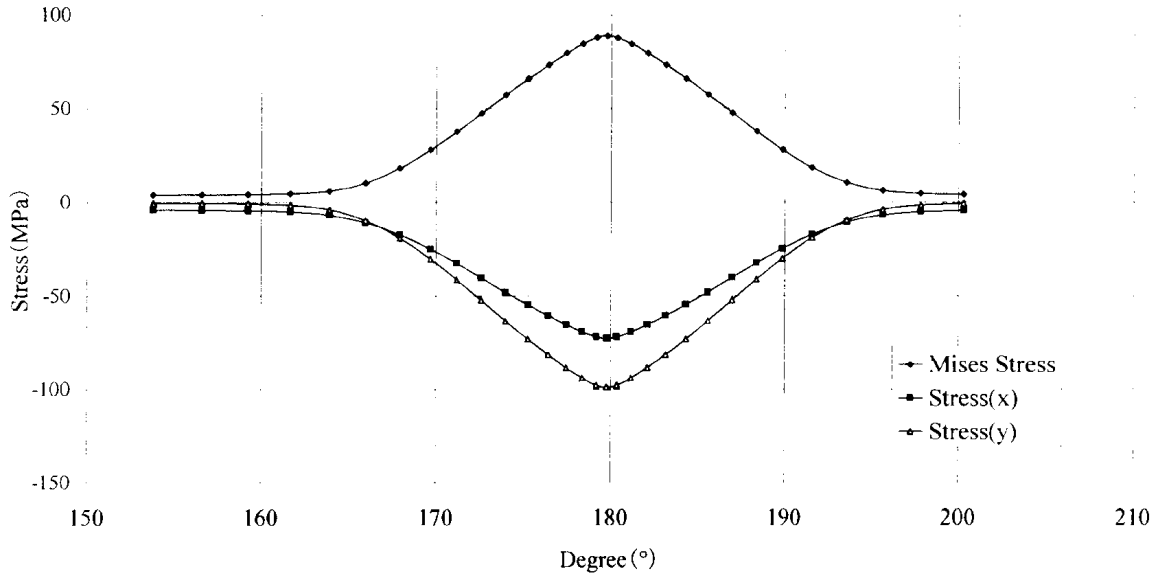


FIG. 14. Stress distribution along the inner surface of circumferential weld.

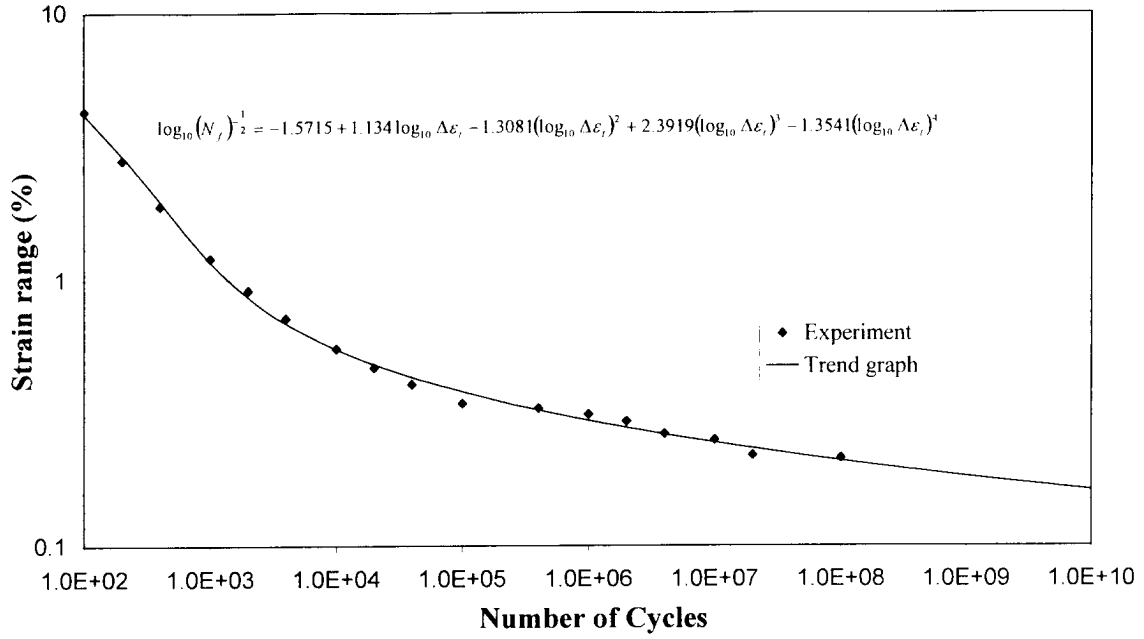


FIG. 15. Best fit fatigue curve for weld joint at 425°C.

In order to evaluate crack propagation rate, the following Japanese data for 304SS (450°C~650°C) [11] was applied without propagation threshold, since technical specification of the benchmark did not provide crack propagation data.

$$da/dN = 9.43 \times 10^{-4} \cdot (\Delta J)^{1.816} \quad (10)$$

where da/dN (mm/cycle) is crack propagation rate per cycle and ΔJ (kgf/mm) is Range of J-integral.

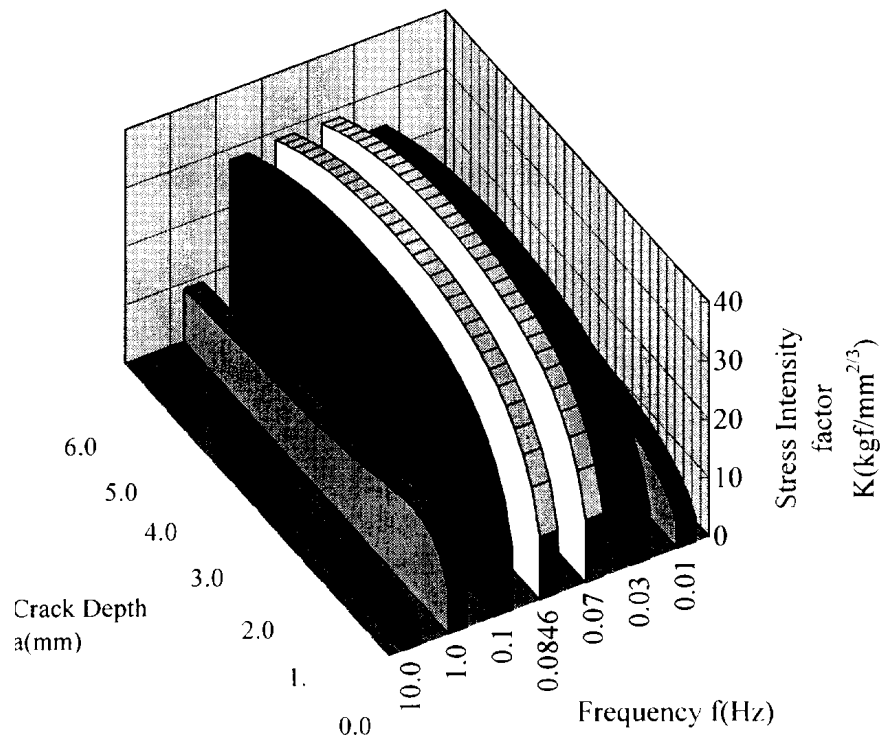


FIG. 16. Distribution of effective stress intensity factor across wall thickness.

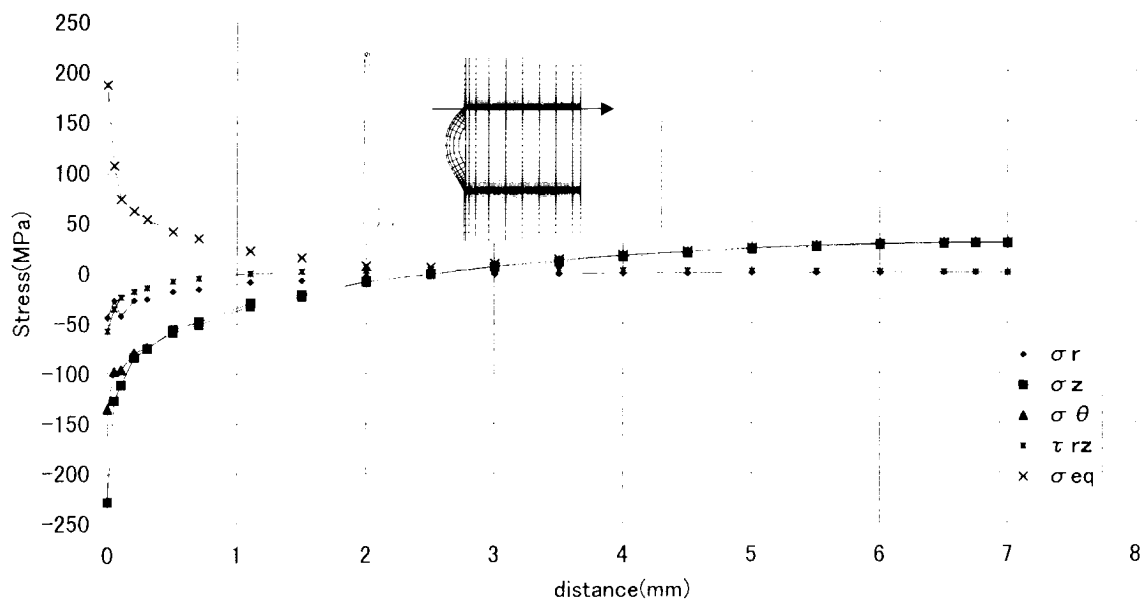


FIG. 17. Stress distribution across wall thickness at circumferential weld (3.3 s).

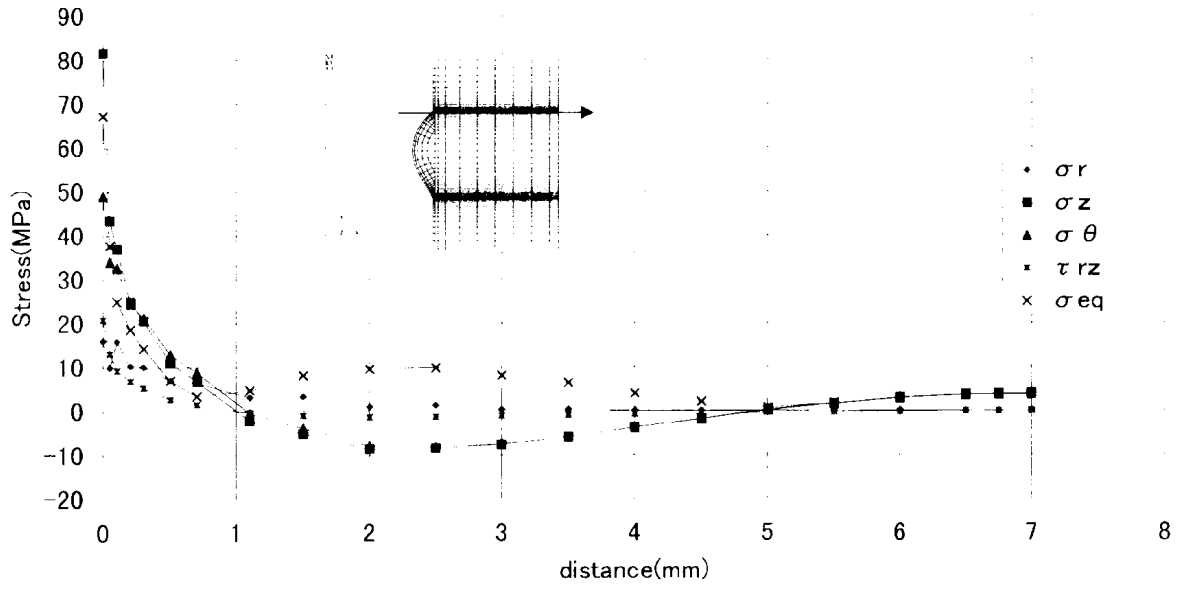


FIG. 18. Stress distribution across wall thickness at circumferential weld (6.0 s).

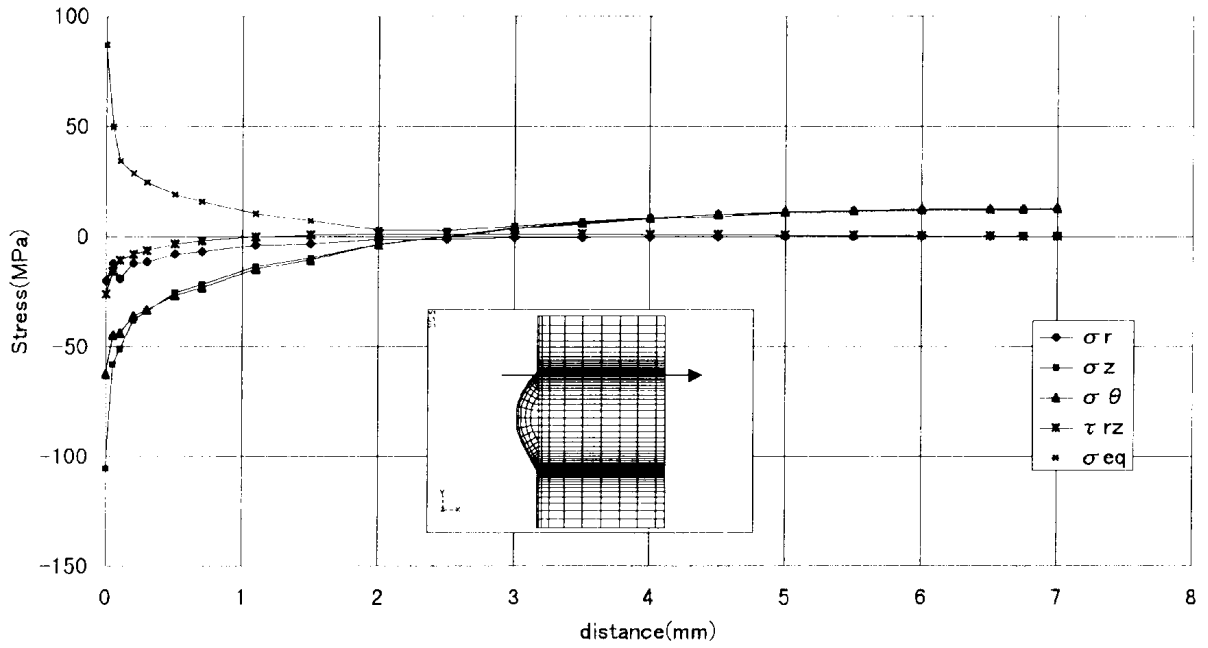


FIG. 19. Stress distribution across wall thickness at circumferential weld (8.55 s).

ΔJ was calculated from K_{eff} under assumption of elastic and plane strain condition.

$$\Delta J = \frac{1-\nu^2}{E} \Delta K_{eff}^2 \quad (11)$$

For crack propagation analysis, initial crack size was assumed to be 0.1 mm, which is corresponding to fatigue damage $D_f = 1$.

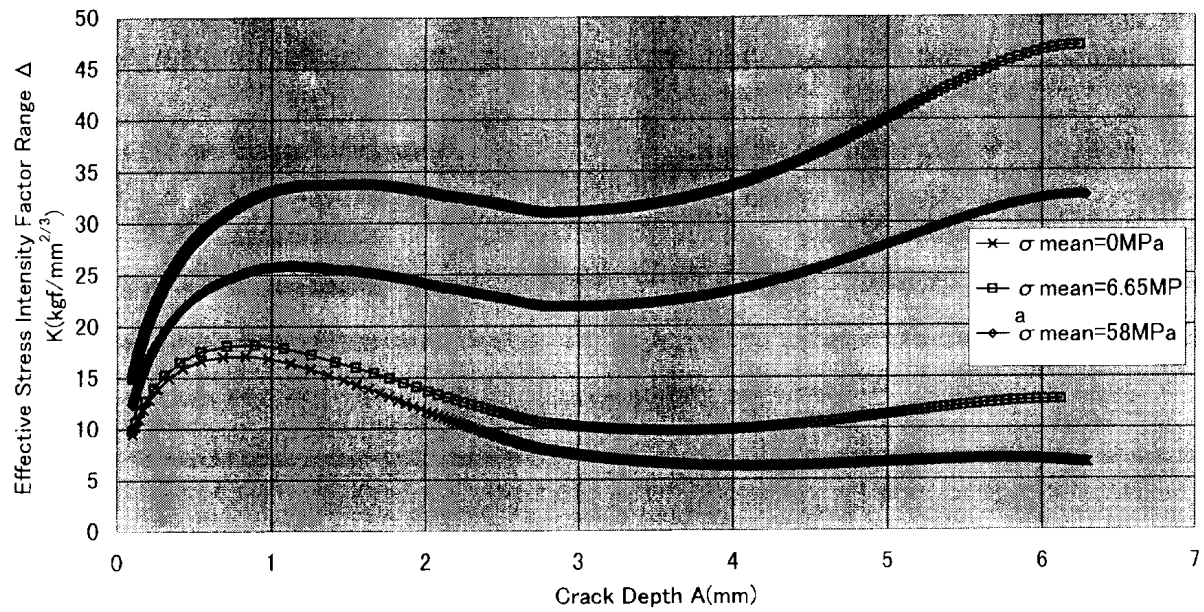


FIG. 20. Distribution of stress intensity factor with consideration of mean stress.

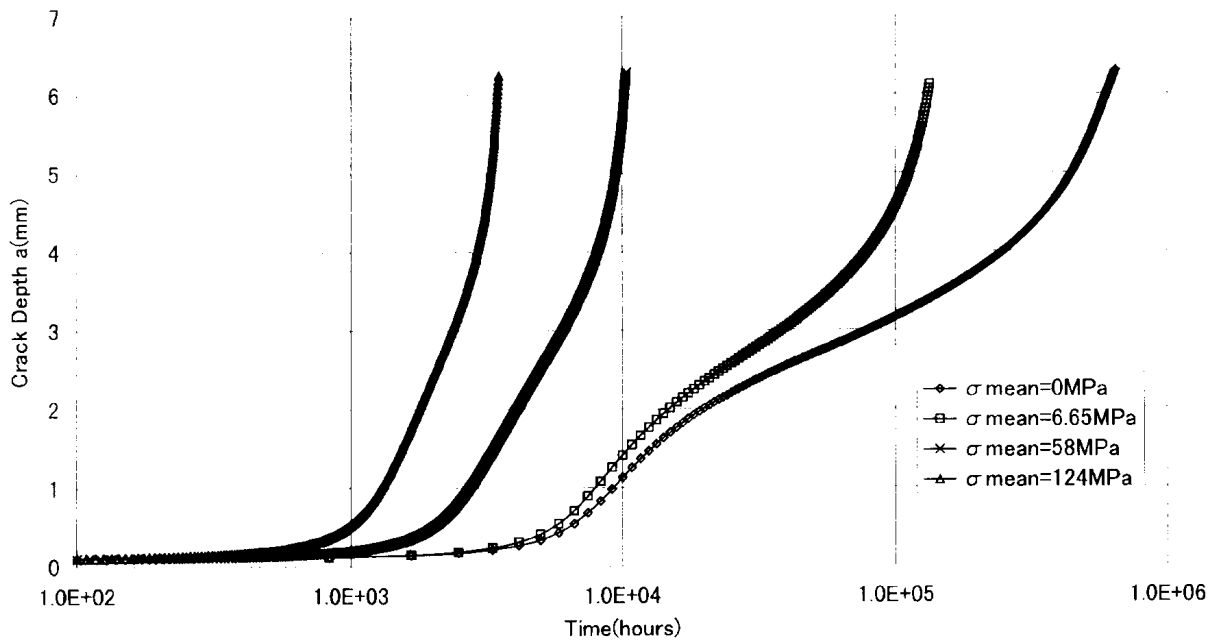


FIG. 21. History of crack growth.

5.2. Crack propagation analysis by approximation of sinusoidal fluctuation

In order to investigate sensitivities of crack propagation rate to frequency of fluctuation, effective stress intensity factors under sinusoidal temperature fluctuation shown in Fig. 4 were calculated. Figure 16 shows distributions of effective stress intensity factors across wall thickness under different frequency of temperature fluctuations. It shows that frequency of 0.085 Hz (Non-dimensional frequency is 1) is the most damageable for crack propagation and it can generate through wall cracks.

5.3. Fracture mechanics analysis with random fluctuation

Figures 17-19 show stress distribution across wall thickness at circumferential weld when calculation time is 3.3 s, 6.0 s, and 8.55 s.

These results show us that, phase delay of fluctuation among inner surface and inside wall should be considered. Based on these stress distribution, effective stress intensity factors were calculated by the CANIS code.

Distributions of effective stress intensity factor ranges were estimated from all calculation time, as in Fig. 20. It shows that, stress intensity factor is much affected by mean stress, especially when crack becomes deep. Figure 21 shows some histories of crack propagation. In the case that mean stress is 58 Mpa, which is a summation of all factors, crack will pass through the wall at 10 300 hours.

6. CONCLUSION

6.1. Thermomechanical analysis results

From view point of design assessment, conventional simplified approach based on 1D theoretical analysis and simplified sinusoidal analysis based on structural response diagram were applied to evaluate amplitudes of stress fluctuations, and were confirmed to be conservative through the comparison with detailed finite element analysis results.

In order to assess failure phenomenon at welded joints, detailed analysis method was applied with taking into account of sensitive factors in both thermomechanical and thermohydraulic area.

Stress calculation results by the detailed analysis approach were shown in Table 3.

TABLE 3. STRESS CALCULATION RESULTS BY DETAILED ANALYSIS APPROACH

Maximum value of stress variation (fluctuating part of stress)	Mean stress (not fluctuating part)
$\Delta\sigma$ Mises= 162 N/mm ² (Base metal)	Mechanical 6.65 N/mm ² Hot Spot -75 N/mm ²
$\Delta\sigma$ Mises= 372 N/mm ² (Welded Joints)	Residual Stress 124 N/mm ²

Since fatigue damage evaluation results in Table 4, there is no possibility of crack initiation at base metal, and crack can be initiated after 3590 hours operation time at the welded joint.

6.2. Fracture mechanics analysis results

Crack propagation analysis results were sensitive to assumed mean stress. Among them, the most possible results obtained by detailed analysis approach were shown in Tables 4, 5, and 6.

TABLE 4. RESULTS OF CRACK INITIATION ASSESSMENT

Fatigue usage fraction, defined as $\Sigma n_i/N_{i_{allowable}}(Df)$	Estimation of crack initiation	Experiment
Df = 0 (Base metal)	No crack (Base metal)	No crack (Base metal)
Df = 25.08 (Welded joints considering aging)	Crack initiate (Welded joints)	Crack initiate (Welded joints)

TABLE 5. RESULTS OF CRACK PROPAGATION ANALYSIS

Time for crack to initiate	Cycle number and associated time needed to have a crack depth of:			Estimated crack depth at 90 000 hours	Experiment at 90 000 hours
	1 mm	3 mm	5 mm		
(Base Metal) ∞ hours				No crack	No crack
(Welded Joints) 3590 hours	6379 hours	9757 hours	13 079 hours	Though wall crack	Though wall crack

TABLE 6. ASSESSMENT OF CRACK INITIATION

No.	Attenuation Factors				Reduction Factors					Mean Stress				Crack
	Turbulent Diffusion	Molecular Diffusion	Transient Heat Convection	Heat Conduction	Stress (Mpa)	Weldment	Surface Finish	Aging	Stress (Mpa)	Hot Spot	Pressure + Expansion	Residual Stress	a (Nf=10 ⁸) (Mpa)	
1					353				353				339	Yes
2	0	0			137				137				339	No
3			0	0	243				243				339	No
4	0	0	0	0	113				113				339	No
5	0	0	0	0	162				162				339	No
6			0	0	243	2.3			558w9				339	Yes
7	0	0	0	0	113	2.3			259.9				339	No
8	0	0	0	0	162	2.3			372.6				339	Yes
9			0	0	243		1.2	1.2	349.92				339	Yes
10	0	0	0	0	113		1.2	1.2	162.72				339	No
11	0	0	0	0	162		1.2	1.2	233.28				339	No
12			0	0	243	2.3		1.2	670.68				339	Yes
13	0	0	0	0	113	2.3		1.2	311.88				339	No
14	0	0	0	0	162	2.3		1.2	447.12				339	Yes
15			0	0	243	2.3		1.2	670.68	6.65			334.6563584	Yes
16	0	0	0	0	113	2.3		1.2	311.88	6.65			334.6563584	No
17	0	0	0	0	162	2.3		1.2	447.12	6.65			334.6563584	Yes
18			0	0	243	2.3		1.2	670.68	6.65	-73	124	301.3442197	Yes
19	0	0	0	0	113	2.3		1.2	311.88	6.65	-73	124	301.3442197	Yes
20	0	0	0	0	162	2.3		1.2	447.12	6.65	-73	124	301.3442197	Yes
21			0	0	243	2.3		1.2	670.68	6.65		124	253.6621387	Yes
22	0	0	0	0	113	2.3		1.2	311.88	6.65		124	253.6621387	Yes
23	0	0	0	0	162	2.3		1.2	447.122	6.65		124	253.6621387	Yes

7. RECOMMENDATIONS

Low frequency components of temperature fluctuation, such as 0.1 Hz for a 7 mm thickness pipe, are damageable for both crack initiation and propagation. When adopting CFD approach for estimation of temperature fluctuation, it is required that enough calculation period and spatial domain to estimate low frequency components.

There are four kinds of attenuation factors of temperature fluctuations, as turbulent diffusion, molecular diffusion, unsteady heat convection, and heat conduction. For consideration of these factors, thermomechanical and thermohydraulic coupled simulation is quite effective. The Structural Response Diagram Approach is also simple and effective for taking into account of unsteady heat convection and heat conduction. Previous understanding of damageable frequency by the Structural Response Diagram is recommended, since it can provide important information to determine thermohydraulic analysis conditions.

As-weld joints should be avoided from mixing area, since strength reduction factors by geometrical discontinuities are large and are difficult to be evaluated.

High cycle fatigue crack propagation is sensitive to mean stress, therefore parametric assessment is recommended to crack propagation evaluation.

ACKNOWLEDGEMENT

The author wishes to express his gratitude to Mr. Hideki Takasho of Joyo Industries and Miss Apisara Yacumpai on structural analysis with FINAS code. Several helpful discussions in the field of Fracture Mechanics with Ichiro Furuhashi of CRC Research Institute Inc. are gratefully acknowledged.

REFERENCES

- [1] INTERNATIONAL ATOMIC ENERGY AGENCY, Benchmark on A Tee Junction of LMFR Secondary Circuit Involving Thermal Striping Phenomena, Technical specifications (1996).
- [2] MURAMATSU, T., Thermohydraulics computer codes system and computational results on thermal striping phenomena at a tee junction of LMFR secondary circuit with the system', paper presented at the 3rd Research Co-ordination Meeting on Harmonization and validation of fast reactor thermomechanical and thermohydraulic codes and relations using experimental data, 20 to 24 April 1998, Lyon (France).
- [4] PNC/JINAS Version 12.0 User's Manual, PNC TN9520 92-006, (1993).
- [5] WATASHI, K., YOSHIDA, H., CANIS computer code for inelastic fracture mechanics, ASME PVP, Vol. 167 (1989), pp. 15-23.
- [6] HOLMAN, J.P., "Heat Transfer", 7th ed., McGraw-Hill, (1990).
- [7] KASAHARA, N., KIKUCHI, M., Proposal of a Strain Concentration Model of Welded Joints for Creep-Fatigue Evaluation of Welded Structures, JSME Int. J., Series A, Vol. 40, No.3, pp. 247-254 (1997).
- [8] MITI, notice 501, Japan, (1997).
- [9] ENDO, M., et al. Damage Evaluation of Metals for Random or varying loading, Proc. of the Symposium on Mech. Behavior of Materials, Vol 1, (1974).
- [10] WU, Xueren, et al., Weight functions and stress intensity factor solutions', Pergamon (1992).
- [11] KOI, M., et al., Crack growth properties of FBR structural materials at elevated temperature, SMiRT 11, L 11 (G)/4, (1991).

Appendix: Structural Response Diagram Approach

A.1. Sinusoidal analysis of Phénix secondary pipe

In order to study structural response characteristics of pipes, thermal stresses were assessed by F.E. analysis with FINAS code, on Phénix secondary pipe, where the inner surface is due to sinusoidal temperature fluctuation of fluid with constant amplitude and the outer surface is insulated. This study assumed constant heat-transfer coefficient, value of which was evaluated as $h = 14500 \text{ kcal/m}^2 \cdot \text{h} \cdot \text{C}$ from turbulent heat convection equation for liquid metal.

Fig. A2 shows F.E. calculated stress amplitude on the inner surface of the structure. Even though amplitude of temperature fluctuation was constant, stress amplitude varies according to frequency and becomes the maximum at the particular frequency as 0.085 Hz. Fig. A3 is predicted fatigue damage during 90 000 hours operation period from stress amplitude of Fig. A2 and frequency number. The most damageable frequency is 0.1 Hz, which is function of stress amplitude and frequency.

A.2. Mechanism of structural responses to sinusoidal temperature fluctuations

Concerning pipes with different thickness and thermal boundary conditions shown in Fig. A4, structural responses to sinusoidal temperature fluctuation of were investigated by finite element calculations. Figures A5-A7 are history of temperature on the inner surface and outer surfaces, when frequencies of liquid are 0.1 Hz, 1.0 Hz, and 10 Hz. Temperature amplitude on the both surfaces becomes large, when frequency is low. Figures A8-A10 are history of stress on the inner surface and outer surfaces, when frequencies of liquid are 0.1 Hz, 1.0 Hz, and 10 Hz. The case of 1.0 Hz has the maximum stress amplitude. General tendency of structural response is as same as the Phénix secondary pipe, however absolute frequency for the maximum stress amplitude is different.

In order to understand mechanism of structural responses to sinusoidal temperature fluctuations, thermal response of a semi-infinite solid were investigated based on 1-D theory.

1 -D heat conduction equation is described as

$$\frac{\partial T}{\partial t} = \frac{\lambda}{\rho c} \frac{\partial^2 T}{\partial x^2} \quad (\text{A.1})$$

where λ is thermal conductivity, c is specific heat, and ρ is density.

When temperature at a surface of a semi-infinite solid was enforced sinusoidal fluctuation as in Fig. A11, boundary condition is

$$T_f = T|_{x=0} = A \sin(\omega t). \quad (\text{A.2})$$

Theoretical solutions of temperature in a semi-finite solid is

$$T_s = T(x, t) = A e^{-kx} \sin(\omega t - kx), \quad (\text{A.3})$$

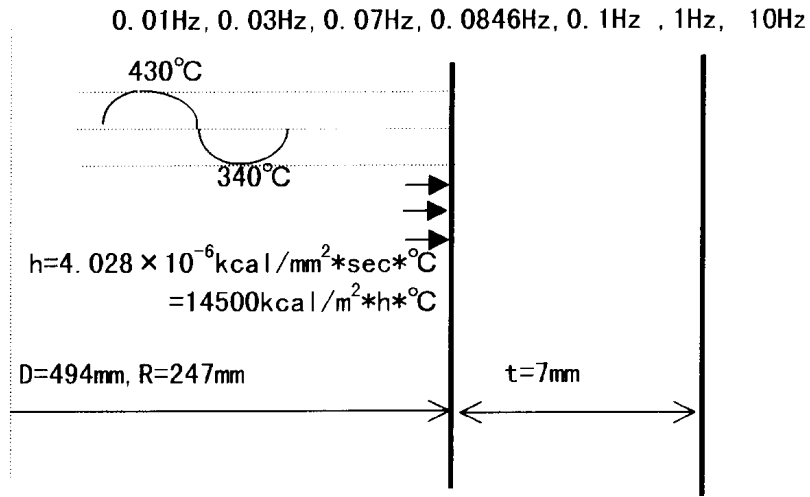


FIG. A1. Thermal stripping of Phénix secondary circuit.

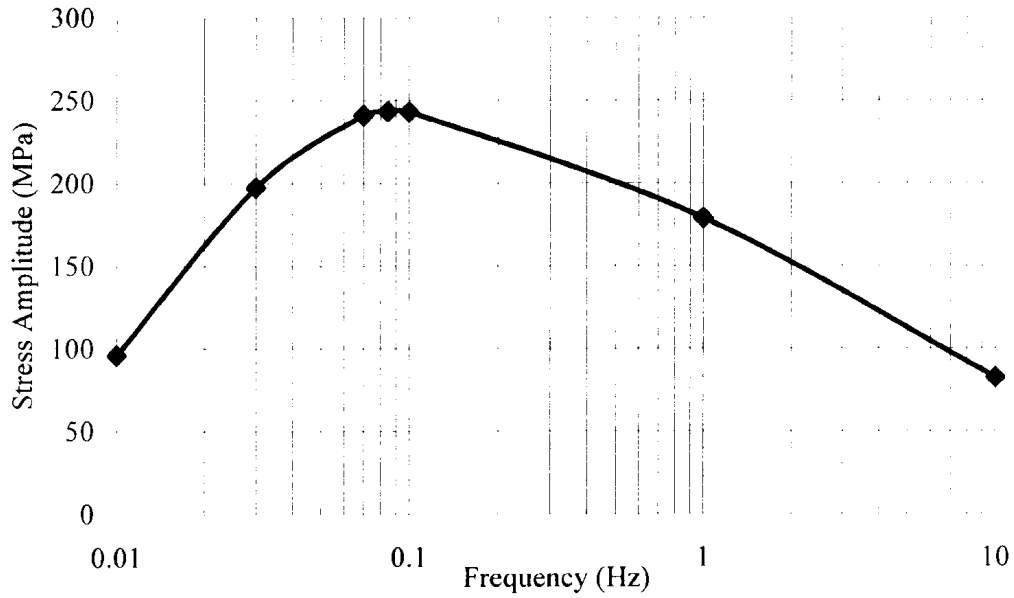


FIG. A2. Stress amplitude induced by sinusoidal temperature fluctuation with constant amplitude.

where

$$k = \sqrt{\frac{\omega}{2a}}, \quad a = \frac{\lambda}{c\rho}.$$

When heat flux temperature into a surface of a semi-infinite solid was enforced sinusoidal fluctuation as in Fig. A12, boundary condition becomes

$$q_0 = -\lambda \left. \frac{\partial T}{\partial x} \right|_{x=0} = A \sin(\omega t). \quad (\text{A.4})$$

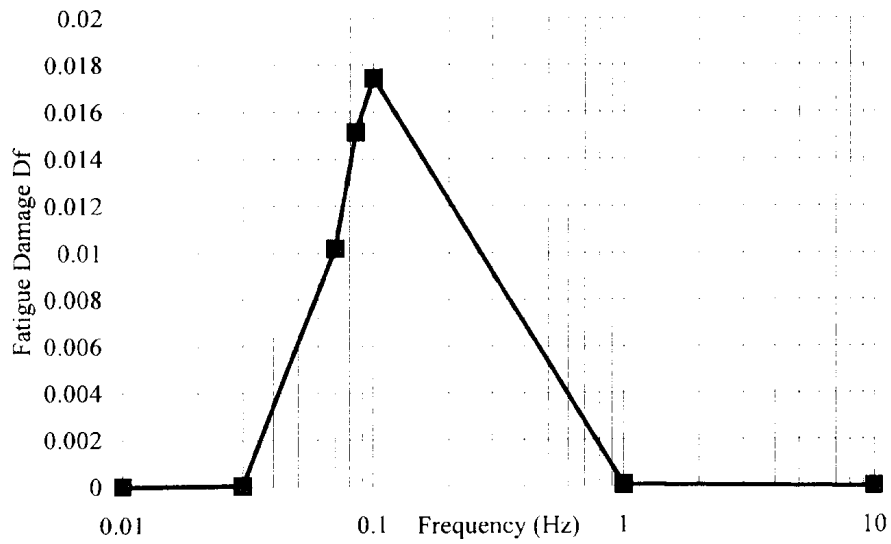


FIG. A3. Fatigue damage induced by sinusoidal temperature fluctuation with constant amplitude.

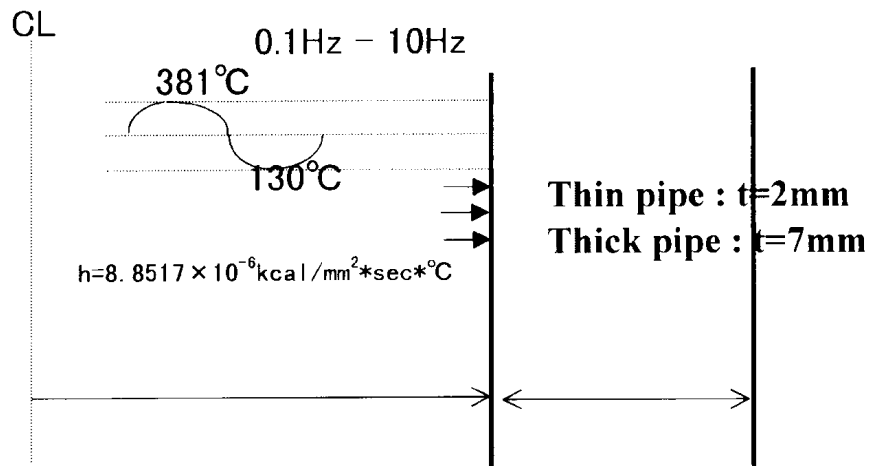


FIG. A4. 1D model due to sinusoidal temperature fluctuation on the surface.

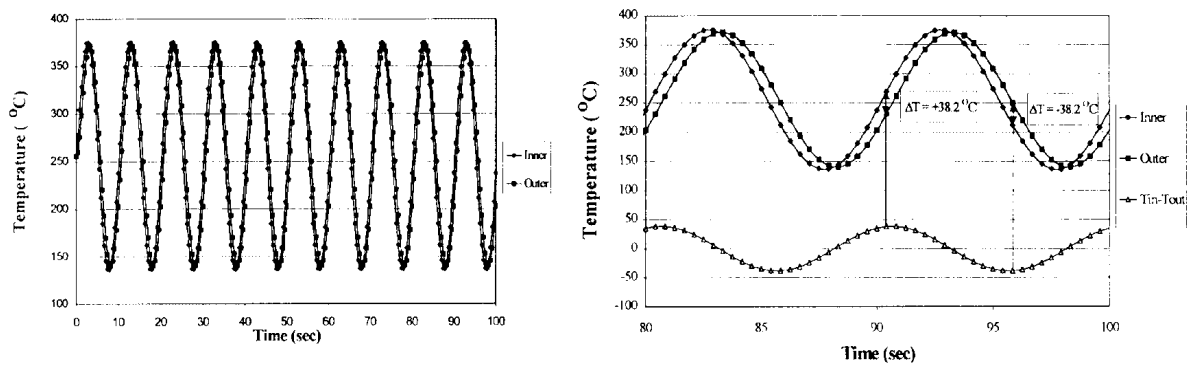


FIG. A5. History of temperature at frequency of liquid = 0.1 Hz.

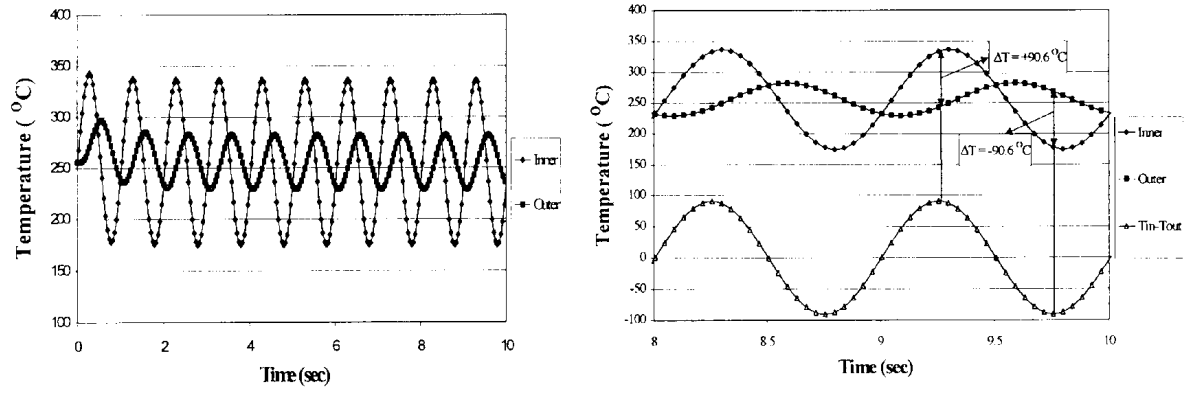


FIG. A6. History of temperature at frequency of liquid = 1.0 Hz.

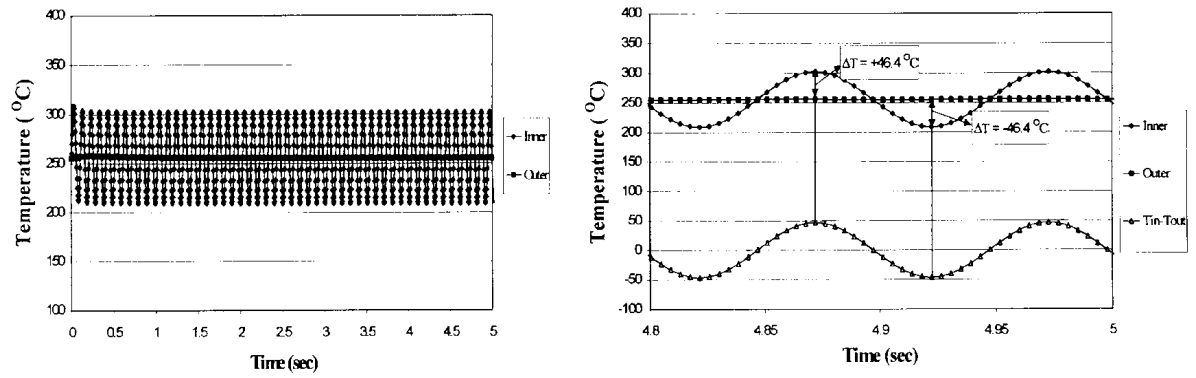


FIG. A7. History of temperature at frequency of liquid = 10 Hz.

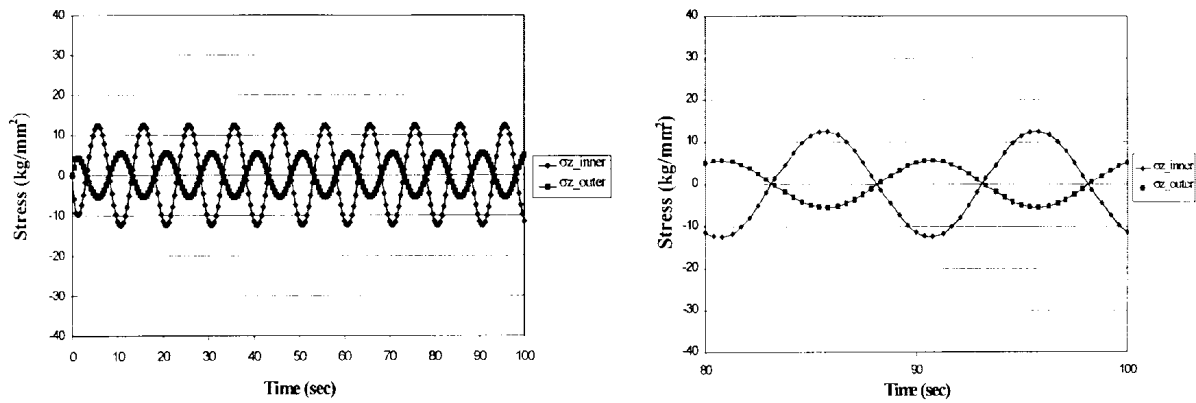


FIG. A8. History of stress at frequency of liquid = 0.1 Hz.

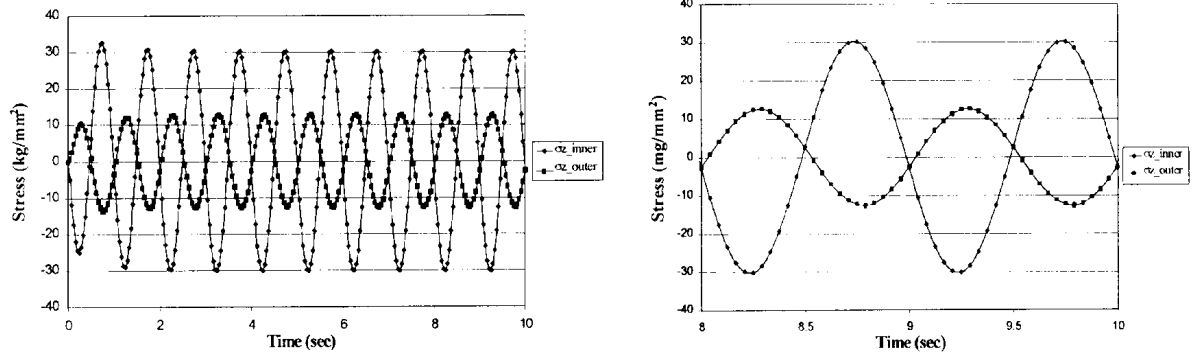


FIG. A9. History of stress at frequency of liquid = 1.0 Hz.

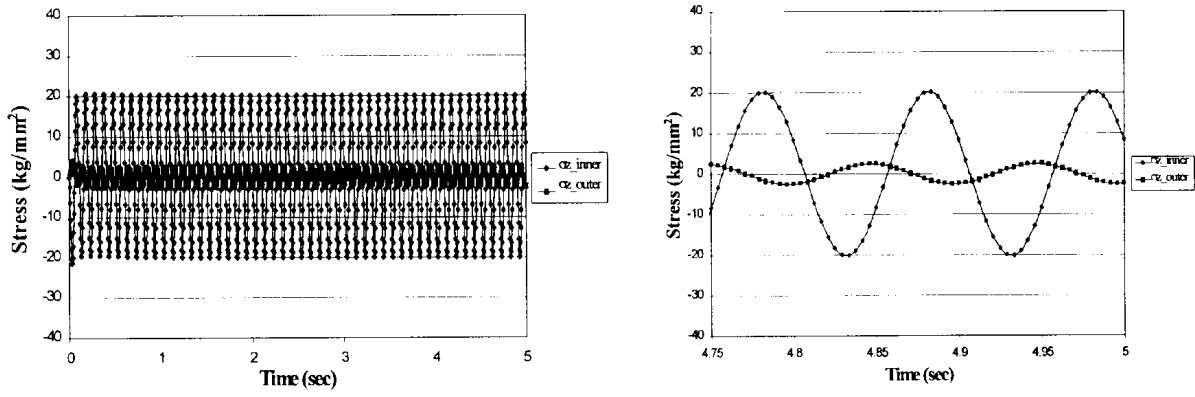
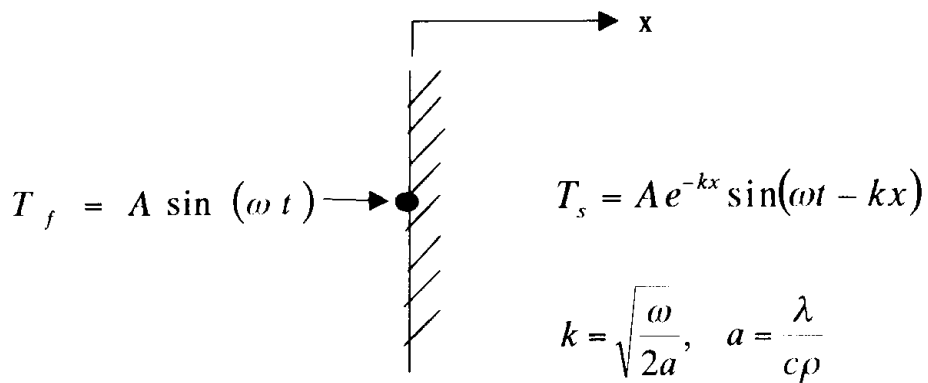
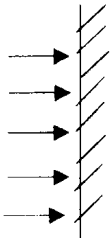


FIG. A10. History of stress at frequency of liquid = 10 Hz.



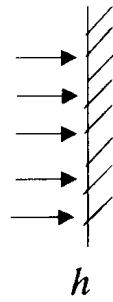
λ : Thermal conductivity, c : Specific heat, ρ : Density

FIG. A11. Thermal response of a semi-infinite solid to sinusoidal temperature fluctuation on the surface.

$$q_0 = -\lambda \left. \frac{\partial T}{\partial x} \right|_{x=0} = A \sin(\omega t)$$


$$T_s = \frac{A}{\sqrt{2\lambda k}} e^{-kx} \sin\left(\omega t - kx - \frac{\pi}{4}\right)$$

FIG. A12. Thermal response of a semi-infinite solid to sinusoidal heat flux fluctuation on the surface.

$$T_f = A \sin(\omega t)$$


$$T_s = \frac{Ah^*}{\sqrt{(h^* + k)^2 + k^2}} e^{-kx} \sin(\omega t - kx - \varepsilon)$$

$$h^* = \frac{h}{\lambda} \quad \varepsilon = \tan^{-1}[k/(h^* + k)]$$

h: Heat-transfer coefficient

FIG. A13. Thermal response of a semi-infinite solid to sinusoidal temperature fluctuation of fluid with heat convection.

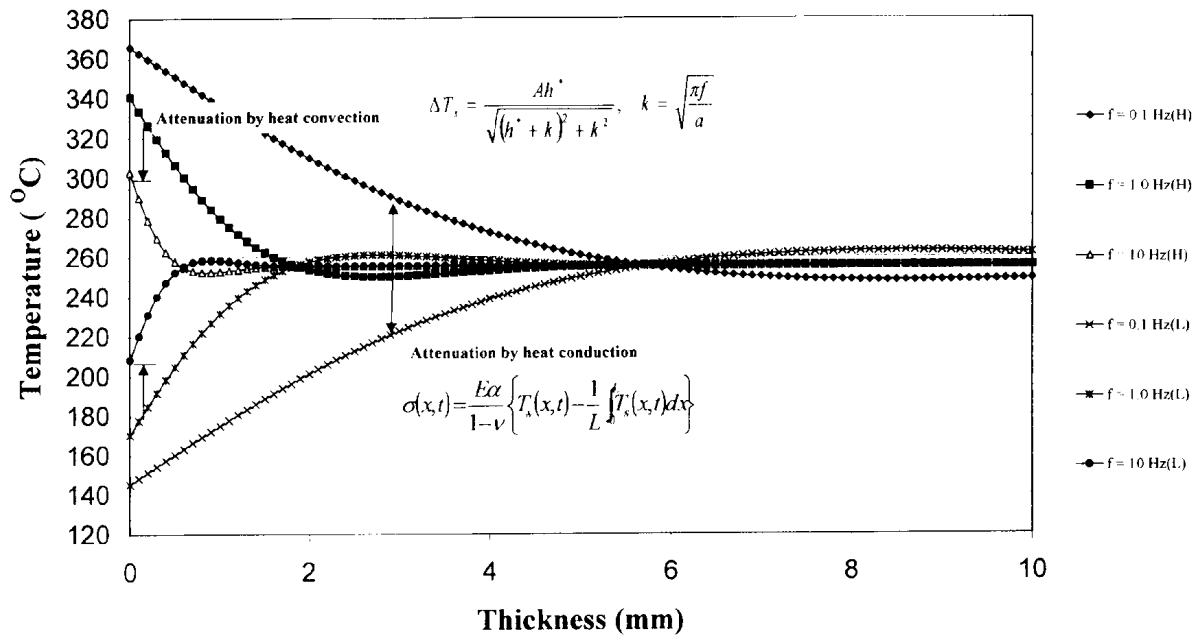


FIG. A14. Temperature profile in a semi-infinite solid due to sinusoidal temperature fluctuation.

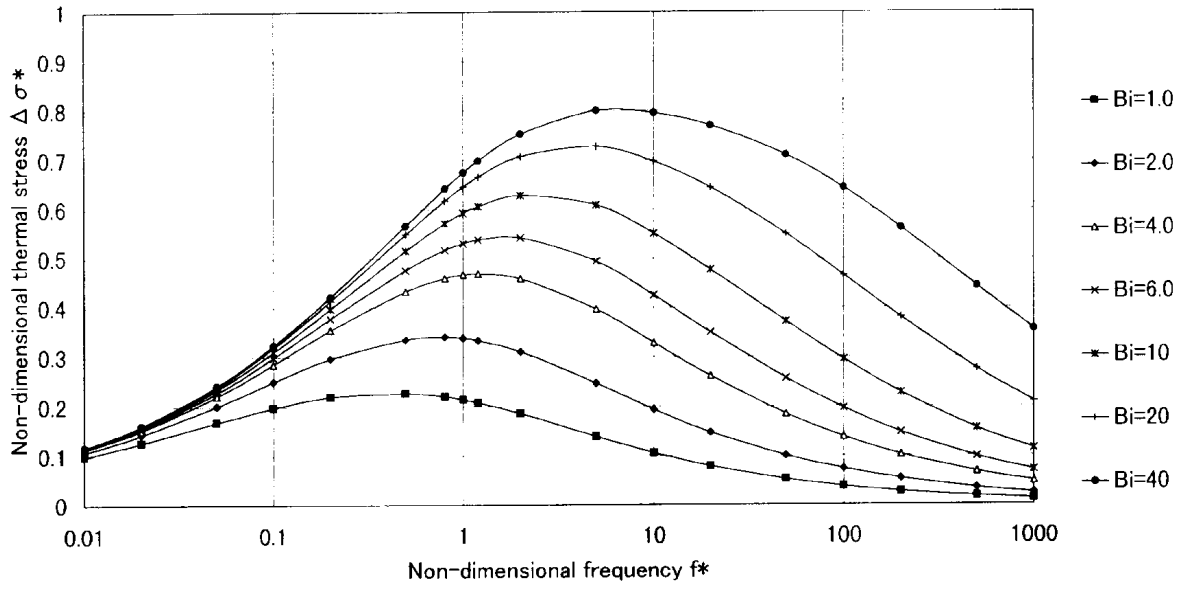


FIG. A15. Non-dimensional structural response diagram based on 1D theory.

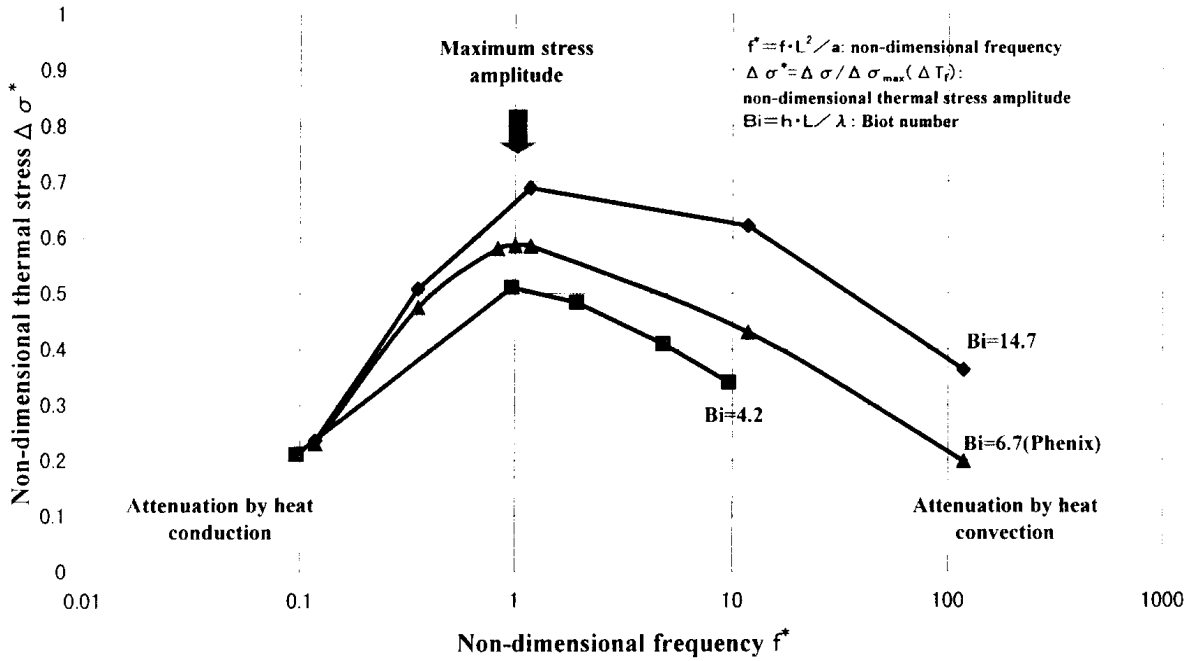


FIG. A16. Non-dimensional structural response diagram based on F.E. calculation.

Theoretical solutions of temperature in a semi-finite solid is

$$T_s = T(x, t) = \frac{A}{\sqrt{2\lambda k}} e^{-kx} \sin\left(\omega t - kx - \frac{\pi}{4}\right). \quad (\text{A.5})$$

When temperature of fluid was enforced sinusoidal fluctuation and transferred to a surface of a semi-infinite solid with a constant heat-transfer coefficient as in Fig. A13, boundary condition is

$$-\lambda \frac{\partial T}{\partial x} \Big|_{x=0} = h(T|_{x=0} - T_f), \quad T_f = A \sin(\omega t) \quad (\text{A.6})$$

where h is heat-transfer coefficient.

Theoretical solutions of temperature in a semi-finite solid is

$$T_s = T(x, t) = \Delta T_s e^{-kx} \sin(\omega t - kx - \varepsilon), \quad (\text{A.7})$$

where

$$\Delta T_s = \frac{Ah^*}{\sqrt{(h^* + k)^2 + k^2}},$$

$$h^* = \frac{h}{\lambda}, \quad \text{and} \quad \varepsilon = \tan^{-1}\left[k / (h^* + k)\right].$$

Solution of Eq. (A.7) can approximate a temperature profile inside pipes with finite thickness due to thermal striping. Main error is that temperature gradients across thickness in finite plates are smaller than one of a semi-infinite plate, because the outer surfaces are insulated. Fig. A14 is temperature profile in a semi-infinite solid due to sinusoidal temperature fluctuation under the same boundary conditions as Fig. A4. In this figure, temperature amplitude is reduced when frequency become high. This trend can be described by Eq. (A.7), which is considered as attenuation factors by heat convection.

Since thermal stress is caused by temperature difference from average temperature, fluctuation of average temperature caused by heat conduction can attenuate stress amplitude. Fig. A14 clarifies that this factor has much influence in the case of low frequency wall small thickness.

By using temperature distribution of Eq. (A.7), induced thermal stress distribution by sinusoidal temperature fluctuation can be quantitatively described as

$$\begin{aligned} \sigma(x, t) &= \frac{E\alpha}{1-\nu} \left\{ T_s(x, t) - \frac{1}{L} \int_0^L T_s(x, t) dx \right\} \\ &= \frac{E\alpha\Delta T_s}{1-\nu} \left\{ e^{-kx} \sin(\omega t - kx - \varepsilon) - \frac{1}{L} \int_0^L e^{-kx} \sin(\omega t - kx - \varepsilon) dx \right\} \\ &= \frac{E\alpha\Delta T_s}{1-\nu} \left[e^{-kx} \sin(\omega t - kx - \varepsilon) + \frac{1}{\sqrt{2kL}} \left\{ e^{-kL} \sin\left(\omega t - kL - \varepsilon - \frac{\pi}{4}\right) - \sin\left(\omega t - \varepsilon - \frac{\pi}{4}\right) \right\} \right]. \end{aligned} \quad (\text{A.8})$$

From Eq. (A.8), stress amplitude is a function of heat convection, frequency, wall thickness, thermal conductivity, specific heat, density, Young's modulus, and thermal expansion ratio.

A.3 Non-dimensional structural response diagram

Since Eq. (A.8) is a complicated equation with many parameters, simplified diagram for design use is developed, by introduction of the following non-dimensional parameters.

Biot Number

$$Bi = \frac{hL}{\lambda}, \quad (A.9)$$

Fourier Number

$$t^* = \frac{ta}{L^2}, \quad (A.10)$$

Non-dimensional frequency defined by

$$f^* = \frac{fL^2}{a}, \quad (A.11)$$

which is proposition of this study,

Non-dimensional thermal stress defined by

$$\sigma^* = \sigma|_{x=0} / \frac{E\alpha\Delta T_f}{1-\nu} \quad (A.12)$$

From Eqs. (A.8-A.12), non-dimensional stress at the inner surface (x=0) is

$$\sigma^* = \alpha(B_i, f^*)\beta(B_i, f^*, t^*), \quad (A.13)$$

where

$$\alpha(B_i, f^*) = \frac{B_i}{\sqrt{(B_i + \sqrt{\pi f^*})^2 + \pi f^*}}, \quad (A.14)$$

$$\beta(B_i, f^*, t^*) = \sin(2\pi f^* t^* - \varepsilon^*) + \frac{1}{\sqrt{2\pi f^*}} \left\{ e^{-\sqrt{\pi f^*}} \sin\left(2\pi f^* t^* - \sqrt{\pi f^*} - \varepsilon^* - \frac{\pi}{4}\right) - \sin\left(2\pi f^* t^* - \varepsilon^* - \frac{\pi}{4}\right) \right\}, \quad (A.15)$$

and

$$\varepsilon^* = \tan^{-1} \left[\sqrt{\pi f^*} / (B_i + \sqrt{\pi f^*}) \right].$$

Since phase delay has no influence on stress amplitude and can be neglected, Eqs. (A.13-A.15) are reduced to,

$$\sigma^* = \alpha(B_i, f^*)\beta(f^*, t^*) \quad (A.16)$$

where

$$\alpha(B_i, f^*) = \frac{B_i}{\sqrt{(B_i + \sqrt{\pi f^*})^2 + \pi f^*}}, \quad (A.17)$$

which is attenuation factor by heat convection, and

$$\beta(f^*, t^*) = \sin(2\pi f^* t^*) + \frac{1}{\sqrt{2\pi f^*}} \left\{ e^{-\sqrt{f^*}} \sin\left(2\pi f^* t^* - \sqrt{f^*} - \frac{\pi}{4}\right) - \sin\left(2\pi f^* t^* - \frac{\pi}{4}\right) \right\}, \quad (\text{A.18})$$

which is attenuation by heat conduction.

By using Eqs.(A.16-A.18), relation between amplitude of non-dimensional thermal stress $\Delta\sigma^*$ and non-dimensional frequency f^* were calculated under the different Biot number B_i as in Fig. A15, which is named Non-dimensional Structural Response Diagram.

Finite Element calculation results were also plotted in the same Diagram as in Fig. A16. Both diagrams are quite similar and proves that Non-dimensional Structural Response Diagram can be applied to thermal striping problem. Reason of slight deference between both diagrams is that the theoretical diagram adopts thermal response of a semi-infinite solid, on the other hand, the F.E. calculated diagram uses finite plates for thermal calculations.

Therefore, it is planned to develop a precise Non-dimensional Structural Response Diagram based on F.E. calculation.

Definition of a heat-transfer coefficient is difficult for the thermal striping problem. This value is, actually not constant during fluctuation. When temperature inside boundary layer can be obtained with precise thermal hydraulic analysis, the effective heat-transfer coefficient becomes large. R&Ds for a heat-transfer problem between fluid and structure under thermal striping phenomenon are required to determine rational Biot number for the Non-dimensional Structural Response Diagram.

THERMOHYDRAULICS COMPUTER CODE SYSTEM AND COMPUTATIONAL RESULTS ON THERMAL STRIPING PHENOMENA AT A TEE JUNCTION OF LMFR SECONDARY CIRCUIT WITH THE SYSTEM

T. MURAMATSU

O-arai Engineering Center,
Japan

Abstract. At the first half, thermal striping evaluation system consisted of the four thermohydraulics computer programs AQUA, DINUS-3, THEMIS and BEMSET, which are represented by a time-and volume-averaged transport analysis, a direct numerical simulation of turbulence flows, a direct simulation Monte Carlo analysis of the continuous fluid flows and a boundary element analysis of structures, respectively, were presented for the evaluation of thermal striping phenomena. This phenomena are recognized as one key unresolved issues from the standpoint of structural integrity of the in-vessel components of a liquid-metal fast reactor. Secondly, numerical results were indicated for the benchmark exercise on thermal striping phenomena at a tee junction pipe coordinated by International Atomic Energy Agency (IAEA). Then the calculated temperature on the outer metal surface of the main pipe was compared with the measured data.

1. A STATE-OF-THE ART REVIEW OF THERMOHYDRAULIC NUMERICAL AND EXPERIMENTAL RESEARCHES

Thermal striping phenomena characterized by stationary random temperature fluctuations are observed in the region immediately above the core exit of liquid-metal-cooled fast reactors (LMFRs) due to the interactions of cold sodium flowing out of a control rod (C/R) assembly and hot, sodium flowing out of adjacent fuel assemblies (F/As). The same phenomena occur in various positions, such as a mixing tee, a combining junction pipe, etc. of the LMFR power plants. Therefore, in the case of the core outlet region, the in-vessel components located in the region, such as upper core structure (UCS), flow guide tube, C/R upper guide tube, and so forth, must be protected against the stationary random thermal process which might induced high-cycle fatigue. In this regard, alloy 718 is generally adopted as a coating material to protect these components against fatigue. Most evaluations of this kind have so far been based on 1:1 or other scale-model experiments using sodium in Japan. In practice, thermal striping conditions in a Japanese prototype Liquid-Metal Fast Breeder Reactor (LMFBR) were evaluated through 1:1 scale model experiments in sodium. In such a conventional approach, an increase in the cost and time to perform the experiments cannot be avoided. Furthermore, in sodium experiments, we often encounter technical difficulties in obtaining adequate amounts and quality of data. For these reasons, establishment of numerical evaluation methods is desirable in support of the experimental approach to understanding fluid temperature fluctuation phenomena. From this viewpoint, we are developing an evaluation system for the thermal striping phenomena based on numerical methods consisting of four thermohydraulics computer programs AQUA, DINUS-3, THEMIS and BEMSET, which are represented by a time- and volume-averaged transport analysis, a direct numerical simulation of turbulence flows, a direct simulation Monte Carlo (DSMC) analysis of the continuous fluid flows and a boundary element analysis of structures, respectively, and of two thermomechanics computer programs FINAS and CANIS, which are formulated by thermoelastic mechanics and fracture mechanics, respectively.

This section presents the outline of the thermal striping thermohydraulics evaluation part consisted of the four computer programs developed at Power Reactor and Nuclear Fuel

Development Corporation (PNC) and their validation results by the use of a fundamental thermal striping experiment in sodium.

1.1. Thermal striping evaluation system based on numerical method

Figure 1 shows an evaluation system for the thermal striping phenomena based on numerical methods developed at PNC. The system consists of six major parts:

1. evaluation of the spatial intensity distribution of the fluid temperature fluctuations containing lower frequency components with the AQUA code,
2. evaluation of the time-series data of the fluid temperature fluctuations including both the lower and higher frequency components with the DINUS-3 code,
3. evaluation of non-stationary heat transfer coefficients between fluid and structure with the THEMIS code,
4. evaluation of the thermal responses characteristics for structures with the BEMSET code,
5. evaluation of the thermal stress distributions in structures with the FINAS code, and
6. evaluation of the crack propagation characteristics of structures with the CANIS code.

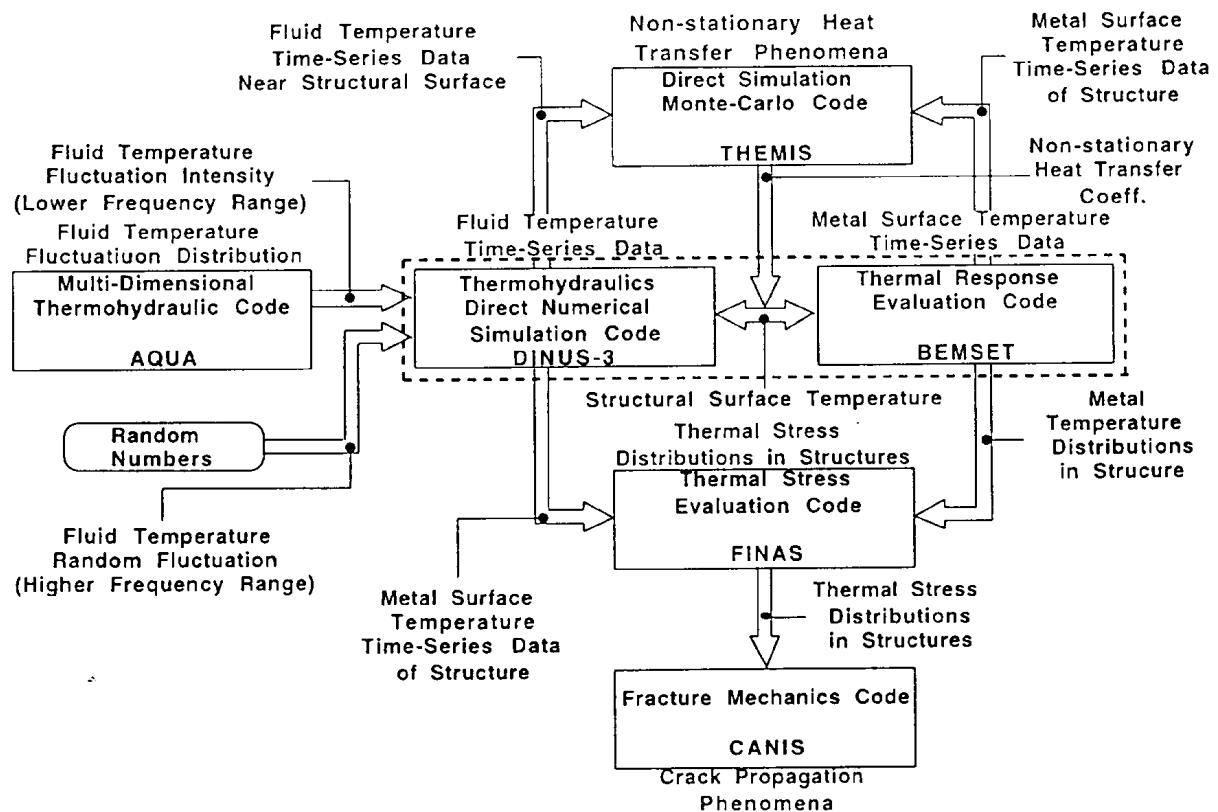


Fig. 1. Evaluation system for the thermal striping phenomena with numerical methods.

1.2. Numerical methods

1.2.1. Time- and volume-averaged multi-dimensional code AQUA [1, 2]

1.2.1.1. Numerical models

A general purpose three-dimensional code AQUA was developed at PNC and designed to deal with incompressible single phase flows in various reactor applications. The code solves mass, momentum and energy conservation equations simultaneously in a finite difference form. The higher order accurate scheme was employed to approximate the convection terms in conservation equations: i.e., Quadratic Upstream Interpolation for Convective Kinematics (QUICK [3]) method. The Filtering, Remedy And Methodology (FRAM [4]) was also implemented to avoid numerical oscillations observed in the higher order schemes in general. The basic numerical algorithm relies on the modified ICE method [5]. The Incomplete Choleski Conjugate Gradient (ICCG [6]) matrix solver is efficiently used in solving a Poisson type pressure equation. An algebraic stress turbulence model (ASM [7]) with intensity transport equation of temperature fluctuations was formulated in the code. As special feature to enhance overall computing efficiency, an adaptive control system based on the Fuzzy theory to control time step sizes was implemented in the code [8, 9].

1.2.1.2. Algebraic stress turbulence model [7]

ASM equations were implemented in the place of the conventional k-ε- turbulence model, which had originally been incorporated in the AQUA code, to aim at better turbulent flow simulations including, those of the thermal striping phenomena. The following are the basic turbulence transport equations and constitutive equations of the ASM formulation.

[Turbulent Kinetic Energy, k]

$$\frac{\partial}{\partial t} \rho k + \frac{\partial}{\partial x_i} \rho u_i k = \frac{\partial}{\partial x_i} \left(C_k \rho \frac{k}{\varepsilon} \overline{u_i' u_i'} \frac{\partial k}{\partial x_i} + \mu_l \frac{\partial k}{\partial x_i} \right) + P' + G' - \rho \varepsilon \quad (1)$$

[Dissipation Rate of k, ε]

$$\begin{aligned} \frac{\partial}{\partial t} \rho \varepsilon + \frac{\partial}{\partial x_i} \rho u_i \varepsilon = & \frac{\partial}{\partial x_i} \left(C_\varepsilon \rho \frac{k}{\varepsilon} \overline{u_i' u_i'} \frac{\partial \varepsilon}{\partial x_i} + \mu_l \frac{\partial \varepsilon}{\partial x_i} \right) \\ & + C_{\varepsilon 1} \frac{\varepsilon}{k} (P' + G') \left(1 + C_{\varepsilon 3} \frac{G'}{P' + G'} \right) - C_{\varepsilon 2} \rho \frac{\varepsilon}{k} \varepsilon \end{aligned} \quad (2)$$

[Intensity of Temperature Fluctuation, $\overline{\theta'^2}$]

$$\frac{\partial}{\partial t} \rho \overline{\theta'^2} + \frac{\partial}{\partial x_j} \rho u_j \overline{\theta'^2} = \frac{\partial}{\partial x_i} \left(- C_\theta \rho \frac{k}{\varepsilon} \overline{u_j' u_i'} \frac{\partial \overline{\theta'^2}}{\partial x_j} + \frac{\lambda}{C_p} \frac{\partial \overline{\theta'^2}}{\partial x_i} \right) - 2 \rho \overline{u_j' \theta'} \frac{\partial T}{\partial x_j} - 2 C_{\theta 1} \rho \frac{k}{\varepsilon} \overline{\theta'^2} \quad (3)$$

$$\begin{aligned}
& \text{[Reynolds Stress, } -\overline{u_i' u_j'}] \\
& -\overline{u_i' u_j'} = \frac{k}{C_{R1} \varepsilon} \frac{(C_{R2} - 1) P_{ij} + (C_{R3} - 1) G_{ij} - \frac{2}{3} \delta_{ij} (C_{R2} P' + C_{R3} G' + (C_{R1} - 1) \varepsilon)}{1 + \left(\frac{P' + G'}{\varepsilon} - 1 \right) / C_{R1}}
\end{aligned} \quad (4)$$

$$\begin{aligned}
& \text{[Turbulent Heat Flux, } -\overline{u_i' \theta'}] \\
& -\overline{u_i' \theta'} = \frac{k}{C_{T1} \varepsilon} \frac{-\left(\overline{u_i' u_j'} \frac{\partial T}{\partial x_j} + \overline{u_j' \theta'} \frac{\partial u_i}{\partial x_j} \right) - (1 + C_{T3}) \beta g_i \overline{\theta'^2} - C_{T2} \overline{u_m' \theta'} \left(\frac{\partial u_i}{\partial x_m} \right)}{1 + \left(\frac{P' + G'}{\varepsilon} - 1 \right) / C_{T1}}
\end{aligned} \quad (5)$$

where

$$P' = -\rho \overline{u_i' u_j'} \frac{\partial u_i}{\partial x_j} \quad (6)$$

$$G' = -\beta g_i \overline{u_i' \theta'} \quad (7)$$

$$P_{ij} = -\overline{u_i' u_j'} \frac{\partial u_j}{\partial x_i} - \overline{u_j' u_i'} \frac{\partial u_i}{\partial x_j} \quad (8)$$

$$G_{ij} = -\beta \left(g_i \overline{u_j' \theta'} + g_j \overline{u_i' \theta'} \right) \quad (9)$$

These equations are characterized by a disuse of such turbulence parameters as turbulent kinetic viscosity ν_t and turbulent heat conductivity λ_t , both of which are based on the Boussinesq's eddy diffusivity hypothesis. The model constants appearing in the above equations were set to the following standard values [7].

C_k	C_ε	$C_{\varepsilon 1}$	$C_{\varepsilon 2}$	$C_{\varepsilon 3}$	C_θ	$C_{\theta 1}$	C_{R1}	C_{R2}	C_{R3}	C_{T1}	C_{T2}	C_{T3}
0.11	0.15	1.44	1.92	0.7	0.13	0.62	2.3	0.5	0.4	3.2	0.5	0.5

As for the boundary treatment of the turbulent kinetic energy k and its dissipation rate ε , the logarithmic law of velocity near boundary wall was used. As for the intensity of temperature fluctuation $\overline{\theta'^2}$ on a wall boundary, where a constant wall temperature could be specified by input data, the following local equilibrium condition could be assumed.

$$\overline{\theta'^2} = -\frac{2}{C_{\theta 1}} \frac{k}{\varepsilon} \overline{u_i' \theta'} \frac{\partial T}{\partial x_i} \quad (10)$$

1.2.2. Direct numerical simulation code DINUS-3 [10, 11]

1.2.2.1. Numerical models

A general purpose direct numerical simulation code DINUS-3 was developed at PNC and designed to understand dominant frequency components of the fluid temperature fluctuations related to thermal striping phenomena. The code solves mass, momentum and energy conservation equations simultaneously in a finite difference form without engineering models such as a turbulence model. A modified third-order upwind scheme [12] was applied for evaluation of convection terms in conservation equations. Time integration scheme depend on the Leap-Frog method [13] to hold a second-order accuracy in time. As a special measure to eliminate numerical instabilities, an advanced adaptive Fuzzy controller with a learning function based on a qualitative inference method was introduced in the code [14].

1.2.2.2. Modified third-order upwind scheme [12]

To simplify, let us consider a one-dimensional convection equation for a scalar transported quantity ϕ

$$\frac{\partial}{\partial t}(\rho\phi) = -\frac{\partial}{\partial x}(\rho u\phi) \quad (11)$$

where ρ and u are the fluid density and velocity. Let us further consider a control cell around a node labeled 0, and denote with subscripts 11, 1, 2, 22 nodes preceding (the first two) and following node 0 in the x-coordinate direction, respectively (see Fig. 2). Subscripts w and e are used to label the surfaces bounding the cell 0 at the left (west) and right (east) sides, respectively.

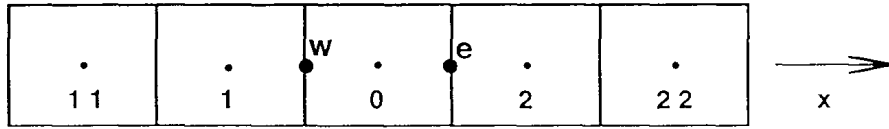


FIG. 2. Control volume 0 and its neighbors.

Discretization of Eq. (11) yields

$$\rho V \left(\phi_0^{n+1} - \phi_0^{n-1} + 2 \Delta t \frac{\partial \phi_0^n}{\partial t} \right) = F_w \phi_w - F_e \phi_e \quad (12)$$

with the definition of the mass flow rate:

$$F = \rho u A \quad (13)$$

Δt is the time increment; A is the flow area on the surface; V is the cell volume; n and $n+1$ denote the present and advanced time steps. In the formulation of the modified third-order upwind scheme, the fluxes of the transported scalar quantity ϕ at the bounding surface of cell 0 are calculated by:

$$\phi_w = \frac{1}{2}(\phi_0 + \phi_1) - \frac{1}{6}\{2(\phi_0 + \phi_{11} - 2\phi_1) - (\phi_2 + \phi_1 - 2\phi_0)\} \quad u_w > 0 \quad (14-a)$$

$$\phi_w = \frac{1}{2}(\phi_0 + \phi_1) + \frac{1}{6}\{2(\phi_1 + \phi_2 - 2\phi_0) - (\phi_{11} + \phi_0 - 2\phi_1)\} \quad u_w < 0 \quad (14-b)$$

$$\phi_e = \frac{1}{2}(\phi_0 + \phi_2) - \frac{1}{6}\{2(\phi_2 + \phi_1 - 2\phi_0) - (\phi_{22} + \phi_0 - 2\phi_2)\} \quad u_e > 0 \quad (15-a)$$

$$\phi_e = \frac{1}{2}(\phi_0 + \phi_2) + \frac{1}{6}\{2(\phi_0 + \phi_{22} - 2\phi_2) - (\phi_1 + \phi_2 - 2\phi_0)\} \quad u_e < 0 \quad (15-b)$$

Using Eqs. (14) and (15) one derives

$$\begin{aligned} F_w \phi_w = & [F_w, 0] \left\{ \frac{1}{2} (\phi_0^i + \phi_1^{i+1}) \right\} - [-F_w, 0] \left\{ \frac{1}{2} (\phi_0^{i+1} + \phi_1^i) \right\} \\ & + [F_w, 0] \left\{ -\frac{1}{6} \left(2 (\phi_0^i + \phi_{11}^i - 2 \phi_1^i) - (\phi_2^i - \phi_1^i - 2 \phi_0^i) \right) \right\} \\ & + [-F_w, 0] \left\{ \frac{1}{6} \left(2 (\phi_1^i + \phi_2^i - 2 \phi_0^i) - (\phi_{11}^i - \phi_0^i - 2 \phi_1^i) \right) \right\} \end{aligned} \quad (16)$$

$$\begin{aligned} F_e \phi_e = & [F_e, 0] \left\{ \frac{1}{2} (\phi_0^{i+1} + \phi_2^i) \right\} - [-F_e, 0] \left\{ \frac{1}{2} (\phi_0^i + \phi_2^{i+1}) \right\} \\ & + [F_e, 0] \left\{ -\frac{1}{6} \left(2 (\phi_2^i + \phi_1^i - 2 \phi_0^i) - (\phi_{22}^i - \phi_0^i - 2 \phi_2^i) \right) \right\} \\ & + [-F_e, 0] \left\{ \frac{1}{6} \left(2 (\phi_0^i + \phi_{22}^i - 2 \phi_2^i) - (\phi_1^i - \phi_2^i - 2 \phi_0^i) \right) \right\} \end{aligned} \quad (17)$$

where $[A, B]$ denotes the maximum of the two real numbers A and B . Superscripts i and $i+1$ denote present and advanced iteration steps, respectively. Inserting Eqs. (16) and (17) into Eq. (12), one derives an algebraic equation of the type

$$a_0 \phi_0^{i+1} + a_1 \phi_1^{i+1} + a_2 \phi_2^{i+1} = b_0 \quad (18)$$

The right-hand-side of Eq. (18) collects all term treated explicitly in time. The system of Eq. (18) has weak diagonal dominance; besides, the off-diagonal coefficients are non-negative. These properties are favorable for the convergence of numerical schemes used for the numerical solution of the system. Because four nodes, neighbors of node 0, need to be considered for every coordinate direction, the third-order upwind scheme implies the treatment of nine and thirteen nodes in two- and three-dimensional cases, respectively.

1.2.3. Direct simulation Monte Carlo code THEMIS [15]

1.2.3.1. Fundamental concepts

A general purpose three-dimensional DSMC code THEMIS was designed to deal with monatomic molecular flows in the wide range of Reynolds number. The code solves the Boltzmann equation by a probabilistic method.

Flow fields are divided into a network of computational cells. The dimensions of the cells must be such that the change in flow properties across each cell is small. All that are wanted are the number density n and the velocity distribution function *in* each cell. The flow velocity u and the temperature T are given as the expectations of $f(\underline{c})$, i.e.

$$3RT = E(c^2) = \int c^2 f(\underline{c}) d\underline{c} - u^2, \quad (20)$$

where \underline{c} is the peculiar velocity and R is the gas constant per unit mass. In the DSMC method, a random sample c_1, c_2, \dots, c_N of size N is employed instead of $f(\underline{c})$. The number N is so chosen as to be proportional to n . The relation between $f(\underline{c})$ and the sample is

$$f(\underline{c}) = \frac{1}{N} \sum_{i=1}^N \delta(\underline{c} - \underline{c}_i). \quad (21)$$

This is exact in the limit $N = \infty$ in the sense that integration of both sides over an arbitrary volume element in the velocity space yields an equal probability. For finite N ,

Eq. (21) is an approximation. The random variables c_1, c_2, \dots, c_N are independent and their probability density functions are equal to $f(\underline{c})$. The variable \underline{c}_i is called the velocity of molecule i and the size N is called the number of simulated molecules. If we substitute Eq. (21) into Eqs. (19) and (20), we have approximate expressions for $E(\underline{c})$ and $E(c^2)$. They are the sample mean $\langle \underline{c} \rangle$ and sample variance $\langle c^2 \rangle$.

$$\langle \underline{c} \rangle = \frac{1}{N} \sum_{i=1}^N \underline{c}_i, \quad (22)$$

$$\langle c^2 \rangle = \frac{1}{N} \sum_{i=1}^N c_i^2 - \langle \underline{c} \rangle^2. \quad (23)$$

The flow properties \underline{u} and T are obtained from:

$$\underline{u} = \langle \underline{c} \rangle, \quad (24)$$

$$3RT = \frac{N}{N-1} \langle c^2 \rangle. \quad (25)$$

The factor $N / (N-1)$ is added to Eq. (25) so that the expectation of the right-hand side may agree with $E(c^2)$.

Now we have seen how to obtain the macroscopic properties \underline{u} and T from the microscopic information $\{c_1, c_2, \dots, c_N\}$. Let us fix our attention on a computational cell. Both N and $\{c_1, c_2, \dots, c_N\}$ for this computational cell change with time. To determine N (or n), we must know the positions of all simulated molecules in the flow fields. The DSMC method is a set of procedures to determine the positions and velocities of simulated molecules as a function of time.

1.2.3.2. Numerical models

In the DSMC method, time is advanced in discrete steps of Δt . The step Δt is chosen to be small compared with the mean free time t_F so that the molecular collision and the collisionless free motion are uncoupled over the interval Δt . Bird [16] introduced the concept from a physical consideration that for $\Delta t \ll t_F$ the distortion of molecular trajectory owing to uncoupling is small. The concept is also an outgrowth from the Boltzmann equation. Let us write the Boltzmann equation as

$$\frac{\partial f}{\partial t} = -Df + Jf, \quad (26)$$

where $Df = \underline{c} \cdot (\partial f / \partial \underline{x})$ and

$$Jf = \int (f' f'_1 - f f_1) g \sigma d\Omega d\underline{c}_1.$$

In terms of the operators D and J , we may write the solution $f(\underline{c}, \underline{x}, \Delta t)$ as

$$f(\underline{c}, \underline{x}, \Delta t) = (1 - \Delta t D + \Delta t J) f(\underline{c}, \underline{x}, 0). \quad (27)$$

Neglecting the second-order term, we may rewrite Eq. (27) as

$$f(\underline{c}, \underline{x}, \Delta t) = (1 + \Delta t J)(1 - \Delta t D) f(\underline{c}, \underline{x}, 0) \quad (28)$$

Neglecting of the second-order term requires not only $\Delta t \ll t_F$ but $\Delta t \ll \Delta t / c$, where Δx is the cell dimension and c is the molecular velocity.

The splitting of the two operators leads to two successive stages of the simulation process. In the first stage, the molecular system undergoes a collisionless free motion due to the operator $(1 - \Delta t D)$. Belotserkovskii and Yanitskii [17] proposed to use a random-walk model in this stage. However, the use of such model is not free of case. Usually the free motion stage is treated as it stands. The second stage is the collisional relaxation due to the operator $(1 - \Delta t J)$. This is discussed in the next paragraph.

As stated before, the fluid in cell can be regarded as spatially uniform. The collisional relaxation of a spatially uniform fluid is described by the Boltzmann equation without the convection term D_f or the Kac equation. The Boltzmann equation is a nonlinear equation for one-particle distribution function $f(\underline{c}, t)$ whereas the Kac equation is a linear equation for N particle distribution function. The latter can be contracted to the Boltzmann equation if all molecular velocities are chaotic, i.e. if they are mutually independent and their probability density functions are equal to $f(\underline{c}, t)$. The theorem on the 'propagation of chaos' states that in the asymptotic sense of $N \rightarrow \infty$ the chaotic property remains valid at any time if it is valid at time $t = 0$. In using the DSMC method, the chaotic property is always satisfied at $t = 0$ because the molecular velocities are independently sampled from a given or assumed probability density function. In actual simulations, however, the number N is finite, so that the theorem is not satisfied in its exact sense. Nevertheless it is most probable that the Kac equation is a good substitute for the Boltzmann equation.

To simulate the collisional relaxation, we need the method to determine $\{\underline{c}_1, \underline{c}_2, \dots, \underline{c}_N\}$ at $t = \Delta t$ from $\{\underline{c}_1, \underline{c}_2, \dots, \underline{c}_N\}$ at $t = 0$. The method should be derived from the Boltzmann or Kac equation. At an early stage of the DSMC method, the method was obtained not from the kinetic equation but from a physical modeling of the molecular collision. Bird's method [16] is the first one. He showed a seeming consistency of his method with the Boltzmann equation.

Whether solutions of the Boltzmann equation can be obtained by the use of the method based on the Kac equation is a question worthy of thinking. To answer the question we need the standard method that is derived from the Boltzmann equation. Such a method was found by Nanbu [18]. He also clarified the interrelation among various methods.

1.2.4. Boundary element method code BEMSET [19]

1.2.4.1. Numerical model

(1) Boundary integral equation for unsteady thermal conduction

Let us consider a three-dimensional region Ω of homogeneous materials as shown in Fig. 3. In the figure, P and Q represent arbitrary boundary points on the region Ω , p and q are arbitrary internal points in the region Ω and Γ is a boundary of the region Ω .

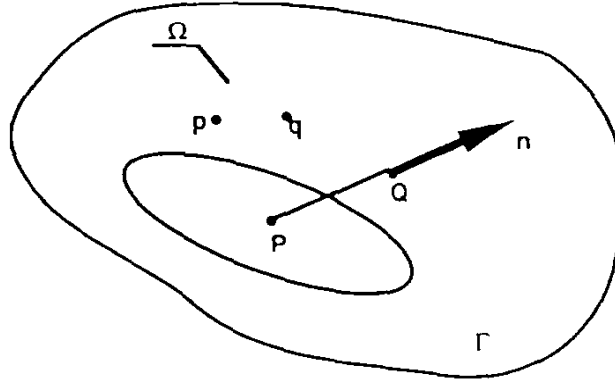


FIG. 3. Three-dimensional region Ω of homogeneous materials.

Temperature transients $T(p, t)$ of the point p are described by the following equation for the condition of $t > 0$:

$$\nabla^2 T(p, t) + \lambda^{-1} W(p, t) = \chi^{-1} \frac{\partial T(p, t)}{\partial t}, \quad (29)$$

where χ, λ, W represent thermal diffusivity, thermal conductivity, time and internal heat source, respectively.

The boundary integral representation of $T(p, t)$ and boundary integral equation of $T(P, t)$ are written as:

$$\begin{aligned} T(p, t) &= \chi \int_0^t \int_{\Gamma} [\varphi(Q, p, t, \tau) T_{,n}(Q, \tau) - \varphi_{,n}(Q, p, t, \tau) T(Q, \tau)] d\Gamma(Q) d\tau \\ &\quad + \chi \lambda^{-1} \int_0^t \int_{\Omega} W(q, \tau) \varphi(q, p, t, \tau) d\Omega(q) d\tau + \int_{\Omega} T(q, 0) \varphi(q, p, t, 0) d\Omega(q), \quad (30) \\ T(P, t) &- \chi \int_0^t \int_{\Gamma_1} \varphi(Q, P, t, \tau) T_{,n}(Q, \tau) d\Gamma(Q) d\tau + \chi \int_0^t \int_{\Gamma_2} \varphi(Q, P, t, \tau) T_{,n}(Q, \tau) d\Gamma(Q) d\tau \\ &= \chi \lambda^{-1} \int_0^t \int_{\Gamma_2} \varphi(Q, P, t, \tau) q_0(Q, \tau) d\Gamma(Q) d\tau - \chi \int_0^t \int_{\Gamma_1} \varphi_{,n}(Q, P, t, \tau) T_0(Q, \tau) d\Gamma(Q) d\tau \\ &\quad + \chi \lambda^{-1} \int_0^t \int_{\Omega} W(q, \tau) \varphi(q, P, t, \tau) d\Omega(q) d\tau + \int_{\Omega} T(q, 0) \varphi(q, P, t, 0) d\Omega(q) \end{aligned}$$

by the uses of the time-dependant fundamental solution schemes [20] and the Green's second identity, respectively. The variables in these formulations have the following meaning:

- φ = fundamental solutions of q or Q at $t=\tau$
- T_0 = boundary temperatures
- q_0 = boundary heat flux
- $T_{,n}$ = boundary temperature gradients
- Γ_1 = Dirichlet type boundaries
- Γ_2 = Neumann type boundaries.

(2) Boundary integral equation for unsteady thermal stress

The boundary integral representation for thermal stress components $u_{kl}(p, t)$ and boundary integral equation I for thermal stress components $u_k(P, t)$ in the coordinate system shown in Fig. 4 are formulated as:

$$\begin{aligned} \sigma_{kl}(p, t) = & \int_{\Gamma} D_{kli}^*(Q, p) p_i(Q, t) d\Gamma(Q) - \int_{\Gamma} S_{kli}^*(Q, p) u_i(Q, t) d\Gamma(Q) + \int_{\Omega} D_{kli}^*(q, p) b_i(q) d\Omega(q) \\ & + \chi \int_0^t \int_{\Gamma} [T(Q, \tau) \sigma_{kl,j}^*(Q, p, t, \tau) n_j - \sigma_{kl}^*(Q, p, t, \tau) T_{,j}(Q, \tau) n_j] d\Gamma(Q) d\tau \\ & - \chi \lambda^{-1} \int_0^t \int_{\Omega} \sigma_{kl}^*(q, p, t, \tau) W(q, \tau) d\Omega(q) d\tau - \int_{\Omega} \sigma_{kl}^*(q, p, t, 0) T(q, 0) d\Omega(q) \quad , \end{aligned} \quad (32)$$

$$\begin{aligned} u_k(P, t) = & \int_{\Gamma_1} p_{ki}^*(Q, P) u_i(Q, t) d\Gamma(Q) - \int_{\Gamma_2} u_{ki}^*(Q, P) p_i(Q, t) d\Gamma(Q) \\ = & \int_{\Gamma_1} u_{ki}^*(Q, P) p_{i0}(Q, t) d\Gamma(Q) - \int_{\Gamma_2} p_{ki}^*(Q, P) u_{i0}(Q, t) d\Gamma(Q) + \int_{\Omega} u_{ki}^*(q, P) b_i(q) d\Omega(q) \\ & + \chi \int_0^t \int_{\Gamma} [T(Q, \tau) u_{k,j}^*(Q, P, t, \tau) n_j - u_{k,j}^*(Q, P, t, \tau) T_{,j}(Q, \tau) n_j] d\Gamma(Q) d\tau \\ & - \chi \lambda^{-1} \int_0^t \int_{\Omega} u_{k,j}^*(q, P, t, \tau) W(q, \tau) d\Omega(q) d\tau - \int_{\Omega} u_{k,j}^*(q, P, t, 0) T(q, 0) d\Omega(q) \end{aligned} \quad (33)$$

by a thermoelastic displacement potential function based on the Betti's reciprocal theorem [21].

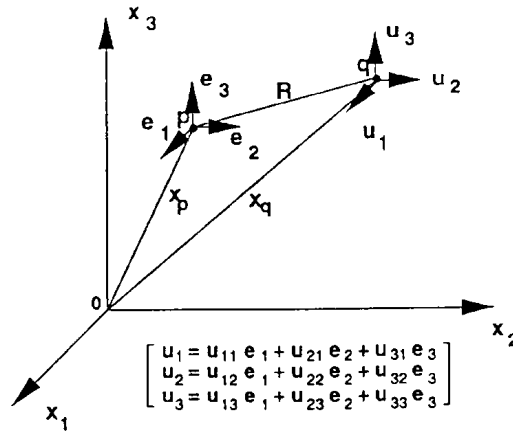


FIG. 4. Coordinate system used in the BEMSET code.

In these formulations, main variables are described by following relations.

$$D_{kli}^*(Q, p) = \frac{1}{4 a \pi (1 - \nu) R^a} \left[(1 - 2\nu) (\delta_{ik} R_l + \delta_{il} R_k - \delta_{kl} R_i) \frac{1}{R} + b \frac{R_i R_l R_k}{R^3} \right] \quad (34)$$

$$S^*_{kli}(Q, p) = \frac{G}{2 a \pi (1 - \nu) R^b} \left\{ b \frac{\partial R}{\partial n} \left[(1 - 2\nu) \delta_{kl} \frac{R_i}{R} + \nu \left(\delta_{ik} \frac{R_l}{R} + \delta_{il} \frac{R_k}{R} \right) - c \frac{R_i R_l R_k}{R^3} \right] \right. \\ \left. + b \nu \left(n_k \frac{R_l R_i}{R^2} + n_l \frac{R_i R_k}{R^2} \right) + (1 - 2\nu) \left(b n_i \frac{R_l R_k}{R^2} + n_l \delta_{ik} + n_k \delta_{il} \right) - (1 - 4\nu) n_i \delta_{kl} \right\} \quad (35)$$

$$\sigma^T_{kl}(q, p, t, \tau) = 2 G \left\{ \frac{m}{\pi^{3/2} R^3} \left(\frac{R_k R_l}{R^2} - \delta_{kl} \right) \gamma\left(\frac{5}{2}, y\right) + \delta_{kl} \gamma\left(\frac{3}{2}, y\right) \right\} \quad (36)$$

$$\sigma^T_{kl,j}(Q, p, t, \tau) = \frac{2 G}{n_j} \left\{ \frac{m}{\pi^{3/2} R^4} \left(n_k \frac{R_l}{R} + n_l \frac{R_k}{R} - 4 \delta_{kl} \frac{\partial R}{\partial n} \right) \gamma\left(\frac{5}{2}, y\right) + 2 \left(\delta_{kl} - \frac{R_k R_l}{R^2} \right) \gamma\left(\frac{7}{2}, y\right) \frac{\partial R}{\partial n} \right\} \quad (37)$$

$$u^T_k(q, p, t, \tau) = \frac{m R_k}{2 \pi^{3/2} R^3} \gamma\left(\frac{3}{2}, y\right) \quad (38)$$

$$u^T_{k,j}(Q, p, t, \tau) n_j = - \frac{m}{\pi^{3/2} R^3} \left[\frac{R_k}{R} \gamma\left(\frac{5}{2}, y\right) \frac{\partial R}{\partial n} - \frac{1}{2} \gamma\left(\frac{3}{2}, y\right) n_k \right] \quad (39)$$

Here, $\gamma(\cdot, \cdot)$ denotes the incomplete Gamma function of the first kind, and is defined by

$$\gamma(z, y) = \int_0^y e^{-x} x^{z-1} dx = \sum_{n=0}^{\infty} \frac{(-1)^n y^{z+n}}{n! (z+n)} \quad (40)$$

The variables in the above equations have the following meaning:

- $u^*(q)$ = displacement at the point q in the Γ region
- $u^*(Q)$ = displacement at the point Q in the Γ region
- $b_i(q)$ = body force at the point q in the Γ region
- $p^*(Q)$ = surface traction at the point Q in the Γ region,

and asterisks mean those variables in the Ω region.

(3) Descretization methods

Boundary integral equations of thermal conduction and thermal stress were discretized by the uses of second-order rectangular elements with an interpolation function ϕ_i (see Fig. 5) and second-order time interpolation methods (see Fig. 6).

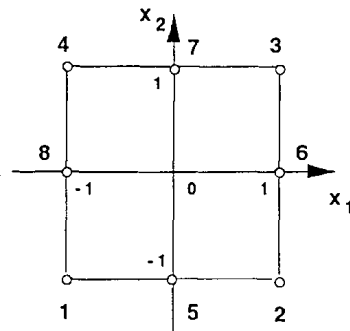


FIG. 5. Node labeling for second-order Rectangular elements.

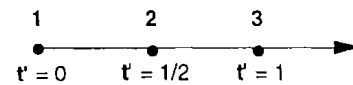


FIG. 6. Second-order time interpolation.

A function u using the second-order rectangular elements is written as:

$$u = \sum_{i=1}^8 \phi_i u_i \quad (41)$$

and interpolation functions are defined by:

$$\begin{aligned}
\phi_1 &= 0.25 (1 - x_1)(1 - x_2)(x_1 - x_2 - 1) \\
\phi_2 &= 0.25 (1 + x_1)(1 - x_2)(x_1 - x_2 - 1) \\
\phi_3 &= 0.25 (1 + x_1)(1 + x_2)(x_1 + x_2 - 1) \\
\phi_4 &= 0.25 (1 - x_1)(1 + x_2)(-x_1 + x_2 - 1) \\
\phi_5 &= 0.5 (1 - x_1^2)(1 - x_2) \\
\phi_6 &= 0.5 (1 - x_2^2)(1 + x_1) \\
\phi_7 &= 0.5 (1 - x_1^2)(1 + x_2) \\
\phi_8 &= 0.5 (1 - x_2^2)(1 - x_1) \quad .
\end{aligned}$$

A physical property ϕ at a time τ is evaluated with the second-order time interpolation methods as:

$$\phi(\tau) = \phi_1 \phi_{f-1}(\tau) + \phi_2 \phi_{f-1/2}(\tau) + \phi_3 \phi_f(\tau) \quad (42)$$

where:

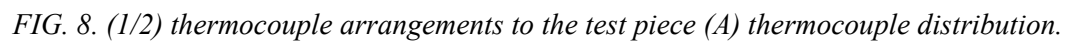
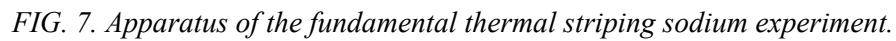
$$\begin{aligned}
\phi_1 &= 2 t'^2 - 3 t' + 1 \\
\phi_2 &= 4 t' (1 - t') \\
\phi_3 &= t' (2 t' - 1) \\
t' &= (\tau - t_{f-1}) / (t_f - t_{f-1}) \\
t_{f-1/2} &= (t_{f-1} + t_f) / 2 \quad .
\end{aligned}$$

1.3. Code validations with a fundamental thermal striping experiment in sodium [22, 23]

1.3.1. Outline of the experiment

Outlines of the experimental setup are shown in Fig. 7. The test section consisted of parallel jet nozzles, test piece, nozzle support, etc. Figure 8 shows the parallel jet nozzles which are oblong slits 5 mm wide and 9 mm. long, and thermocouple arrangements to the test piece.

Totally 17 thermocouples were attached to the test piece to measure temperature fluctuations at fully turbulence region (T), laminar sub-layer region (L), test piece surface (S) and the inner positions of the test piece ($MA_{0.2}$, $MA_{0.3}$, $MB_{0.3}$ and $MB_{0.5}$). In the experiments, time-series data of the temperature fluctuations were measured under the three jet velocity conditions ($V_{hot} = V_{cold} = 1.0m/s$, $1.5m/s$ $2.0m/s$) while the sodium temperature difference between both the nozzles were kept constant ($T_{hot} - T_{cold} = \Delta t = 40^\circ C$). The transient response of thermocouples was fast enough *time constant* $\tau = 30m/s$) to measure temperature fluctuations. In the experiment, temperature transient data were measured simultaneously for 100 sec with 200 Hz of sampling rate.



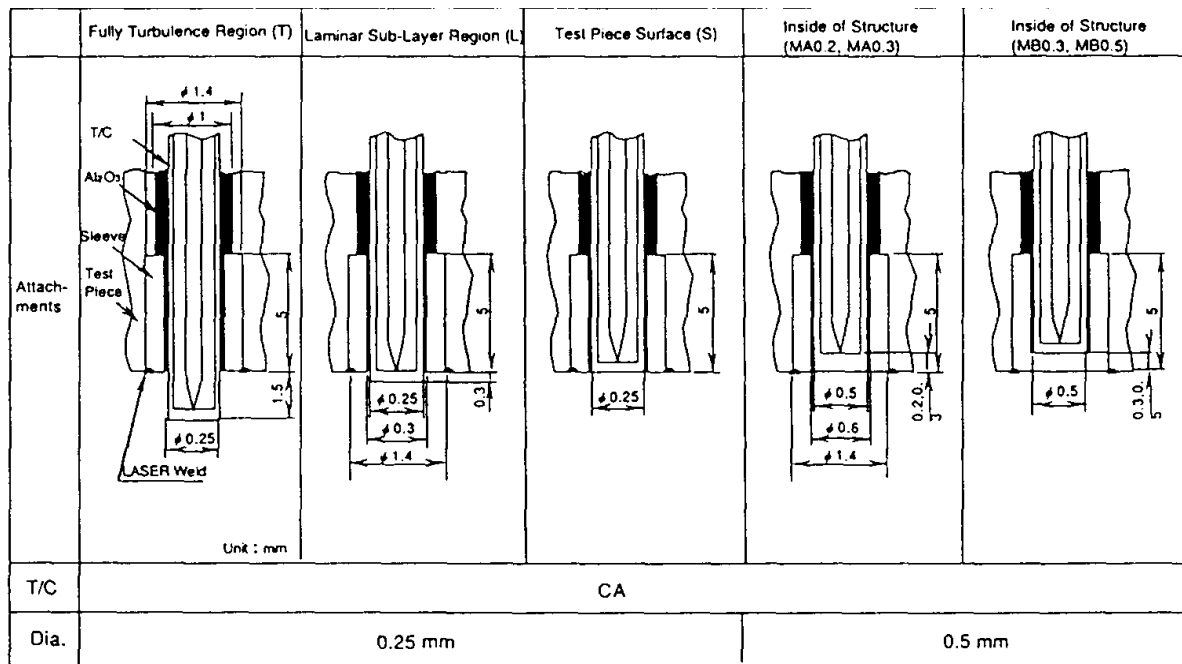


FIG. 8. (2/2) Thermocouple arrangements to the test piece (B) thermocouple specification.

1.3.2. Outline of the experimental results

Figure 9 shows the measured temperature transients (Sections 5-11) under the condition of ($V_{hot} = V_{cold} = 2.0 \text{ m/s}$).

As shown in the figure, the amplitude of the temperature fluctuations decreases drastically toward the inside of the test piece from the fully turbulence region of sodium flows. Also the higher frequency components of the temperature fluctuations show the similar tendency. One of the principal interpretations is that the sodium temperature fluctuations in the fully turbulence region were damped due to four effects; i.e., mixing by turbulence flows, passing through laminar sub-layer, non-linear transient heat transfer to the test piece surface from sodium, and heat conduction in the structure.

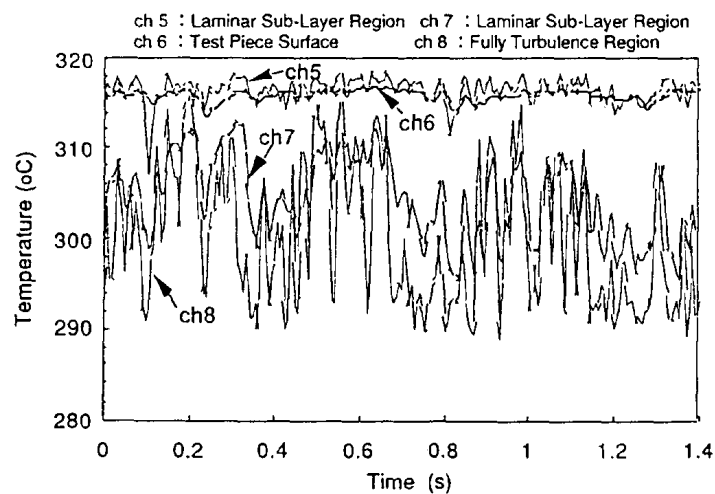


FIG. 9. (1/2) Measured temperature transients under the condition of ($V_{hot} = V_{cold} = 2.0 \text{ m/s}$).

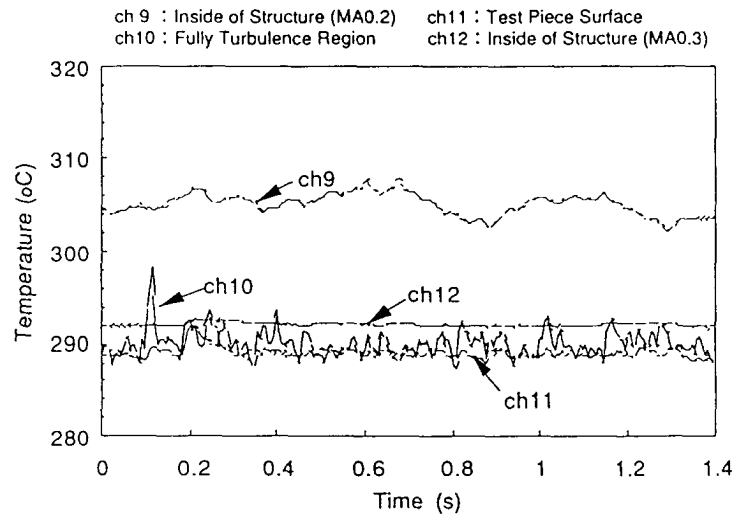


FIG. 9. (2/2) Measured temperature transients under the condition of ($V_{hot} = V_{cold} = 2.0 \text{ m/s}$).

1.3.3. Outline of the calculations with the DINUS-3 and BEMSET codes

Calculations were carried out for the total of three cases, i.e., ($V_{hot} = V_{cold} = 1.0 \text{ m/s}$, 1.5 m/s , 2.0 m/s), by the DINUS -3 and BEMSET codes. The AQUA and THEMIS codes were not utilized in these calculations. Author used a three-dimensional mesh and element arrangements shown in Fig. 10. Computational cells that contained no solid structure inside counted up to 25,840, and boundary elements numbered up to 260.

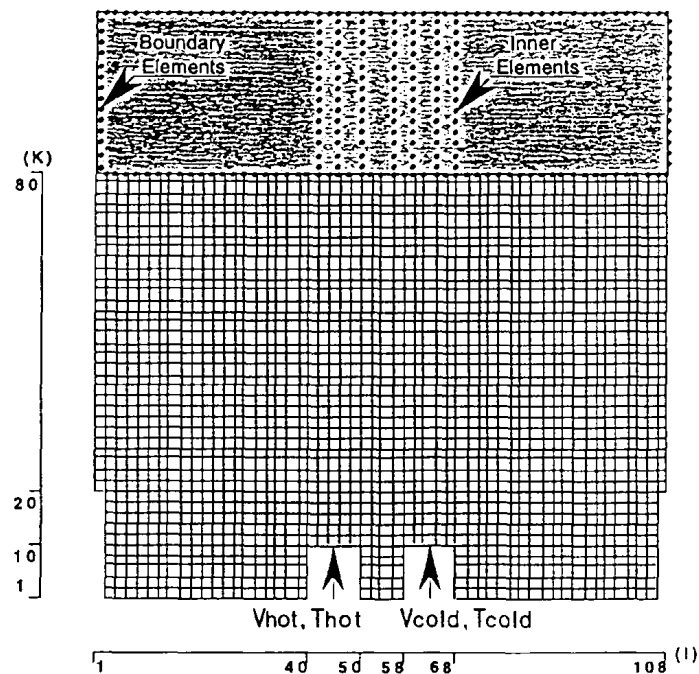


FIG. 10. Mesh and boundary elements for the analyses.

The no-slip condition for the velocity components was assumed on the test piece surface in the DINUS-3 calculations. As for the BEMSET calculations, it was set to a constant temperature conduction coefficient ($22.0 \text{ mm}^2/\text{s}$ for SUS304 stainless steel of 300°C), a constant upper wall temperature of the test piece (300°C) and heat transfer coefficients of fully developed turbulent flows ($\text{Nu} = 5.0 + 0.25 \text{ Pe}^{0.8}$); where Nu and Pe represent Nusselt and Peclet numbers, respectively.

Given all thermohydraulic data at $t = 0$, the transient was calculated up to a quasi-steady-state level $[(\phi^{n+1} - \phi^n) / \phi^n = 10^{-4}]$ using a time marching method; where ϕ represents three velocity components in the x-, y- and z-directions, i.e., u, v, and w, respectively, enthalpy in sodium h, and temperatures in the test piece T; n+1 indicates the advanced time step and n current time step. Then a restart transient calculation storing calculated data was continued up to a 10-s simulation time with a constant time interval of 10 ms.

1.3.4. Outline of the calculated results

1.3.4.1. Transient characteristics

Figure 11 shows calculated instantaneous distributions for velocity vector and sodium temperature on the x-z plane at $J = 2$ under the condition of ($V_{hot} = V_{cold} = 2.0 \text{ m/s}$), respectively.

The sodium temperature was normalized by the maximum temperature difference $\Delta t = 40^\circ\text{C}$ between both the nozzles. The strong heterogeneity with thermally instabilities of the fields were evaluated, as shown in the figure.

Figure 12 indicates temperature transients for a 0.2-s simulation time at four spatial positions; sodium temperatures at 10 mm and 5 mm from the test piece surface, metal temperatures at the test piece surface and at 0.5 mm. from the test piece surface. The amplitudes and higher frequency components of the temperature fluctuations was decreased drastically toward the inside of the test piece from the fully turbulence region of sodium flows.

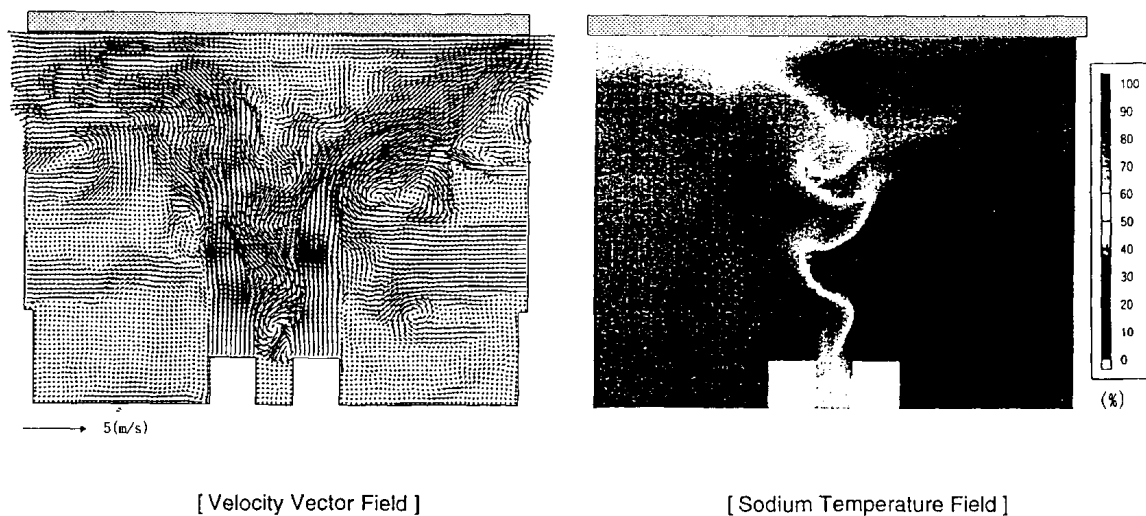


FIG. 11. Calculated instantaneous distributions under the condition of ($V_{hot} = V_{cold} = 2.0 \text{ m/s}$).

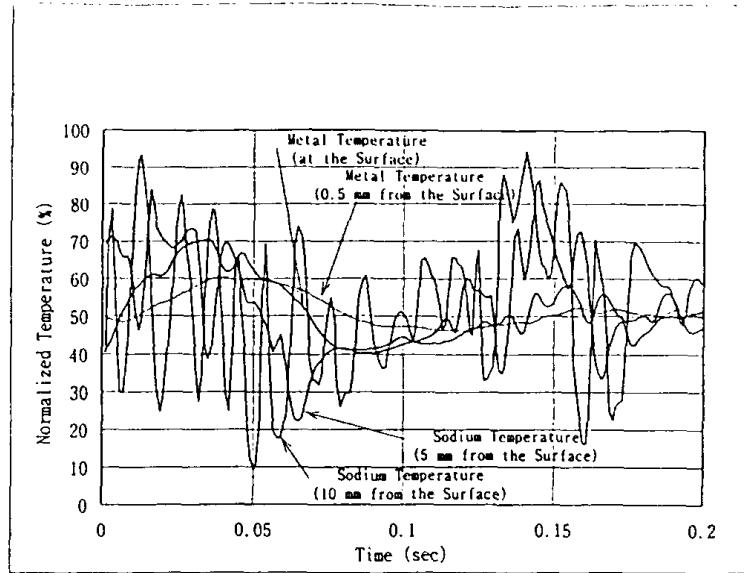


FIG. 12. Calculated temperature transients near the wall under the condition of $(V_{hot} = V_{cold} = 2.0 \text{ m/s})$.

1.3.4.2. Damping characteristics

Figure 13 compares the calculation with the experiment with respect to a distribution of the temperature fluctuation amplitudes near the test piece surface under the condition of $(V_{hot} = V_{cold} = 2.0 \text{ m/s})$. As shown in the comparison, good agreement between the calculation and the experiment was obtained for the drastically decreasing of the temperature fluctuation amplitude near the wall.

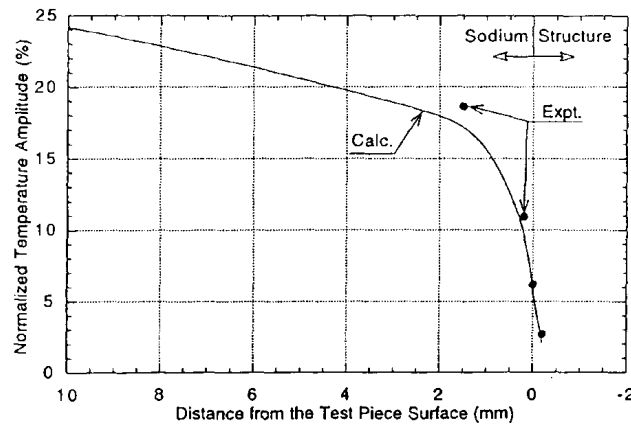


FIG. 13. Comparison of temperature fluctuation amplitudes under the condition of $(V_{hot} = V_{cold} = 2.0 \text{ m/s})$.

Comparisons of allotment ratios for the damping effects of the temperature fluctuation amplitudes between the calculations and the experiments are shown in Fig. 14, for the three experimental conditions $(V_{hot} = V_{cold} = 1.0 \text{ m/s}, 1.5 \text{ m/s}, 2.0 \text{ m/s})$. The experimental results indicated that the damping effect due to the mixing in the fully turbulence region decreased with increasing sodium flow velocity at the outlet plane of the nozzles. One of the main reasons for this behavior was considered to be that the passing time through the fully

turbulence region of the temperature fluctuations was decreased with the increased nozzle velocity. On the contrary, measured damping effect due to the non-linear transient heat transfer to the test piece surface from sodium was increased with increasing sodium flow velocity. This is caused by the emphasis for the difference of a time scale on heat transport between sodium and structures, and is explanation an actualization of the non-linear heat transfer characteristics between sodium and structures.

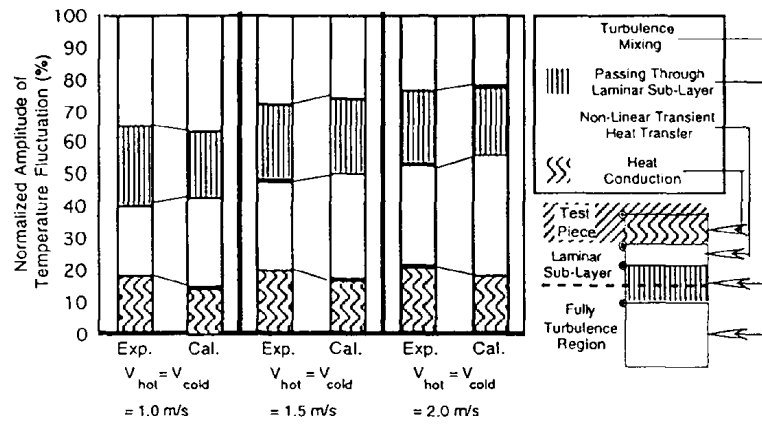


FIG. 14. Comparison of the allotment ratios for damping characteristics.

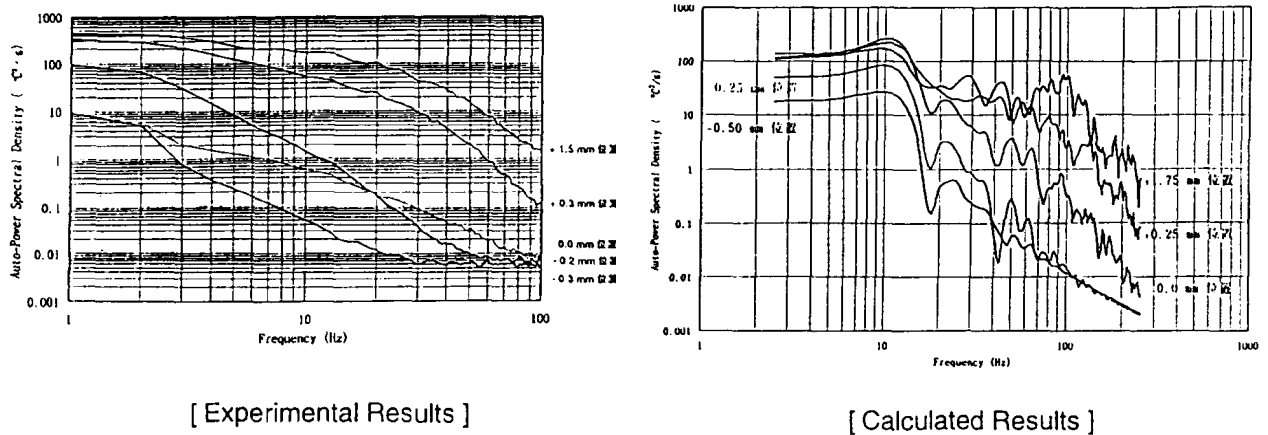


FIG. 15. Comparison of auto-power spectral density functions under the condition of $V_{hot} = V_{cold} = 2.0 \text{ m/s}$.

Calculations follow these trends very well and the figure show good agreement of the calculational results with the experiments.

1.3.4.3. Frequency characteristics

Figure 15 compares the auto-power spectral density functions of the temperature fluctuations between the calculations and the experiments under the condition of $V_{hot} = V_{cold} = 2.0 \text{ m/s}$. The comparisons were carried out for the total of five points, i.e., fully turbulence region (1.5 mm and 1.25 mm from the test piece surface for the experiment and the DINUS3 calculation, respectively); laminar sub-layer region (0.3 mm and 0.25 mm

from the test piece surface for the experiment and the DINUS-3 calculation, respectively); test piece surface (for the experiment and the BENTSET calculation); inside of the test piece (0.2 mm and 0.25 mm from the test piece surface for the experiment and the BEMSET calculation, respectively); and more inside of the test piece (0.3 mm and 0.75 mm from the test piece surface for the experiment and the BEMSET calculation, respectively). As for the experimental results, higher frequency components (> 20 Hz for the sodium temperature fluctuations; Sections 7 and 8, and > 2 Hz for the metal temperature fluctuations; Sections 9, 11, and 12) were attenuated suddenly due to the presence of the damping effects. From the tendencies of these attenuations, it became clear that the damping effects have a large difference on frequency response characteristics. In the results with the calculations, the predicted tendencies of the auto-power spectral density functions a reed well with the experimental results.

2. COMPUTATIONS OF THE BENCHMARK EXERCISE [24]

2.1. Benchmark specifications

This benchmark problem deals with the mixing of two flows at different temperatures in the secondary circuit of the French LMFBR Phénix. The Phénix reactor is a 250 MWe demonstration plant, with three secondary loops, modular steam generators and integrated primary circuit. The main features of the secondary circuit with a tee junction area are shown in Fig. 16.

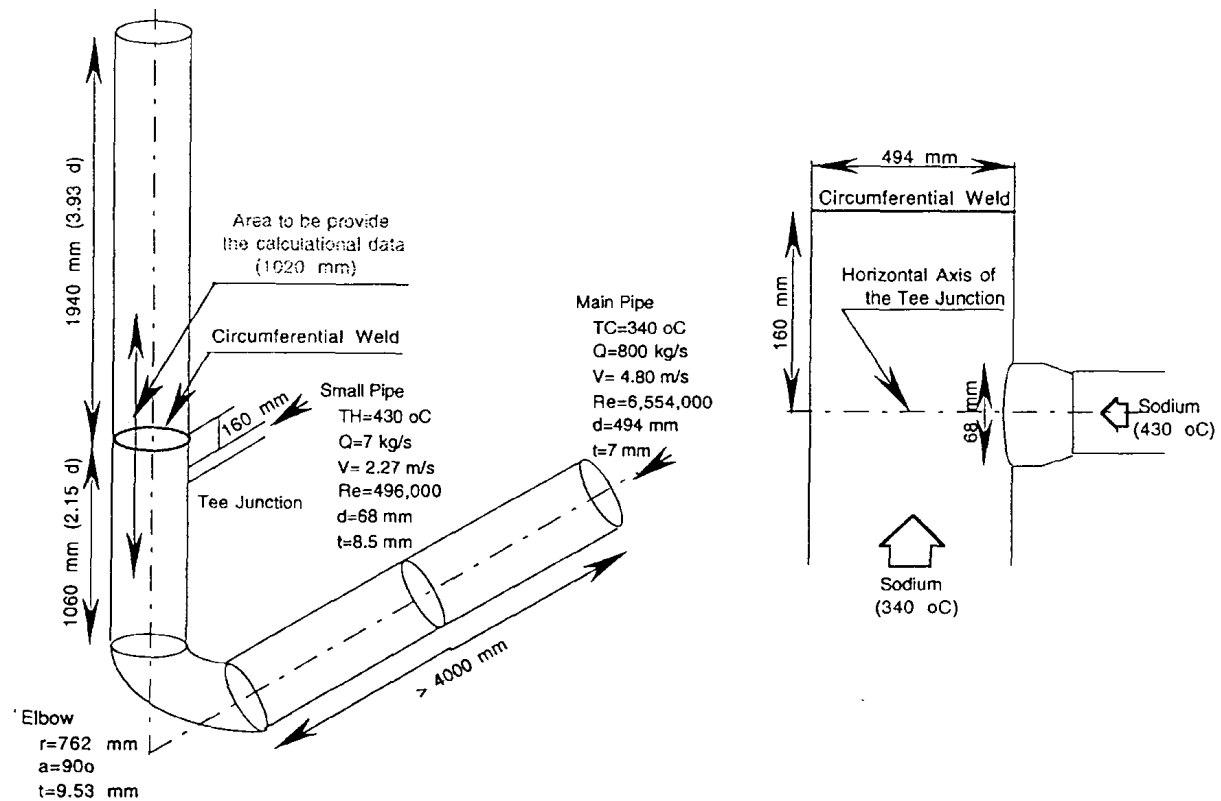


FIG. 16. Geometrical characteristics of the Phénix secondary circuit.

The main pipe in the tee junction area consists in a horizontal straight part, an elbow, and a vertical straight part where the tee junction is connected. In the straight part, the main pipe has the following characteristics:

- inner diameter = 494 mm;
- thickness = 7 mm.

The elbow is characterized by the following data:

- angle = 90°;
- radius = 762 mm;
- thickness = 9.35 mm.

Circumferential weld is located 160 mm downstream from the tee junction, in the vertical straight part of the main pipe.

The small pipe connected to the main pipe has the following, characteristics at the tee junction

- inner diameter = 68 mm;
- thickness = 8.5 mm.

During nominal operation, sodium at 340°C ($Q = 800$ kg/s) flows into the main pipe of the secondary circuit. A small pipe, connected with the tee junction to main pipe, discharges sodium 430°C ($Q = 7$ kg/s) into the main pipe. Two convergent flows at different temperatures ($\Delta t = 90^\circ\text{C}$) are therefore mixed in the tee junction area.

After the completion of thermohydraulic and thermal calculations, each participant to the benchmark exercise shall:

- characterize the mixing area, which means locate, define the dimensions of the mixing, area, define the part of the pipe subjected to the mixing phenomenon.
- provide isothermal lines (mean temperature) on the parts of the pipe as defined previously, etc.

2.2. Numerical analysis

2.2.1. Calculation and boundary conditions for the DINUS-3 code

Calculations by the DINUS-3 Code were carried out for a partially domain of the secondary circuit with a tee junction area shown in Fig. 17. The computational domain was totally 620 mm in axial direction.

Figure 18 shows the mesh arrangement for the DINUS-3 calculations. The domain was divided by non-uniform meshes in a three-dimensional cylindrical coordinate. Computational cells that contained no solid structure inside counted up to 177,570 ($r - \theta - z$; 22x77x115).

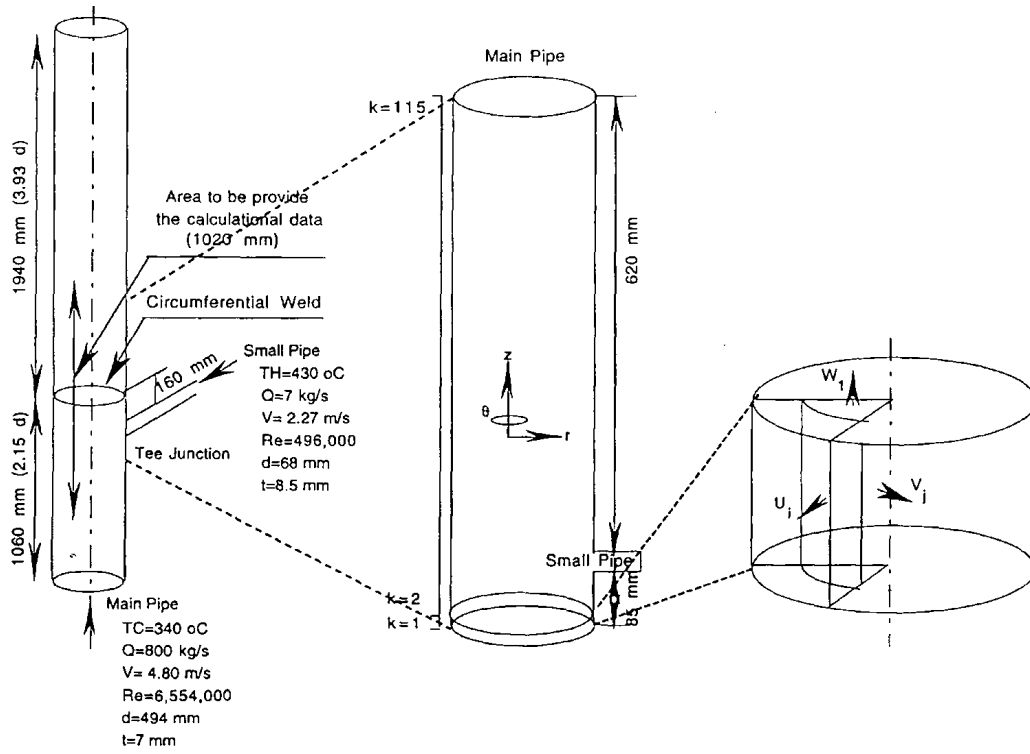


FIG. 17. Computational domain for the benchmark exercise.

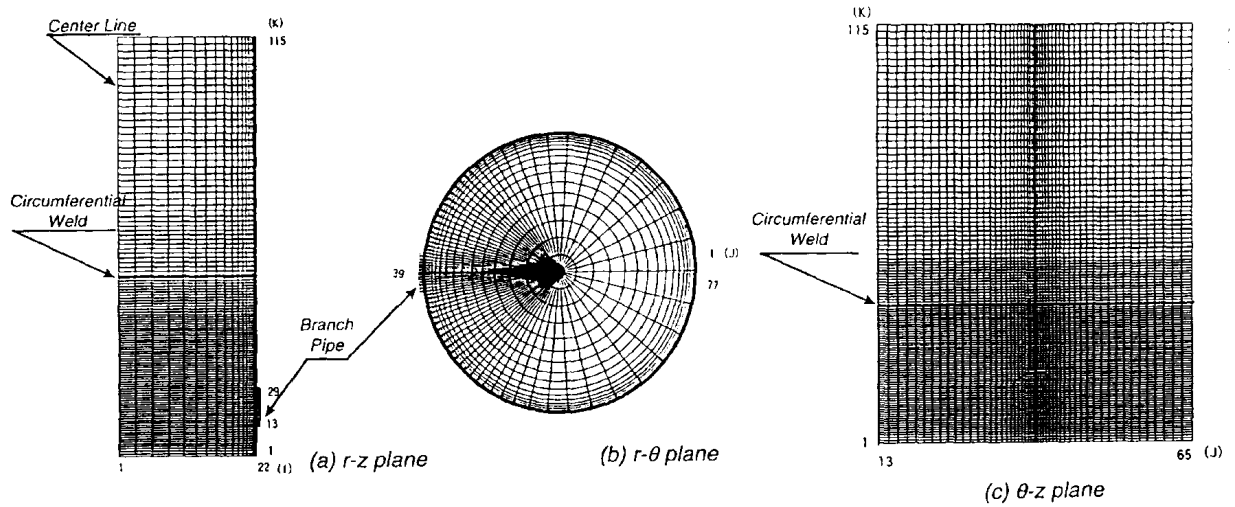


FIG. 18. Mesh arrangements for the benchmark exercise (DINUS-3).

The no-slip condition for the velocity components and three-dimensional thermal conduction for temperature using the BEMSET code were assumed on the solid surfaces of the main and small pipes.

Inlet boundary conditions were set for mean velocity components U , V and W simulating secondary flows and the Reynolds stresses using an out-pile experiment [25]. These distributions at the inlet boundary ($K = 1$) indicated in Figs. 19-21.

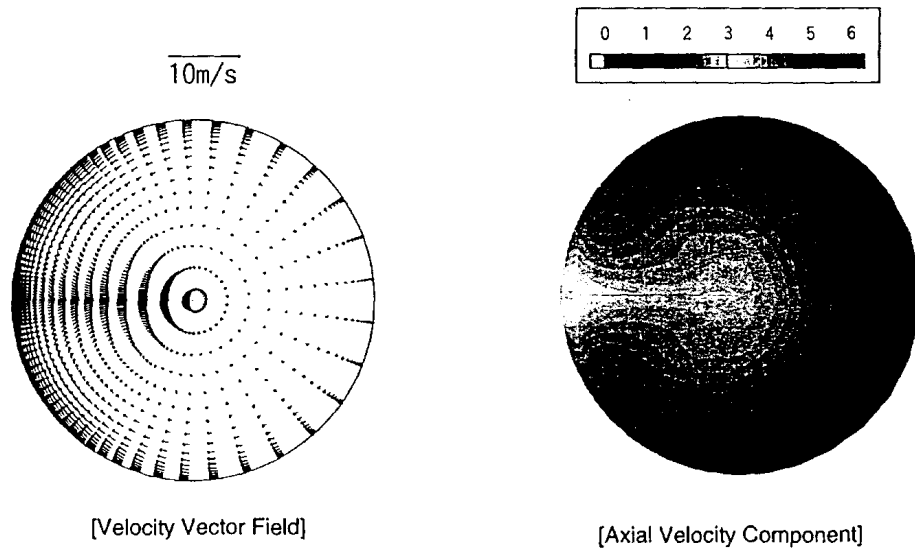


FIG. 19. Mean velocity distributions for the inlet boundary plane.

Given all thermohydraulics data at $t = 0$, a transient was calculated up to a steady-state level $[(\phi^{n+1} - \phi^n) / \phi^n = 10^{-4}]$ using a time marching methods; where ϕ represents three velocity components in the x-, y-, and z-directions, i.e., u, v, and w, respectively, and enthalpy h; n+1 indicates the advanced time step and n the current time step.

2.2.2. Computational results with the DINUS-3 code

Figure 22 shows calculated instantaneous vertical distributions ($J = 39$ and 46) for velocity and sodium temperature fields. Hot sodium from the small pipe mixed actively in the downstream region of the tee junction. Figure 23 gives calculated instantaneous circumferential distributions ($I = 20$) of velocity and temperature fields. As shown in Fig. 23, hot sodium from the small pipe rose into the cold sodium of the main pipe with thermally instabilities.

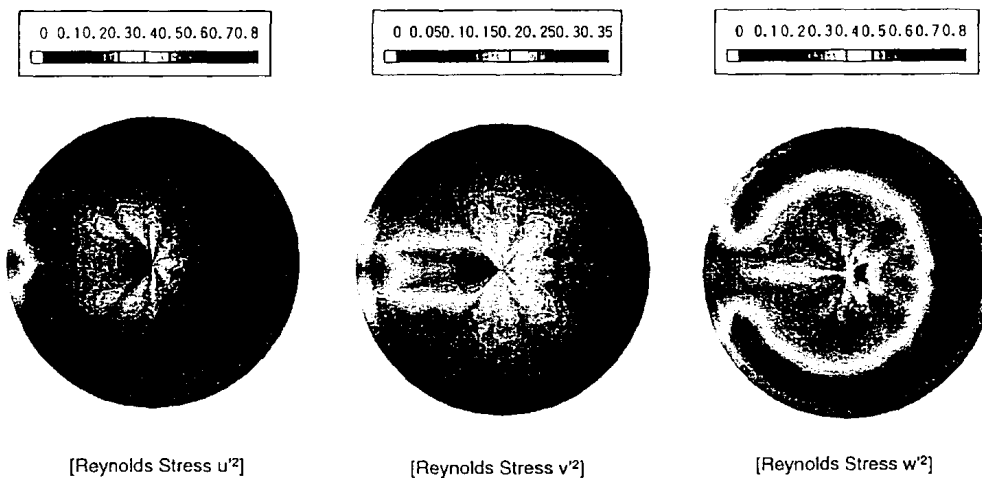


FIG. 20. Normal stress distributions for the inlet boundary plane.

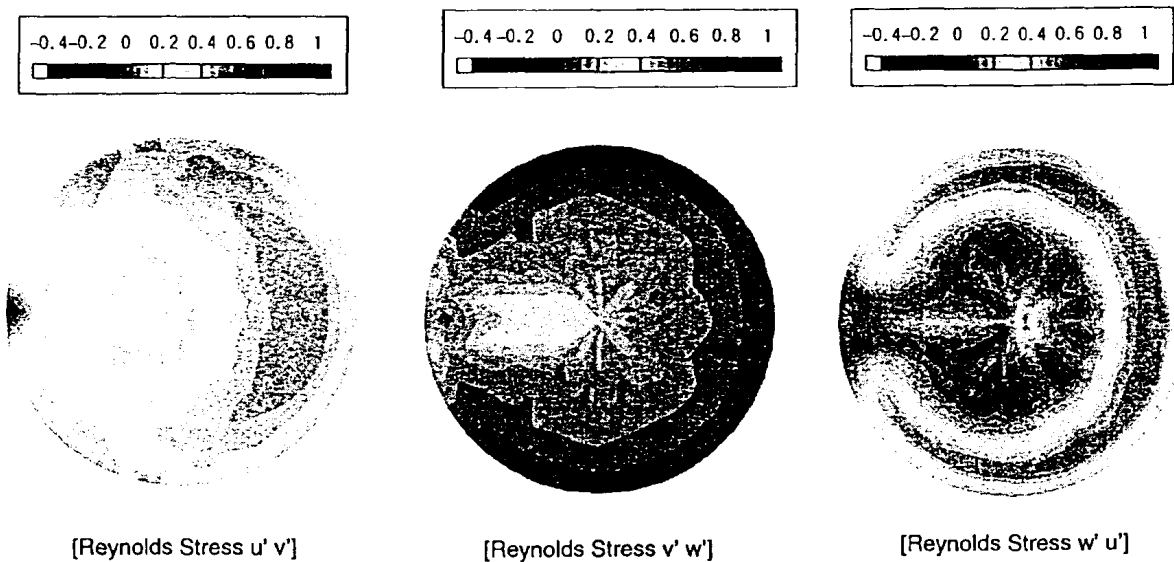


FIG. 21. Reynolds stress distributions for the inlet boundary plane.

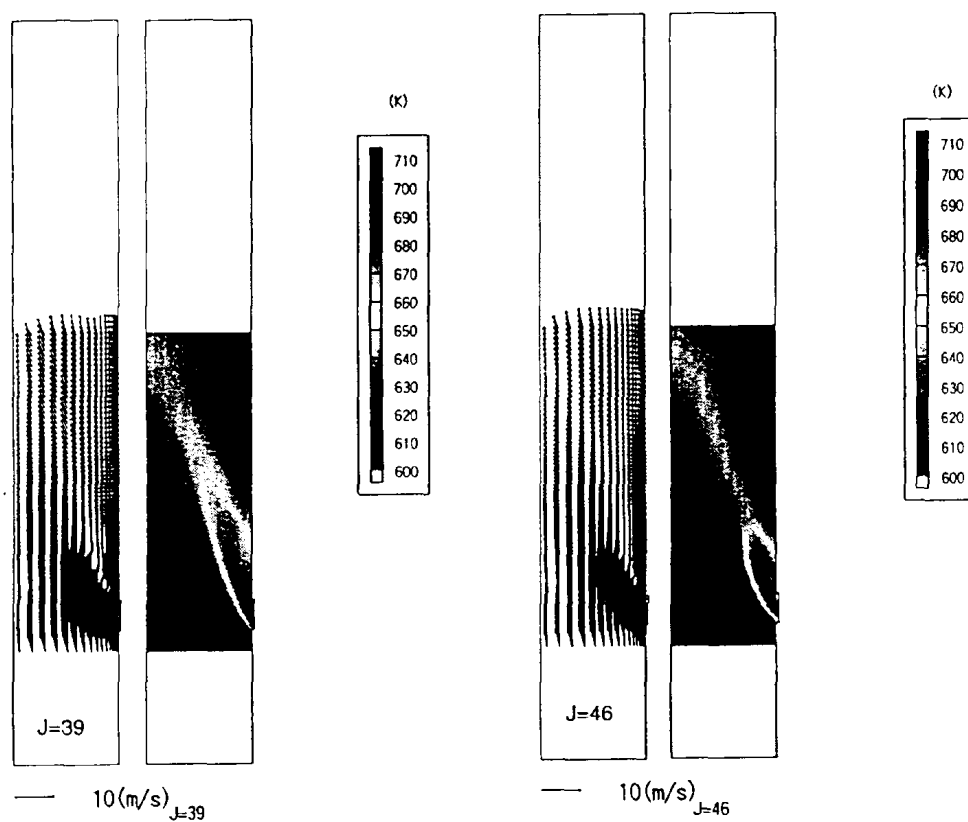
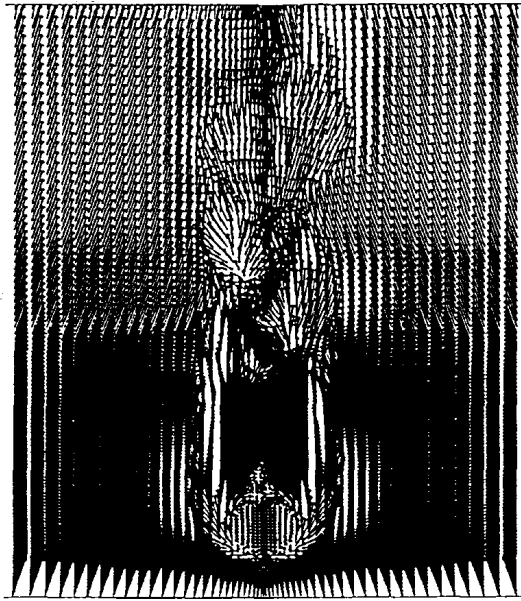
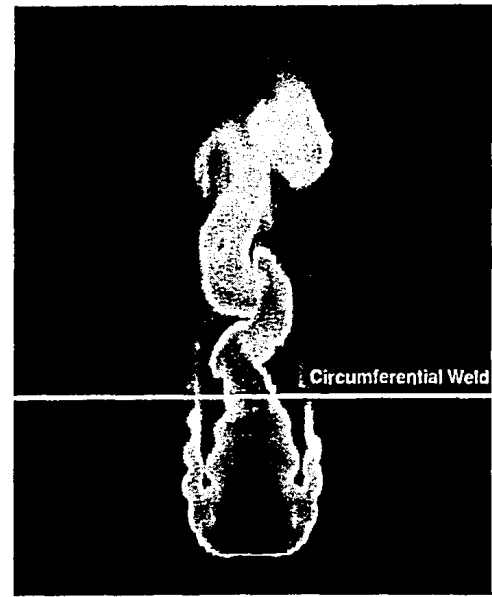


FIG. 22. Calculated instantaneous vertical distributions ($J = 39, 46$).



(a) Velocity Vector Field



(b) Sodium Temperature Field

FIG. 23. Calculated instantaneous circumferential distributions ($I = 20$).

2.2.3. Calculation and boundary conditions for the BEMSET code

Calculations with the BEMSET code were performed for the main pipe using the three-dimensional model shown in Fig. 24. Total number of boundary elements was 14 280. The following are material properties of AISI 304 stainless steel (grade: Z5 CN 18. 10.) used in the calculations:

Steel Density	: $\rho = 7975.5 - 0.432 \times T$,
Specific heat coefficient	: $C_p = 466.5 + 0.208 \times T$,
Thermal Conductivity	: $\lambda = 13.513 + 0.01509 \times T - 9.9983 \times 10^{-7} \times T^2$,
Mean Thermal Expansion	: $\alpha = 16.3 + 0.004 \times T$, and
Young's Modulus	: $E = 196.5 - 0.088 \times T$,

where T indicates metal temperature.

An explicit scheme was utilized in the every iterative procedure between the DINUS-3 and BEMSET calculations. Thereby the inner solid wall temperatures of the main pipe were evaluated mutually in the iteration and were used as temperature boundary conditions through interpolations for both codes at every time step. It is noted that the heat transfer coefficient between sodium and the pipe wall was set to that hold for turbulence flows. In a word, no the THENUS code was applied for the evaluation of non-stationary heat transfer phenomena in the benchmark calculation.

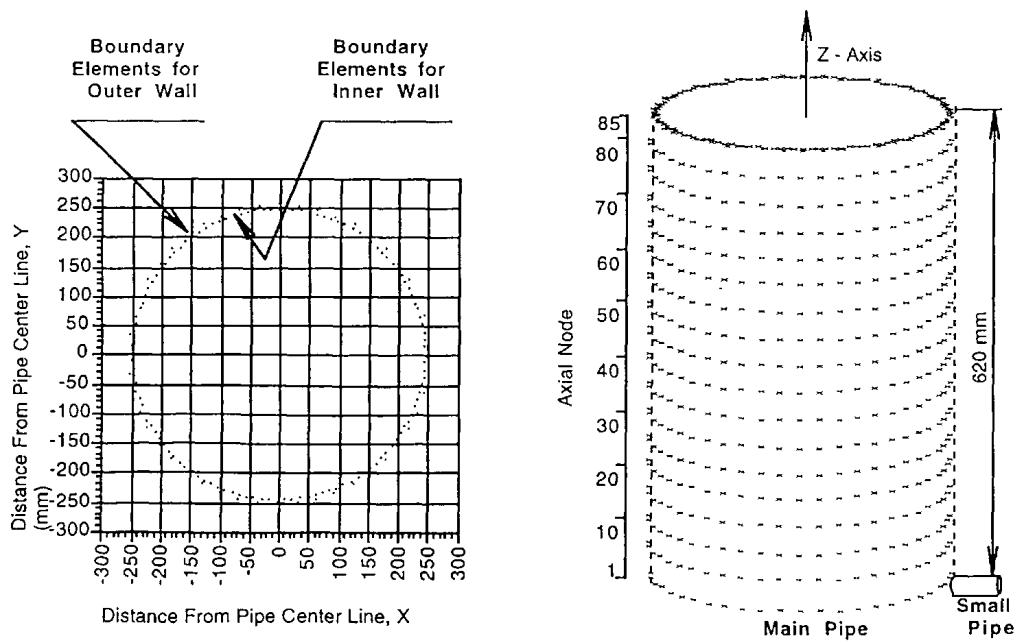


FIG. 24. Boundary element arrangement for the benchmark exercise (BEMSET).

2.2.4. Calculational results with the BEMSET code

Figure 25 compares calculated instantaneous circumferential temperature distributions of the sodium ($I = 20$) and the inner metal walls of the main pipe. As shown in the figure, thermally instabilities in sodium calculated by the DINUS-3 code was transmitted to the inner walls of the main pipe. Therefore, the downstream region of the tee junction is subjected to the stationary random thermal process due to the instabilities.

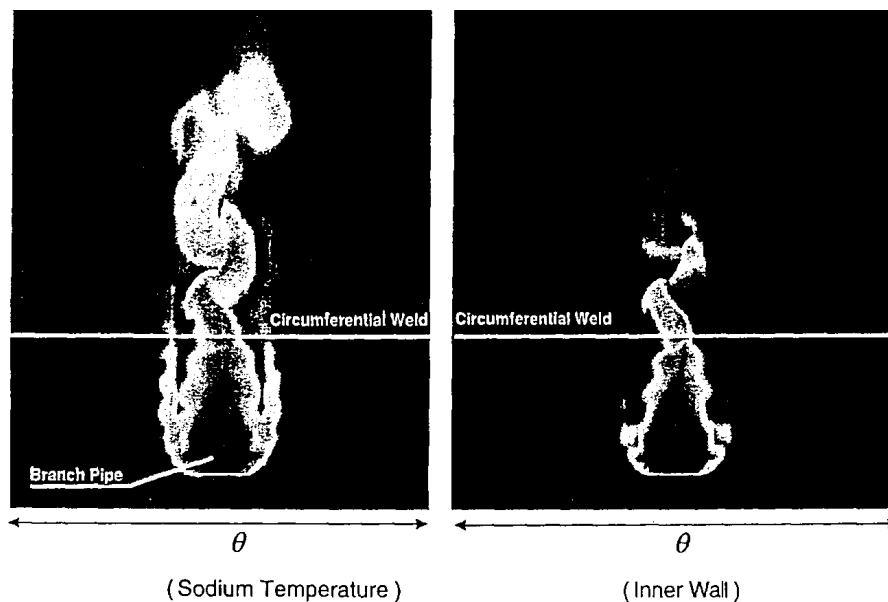


FIG. 25. Calculated instantaneous circumferential distributions of sodium and inner metal temperatures.

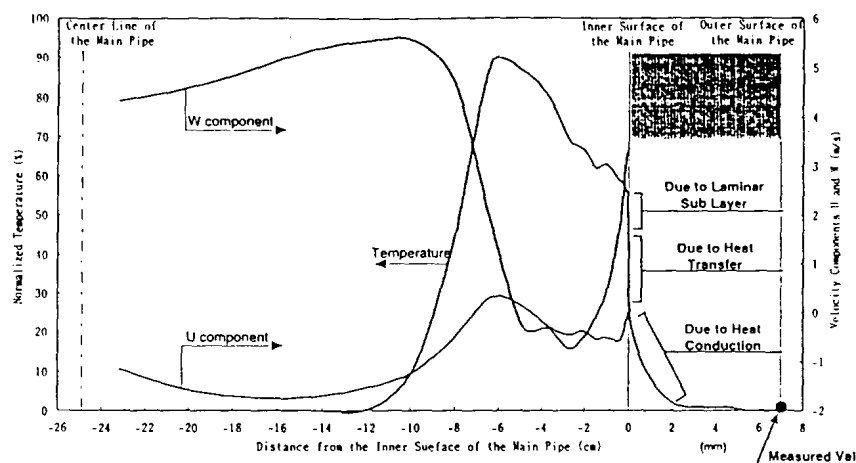


FIG. 26. Calculated radial temperature distributions at the T/C-5 position..

Figure 26 shows calculated radial distributions at the T/C-5 position (160 mm downstream and 100 mm circumference from the center line of the small pipe, on the circumferential weld line). As shown in the figure, the sodium temperature decreased drastically toward the inside from the fully turbulence region of the main pipe. This interpretation that the sodium temperature in the fully turbulence region were damped due to four effects; i.e., mixing by turbulence flows, passing through laminar sub-layer, non-linear transient heat transfer to the main pipe surface from sodium, and heat conduction in the main pipe. The outer metal temperature calculated by the BEMSET code agreed well with the measured value at the T/C-5 position.

3. CONCLUSIONS

Mathematical models of the four computer programs AQUA, DINUS-3, THEMIS and BEMSET developed at PNC, Japan and their validation results with a fundamental sodium experiment were presented for the evaluation of thermal striping phenomena, which are recognized as one of key unresolved issues from the standpoint of structural integrity of the in-vessel components of an LMFBR. These codes are utilized as an evaluation system of the phenomena with a organic combination.

Secondly, numerical results were indicated for the benchmark exercise on a tee junction of LMFR secondary circuit involving thermal striping phenomena using the two codes DINUS-3 and BEMSET, which are represented by a direct numerical simulation of turbulence flows and a boundary element analysis of structures, respectively. Then the calculated temperature on the outer metal surface of the main pipe was compared with the actual data measured at the T/C-5 position. The comparison showed good agreement of the calculation with the measurement.

REFERENCES

- [1] MURANATSU, T., NINOKATA, H., Intensity Evaluation of the Temperature Fluctuations Related to Thermal Striping Phenomena Using the Algebraic Stress Turbulence Model, Proc. ANS Winter Meeting, San Francisco, USA, pp. 156-162 (1991).

- [2] MURAMATSU, T., NINOKATA, H., Thermal Striping Temperature Fluctuation Analysis Using the Algebraic Stress Turbulence Model in Water and Sodium, JSME Int. Journal, Series II, Vol. 35. No. 4, pp. 486-496 (1992).
- [3] LEONARD, B.P., A Stable and Accurate Convective Modeling Procedure Based on Quadratic Upstream Interpolation, Comp. Methods in Appl. Mech. and Eng., Vol. 19, pp. 59 (1978).
- [4] CHAPMAN, M., FRAM-Nonlinear Damping Algorithms for the Continuity Equation, Comp. Phys., Vol. 44, pp. 323 (1981).
- [5] HARLOW, F.H., AMSDEN, A.A., A Numerical Fluid Dynamics Calculation Method for All Flow Speeds, Comp. Phys., Vol. 8, pp. 197 (1971).
- [6] MEIJERINK, J.A., VAN DER VORST, An Iterative Solution Method for Linear Systems of Which the Coefficient Matrix is a Symmetric M - Matrix, math. Comp., Vol. 31, pp. 148 (1977).
- [7] RODI, W., A New Algebraic Relation for Calculating the Reynolds Stress, ZAMM, Vol. 56, T219-221 (1976).
- [8] MURAMATSU, T., NINOKATA, H., Adaptive Control System Using the Fuzzy Theory for Transient Multi-Dimensional Thermohydraulics Calculations, Proc. Int. Conf. on Supercomputing in Nuclear Applications, Mito, Japan, pp. 69-73 (1990).
- [9] MURAMATSU, T., NINOKATA, H., Adaptive Control System Using the Fuzzy Theory for Transient Multi-Dimensional Thermohydraulics Calculations, int. Journal for Numerical Methods in Engineering, Vol. 37, pp. 3397-3415 (1994).
- [10] MURAMATSU, T., Frequency Evaluation of Temperature Fluctuations Related to Thermal Striping Phenomena Using a Direct numerical Simulation Code DINUS-3, Proc. ASME PVP Conf., Vol. 253, Colorado, USA (1993).
- [11] MURAMATSU, T., Investigation of Sodium Temperature Fluctuation Characteristics Related to Thermal Striping Phenomena Using the DINUS-3 Code, Proc. ASME PVP Conf., Vol. 270, Minnesota, USA (1994).
- [12] KAWAMURA, T., Direct Numerical Simulation of a Turbulent Inner Flow by Finite-Difference Methods, AIAA paper, pp. 1-10 (1985).
- [13] ROACHE, P.J., Computational Fluid Dynamics, Helmosa Publishers Inc., (1976).
- [14] MURAMATSU, T., Development of Elimination Method for Numerical Instabilities in Thermohydraulic Analysis Using Fuzzy Inference, Proc. JSME 3rd Design and System Conf., (1993) (in Japanese).
- [15] MURAMATSU, T., A Direct Simulation Monte Carlo Code THEN41S for the Evaluation of Nonstationary Heat Transfer Phenomena in LMFR Thermohydraulics, Proc. 8th IAHR Working Group Meeting on Advanced Nuclear Reactors Thermal Hydraulics (1995).
- [16] BIRD, G.A., Molecular Gas Dynamics, Oxford University Press (1976).
- [17] BELOTSEKOVSKII, O. M., YANITSKII, V.Y., J. Fluid Mech., Soviet Research, Vol. 7, No. 42 (1978).
- [18] NANBU, K., Derivation from Kac's Master Equation of the Stochastic Laws for Simulating Molecular Collisions, J. Phys. Soc. Japan, Vol. 52 (1983).
- [19] MURAMATSU, T., Thermal Response Evaluation of Austenitic Stainless Steels Due to Random Sodium Temperature Fluctuations Using BEMSET and DINUS-3 Codes, Proc. ASME PVP Conf., Vol. 337, Montreal, Canada (1996).
- [20] BREBBIA, C.A., TELLES, J.C.F., WROBEL, L.C., Boundary Element Techniques -Theory and Applications in Engineering, Springer Verlag (1984).
- [21] SHARP, S., CROUCH, S.L., Boundary Integral Methods for Thermoelasticity Problems, Trans. ASME, J. Applied Mechanics, Vol. 53, pp. 298-302, 1986.

- [22] MURAMATSU, T., Development of Analytical Model for Evaluating Temperature Fluctuation in Coolant (XI), Validation of the Evaluation Model for Thermally Fluid-Structure Interaction Phenomena, PNC Technical Report, TN9410 97-039 (1997) (in Japanese).
- [23] MURAMATSU, T., Numerical Analysis of Non-Stationary Thermally Response Characteristics for a Fluid-Structure Interaction System, Proc. ASME PVP Conf., San Diego, USA (1998).
- [24] MURAMATSU, T., IAEA Coordinated Research Program on Harmonization and Validation of Fast Reactor Thermomechanical and Thermohydraulic Codes Using Experimental Data (1), Thermohydraulic Benchmark Analysis on High-Cycle Thermal Fatigue Events Occurred at French Fast Breeder Reactor Phenix, PNC Technical Report, TN9410 97-058 (1997) (in Japanese).
- [25] SUDOU, K., TAKAMI, T. AND YANO, K., Turbulent Flow in a Circular-Sectioned 90° Bend, JSME Int. Journal, Vol. 58, No. 548 (1992) (in Japanese).

RECENT ACTIVITIES RELATED TO THERMO-MECHANICAL FATIGUE, CREEP AND FRACTURE MECHANICS IN KOREA NUCLEAR FIELDS

H.-Y. LEE, J.-B. KIM, B. YOO

Korea Atomic Energy Research Institute, Republic of Korea

Y.Y.-W. PARK

Korea Institute of Nuclear Safety, Republic of Korea

Abstract. In this study, recent activities and achievements of researches and developments related to thermo-mechanical fatigue, high temperature creep and fracture mechanics in the fields of Korean nuclear industry were surveyed and summarized.

1. INTRODUCTION

In nuclear power plants, rapid heating, cooling and high temperature hold periods has produced high stress and strain so that the components of plants may be damaged due to thermo-mechanical fatigue, fracture, creep, and creep-fatigue interaction behaviors. When cracks are present in components operated at high temperature, it is of important concern for safe and reliable operation to predict crack growth rates under fatigue loading caused by startup, steady state and shutdown operation procedures. In general, a crack initiates from the defects, propagates, and finally leads to catastrophic failure. Therefore, it is of concern to predict crack initiation and to evaluate crack growth behavior precisely under various operating conditions to assure structural integrity of nuclear power plant components.

2. THERMO-MECHANICAL FATIGUE, CREEP AND FRACTURE MECHANICS

2.1. Plant life time extension program using fatigue and fracture mechanics technologies

The KEPCO (Korea Electric Power Corporation) has been conducting a feasibility study regarding Kori unit 1, which has been in service since 1978, and thirteen major components were selected by the systematic screening of systems, structures, and components SCs) for technical evaluation. As an integral part of the project, the fatigue lives and aging mechanisms of major components were evaluated. The remaining fatigue lives of the major components were evaluated using simple calculation procedures and detailed fatigue cycle counting. The result showed that, for thirteen major components, there were sufficient fatigue margins for extended operations beyond the 30 year licensed period.

Through the feasibility study, the potential aging mechanisms of RPV, which were classified as being the most important components of plant life extension, were identified and evaluated. The residual life evaluation of RPV revealed that from the fatigue point of view, RPV can be operated over 60 years. However, irradiation embrittlement of the belt-line welded region was identified as the potentially life-limiting aging mechanism of RPV. The weld metal of the Kori-1 belt-line region showed low USE, that is, below 50 fl-lbs, since the first surveillance test. It was the characteristics of the Linde 80 welds containing large amounts of copper and nickel.

Detailed fracture mechanics analysis was done in accordance with 10CFR50 App. G&H to verify the safety of RPV. It was shown that, despite the low USE, the RPV could maintain its integrity over a 40 year operating time. In the analysis, another aspect of RPV integrity, the

PTS criteria, was also evaluated. RT_{PTS} was calculated according to the methods given in the PTS rule and Regulatory Guides. PTS screening criteria for the circumferential weld was projected to exceed at 27.4 EFPY (or 34 operating years), well ahead of the 40 operating years. The necessity of a plant-specific PTS analysis was well recognized by KEPCO during the feasibility study. As a result, the PTS project was initiated at the beginning of 1997 and scheduled to be completed in 2 years. The results of the PTS analysis will be available soon and will be incorporated into the license renewal application documents of Kori-1.

A direct method to determine the fracture toughness transition curve for evaluating the structural integrity of the embrittled pressure vessel is introduced using the Weibull probabilistic distribution characteristics of cleavage fracture toughness. It is the theoretical base of the ASTM draft 13 and may replace the conventional method of the ASME Section XI, Appendix G, which is based on the K_{IR} reference curve and RT_{NDT} shift. The cleavage fracture toughness, K_{JC} , in the transition region shows a large scatter band as well as an apparent size dependency. Using relatively small-sized fracture toughness specimens, called pre-cracked Charpy, available in normal surveillance capsules, a direct method of measuring fracture toughness is underway.

A fracture mechanics analysis has been performed to evaluate the consequences of primary water stress corrosion cracking (PWSCC) associated with Alloy 600 RV Head penetrations in Korean nuclear power plants. The crack growth mechanism of the penetration tubes is due to the primary water stress corrosion cracking, which is mainly related to the stress and temperature. For the parametric evaluation, it is assumed that an ID-initiated axial crack propagates through the penetration tube near the J-groove weld. Although unlikely to occur, it is further assumed that a circumferential crack exists potentially. This study presents the method of evaluation for the axial surface crack, axial through-wall crack, circumferential surface crack, and circumferential through-wall crack.

Development of nondestructive evaluation techniques, especially for monitoring and measuring neutron irradiation damage (embrittlement) and the fracture toughness of reactor pressure vessels has been a subject of considerable interest for years, with relation to the safe operation and life extension of a reactor. Recently, a mechanical properties measurement using Barkhausen noise analysis was conducted. The results of each evaluation on the microstructure and the mechanical properties were interpreted together to explore the relationship between microstructure and mechanical parameters.

2.2. Thermo-mechanical fatigue and creep damage

The operation data accumulated by the fatigue monitoring system can also be used as a structural integrity assessment procedure as well as an important reference data for the development and design of the next nuclear power plant. A fatigue monitoring program, K-FAMS (KAERI-Fatigue Monitoring System) [1] that has the capability of computing the real time transient fatigue usage factor was developed to provide important information for the structural reliability, the safe operation and the optimal time of inspection/maintenance of the nuclear power plant components and it was applied to the pressurizer surge line of the YGN unit 1. The developed program includes the stress calculation module with consideration of both thermal and mechanical property changes according to the measured temperature variation and the fatigue analysis module as well as stress intensity factor calculation module by way of Green's function approach.

While K-FAMS was developed to be used in the PVsTR operating temperature range, KHIC (Korea Heavy Industry Co.) is now developing hardware and software systems [2] for real time on-line monitoring to monitor the operating data and to calculate the accumulated damage caused by start-up and shutdown as well as unexpected loading conditions. The utility, KEPCO, requires to keep track of steam temperature, pressure and high temperature strain of components while power plant is operating and the high temperature and pressure environment induce damage by creep, fatigue, and creep-fatigue interaction. Thermal stresses can be calculated using Green's function method with measured temperature, flow rate, and pressure, and stress redistribution due to creep behavior can be calculated using creep equation. Linear summation of fatigue damage (Miner's rule) to each stress cycle and linear summation of each creep damage (Robinson's rule) are used for damage evaluation and the damage envelop curve from ASME code Subsection NH is used to judge the structural integrity.

A relational fatigue strength database system [3] for power plant structural materials was developed on a personal computer using database management system FoxPro. The database system contains 3018 S-N curves, 311 ϵ -N curves and 809 da/dN- ΔK curves including 280 fracture toughness data according to ASTM standards. Extensive experimental strain-life curves data on 116 steels, 16 aluminum alloys and 6 titanium alloys were included and a simple fatigue strength assessment system utilizing fatigue expert system and fatigue strength database was developed for the prediction of crack initiation life of materials for the moderate range of operating temperatures.

For the improvement of experimental techniques to understand the high temperature fatigue behavior, a new experimental system using remote measurement system (RMS) with an image processing technique [4] was applied for observing the growth behavior of a small surface fatigue crack in a type of 304 stainless steel at elevated temperature and the measurement error was within 0.8%. This system can measure a surface crack down to 30 μm at elevated temperature and this method is more convenient and may reduce the testing time in comparison to the conventional replication method. From the surface crack propagation test for SS304, it was observed that the growth rates of surface fatigue crack at elevated temperatures were faster than those at room temperature.

With industrial development, welding becomes popular to join two parts due to its relatively easy process among several joining methods like bolting, etc. One aspect which is of particular concern is that a significant proportion of weld failures have occurred long before the design life of the plant has been reached. The reason for this lies in the manufacturing process and the design processes which deal with the mechanical properties of weld metal as basically the same as parent metal. Many of welded structures cannot be inspected or repaired in a nuclear power plant and premature weld failures could occur. Thus, it is very important to understand the behavior of a welded zone for both original state and degraded state at the later stage of plant life, then to improve the welding process and design procedures concerning welded parts. In general, a crack initiates from the defects, propagates, and finally leads to failure. And there is thermal plastic strain due to welding heat. As a result, high residual stress is distributed in the weld. It leads to a reduction in fracture and fatigue strengths of welded joints. The effects of residual stress and its redistribution in a weld on the fatigue propagation were investigated [5]. Fatigue tests with structural material of SS330 were conducted using center notched specimens machined from welded plates. The residual stress and its redistribution during crack growth were measured by a magnetizing stress indicator and the hole drilling method which reduce difficulties in accurate measurement of residual stresses. It

was observed that the tensile to compressive residual stress transition point moved with the same direction of crack propagation and the residual stress of the weld was affected and redistributed by magnitude of external loading, number of cycles, and crack propagation.

The replication technique has been applied to a welded 0.5Cr-0.5Mo-0.25V steel to evaluate the creep damage of main steam pipe on fossil and nuclear power plants [6]. Numerical simulations for estimating the creep damage in the welded joints are also performed and the results show that the creep degradation of the material can be well described by means of 'A' parameter which is the ratio of the number of cavitating grain boundaries intersecting the line and total number of grain boundaries intersecting a line. Kachanov-Rabotove equation incorporating primary creep effects is confirmed to be suitable to simulated the creep behavior of welded joint in 0.5Cr-0.5Mo-0.25V steel and the replication technique has proved to be a suitable method for non-destructive detection of creep damage.

Besides, KIMM (Korea Institute of Machinery and Materials) developed a high temperature turbine blade material and manufacturing process for it to improve the efficiency and reliability using both fluid and structural engineering technologies while KSRI (Korea Standards Research Institute) has been performing many activities of high temperature creep-fatigue analysis and experiments fields. KAERI (Korea Atomic Energy Research Institute) has concentrated on developing structural steels for nuclear application [7] by performing various tests including fatigue tests with/without aging effects. And a supplementary program utilizing Chaboche viscoplastic constitutive equation was implemented into ABAQUS user program with a general midpoint integration method. The solution of a nonlinear system of algebraic equations arising from time discretization with Newton's method is determined using the line search technique and the strategy to control the time increment size for the improvement of the accuracy of the numerical integration is proposed [8,9]. For the evaluation due to creep fatigue interaction, damage evolution equation is now under development to improve the structural integrity assessment methodology in KAERI and KAIST. Another new damage function based on a model for the creep fatigue life prediction in terms of nucleation and growth of grain boundary cavities is proposed by Nam [10]. This damage function is a combination of the terms related to the cavitation damage in the life prediction equation and is generally applicable to the materials in which failure is controlled by the grain boundary cavitation damage. Using this damage function, normalized Coffin-Manson plots to make the master curve is presented to improve the reliability and the economy of high temperature structure design.

2.3 Fracture mechanics

The YGN unit 3 was the first NPP in Korea in which the leak-before-break concept was applied from the design stage. There are four piping systems designed with the LBB concept: primary circuit, pressurizer surge line, safety injection and safety shut down lines. Since then, research activities on LBB have become a hot issue of fracture mechanics in Korean nuclear industries. Utility and engineering companies have tried to extend the application of the LBB concept to piping systems other than those already accepted by regulation. For instance, LBB is being considered for the Main Steam Line (MSL) piping inside the containment to achieve cost effectiveness and safety improvement in the Korean Next Generation Reactor (KNGR). To apply the LBB concept to the KNGR, many kinds of Leak Detection Systems (LDS) are being investigated and evaluation techniques are under development.

In order to reduce the computing time and the man-power required for the application of LBB during the design process, a Piping Evaluation Diagram (PED), which will be able to account for the variation of material properties, is being developed. For the implementation of LBB procedure in the design of nuclear power plant component like reactor vessel and pipe, fracture mechanics technique is essential. Elastic and elastic-plastic fracture mechanics analyses have been widely used in the nuclear industry over the years to assess the integrity of a variety of components with known or postulated defects. However, the detail analyses procedures have not yet been systemized because of the complicity of the procedures.

A simplified structural analysis method [11] using elastoplastic fracture mechanics and conventional piping analysis program was developed for the demonstration of LBB for piping systems of a nuclear power plant. This method takes count of a significant change in the flexibility of the region containing the large leakage crack which influences the determination of resulting loads for the small diameter pipe. In view of LBB application, the resulting loads can be significantly reduced and this gives more beneficial results as compared to the case with load neglecting cracked pipe behavior.

New Z-factors for both nuclear ferritic and austenitic steels are proposed to improve the z-factor method in ASME code Section XI's recommendations for the estimation of a surface crack in nuclear pipings [12]. Results from 48 experiments show agreements with measured Z-factors.

Stress intensity factor K is the most widely used fracture parameter employed in the linear elastic fracture mechanics and the convenient stress intensity calculation method using BEM was proposed [13]. An approximate weight function technique using indirect boundary integral equation method was presented and applied to the analysis of a hollow cylinder with circumferential or radial cracks. An explicit closed form stress intensity factor solution was derived. The calculation procedure of stress intensity factor using one closed form solution is very simple and straightforward and the accuracy of the proposed method was confirmed from several analyses.

The efficient numerical method of stress intensity calculation against thermal transient loading was proposed [14] using Green's function concept and Duhamel's theorem. The Green's function of proposed method represents the change in stress intensity factor for the cracked body subjected to a Heaviside step function of the boundary temperature. The stress intensity factor obtained from the proposed method has shown agreement with those evaluated by the finite element method, which is time consuming, and costly compared to the proposed method.

An alternative to the stress intensity factor, which is valid for elastic dominant problems, the use of J , which is path independent contour integral for elastic and nonlinear elastic materials introduced by Rice, is popular in elastic-plastic deformation fields even though it is path-dependent in general elastic-plastic or viscoplastic materials. Kim [15] investigated the utility of the rate forms of the Kishimoto's modified J integral and Blackburn's modified J integral, which were modified to overcome the path dependency of J integral in inelastic deformation fields, to show usefulness of rate forms of modified J integrals to predict the dynamic crack growth at elevated temperature by performing experiments and finite element analysis with Alloy 718.

In the high temperature components like turbine, boiler and LMFBR structures, it is often difficult to predict creep crack growth due to the complicated material behavior under high temperature and environment. Thus, many researches in both analytical and experimental ways have been performed, but there is no one solid procedure or method yet to analyze creep crack initiation and growth behavior, which can be, applied to the operating power plant components. Guideline for creep crack growth (CCG) test at elevated temperatures were set up in the collaborative work of KSRI (Korea) and NRIM (Japan) [16]. From the test with 306 type stainless steel following a unified evaluation procedure, it was obtained that CCG rate is dependent on both temperature and loading condition and can be characterized with creep fracture mechanism. It is revealed that the growth rate of creep crack with wedge type intergranular fracture is faster than that with transgranular fracture and this difference in crack growth rate between these fracture modes are attributed to the effect of creep ductility.

A new C_t estimation equation [17], which is known as one of good creep fracture parameters modified from J integral, was proposed which considers the effect of load increasing time on crack driving force during the succeeding load hold period for the nuclear power plant turbine rotor material, 1Cr-1Mo-0.25V steel. The main cause of the initial transient crack growth behavior turned out to be the difference of crack growth mechanisms caused by crack-tip oxidation, and the data scatter band was decreased with using the proposed C_t estimation equation.

4. CONCLUSIONS

Recent activities related to thermo-mechanical fatigue, high temperature creep and fracture mechanics in the Korean nuclear industry were surveyed and summarized as follows:

- Plant life time extension program for Kori unit 1 based upon fatigue and fracture mechanics
- Fatigue monitoring systems development for both PWR operating temperature and high temperature, and fatigue strength database development using expert system
- Fatigue crack propagation investigation for nuclear power plant steels using experimental techniques such as replication method and remote measurement system
- Creep damage evaluation method using new damage function and viscoplasticity finite element analysis program
- LBB methodology, application and new development
- Development of convenient methods of calculating stress intensity factors for thermal loadings
- Analysis of time dependent high temperature crack growth using modified J integral
- Creep crack growth test guidelines and the development of new C_t equation
- Some activities of national research institutes (KIMM, KSRI, KAERI and KAIST) related to thermo-mechanical fatigue, creep and fracture mechanics.

To design the safety components for both LWR and LMFBR and to maintain the structural integrity of structures in very high reliability are key concerns of nuclear safety since the Korean government affirmed that nuclear safety should take the first priority in the development of nuclear energy. In this regard, fatigue and fracture mechanics play an important role in assuring the overall safety of LWR nuclear power plant components as well as LMFBR. Even though activities of fracture mechanics for LWRs have been conducted for

reactor vessel and pipings, much more effort should be invested in understanding aging mechanism of nuclear components, the probabilistic safety assessment, NDE, thermo-mechanical fatigue, fracture mechanics, creep fatigue and creep fracture mechanics.

Since service conditions for structures at elevated temperatures in KALIMER are severe enough to cause inelastic deformation due to creep and plasticity, utmost efforts should be made in developing and improving high temperature structural analysis techniques concerning creep, fatigue, creep-fatigue interaction and thermo-mechanical fatigue damage evaluation.

REFERENCES

- [1] YOO, B., Development of Fatigue Monitoring System in Nuclear Power Plants, KAERI/RR-1307/93, Korea, Republic of (1994).
- [2] KIM, H.J., et al., On-line Monitoring System for Damage Assessment of Components in Boller, Proc. Of the KSME 1997 Fall Annual Meeting A, p. 1030, (1997).
- [3] PARK, J.H., Strength Assessment - Implementation of Fatigue Strength Database and Fatigue Expert System, Ph.D. Thesis in Dept. of Mech. Engr., KAIST, Korea, Republic of (1995)
- [4] NAHM, S.H. et. al., Measurement of Elevated Temperature Surface Fatigue Cracks by Remote Measurement System, Proc. Asian Pacific Conf. Fracture and Strength '96, pp 677-682, Korea, Republic of (1996).
- [5] LEE, Y.B., et al., A Study of Fatigue Behavior Considering Effects of Redistributing Residual Stress and Crack Closure in SS330 Weldment, Proc. Asian Pacific. Conf. Fracture and Strength '96, pp 349-354, Korea, Republic of (1996).
- [6] KIM, K.Y., SONG, G.W., The Creep Damage Assessment of High Pressure Steam Pipe Exposed at High Temperature in Fossil Power Plants, Proc. Asian Pacific. Conf. Fracture and Strength '96, pp 399-404, Korea, Republic of (1996).
- [7] Advanced Nuclear Materials Development, KAERI/RR-1519/94, Korea, Republic of (1995).
- [8] Creep Fatigue Damage Evaluation of Y-Piece Structure in LMFBR Reactor with Chaboche Viscoplastic Constitutive Equations, Proc. Asian Pacific Conference for Fracture and Strength '96, pp 819-824, Korea, Republic of (1996).
- [9] YOUN, S.S. et. al., Development of Implicit Integration Procedure for Viscoplastic Model, Trans. KSME, submitted, (1998).
- [10] NAM, S.W., YOON, Y.C., CHOI, B.G., The Normalized Coffin-Manson Plot in Terms of a New Damage Function Based on Grain Boundary Cavitation under Creep-Fatigue Condition, Proc. 4th Symp. Material Degradation and Life Prediction, pp 1-14, Korea, Republic of (1994).
- [11] YOU, Y.J., et. al, Development of Simplified Structural Analysis Methodology Using Elastic-Plastic Fracture Mechanics, KAERI/RR-1243/93, Korea, Republic of (1993)
- [12] CHOI, Y.H., Development of New Z-Factor to Evaluate Circumferential Surface Crack Behavior in Nuclear Piping, et. al, Proc. Asian Pacific. Conf. Fracture and Strength '96, pp 907-912, Korea, Republic of (1996).
- [13] LEE, H.Y. et al., Stress Intensity Factor Solution for Radial and Circumferential Cracks in Hollow Cylinders Using Indirect Boundary Integral, Int. J. Pres.Ves. & Piping 69, pp 45-52 (1996).
- [14] KIM, Y.W., LEE, J.H., YOO, B., An Analysis of Stress Intensity Factor for Thermal Transient Problems Based on Green's Function, Engr. Frac. Mech., Vol.49, No.3, pp 393-403 (1994).

- [15] KIM, K.S., Time Dependent Crack Growth Characterization Using Rate Integrals,. Proc. 4th Symp. Material Degradation and Life Prediction, pp 102-117, Korea, Republic of (1994).
- [16] HUH, Y.H., KIM, J.J., TABUCHI, M., YAGI, K.K., Creep Crack Growth Behavior of Stainless Steel 316 at Elevated Temperatures, Trans. KSME, Vol. 19, No. 11, pp 2806-2816, (1995).
- [17] YOUN, K.B., Development of General Model for Predicting Crack Growth Rates at High Temperature, KRISS0-94-040-IR, Korea, Republic of (1994).

TEE-JUNCTION OF LMFR SECONDARY CIRCUIT INVOLVING THERMAL, THERMOMECHANICAL AND FRACTURE MECHANICS ASSESSMENT ON A STRIPING PHENOMENON

H.-Y. LEE, J.-B. KIM, B. YOO
Korea Atomic Energy Research Institute,
Republic of Korea

Abstract. This paper presents the thermomechanical and fracture mechanics evaluation procedure of thermal striping damage on the secondary piping of LMFR using Green's function method and standard FEM. The thermohydraulic loading conditions used in the present analysis are simplified sinusoidal thermal loads and the random type thermal loads. The thermomechanical fatigue damage was evaluated according to ASME code subsection NH. The results of fatigue analysis for the sinusoidal and random type load cases showed that fatigue failure would occur at a welded joint during 90 000 hours of operation. The assessment for the fracture behavior of the welded joint showed that the crack would be initiated at an early stage of the operation. The fatigue crack was evaluated to propagate up to 5 mm along the thickness direction during the first 940.7 and 42 698.9 hours of operation for the sinusoidal and the random loading cases, respectively. However, it was evaluated that the crack would be arrested because of the low level of the primary stresses. The fatigue and crack propagation analyses for the random type loads were performed by Green's function method.

1. INTRODUCTION

The thermal striping phenomenon, due to imperfect mixing of sodium streams at different temperatures is one of the most significant problems in liquid metal fast reactors (LMFRs). The thermal fluctuations in LMFRs were caused by a cyclic movement of temperature distribution, which usually occurred in the lower part of the hot pool inside the reactor vessel, and caused by mixing and fluctuating of the two flows at different temperatures. These types of thermal fluctuations induced the cracks in reality such as the crack in the expansion tank of Phénix secondary loops, the crack at tee-junction of Superphenix [1].

In this study, an efficient numerical method based on Green's function concept and Duhamel's integral theorem was used to calculate thermal strains and the SIFs (stress intensity factors) to evaluate fatigue damage and crack propagation under thermal striping loads for the tee-junction of secondary piping system.

Compared with the transient finite element method, the present method is confirmed to be effective in view of computational aspect without sacrificing the solution accuracy.

2. DESCRIPTION OF BENCHMARK PROBLEM

The present technical problem deals with the mixing of two flows at different temperatures in the secondary circuit of the French Phénix during normal operation [2]. The sodium in the small pipe flows into the main pipe of the secondary circuit as shown in Fig. 1. A small pipe, connected with a tee junction to the main pipe discharges sodium at 430°C into the main pipe. Two convergent flows, at different temperatures ($\Delta T = 90^\circ\text{C}$) are mixed in the tee junction area. There is a circumferential weld at 160 mm upstream from the horizontal axis of the tee-junction. The internal pressure of the main pipe is 2.2 bar. The circumferential weld on the main pipe is as-welded condition at both inner and outer surfaces. The thermal striping damage is to be evaluated after the reactor has operated for 90 000 hours. No creep is taken into account due to the low temperature level.

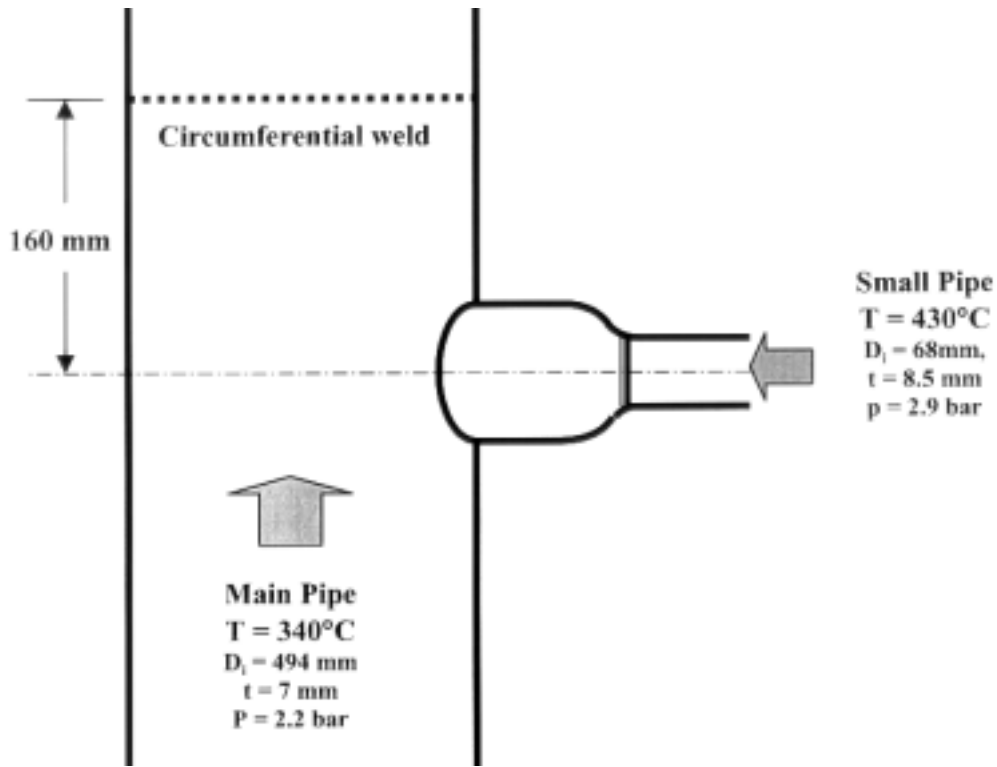


FIG. 1. Tee-junction of Phénix secondary piping.

3. THERMOMECHANICAL ANALYSIS

3.1. Description of computer code

In the present analysis, the ABAQUS version 5.7 [3] was used for heat transfer, thermal stress and fracture mechanics analyses. In addition, Fortran programs were made to carry out thermal stress and fracture analyses using Green's function method and damage evaluation according to the design code. In this study, ASME section III subsection NH was used for fatigue damage evaluation.

As for the constitutive model, elastic analysis was performed mostly. However, elastic-plastic analysis using the “combined model” was also applied to estimate the amount of plasticity. The “combined model” without creep effect implemented in ABAQUS version 5.7 was used.

3.2. Green's function approach

The Green's function is usually defined as the response of a system to a standard step or impulse input. The important property of the Green's function is that, when suitably defined, it contains all essential information of the system. Based on the Green's function concept and the Duhamel's theorem, the change of thermal stresses at time τ due to a small change of the temperature boundary at time τ can be expressed as follows

$$\Delta\sigma_{ij} = G_{\sigma_{ij}}(t - \tau) \Delta\Theta(\tau) \quad (1)$$

where the stress Green's function, $G_{\sigma_{ij}}(t - \tau)$ can be determined using unit step thermal loading.

Equation (1) can be rewritten as

$$\sigma_{ij}(t) = \int_{t-t_d}^t G_{\sigma_{ij}}(t - \tau) \frac{d\Theta}{d\tau} d\tau + G_{\sigma_{ij}}(t_d) \{\Theta(t - t_d) - \Theta(0)\} \quad (2)$$

where

$$\tau_i = \tau_{i-1} + \Delta \tau.$$

Equation (2) shows that the integration over the time range t_d is only necessary for the calculation of the parameters such as stress, strain and the SIF. The integration range, t_d is divided into n steps for the numerical integration. Then equation (2) is expressed as

$$\sigma_{ij}(t) = \sum_{i=1}^n G_{\sigma_{ij}}(t - \tau_i) \{\Theta(\tau_i) - \Theta(\tau_{i-1})\} + G_{\sigma_{ij}}(t_d) \{\Theta(t - t_d) - \Theta(0)\} \quad (3)$$

Similarly, the Green's function for the SIF under unit step change of boundary temperature can be determined. The same procedure as the above will be followed and the final expression is

$$K_I(t) = \sum_{i=1}^n G_{K_I}(t - \tau_i) \{\Theta(\tau_i) - \Theta(\tau_{i-1})\} + G_{K_I}(t_d) \{\Theta(t - t_d) - \Theta(0)\} \quad (4)$$

The Green's function method (GFM) for the SIF enables these fracture parameters to be calculated very efficiently using a simple integration scheme under thermal loads. The validity of GFM for the SIF of the present model is shown in Fig. 2 under triangular thermal loads for temperature difference of $\Delta T = \pm 45^\circ C$ with 0.033 Hz (1 period = 30 s). This figure shows that the SIT by GFM is in good agreement with standard FEM.

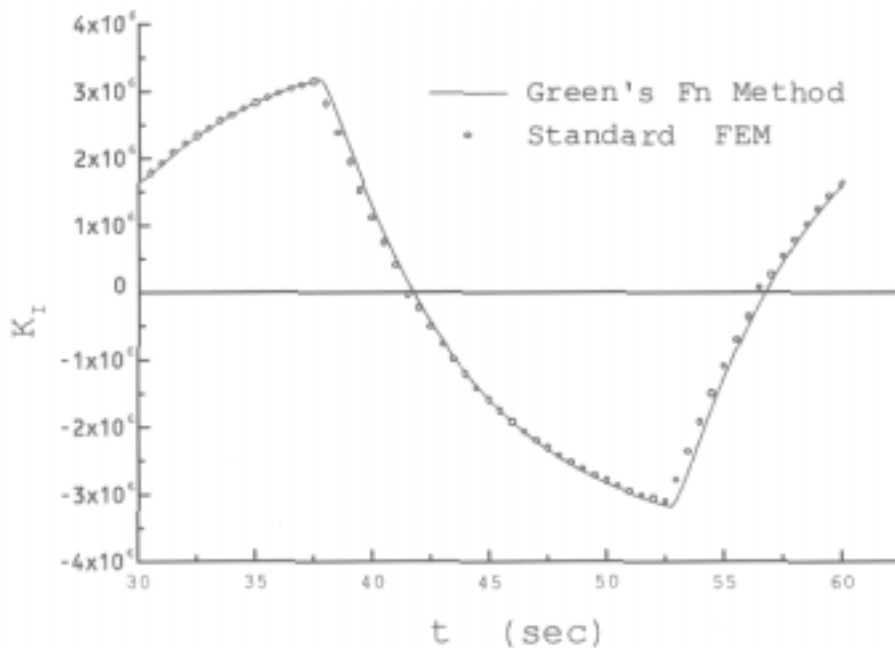


FIG. 2. Variation of stress intensity factors for triangular thermal load of 0.033 Hz.

3.3. Description of the model

For thermomechanical analysis, an axisymmetric model for the heat affected zone of the welded joint with 1540 isoparametric quadratic elements as shown in Fig. 3 were used. The model has 14 elements along the thickness direction. The axial displacements were constrained at the bottom line of the model as boundary conditions for the axisymmetric model.

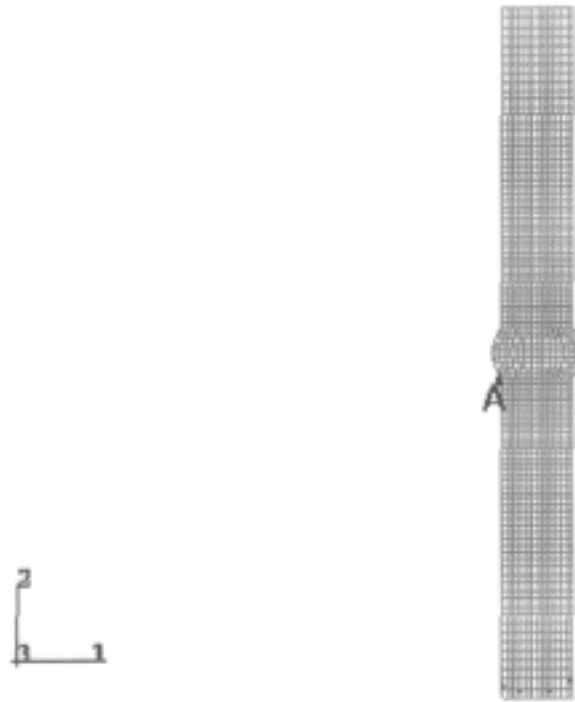


FIG. 3. Axisymmetric model of the Tee-Junction.

3.4. Loading conditions

3.4.1. Thermo-Hydraulic (TH) loading

Two types of thermal loading conditions were considered. Thermal fluctuations were assumed to occur in simplified sinusoidal form with constant alternating magnitude of 90°C , which is the temperature difference of the hot and cold fluids. As another case of the temperature difference (ΔT), the case of $\Delta T = 70^{\circ}\text{C}$ was also considered from power spectral density analysis results. The striping frequencies considered here were 0.1 Hz, 0.5 Hz, and 1.0 Hz, which are usually the most damaging ones on the wall of the piping.

The temperature histories predicted by AEA [4] at the location of 80 mm upstream from the centerline of the small pipe were used, which is random type as shown in Fig. 4.

3.4.2. Mechanical loading

The reaction forces and moments that were given in the technical specification [2] considered.

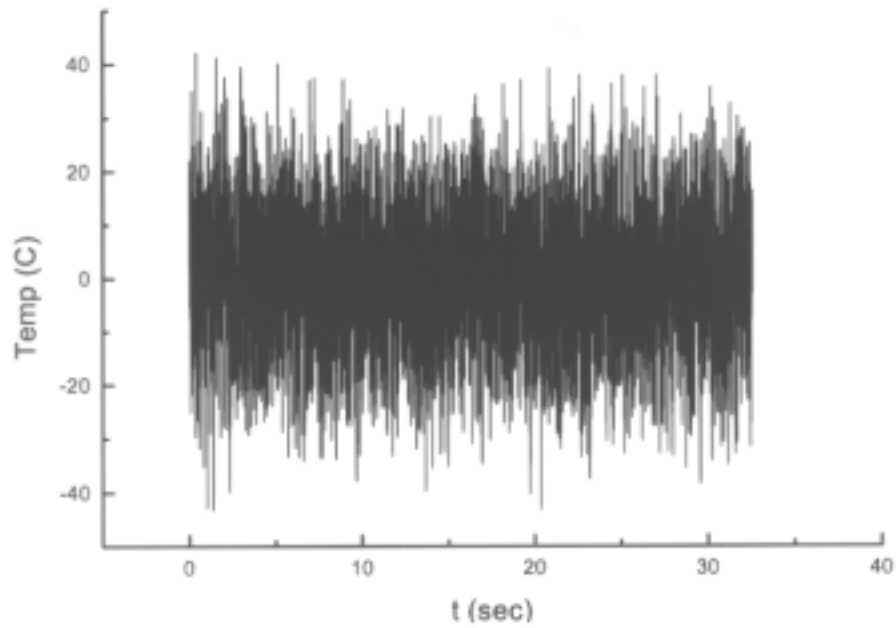


FIG. 4. Temperature history at the location of 80 mm upstream from small pipe.

3.5. Thermal analysis

The temperature history at geometrically discontinuous welded point A of Fig. 3 is shown in Fig. 5 which shows that the temperature fluctuates with a magnitude of around 90°C while the predicted temperature profile computed by AEA was a random type as shown in Fig. 4. The temperature distribution through the thickness direction for the simplified sinusoidal loading of 0.5 Hz at $t = 1.5$ sec and $t = 8.0$ sec is moving as shown in Fig. 6.

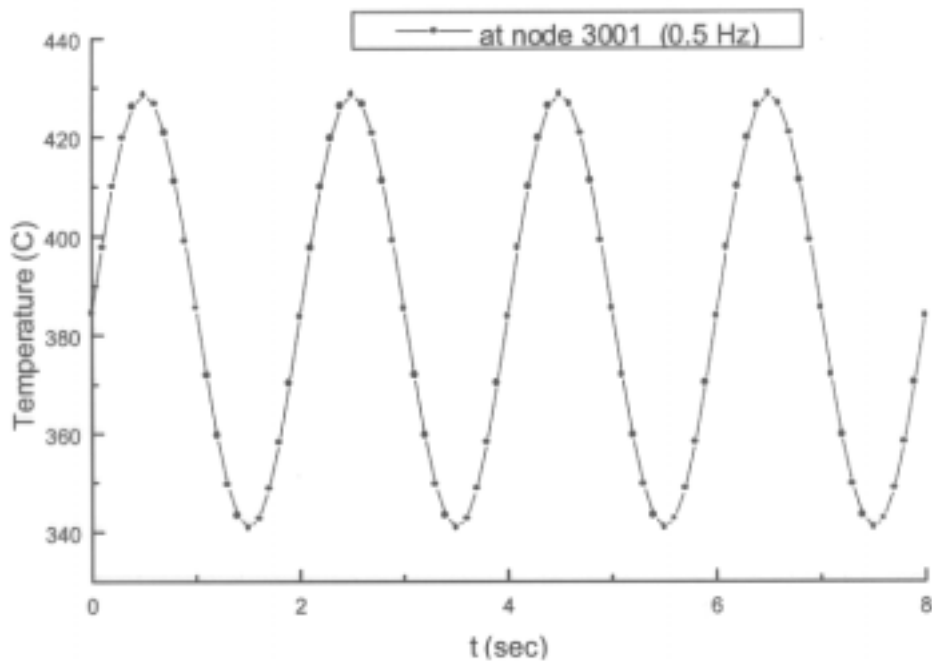


FIG. 5. Temperature history at welded point A.

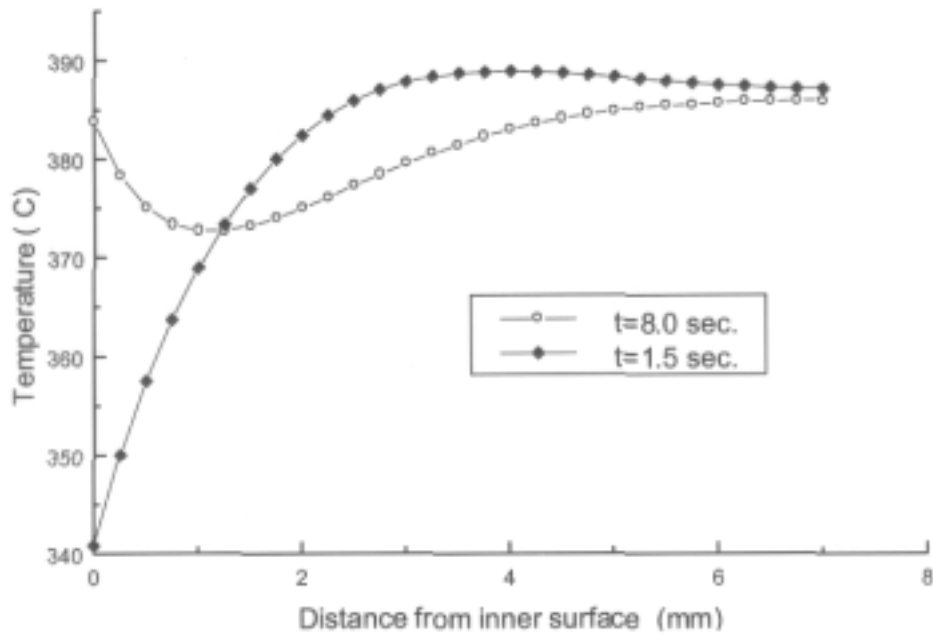


FIG. 6. Temperature profile along the thickness direction for sinusoidal load.

3.6. Stress analysis

The computed maximum values of the stress intensities, $\Delta\sigma$ for various cases are shown in Table 1. The most critical load case of elastic regime is the case of 0.5 Hz as shown in Table 1, which has $\Delta\sigma = 292.7$ MPa. The history of Tresca stress which is defined as stress intensity in ASME code N-H is shown in Fig. 7 for the case of 0.5 Hz, and the stress intensity profile along the thickness direction shows maximum value of 292.7 MPa at $t = 1.5$ s as shown in Fig. 8.

TABLE 1. MAXIMUM VALUES OF STRESS INTENSITIES FOR VARIOUS LOADING CASES

Analysis type	Frequency (Hz)	Stress intensities (MPa)	
		Sinusoidal load	Random type load
Elastic	0.1	265.7	
	0.5	292.7	173.3
	1.0	269.4	
Elastic-plastic	0.5	205.78	

It is interesting to note that the magnitude of the shear strain (ε_{zr}) level at the welded joint of location 'A' of Fig. 3 is as high as that of radial strain (ε_{rr}) as shown in Fig. 9 while the other strain components ($\varepsilon_{zz}, \varepsilon_{\theta\theta}$) are relatively small. The variations of the equivalent strain range ($\Delta\varepsilon_{eq}$) for random type loads are shown in Fig. 10, which show that the maximum value of $\Delta\varepsilon_{eq}$ at the critical location of 'A' is 0.00183. The sampling time of the data is 0.1 s. The history of Mises stress is shown in Fig. 11, which shows that the maximum value of Mises stress is 173.3 Mpa. As shown in Table 1, this value is the smallest one among the load cases. The stress components under the random type thermal loads calculated by

Green's function method are shown in Figs. 12 and 13. The maximum value of stress components were

$$\sigma_{rr} = 42.67 \text{ MPa},$$

$$\sigma_{\theta\theta} = 186.67 \text{ MPa},$$

$$\sigma_{zz} = 211.05 \text{ MPa},$$

$$\sigma_{zr} = 57.05 \text{ MPa}.$$

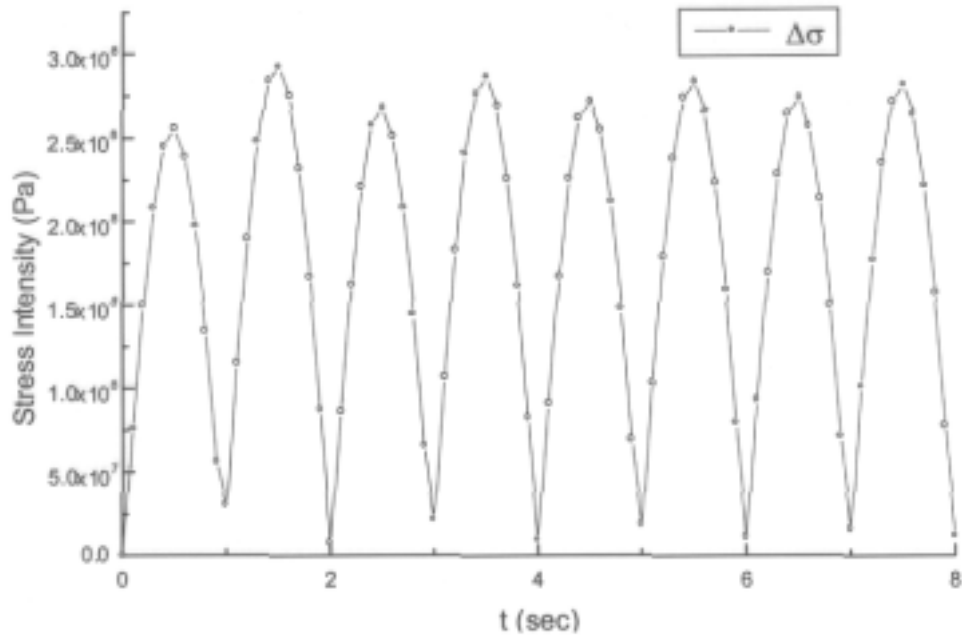


FIG. 7. Stress intensity history for sinusoidal load.

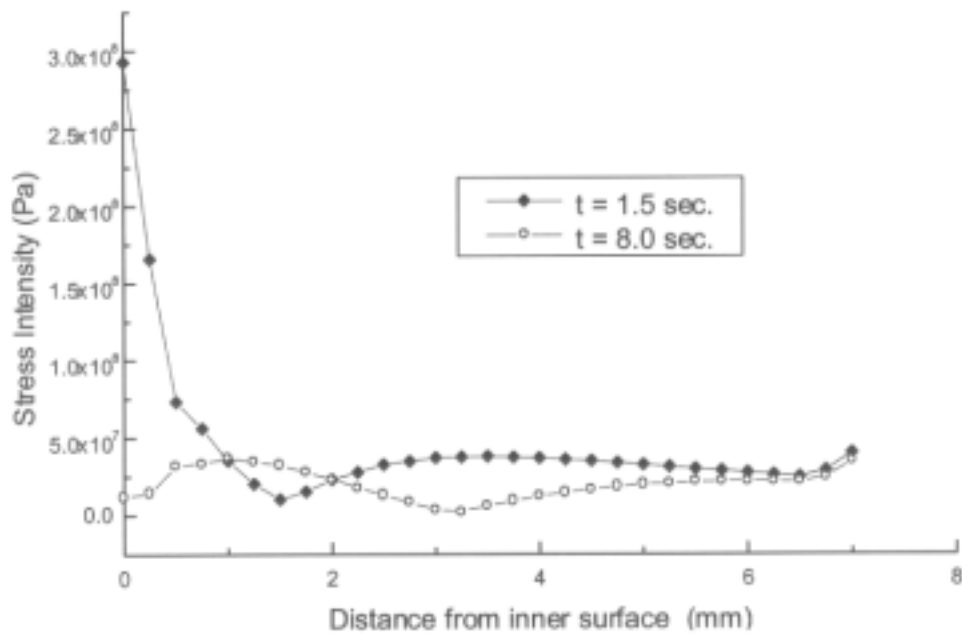


FIG. 8. Stress intensity profile along the thickness direction.

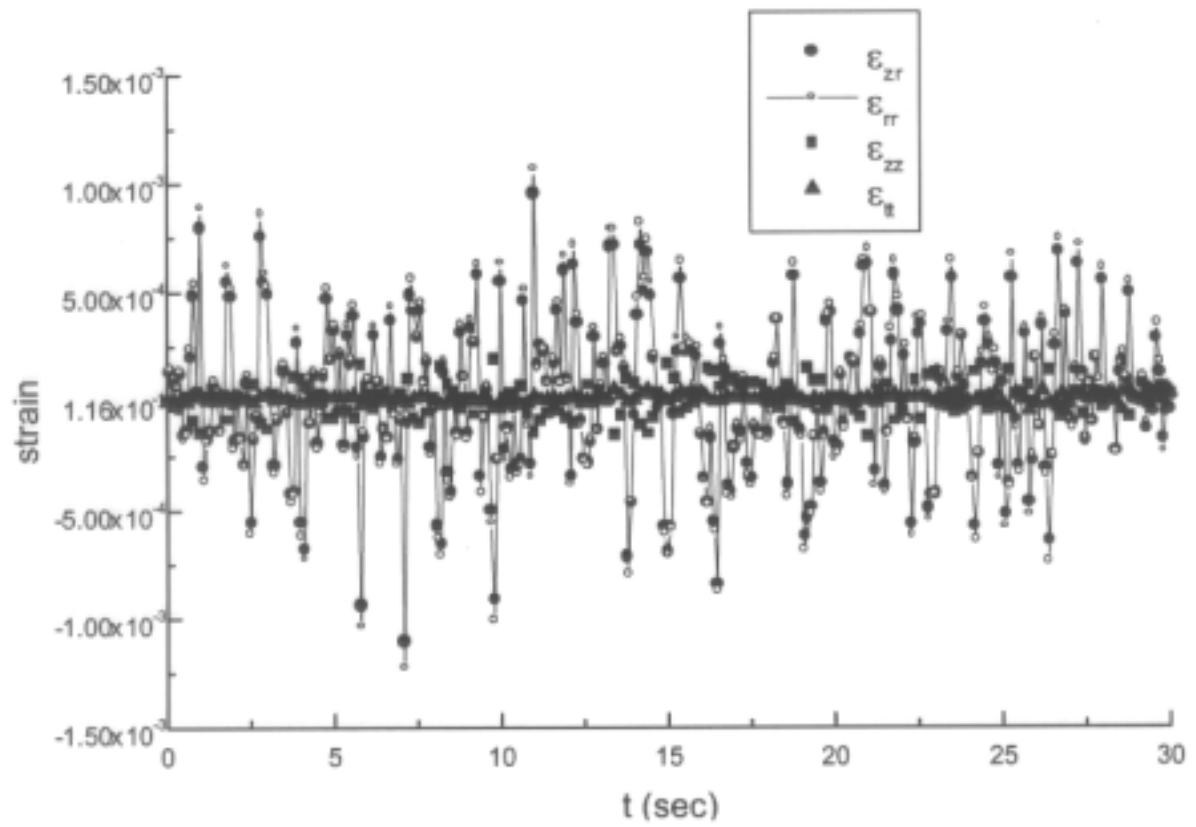


FIG. 9. History of strain components.

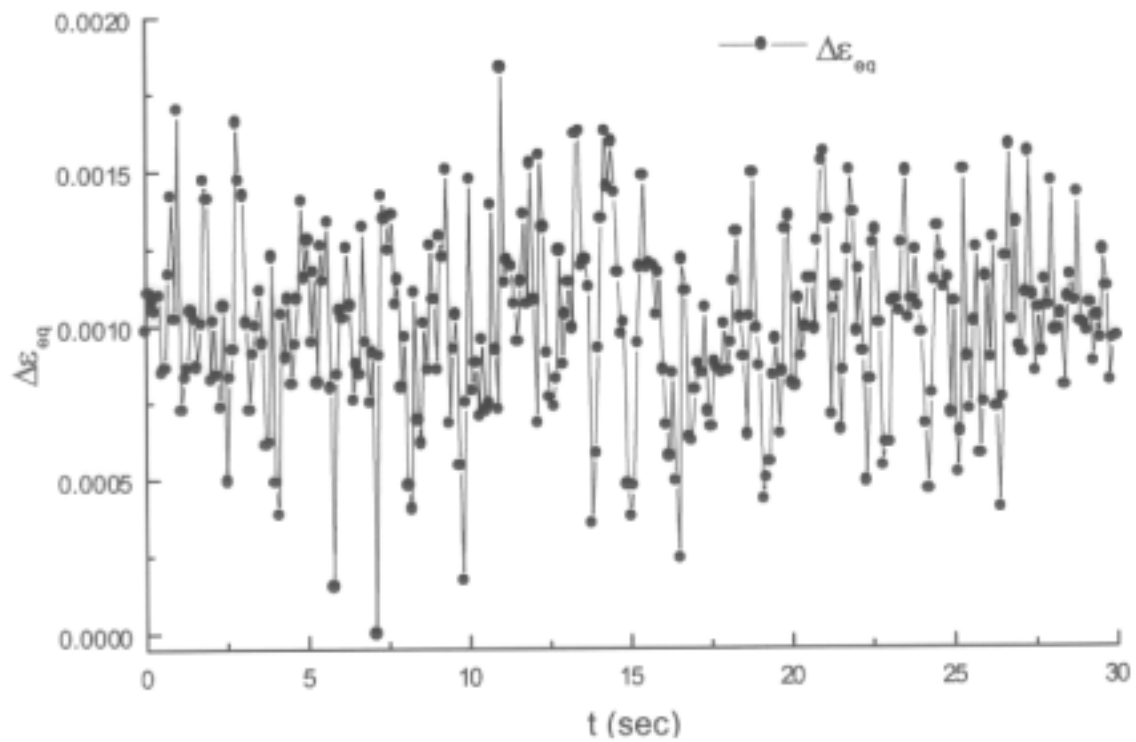


FIG. 10. History of equivalent strain ranges for random type thermal load.

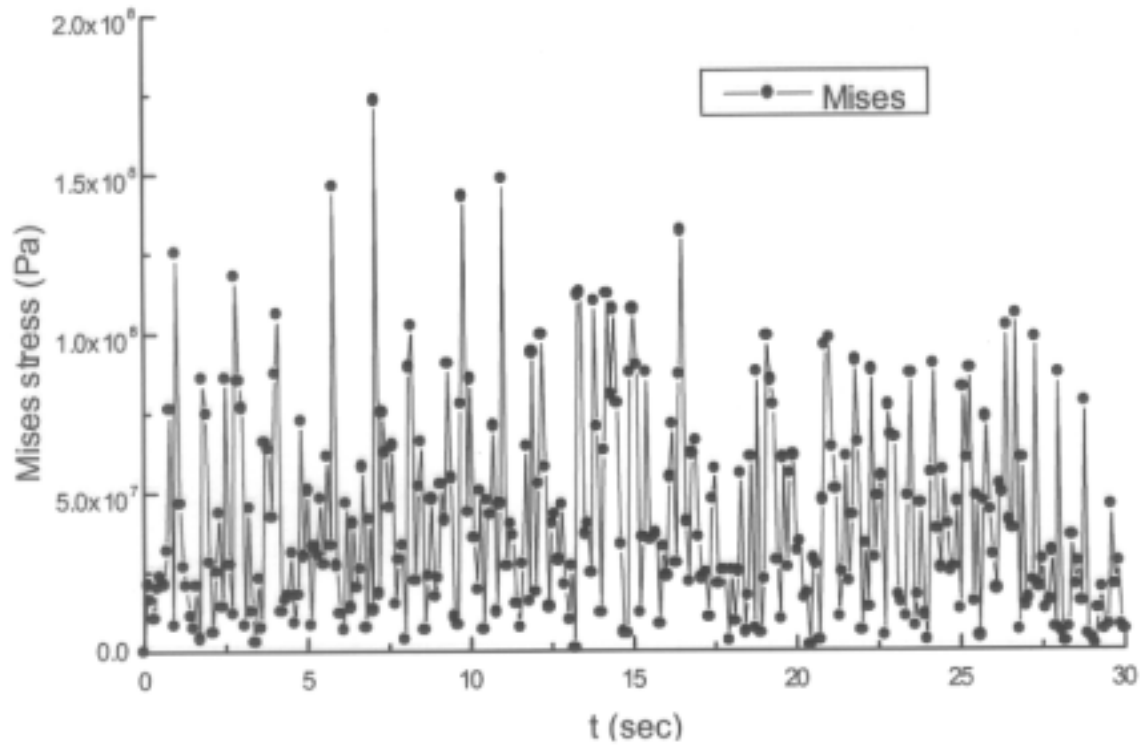


FIG. 11. History of Mises stress for random type thermal load.

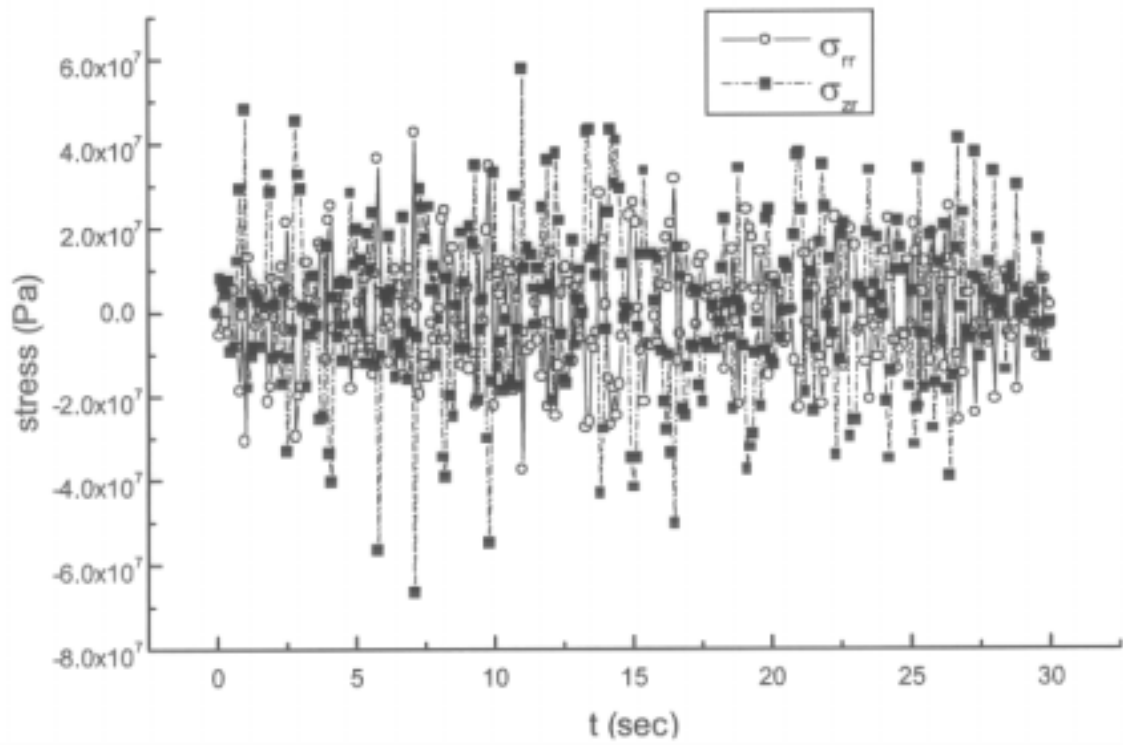


FIG. 12. Variation of σ_{rr} and σ_{zr} for sinusoidal load case of 0.5 Hz.

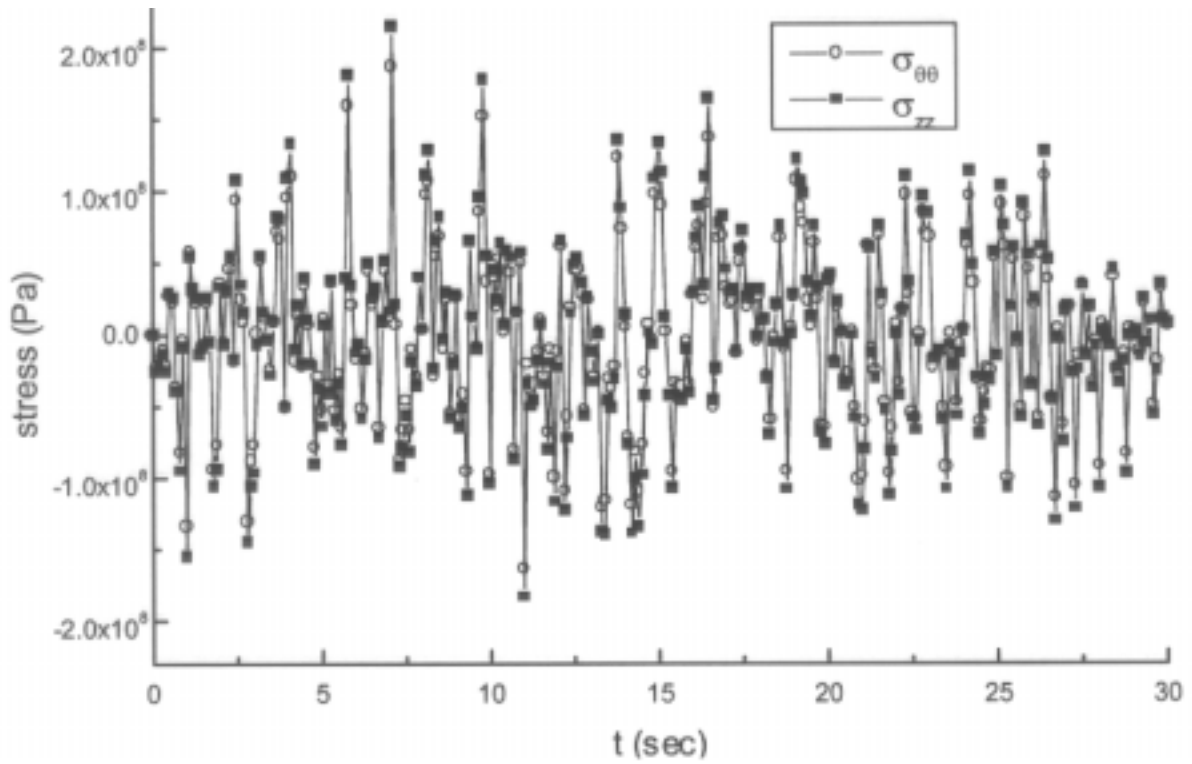


FIG. 13. Variation of Variation of $\sigma_{\theta\theta}$ and σ_{zz} for random type load case.

The calculated stress results due to the reaction force and moments at the welded joint of the inner surface were very small. The hoop stress due to the internal pressure was 7.863 MPa, the axial stress due to bending at the outermost location of the pipe was 1.838 MPa and the shear stress due to torsion of the pipe was 0.39 MPa. These stationary stresses would act as mean stresses in fatigue and crack propagation analysis. However, the contribution of these stresses under the stationary load to striping damage was small. The magnitude of the equivalent plastic strain was about two orders lower than the elastic total strain.

3.7. Results of fatigue damage evaluation

The fatigue damage evaluation was performed according to ASME code subsection NH [5]. The evaluation results of fatigue damage at the joint location of 'A' for various loading cases are shown in Table 2. As shown in the table, the case of 0.5 Hz was most severe among the three cases for the elastic analyses. The usage value of 5890.9 shows that fatigue failure would occur at the early stage of operation. The evaluated damage results by inelastic analysis were 1080 for 0.1 Hz, and 1,542.9 for 0.5 Hz.

The damage evaluation for the case of random type thermal loads showed lower level fatigue usage than that of those sinusoidal load cases. The analyses of the sinusoidal loading cases were performed using standard FEM, while that of random type loading was performed using Green's function method.

The above evaluation results show that fatigue failure occurs in the welded joint.

TABLE 2. FATIGUE USAGE FACTORS FOR 90 000 HOURS

	Frequency (Hz)	Fatigue Usage	
		Sinusoidal load ($\Delta T = 90^{\circ}C$)	Random type load
Elastic	0.1	1620.0	166.15
	0.5	5890.9	
	1.0	4628.6	
Elastic-plastic	0.1	1080.0	
	0.5	1542.9	

4. FRACTURE MECHANICS ASSESSMENT

4.1. Description of the criteria

The fatigue crack propagation analysis was carried out for the simplified sinusoidal temperature history and the random type temperature data.

4.1.1. Crack initiation

The crack propagation threshold value is expressed as follows for AISI 304 material [6]

$$K_{th} = -4R + 6.5, \quad (MPa\sqrt{m})$$

where

$$R = \frac{K_{min}}{K_{max}},$$

The initial crack length was set as 0.5 mm in this study.

4.1.2. Crack propagation

The propagation law with the effective SIF parameter was employed as follows [6];

$$\frac{da}{dN} = C (\Delta K_{eff})^n \quad (6)$$

where

$$C = 7.5 \times 10^{-13},$$

$$n = 4,$$

ΔK_{eff} is shown in the appendix ZG of RCC-M code, and the unit of the SIF is $MPa (m)^{0.5}$.

4.2. Evaluation of crack propagation

4.2.1. Results of crack initiation analysis

The analysis results of crack initiation for the crack length of 0.5 mm are shown in Table 3. The elastic analysis results for the frequencies of 0.1 Hz and 0.5 Hz showed that the crack would be initiated for both $\Delta T = 90^\circ\text{C}$ and 70°C cases. The calculated stress intensity factor range shows that the case of 0.5 Hz is the most critical among the load cases considered here.

TABLE 3. CALCULATED STRESS INTENSITY FACTOR RANGES FOR $a_0 = 0.5$ MM

Frequency (Hz)	ΔK_I (MPa $\text{m}^{0.5}$)		
	Sinusoidal load		Random type load
	$\Delta T = 90^\circ\text{C}$	$\Delta T = 70^\circ\text{C}$	
0.1	7.6	6.6	4.22
0.5	8.0	7.2	

For random type loading case, the SIF range is smaller than the sinusoidal loading cases as shown in Table 3 and Fig. 11. The sampling time in Fig. 11 is 0.1 s.

4.2.2. Results of crack propagation

The crack propagation analysis using Green's function method requires determination of the SIF range for the incremental crack lengths. To perform crack propagation analysis, ΔK should be expressed as a function of crack length. Then, the fatigue lifetime can be easily determined by integrating the crack propagation equation.

The crack propagation analysis requires polynomial regression of ΔK as a function of crack length a . The polynomial expressions for the sinusoidal load and random type load over the crack length of 0.5 mm to 6.5 mm are as follows;

(1) Sinusoidal load

To determine the fatigue crack lifetime, it is necessary to express ΔK as a function of the crack length a in the crack propagation law of equation (5). The variations of ΔK for each stage of the incremental crack length were calculated using the Green's function for the corresponding crack length. The polynomial regression of ΔK over the crack length is expressed with the 5th order polynomial curve fitting as

$$\Delta K = 7.71 - 1853.12a + 1.58 \times 10^6 a^2 - 5.71 \times 10^8 a^3 + 1.08 \times 10^{11} a^4 - 7.88 \times 10^{12} a^5. \text{ (MPa}\sqrt{\text{m}}\text{)}$$

The estimated lifetimes for a crack tip to propagate 1 mm, 3 mm, and 5 mm along the thickness direction are shown in Table 4. As shown in Table 4, the crack would be propagated up to 5 mm in 940.7 hours. Figure 14 shows the variation of the SIFs for the frequency of 0.5 Hz. The Green's functions for every 0.5 mm increase of the crack length over 0.5 mm to 6.5 mm were predetermined and used to calculate the SIFs.

TABLE 4. ANALYSIS RESULTS OF CRACK PROPAGATION

a	Estimated lifetime (hours)	
	Sinusoidal load	Random type load
1 mm	153.0	2,665.2
3 mm	681.8	27,910.9
5 mm	940.7	42,698.9
Crack depth at 90 000 hours	5 mm < a < 7 mm	5 mm < a < 7 mm

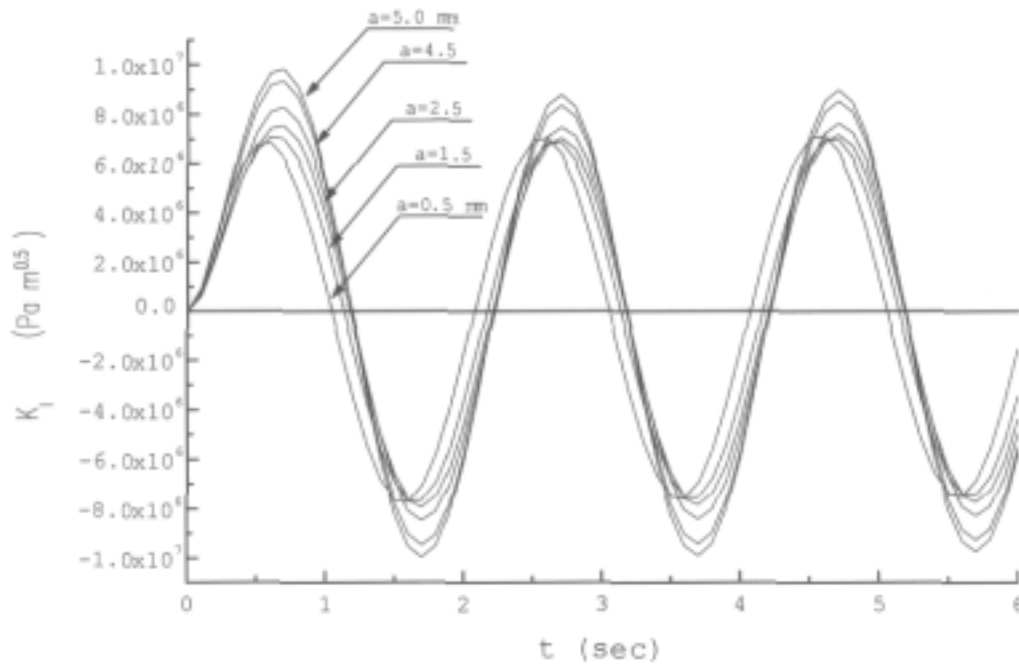


FIG. 14. Variation of stress intensity factors for sinusoidal load case of 0.5 Hz.

(2) Random type load

The variation of the SIF is shown in Fig. 15. The polynomial expression of ΔK for the random type load is

$$\Delta K = 7.45 - 9724.97a + 7.97 \times 10^6 a^2 - 3.32 \times 10^9 a^3 + 7.36 \times 10^{11} a^4 - 8.11 \times 10^{11} a^5 + 3.46 \times 10^{15} a^6, \quad (\text{MPa}\sqrt{\text{m}})$$

The estimated lifetime up to $a = 5$ mm for this random type load was 42 689.9 hours as shown in Table 4, which is far longer than that of the sinusoidal load case.

As for the crack propagation for $a > 5.0$ mm which is over 70% of the thickness, it is no longer valid to apply the Paris law. The engineering judgement says that the crack would not penetrate through the thickness because the primary stress level is very low.

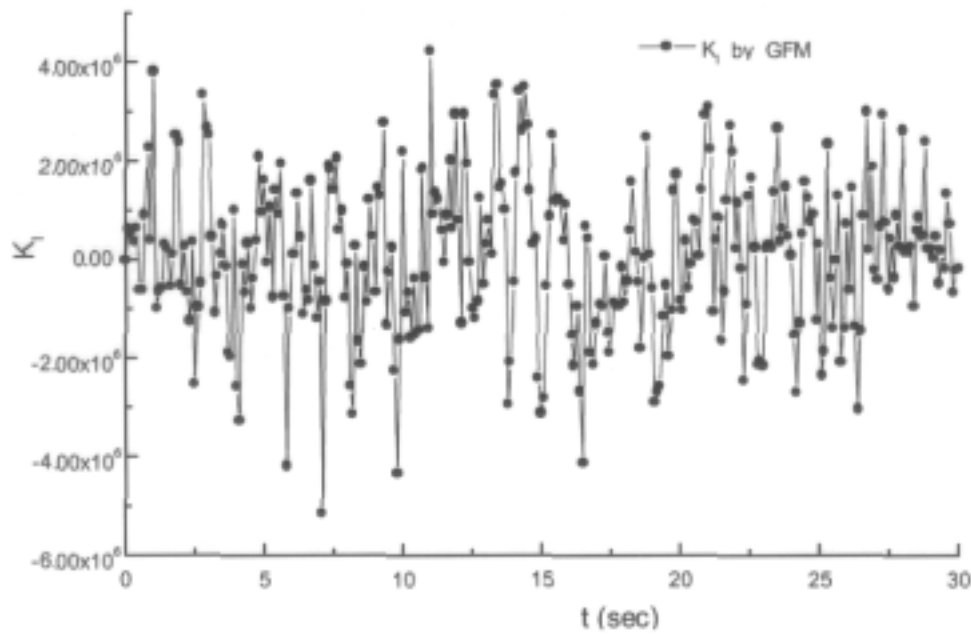


FIG. 15. Variation of stress intensity factors for random type load case.

5. CONCLUSIONS

The evaluation of the thermomechanical fatigue and fracture behavior of Phénix secondary circuit tee-junction having a welded joint at the upstream of its main piping was carried out using Green's function method as well as standard FEM. Two types of thermohydraulic loading were considered. One is the simplified sinusoidal temperature fluctuation with the alternating temperature difference of the two fluids with respect to the frequencies of 0.1 Hz, 0.5 Hz, and 1.0 Hz. The other is random type thermal loading [4].

The analysis results can be summarized as follows. The fatigue evaluation showed that the frequency of 0.5 Hz is most damaging and fatigue failure in the circumferential welded joint of the inner surface during 90 000 hours of operation occurred by both elastic and inelastic analysis. The fatigue usage for the load case of 0.5 Hz was evaluated as 5890.9 by elastic analysis while 1542.9 by elastic-plastic analysis. The predicted fatigue usage for the random type load by Green's function method was estimated to be 166.15, which shows fatigue failure would occur even though the usage factor is lower than those of the sinusoidal load cases.

The crack propagation analyses showed that crack would be propagated up to 5 mm at 940.7 hours for sinusoidal load case and at 42 698.9 hours for random type load case. The results indicate that crack would be propagated at least 5 mm during 90 000 hours of operation.

However, it is estimated that the crack would not penetrate the thickness of the wall from the engineering judgement because the level of primary stress is very low. Therefore, the crack would be initiated and propagated quickly up to 5 mm through the thickness direction and the crack would be arrested between 5 mm and 7 mm for the two load cases.

The Green's function approach (GFA) was mainly employed for the random load case for the numerical efficiency in this study. The GFA was evaluated to enable the calculation of fatigue usage or crack propagation lifetime by simple numerical integration procedure.

Acknowledgements

The thermohydraulic load data used in this study were supplied by AEA with the aid of Novatome. The authors would like to express their appreciation to the companies.

REFERENCES

- [1] INTERNATIONAL ATOMIC ENERGY AGENCY, Correlation between material properties and thermohydraulics conditions in LMFRs, Specialists meeting, 17-20 April, Aix-En-Provence, France (1994).
- [2] ABAQUS version 5.7, H.K.S Inc., (1998).
- [3] ABAQUS version 5.7, H.K.S Inc., (1998).
- [4] Thermal striping benchmark exercise - Thermohydraulic analysis of the Tee-Junction, UK AEA Technology, (1996).
- [5] ASME Section III Subsection NH, Class I Components in Elevated Temperature Service (1995).
- [6] GELINEAU, O., SPERANDIO, M., Bench mark on Tee Junction of LMFR Secondary Circuit Involving Thermal Striping Phenomena - Fatigue and Fracture Mechanics Assessment, paper presented at the Research Co-ordination Meeting, 6-10 October, 1997, Obninsk, Russian Federation.

RESULTS OF THE THERMOMECHANICAL AND FRACTURE MECHANICAL ANALYSIS OF PIPELINE TEE-JUNCTION BREAK UNDER CONDITIONS OF INTERACTION BETWEEN HOT SODIUM JET AND MAIN COLD SODIUM FLOW

P.N. BIRBYER, A.I. KIRYUSHIN, V.V. ZHUKOV, V.A. SOBOLEV,
S.A. SOLOVIEV

OKB Mechanical Engineering,
Nizhny Novgorod, Russian Federation

Abstract. Benchmark problem is considered associated with determination of thermo-mechanical stresses in the region of a tee where the interaction of hot sodium jet with cold sodium flow occurs. Using the results of a thermo-hydraulic analysis swings and frequencies of temperature pulsations on the wall of the pipeline are determined. The analysis of stresses, cyclic strength calculation and analysis of cracks progress under specified initial defect for the pipeline element were performed using the obtained data.

1. PURPOSE OF THE CALCULATION

The benchmark problem under consideration is associated with determination of thermo-hydraulic and thermo-mechanical characteristics of a tee where the interaction of hot sodium jet with cold main sodium flow occurs.

The unit analyzed and initial data correspond to the actual design of PHENIX reactor secondary circuit pipeline tee and its operation conditions.

In this report strength aspect of the task set is considered: determination of thermo-mechanical stresses in a tee in the region of interaction of two different temperature sodium flows. On the basis of stresses obtained and specified temperature pulsations an estimate of cyclic strength was performed. The crack progress was calculated.

Calculation of temperatures on a pipeline element and calculation of stresses was performed using computer code ANSYS. The cyclic strength analysis aiming at elimination of cracks appearance is performed according to Ref. [1]. The crack kinematic calculation is carried out by means of fracture mechanics techniques. The crack progress is described by the fatigue fracture equation by Paris.

2. THERMO-MECHANICAL ANALYSIS

2.1. Computer code description

Calculation analysis was performed using computer code ANSYS. The "finite element method" used in the code is destined for calculation of a wide range of problems including thermo-mechanical ones. This code has International Quality Certificate ISO9001.

2.2. Description of calculation model

Main attention was paid to the zone of mixing two flows of sodium in the region of pipelines' T-junction, thus, the calculation field when determining the temperature and stresses was limited by the very zone.

3-D and 2-D calculation models were considered. The calculation according to a 3-D model was performed in order to analyze the T-junction stressed state. A 2-D model, because of smaller division and increased iterations quantity allowed a more scrupulous determination of the stressed state in the welding area.

Main geometrical data of a tee is: main pipe outer diameter is 508 mm, wall thickness is 7 mm, small tube outer diameter is 85 mm, wall thickness is 5 mm. Circular weld on the main tube is located downstream at 160 mm from small tube axis.

3-D calculation model of one half of the tee is represented by solid finite elements in 3D formulation. The calculation model is given in Fig. 1. In this Figure the calculation zone of hot jet near the tube wall is also depicted (isotherms are given in °C).

A 2-D calculation model and welded joint area are shown in Fig. 2.

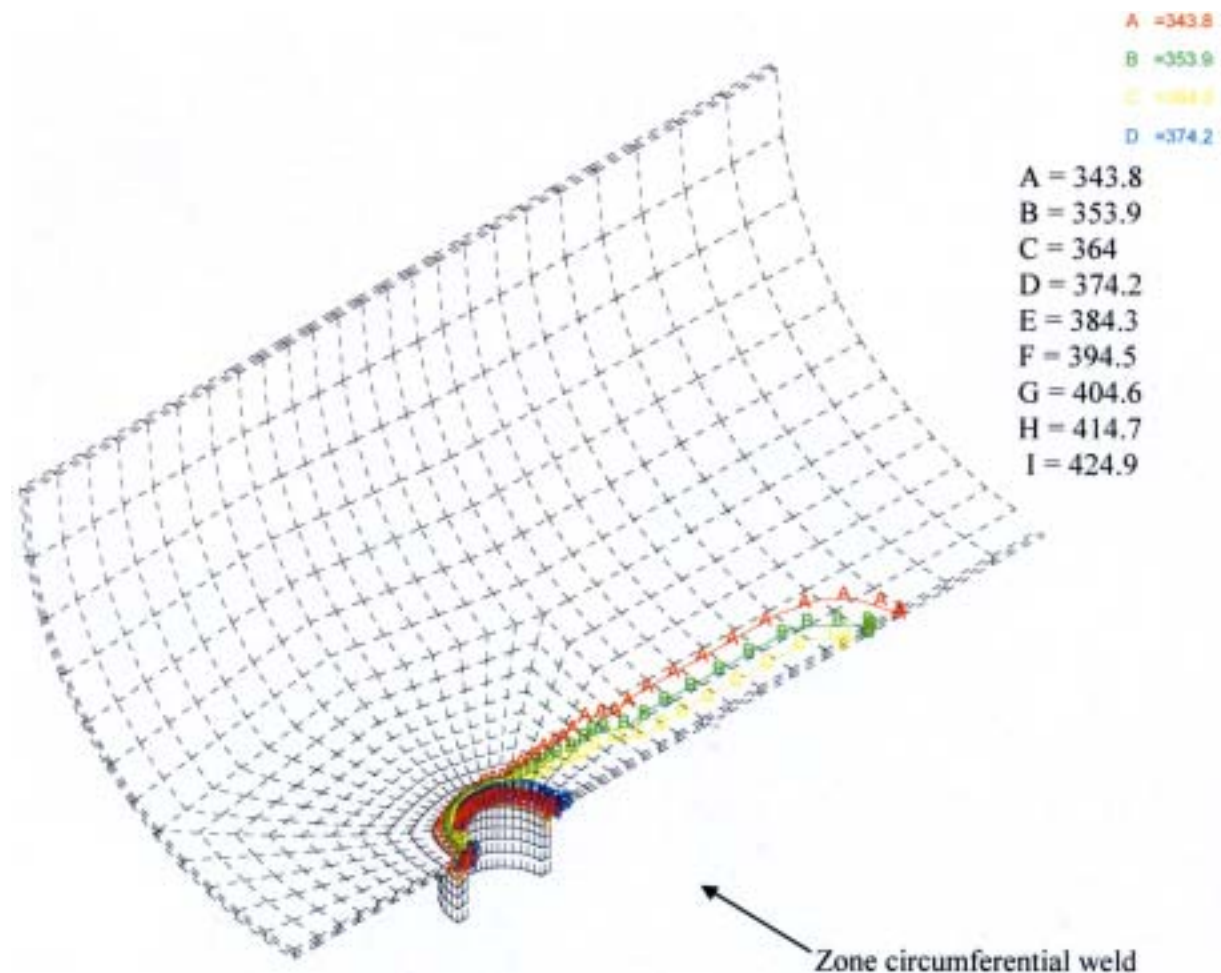


FIG. 1. 3-D calculation model of a tee with representation of hot jet zone near the wall.

2.3. Boundary conditions

On the first stage the analysis performed provided for determination of temperature fields in the pipeline zone under consideration with subsequent calculation of stresses. Each kind of analysis presupposed their own boundary conditions.

On the basis of thermo-hydraulic analysis performed the following is established. The hot jet penetrates into the main flow at a distance not exceeding one diameter of inlet opening. Then it enters a small turbulent region near the main tube wall and extending downstream by approximately two diameters of inlet opening from its axis. Average value of hot jet temperature is 400 °C.

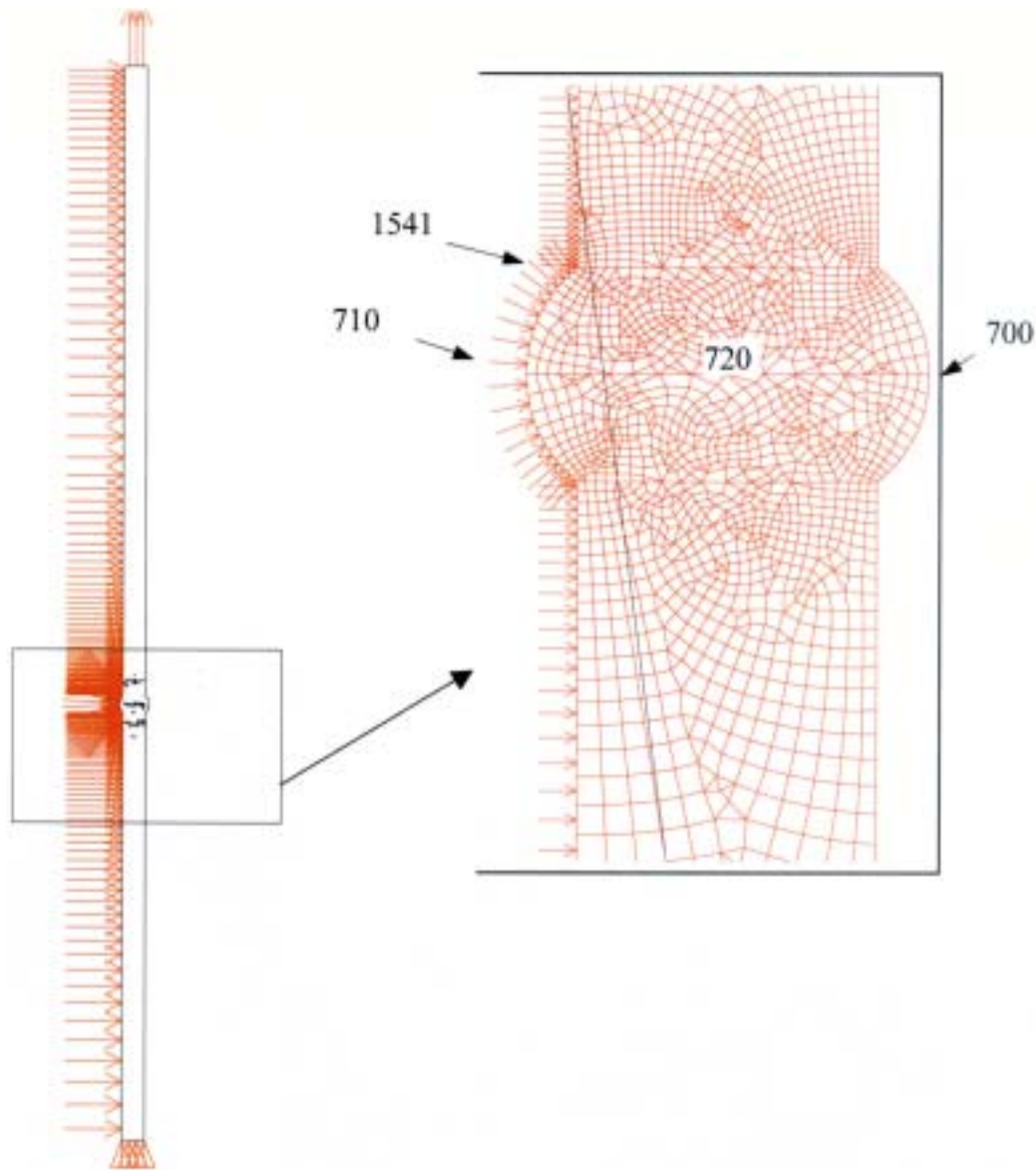


FIG.2. 2-D calculation model and welded joint area.

Because of the absence of true presentation of pulsations frequencies of coolant near the wall with a sufficient degree of conservatism the sodium pulsation characteristics near the main pipeline wall are determined as follows:

- swing of temperature pulsations near pipeline wall $\Delta T = 400 - 340 \text{ }^{\circ}\text{C}$;
- “temperature-time” dependence is incidental and frequencies vary from 0,01 to 2 Hz.

The following boundary conditions are assumed for the thermal analysis:

- Coolant temperature in the main tube is $340 \text{ }^{\circ}\text{C}$ and in small tube - $430 \text{ }^{\circ}\text{C}$.
- Coolant temperature near wall in the zone of hot jet varies from $340 \text{ }^{\circ}\text{C}$ to $400 \text{ }^{\circ}\text{C}$ according to the linear law. Discrete values of pulsation frequencies 0,01, 0,5 , 1, 2 Hz with above mentioned constant amplitude $60 \text{ }^{\circ}\text{C}$ from peak to peak are assumed for the analysis.
- Value of coefficient of heat transfer from sodium to tube wall is $62700 \text{ W}/(\text{m}^2 \cdot ^{\circ}\text{C})$.
- On the pipeline outer boundary no heat transfer to outside is assumed.

3-D calculation model represents 1/2 of tee unit, therefore, in the plane of symmetry kinematic conditions of symmetry were assumed.

Pressure in the main pipe is assumed to be 0,22 MPa (2,2 bar) and in small tube - 0,29 MPa (2,9 bar). From the side of isolated tube sections the tee is assumed to be subjected to pressure available. Weight and compensation loads were not applied to this calculation model. Calculation of their impact is done separately.

A 2-D model is also mechanically loaded by pressure effect.

Temperatures for calculation of stresses were assumed from the file of thermal problem calculation.

2.4. Physico-mechanical properties of material

The material of both tubes is AISI 304 steel. Weld material corresponds to 16Cr-8Ni-2Mo steel. Physico-mechanical properties of material are assumed in accordance with technical description of benchmark problem. Properties of weld material are assumed to be analogous to those of base material.

2.5. Results of thermal analysis

In Fig. 3 - 6 plots of temperature variation in the zone of weld on tube inner surface (node 710 in Fig. 2), in the middle part (node 720) and on tube outer surface (node 700) are given for frequencies of 0,01 , 0,5 , 1, 2 Hz.

Values of swings of temperature pulsations (°C) on the tube inner surface, in the middle of tube and on the outer surface in welded joint areas and on the smooth of the main tube are given in Table 1.

The files obtained of thermal task solution were used when determining the stresses.

TABLE 1. VALUES OF TEMPERATURE PULSATIONS (°C) SWING IN THE CYCLE OF TEMPERATURE VARIATIONS

Calculation value	Frequency, Hz											
	0,01	0,02	0,05	0,1	0,15	0,2	0,3	0,5	0,66	1	2	5
Welded joint												
ΔT_{in}	59,2	58,3	56,6	55,3	54,2	53,2	51,4	48,7	47	43,8	38,5	31
ΔT_{mid}	48,2	40,9	23,6	13,1	10,6	8,2	5,4	3,1	2,1	0,49	0,08	≈0
ΔT_{out}	48,6	39,6	21,2	8,8	5,7	3,2	1,2	0,4	0,15	0,01	≈0	≈0
Base metal												
ΔT_{in}	58,8	57,5	55,1	53,3	52,1	51,1	49,3	46,5	44,8	41,6	35	27
ΔT_{mid}	48,6	42,3	25,2	13,4	11,1	8	5	3,1	1,9	0,6	0,08	≈0
ΔT_{out}	49,1	40,5	23,3	10,6	6,7	4,7	2	0,8	0,4	0,04	≈0	≈0

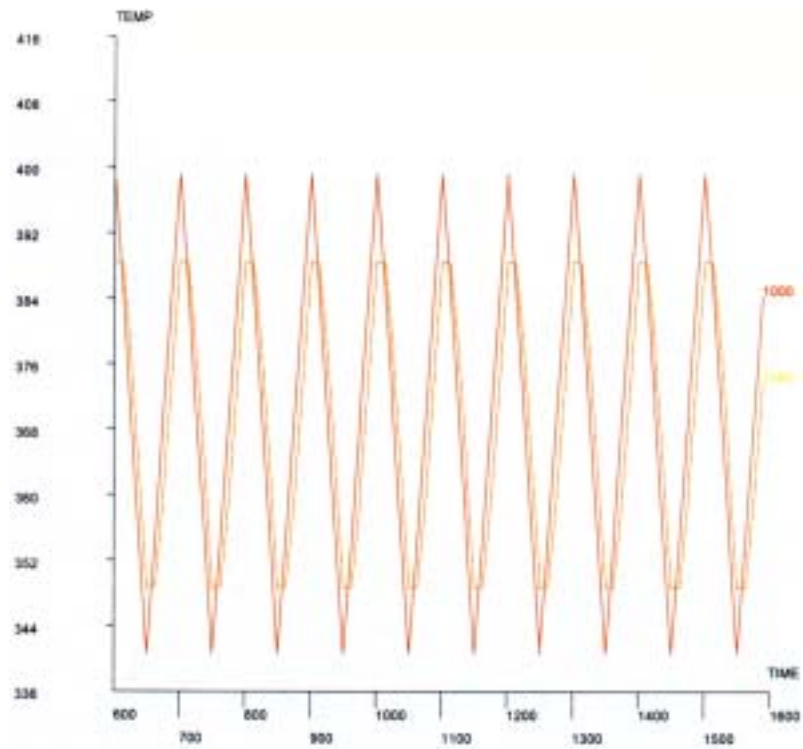


FIG. 3. Variation of temperatures ($^{\circ}\text{C}$) on tube inner and middle part at pulsation frequency of 0,01 Hz

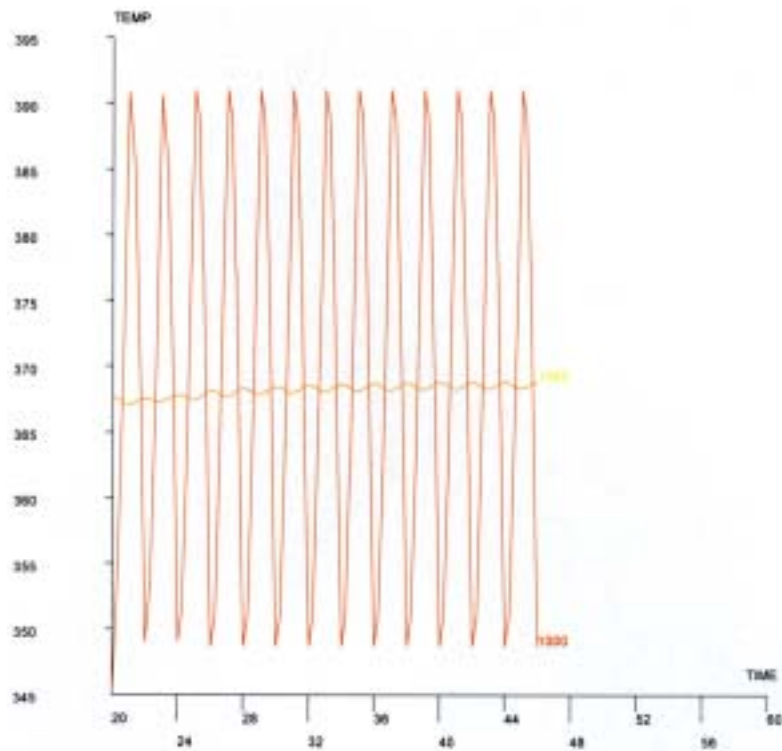


FIG. 4. Variation of temperatures ($^{\circ}\text{C}$) on tube inner, outer and middle side at pulsation frequency of 0,5 Hz

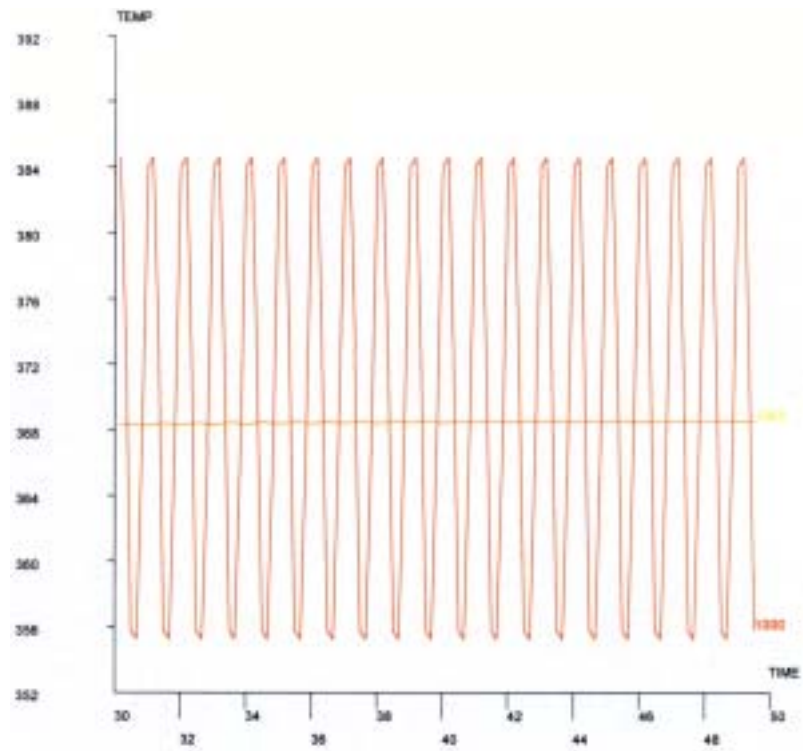


FIG. 5. Variation of temperatures ($^{\circ}\text{C}$) on tube inner and middle side at pulsation frequency of 1 Hz

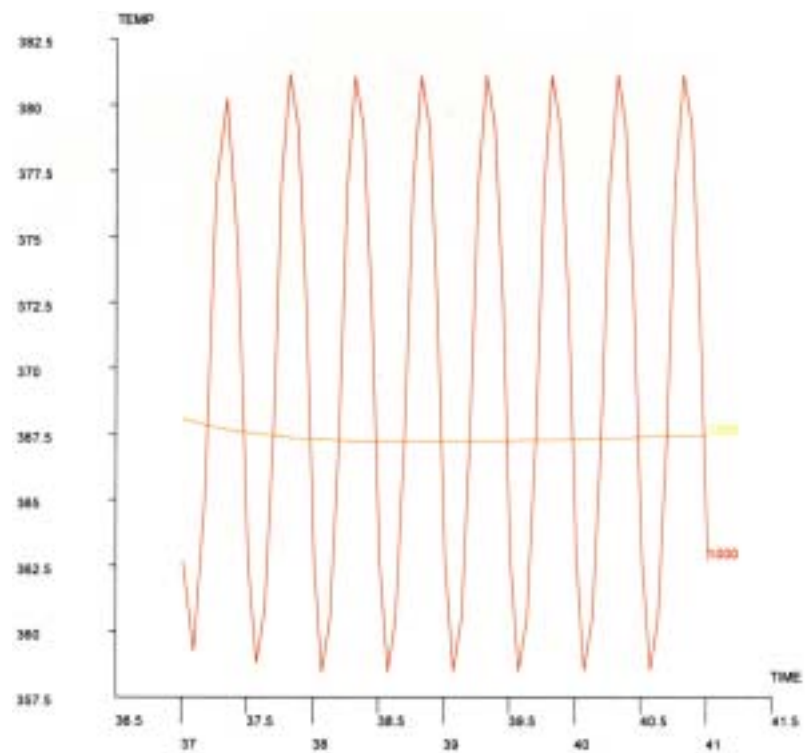


FIG. 6. Variation of temperatures ($^{\circ}\text{C}$) on tube inner and middle side at pulsation frequency of 2 Hz

2.6. Results of thermo-mechanical analysis

Stressed state from impact of sodium pressure is represented as isolines of reduced stresses $\sigma_i = \sigma_{\max} - \sigma_{\min}$ in Fig. 7. Total membrane stresses for main tube are $\sigma_m = 8$ MPa. Total membrane stresses for small tube were $\sigma_m = 1,3$ MPa. Maximum reduced stresses $\sigma_i^{\max} = 22$ MPa turned to be in the zone of joining of main and small tubes. According to Ref. [1] conditions of static strength $\sigma_i^{\max} < [\sigma] = R^T_{p0.2} / 1,5 = 80,6$ MPa are met.

Maximum stresses of $\sigma_i = 202$ MPa from impact of pressure and temperature drops turned to be also in the zone. The pattern of distributions of stresses σ_i is given in Fig. 8. In this zone the temperature distribution is steady and is changed only with operation modes. It was not considered in this benchmark problem.

Stresses in the tube from loads and compensation do not exceed appr. 5 MPa and within the mode are also steady, therefore their impact on the operability of the unit considered is negligible. The constant stress component is appr. 10 MPa.

TABLE 2. VALUES OF STRESSES IN THE CYCLE OF TEMPERATURE VARIATIONS, MPA

Calculation value	Frequency, Hz											
	0,01	0,02	0,05	0,1	0,15	0,2	0,3	0,5	0,66	1	2	5
Welded joint												
σ_L^{\max}	50	87	157	185	194	196	195	187	179	162	129	86
σ_L^{\min}	-33	-68	-136	-164	-172	-175	-173	-166	-158	-142	-123	-90
Base metal												
σ_L^{\max}	30	49	85	98	102	102	100	97	95	90	75	46
σ_L^{\min}	-17	-35	-70	-84	-87	-88	-87	-86	-84	-78	-69	-43

As the results of thermal analysis have shown the variation of tube wall temperatures is very fast. Therefore, determination of stresses were done for each iteration of thermal solution within the cycle of temperature variations. In Table 2 values of maximum and minimum values of reduced stresses σ_i (σ_L) on the inner surface of main tube in the region of weld and base metal (node 1541 in Fig. 2) and on the smooth part are given. The indicated swings of stresses were therefore considered in the analysis of tee cyclic strength.

Stressed state σ_i (MPa) in the zone of weld corresponding to extreme values of stresses' swing at pulsation frequency of 0,2 , 0,5 and 2 Hz is given in Fig. 9 - 11.

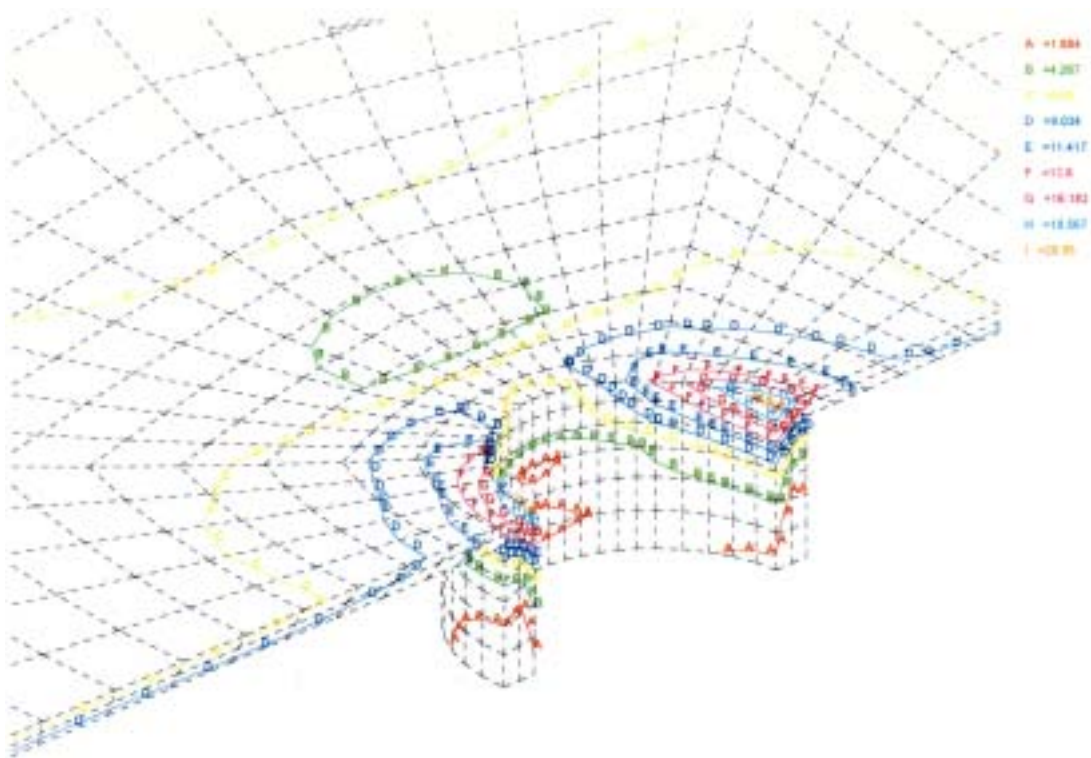


FIG. 7. Distribution of isolines of reduced stresses σ_i (MPa) in the tee from sodium pressure.

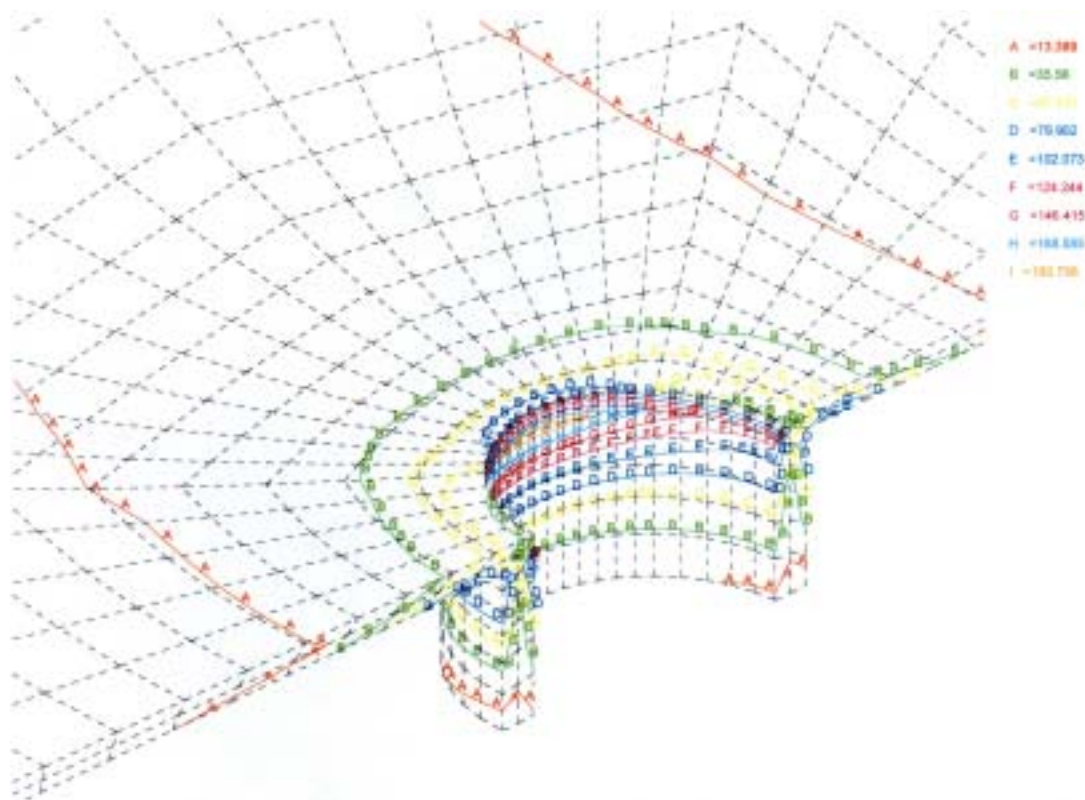


FIG. 8. Distribution of isolines of reduced stresses σ_i (MPa) in the tee from sodium pressure and pressure differences.

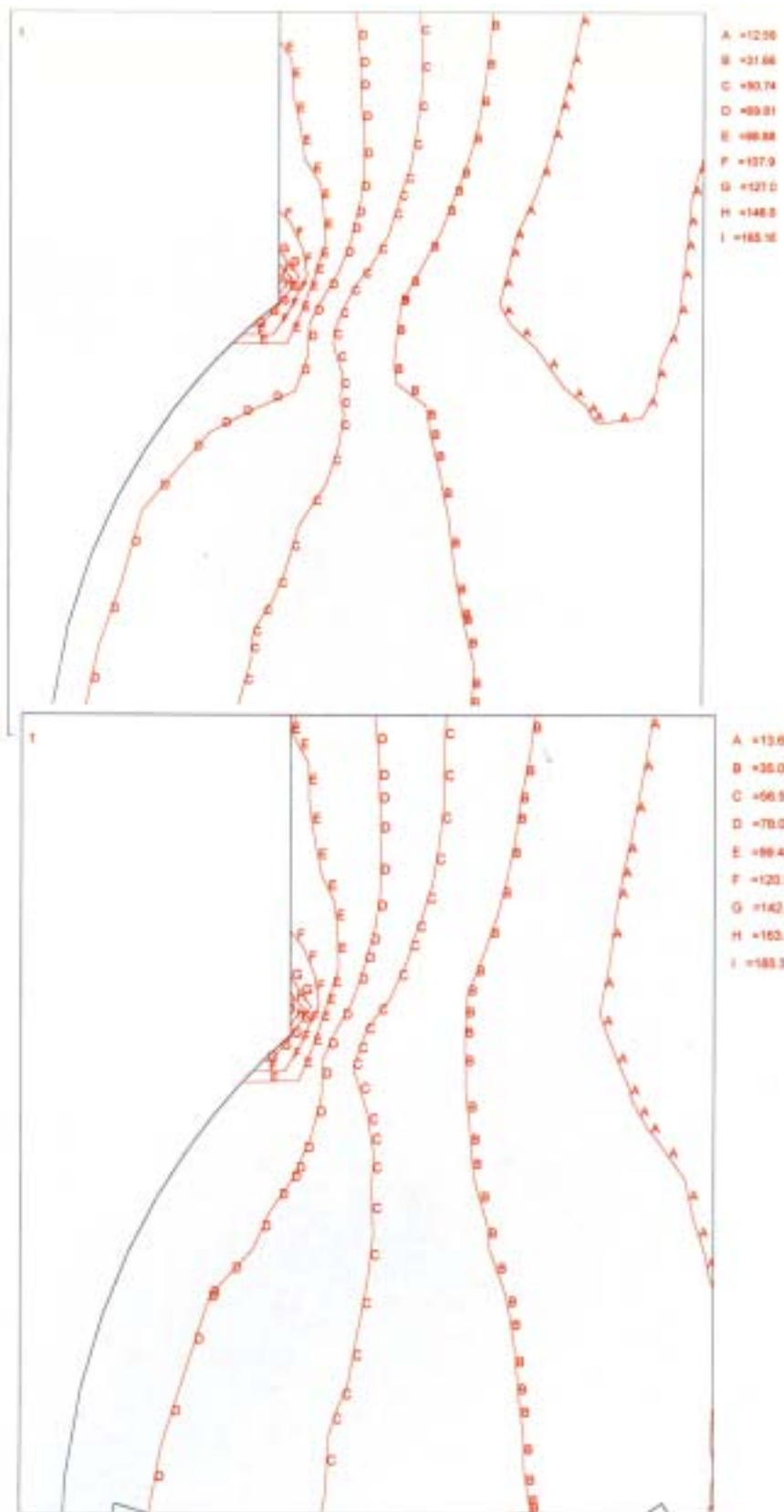


FIG. 9. Stressed state σ_i (MPa) in the zone of weld corresponding to extreme values of stresses' swing at pulsation frequency of 0,2 Hz.

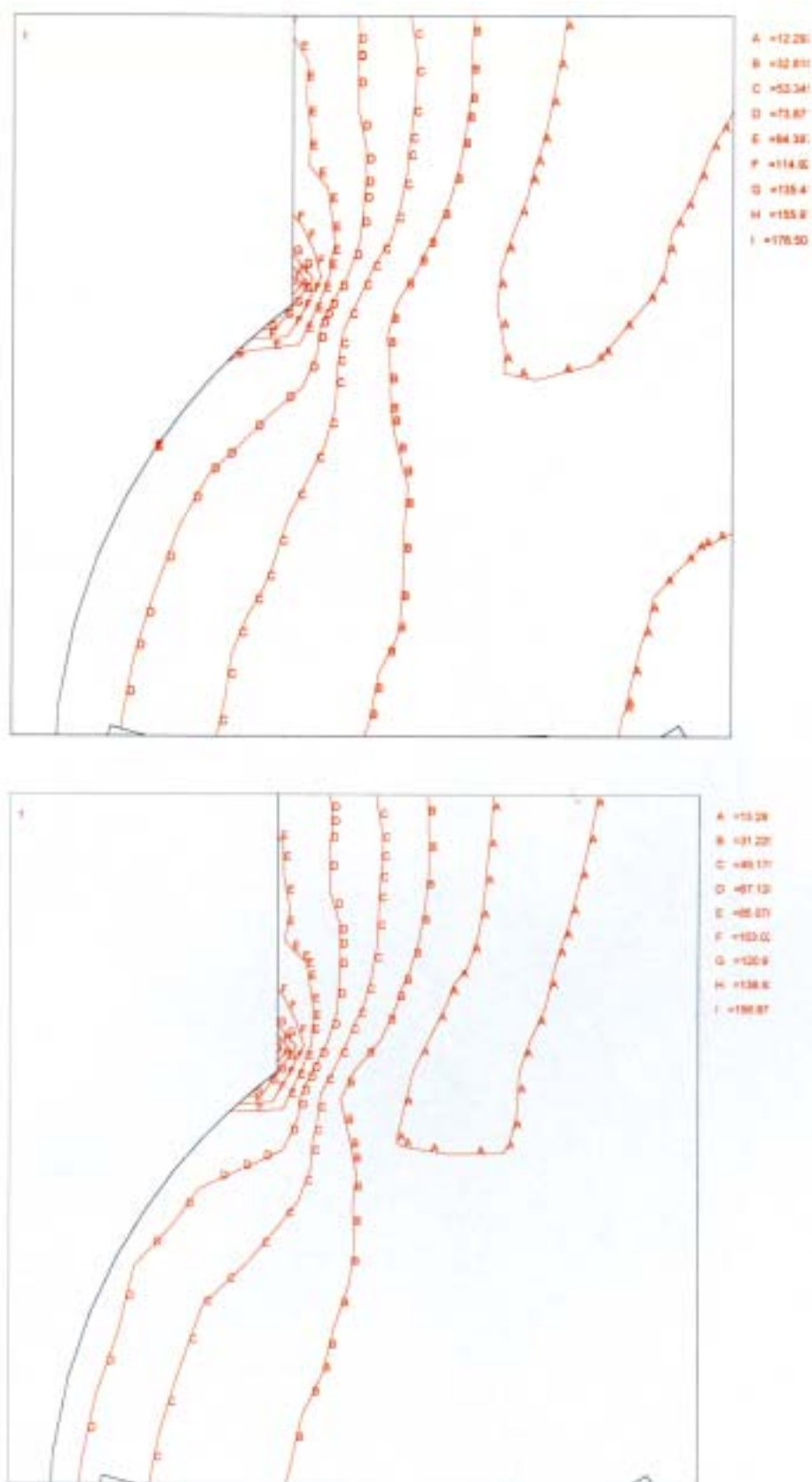


FIG. 10. Stressed state σ_i (MPa) in the zone of weld corresponding to extreme values of

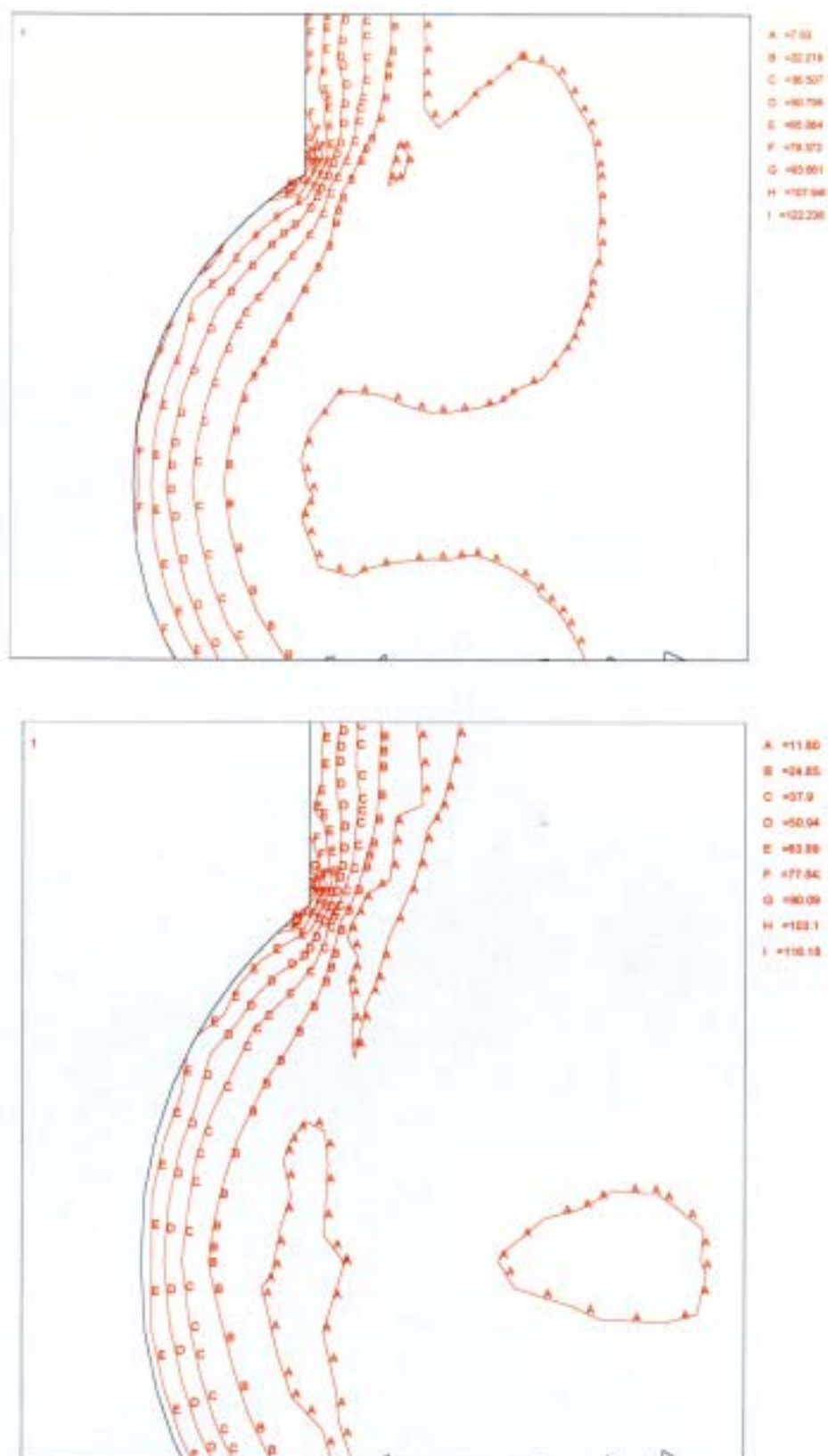


FIG. 11. Stressed state σ_i (MPa) in the zone of weld corresponding to extreme values of stresses' swing at pulsation frequency of 2 Hz

3. ANALYSIS OF CYCLIC STRENGTH

3.1. Description of calculation method

In accordance with Ref. [1] verification calculation for strength at cyclic loading is done to exclude fatigue cracks' appearance in course of operation. It is achieved by means of local stress level limitation in the concentration areas.

The amplitude of operation stress should not exceed the allowable amplitude of stress $[\sigma_{aF}]$ obtained for a specified number of cycles. If the amplitude of stresses is specified the operation number of cycles N should not exceed the allowable number of cycles $[N_o]$.

If the loading process consists of a number of cycles characterized by the amplitudes of stresses $(\sigma_{aF})_i$ and by corresponding numbers N_i of cycles the strength condition should be met for accumulated fatigue damage (a) Ref. [1].

$$\sum \frac{N_i}{[N]_i} = a \leq 1 ,$$

where N_i - expected number of i -th loading;

$[N]_i$ - allowable number of cycles for i -th loading.

Determination of allowable number of cycles by specified amplitudes of stresses at a number of cycles $N \leq 10^{12}$ is done by formulae (1) relating the allowable amplitudes of arbitrary stresses $[\sigma_{aF}]$ and the allowable number of cycles $[N]$. When solving the problem considered calculation for cyclic strength is performed with coefficients of strength margin by stresses $n_\sigma = 2$ and number of cycles $n_N = 10$ Ref.[1].

Procedure for calculation of local arbitrary reduced stress $(\sigma_F)_L$ is regulated by the Ref. [1].

If to a moment L stress (σ_L) is in elastic-plastic region and acquires to this moment the largest absolute value among all preceding positive and negative stresses (σ_L) , then $(\sigma_F)_L$ is determined by a formula:

$$(\sigma_F)_L = \text{sign}[(\sigma_L)_L - (\sigma_L)_h] \cdot (\xi \cdot R_{pe}^T)^{\frac{v-1}{v+1}} \times \\ \times \left\{ \frac{1+v}{2} [(\sigma_L)_L - (\sigma_L)_h]^2 + \frac{1-v}{2} (\xi \cdot R_{pe}^T)^2 \right\}^{\frac{1}{1+v}} + (\sigma_F)_h , \quad (1)$$

where in this case $(\sigma_L)_h = (\sigma_F)_h = 0$, and $\xi=1$.

Hardening index v and proportionality limit R_{pe}^T are determined by formulae from Ref. [1].

If to moment L formula (1) was used even one time then for determination of stress $(\sigma_F)_L$ half-cycle L, h is considered.

If $|(\sigma_L)_L - (\sigma_L)_h| \leq 2 \cdot R_{pe}^T$, then $(\sigma_F)_L$ is calculated by a formula $(\sigma_F)_L = (\sigma_L)_L - (\sigma_L)_h + (\sigma_F)_h$.

If $|(\sigma_L)_L - (\sigma_L)_h| > 2 \cdot R_{pe}^T$, then $(\sigma_F)_L$ is calculated by a formula (1) where coefficient ξ is taken equal to 2

If at calculation of $(\sigma_F)_L$ and determination of plot of its variation formula (1) is used even one time then two similar blocks stresses (σ_L) variation are considered one after another.

The allowable stresses amplitudes for the welded joint $[\sigma_{aF}]_s$ except a welded joint with partial melt are determined by the formula

$$[\sigma_{aF}]_s = j_s \cdot [\sigma_{aF}],$$

where $[\sigma_{aF}]$ - allowable conditional elastic stresses amplitude;

j_s - is the cyclic strength reduction coefficient depending on weld type of materials to be welded and on thermal treatment after weld ($j_s \leq 1$). j_s is taken to be equal to 1.

Values of j_s for some welded joints are given in Ref. [1]. Values of j_s for other weld types are determined experimentally. If the data on j_s value is missing, estimation may be used. So, according to Ref. [1] j_s may be taken to be equal to 0,6 - 0,7 for austenitic steels weld.

3.2. Estimation of structure damageability at cyclic loading

The analysis was done for the zone of adjoining of hot jet to a wall of main piping in the area of weld location and in the base metal. On the basis of thermo-mechanical analysis performed for each frequency loading half-cycles (cycles) are formed of σ_L reduced stresses' variation (see Table 2) and conditional elastic stresses. Because of lack of data on dynamics of sodium temperature variation near the wall and, consequently of stresses the damageability of structure is estimated individually by each frequency impact.

The results of calculation of fatigue damage and allowable number of half-cycles (cycles - operation time) for calculated values of sodium pulsation frequencies are given in Table 3.

As seen from the results of cyclic strength the damageability increases with the increase of pulsations' frequency and then begins to decrease. Maximum of damageability is attributed to 0,66 Hz frequency pulsation. Time of operation at which the cyclic strength condition for given frequency for a welded joint is met amounts to 9 hours and to 730 hours for the base metal.

TABLE 3. RESULTS OF CYCLIC STRENGTH CALCULATION

Calculated value	Frequency, Hz										
	0,01	0,02	0,05	0,1	0,15	0,2	0,3	0,5	0,66	1	2
Welded joint											
Amplitude of conditional elastic stress, σ_{aF} , MPa	41,5	77,5	162	207	222	226	223	210	197	171	133
Allowable number of cycles, [N]	$3,8 \times 10^9$	$5,1 \times 10^6$	$4,9 \times 10^4$	$1,94 \times 10^4$	$1,52 \times 10^4$	$1,42 \times 10^4$	$1,48 \times 10^4$	$1,83 \times 10^4$	$2,32 \times 10^4$	4×10^4	15×10^4
Base metal											
Amplitude of conditional elastic stress, σ_{aF} , MPa	23,5	42	77,5	91	95	95,4	94	92	90	84	72
Allowable number of cycles, [N]	1×10^{12}	$3,5 \times 10^9$	$5,45 \times 10^6$	$1,49 \times 10^6$	$1,1 \times 10^6$	$1,07 \times 10^6$	$1,22 \times 10^6$	$1,47 \times 10^6$	$1,75 \times 10^6$	$2,87 \times 10^6$	$1,19 \times 10^7$

4. ANALYSIS OF FRACTURE MECHANICS

4.1. General statements

Performance of the analysis on the probability of an initial defect like crack and determination of time of its growth is not foreseen by the Ref. [1]. Nevertheless, there are some methodology recommendations on the defects progress study and on the structural allowable defects determination for calculations of ultimate states.

Computer code description

The calculation is carried out by means of computer code “ANKORT” developed in OKBM.

Load conditions are characterized by the ΔK stresses intensity coefficient range, asymmetry coefficient R and load duration, i.e. number of load cycles N .

Cracks progress is described by the kinetic equation of fatigue fracture

$$\frac{\partial a(c)}{\partial N} = C_0 \left(\frac{\Delta K}{\sqrt{1-R}} \right)^n, \text{ (mm / cycle)}$$

where C_0 , n are material characteristics determined experimentally.

For austenitic steels $C_0 = 4,2 \cdot 10^{-8}$, $n = 2,9$.

The calculation in the brittle area is carried out by means of linear fracture mechanics techniques, in quasibrittle and viscosity areas - by means of non-linear fracture mechanics techniques taking into account the ultimate plastic state and with the use of the conditionally elastic stresses coefficient K_{Ie} and its critical value K_{Iec} .

The form of calculation defect is conditioned as a semi elliptic crack with semiaxes a (depth) and c (length). a is taken to be equal to 0,1 mm, $c = 0,5$ mm.

It is given that crack progress initiation occurs when the range ΔK exceeds a certain threshold value K_{th} .

If $\Delta K_i \geq (10^{-8}/C_0)^{1/n}$, the defect is growing.

The stresses intensity coefficient is determined by means of methods revealed by Ref. [1] developers.

Crack kinetics calculation

Input calculation information includes mechanical properties of a structural material, stressed state, dimensions of the initial defect and structure dimensions.

The calculation considers a cyclic load with the frequency of 0,5 Hz. Stresses behavior along the wall thickness in the top of a crack initiated in the welded joint area is shown in Fig. 12. Stresses behavior along the wall thickness in the top of a crack initiated in the base metal is shown in Fig. 13.

Crack progress analysis results

The analysis of a crack progress with the initial defect $a = 0.1$ mm results in a form of diagrams showing the dependence of crack depth a on load cycles number N . Crack progress for the welded joint area is shown in Fig. 14, and for the base metal - in Fig. 15.

Taking into account the given data (in course of temperature fluctuations 0,5 Hz) the period of crack progress through a welded joint is 750 hours, in the base metal - 2430 hours.

Additional investigations show that the initial defect in a form of crack does not progress if the stress level does not exceed the value of 50 MPa.

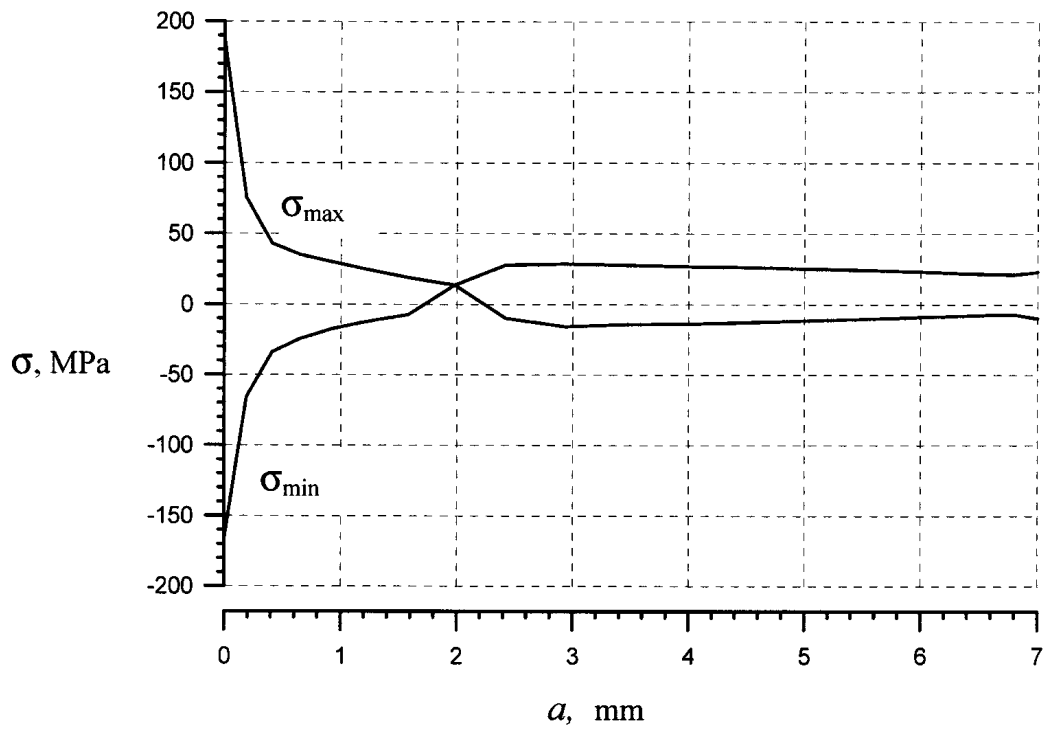


FIG. 12. Stresses behavior along the wall thickness in the welded joint area.

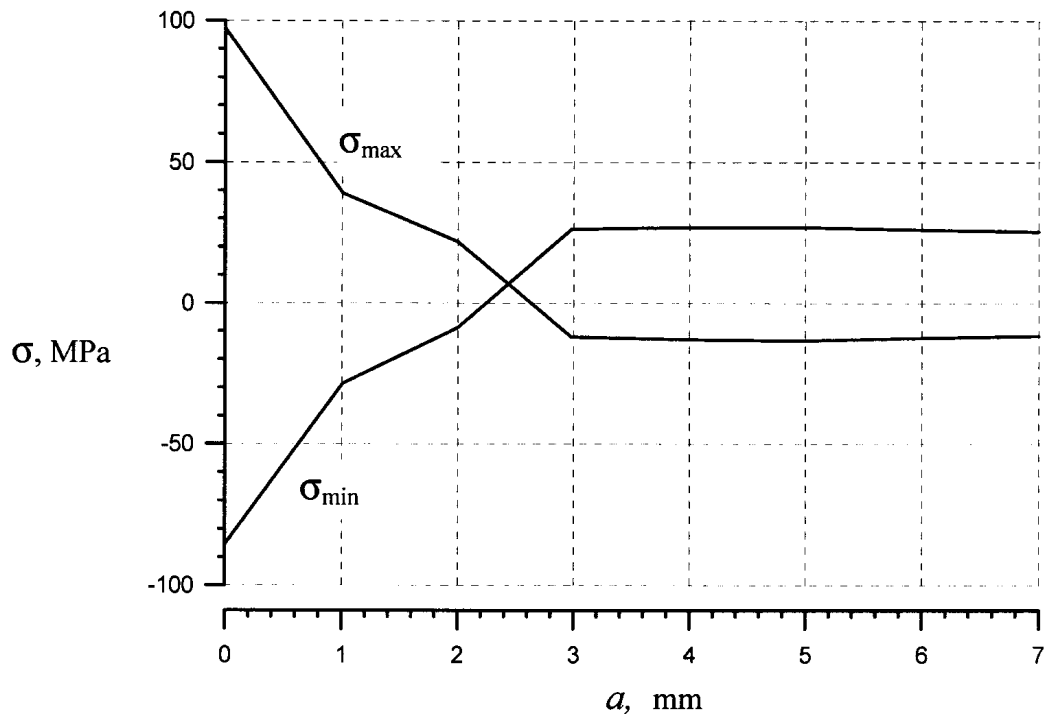


FIG. 13. Stresses behavior along the wall thickness in the base metal.

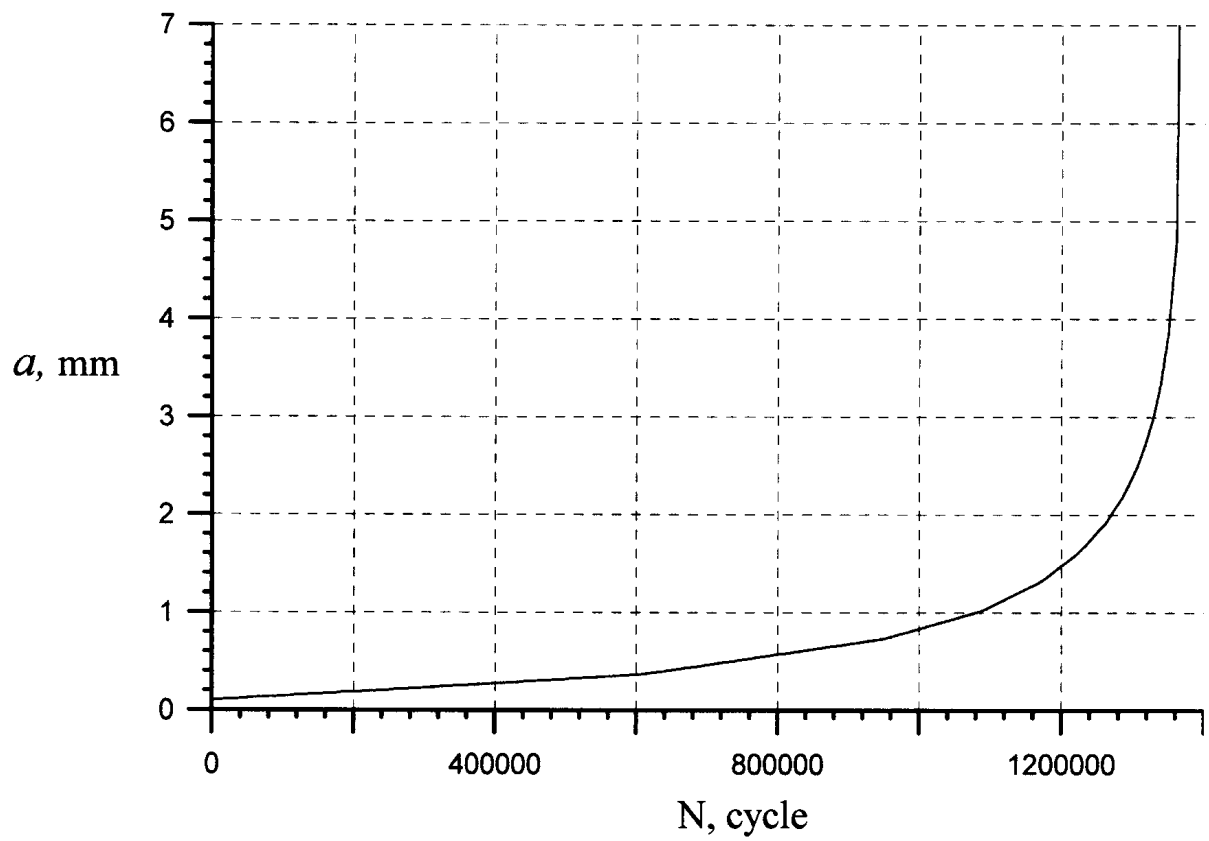


FIG. 14. Crack progress behavior in the weld area.

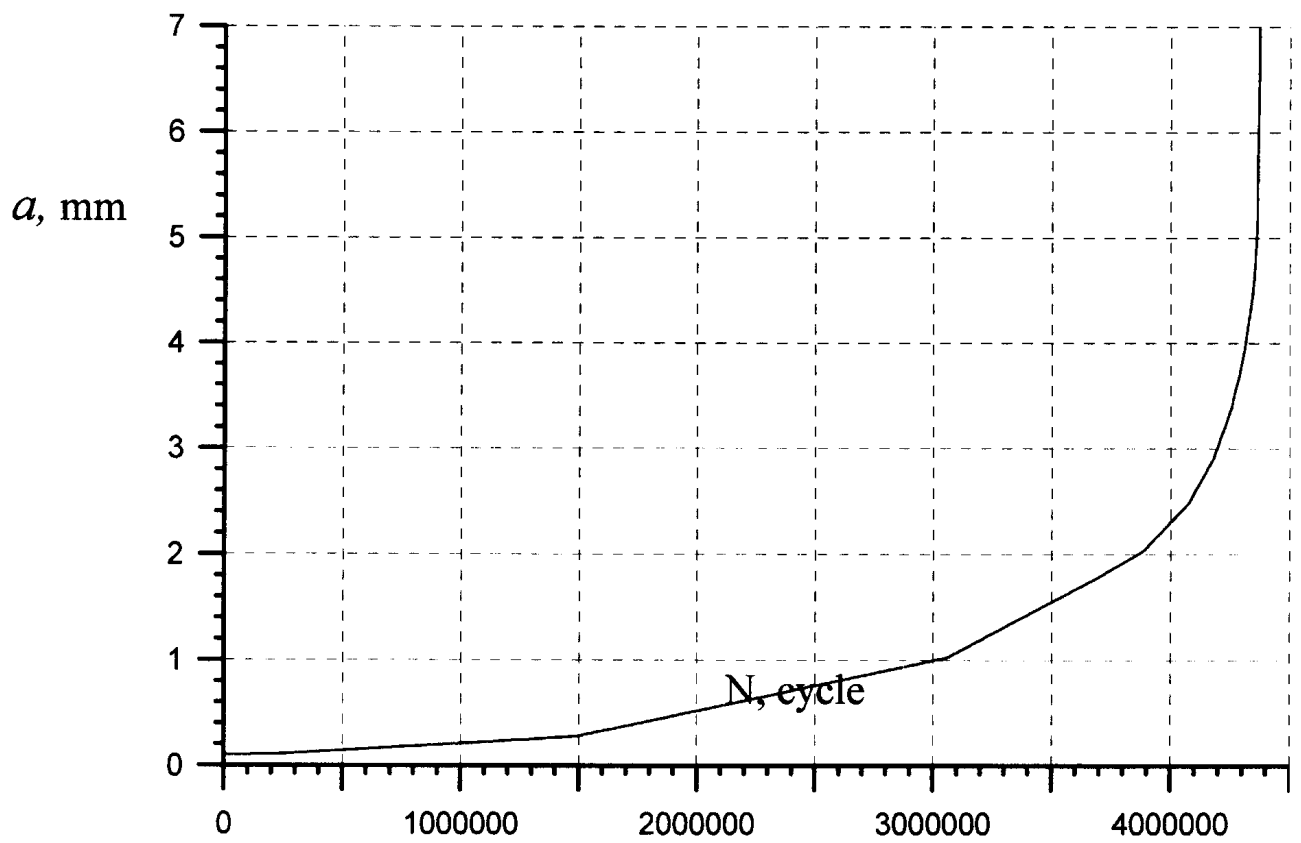


FIG. 15. Crack progress behavior in the base metal.

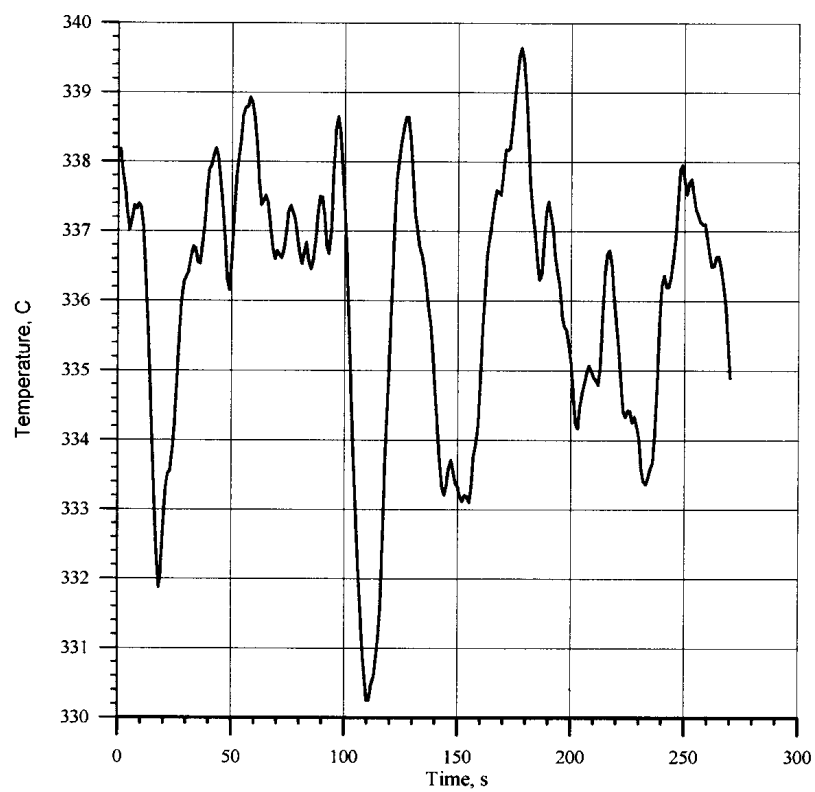


FIG. 16.

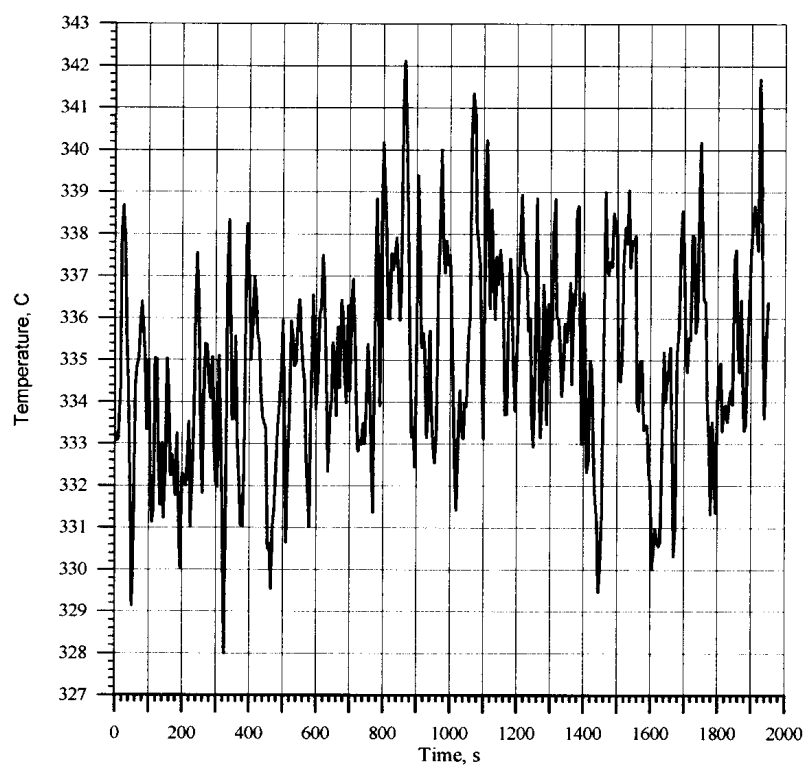


FIG. 17.

5. DISCUSSION OF THE ACHIEVED RESULTS

The data received from NOVATOME can bring certain changes in the coolant temperature pulsations in the low-frequency range. The behavior of pulsations on the outer surface of tube according to the analyzed data is given in Fig. 16, 17. Figure 16 corresponds to the period for the signal to be sensed equal to 1 sec, figure 17 - to the period of 5 sec.

As one may suppose, the results of temperature measurement on the pipeline outer surface show only low-frequency pulsations. Their swing from peak to peak is low enough ($\approx 8 - 14^\circ\text{C}$). But it should be noted that the period of temperature fluctuations measurement may be insufficient to reveal seldom pulsations with the highest possible temperature swing. Approximately 24 hours is considered to be the recommended period for continuous measurement.

6. CONCLUSION

Thermo-mechanical analysis, cyclic strength analysis of a tee and fracture mechanics analysis are performed in the region where mixing of hot sodium jet with cold main flow of sodium occurs.

Basing on the analysis performed, with the assumptions accepted, the following is stated:

a) With increase of pulsations' frequency the depth of penetration and swing of temperatures across the tube wall decreases and, therefore, stresses also decrease.

b) A degree law is established of variation of cyclical damageability versus number of hot jet impacts. To 0,66 Hz frequency growth of damageability of a structure occurs and the subsequent frequency increase is accompanied by the decrease of damageability.

c) Perturbation at frequency of 0,66 Hz gives the most damageability. The time of operation at which a condition of cyclic strength is met Ref. [1] at hot jet pulsation frequency of 0,66 Hz amounts to only 10 hours.

d) Taking into account the given data (in course of temperature fluctuations 0,5 Hz) the period of crack progress through a welded joint is 750 hours, in the base metal - 2430 hours.

On the basis of thermomechanical analysis and cyclic strength calculation crack appearance is possible in the zone where hot jet meets the main pipeline wall. Besides, the presence of microfaults in the weld can initiate a crack and its subsequent growth at sodium temperature pulsations.

The analysis of the achieved results and analysis of the available experimental data on temperature pulsations show more conservatism in the adopted approach to temperature fluctuations.

But the absence of pulsations is also useful to engineering. The achieved negative results require corrections to be brought to the design, fabrication and operation of the developed articles.

It should be also noted that the information on real temperature fluctuations of the flow, temperature variations on the pipeline wall inner surface would let reduce the adopted conservatism level and deeper estimate the degree of structure damageability.

REFERENCE

- [1] Norms for NPP Equipment and Pipelines Strength Analysis PNAE G-7-002-86. Moscow., 1989.

COMPUTATIONAL INVESTIGATION OF TERMOHYDRAULIC ASPECTS OF TWO CONVERGENT FLOWS AT DIFFERENT TEMPERATURES MIXED IN THE TEE JUNCTION AREA

S.I. SCHERBAKOV

Institute of Physics and Power Engineering,
Obninsk, Russian Federation

Abstract. Comparison of calculational results, obtained by the participants of the benchmark on a T-junction of LMFR secondary circuit was carried out. Two-dimensional calculational termohydraulic model of the T-junction was developed, allowing to perform numerous alternative calculations in a short time. Explanation is proposed of appearance near the wall of low-frequency pulsations of velocity and temperature in a mixing streams area. Calculations of transient periodic flow and temperature fields in fluid and a pipe wall for the T-junction was carried out.

1. INTRODUCTION

The participants of the benchmark on a "Tee junction of LMFR secondary circuit" have executed in 1996 computational researches of a structure of flow and temperature fields in a mixing area of sodium streams for the pipe T-junction of the PHÉNIX reactor secondary circuit. The main interest of these researches lays in learning of instability of temperatures fluid and metal of the main pipe wall in area of pipes connection. In this place there is a welded seam on the main pipe. Results obtained by the participants benchmark are in general similar each other and consist in following:

- the small jet after a penetration in main stream flows past close to a main pipe wall,
 - the mixing area of jets makes oscillations about the average position, the frequency of pulsations makes 3-8 Hz,
 - because of a difference of temperatures between main stream and the varying area of mixing, pulsations of temperature arise on an internal surface of the main pipe.
- These pulsation reach 20-25°C.

In 1997, a termomechanical and fracture mechanics analysis of walls of the main pipeline and welded seam in conditions of instability of temperature of an inner skin was executed by the participants. Among other, these researches have shown, that the violation of integrity of a welded seam for given time (90 000 hours on the Phénix reactor) cannot take place, if the frequency of temperature pulsations on a wall exceeds 0.5 Hz. The cracks in a welded seam can appear only from long-duration effect of low-frequency pulsations of temperature on an inner pipe wall. So, a variance between results of termohydraulic calculations and conclusion from termomechanical calculations was occurred. Under the judgment of the author, there are several reasons, because of which there are not enough low-frequency pulsings in results of termohydraulic calculations.

The first reason. The participants mainly used 3D codes with a large number of calculational cells. These codes require appreciable costs of time for one step of changes calculation. Because of time limitations the participants have calculated processes by duration

0.1-2 s. At such time of the process it certainly is impossible to identify low-frequency oscillations. On experience of the author the duration of the non-stationary process of mixing of jets direct calculation should not be less than 30-40 s at time step no more than 0.02 s. Only after this time, the process becomes periodic in the whole frequencies spectrum. The time step is determined by the highest frequencies in the solution, and the duration of calculation - the lowest frequencies.

The second reason. The sizes and the velocity of main stream and small jet do not yield simple reasons of low frequencies of oscillations existence. Low frequencies in a solution are result of combinative oscillations. They arise because of addition of high frequencies of various types. The frequencies interference happens due to restriction of a varying jet moving, in the case when the jet is located about a wall of the pipe. This one more, indirect, confirmation that the small jet is located close to a wall of the main pipe. Calculation results presented by participants, especially the most advanced, indicate that small jets are situated too far from a wall. The cause is hardly set boundary conditions at an entrance of a small jet main stream.

This report objectives are:

- an analysis of calculational results, obtained by the participants of the benchmark for mixing of two streams in a T-junction,
- development of a simple computer two-dimensional model of pipe T-junction for calculation of long time oscillatory termohydraulic processes,
- carrying out the T-junction of LMFR secondary circuit calculations, substantiation of low-frequency temperature pulsations appearance on the pipe wall.

2. A COMPARISON OF TERMOHYDRAULIC CALCULATIONS RESULTS OBTAINED BY THE PARTICIPANTS OF THE BENCHMARK

The hydraulic and temperature calculations of flow mixing in T-junction were carried out by the participants of the benchmark in 1996. The results of these calculations were represented on First Research Co-ordination Meeting in France from 25 to 27 November 1996. The purpose of the calculation was to obtain the spatial distribution of liquid temperatures and velocities and tube wall temperatures averaged on time as well as temperature fluctuation frequencies and amplitudes.

Each participant developed his calculation model and chose computer code independently. The computational models used differ in number of calculational cells, their geometry, in size of the investigated part of the pipe, in cells of the pipe wall presence. All computational models, except of one, are three-dimensional. In one case a two-dimensional computational model is applied. There are a liquid layer about a pipe wall and cells of the pipe wall. The computational codes used and sequence of realization at the different authors differ in yet more large variety. The features of computational codes are not being considered here, while it is possible to tell the following about the calculation procedure. The participants used these for obtaining the results:

- direct non-stationary calculation of velocity and temperatures,
- a sequence of several calculations on different algorithms or codes: a calculation of stationary velocities and temperatures, then a calculation of turbulent pulsations and temperature pulsations, based on these data,

- an evaluation of temperature pulsations of the wall pipe by a direct non-stationary calculation, or by a recalculation using special algorithms.

2.1. Mean characteristics

Despite differences in task settings, the participants have obtained qualitatively consistent results for the average characteristics of the mixing area in the T-junction. In all reports a similar layout of the small jet in the pipe space, same width of streams intermixing zone are obtained. Mean temperatures values of an inner pipe skin, obtained for the thermocouple locations, are given in Table 1. These results are different for different authors.

TABLE 1. PREDICTED MEAN TEMPERATURES (INNER SKIN)

Participant	T1	T2	T3	T15	T6	T1-T6	T2-T6
Italy	684	681	661				
India (3)	676	659	647	642	634	42	25
UK	677	637	625	619	615	62	22
Korea	672	667	655	641	626	46	41
Russia	656	650	647	641	635	21	15
Japan	~683	~655	~625	~618	~618	65	37
India (1)	647	640	635	632	628	19	12
Experience (outer skin)		633	628	623	618		15

It is necessary to explain physical reasons of obtained differences. The behavior of the temperature variations on an inner pipe wall in the direction of fluid velocity (from T1 to T6 in Table 1) is determined by parameters of a small jet layout namely the depth of its penetration into the main flow in a junction place, the declination to a pipe wall, the presence of reflexive current. So, for example, the temperature gradient is very big in the place of the jet come off from a wall. Small variations of a penetration depth and declination of the jet result in significant changes of the temperature distribution in a pipe wall. Thus, the calculational values of mean temperatures of a pipe wall may differ in different calculations, especially when the small jet is located close to the wall.

Authors have obtained different flow patterns. The main difference consists in a declination angle of the small jet to a wall. It has resulted in differences of mean temperatures in the participants' results. The maximum angle of declination is shown in presentations of the participants from United Kingdom and Japan. This can be explained by that the flow pattern of the small jet is being determined mainly by the boundary conditions in the small pipe: such as velocity profile, subtle details of pipes junction, the small jet compression at the nozzle outlet and its turning inside the nozzle. The distribution of velocity mean square on an entrance of the small jet in to the main flow is essentially important for hydraulic calculations.

A conclusion has been made is that it is not permissible to restrict a calculation model by the boundaries of an area where the change of boundary condition causes solution changing. A nonsensitivity of solution from variation of boundary conditions on selected boundaries is needed to be proved first. Or a problem of a jet exit from a long pipe in to a liquid bulk is to be calculated first and then these data should be used in calculation of

T-junction itself. The ignoring of the indicated requirements to the determination of calculation model boundary is a principal drawback of all works performed, which caused the differences in evaluation of mean temperatures of the pipe wall. As shown in the Indian report, these temperature differences of a wall can be obtained in different calculations while using the same code and different computational models.

The analysis of presented by Framatome-Novatome experimental data has shown, that the temperature difference between the neighboring thermocouples is constant. This will be observed if when the small jet is being kept close to the pipe wall without separation. Thus the patterns of mean flow, obtained in Italy, Korea, Russia, seem to be more correct on this parameter.

2.2. Pulsation characteristics

Pulsation characteristics of the liquid and the pipe wall temperature profiles, obtained by the participants of the benchmark, differ much from each other. This is because of the were used quite different methods of pulsation characteristics obtaining.

In some papers (listed in Table 11), steady state or mean on time values of the liquid velocity and temperature have been calculated preliminary. Then, on the basis of these data, the amplitudes of temperature pulsations on the pipe wall and their frequency spectrum were evaluated using another codes and models. The amplitudes of fluid temperature pulsation obtained in such a way, are approx proportional to a gradient of mean temperature in the mixing area. Therefore the distribution of pulsation amplitude in the fluid and pipe wall reminds the mean temperature gradient distribution. Such temperature pulsations are caused by the turbulent flow, they have a statistical character and a high frequency spectrum up to 1 kHz. Their maximum is observed in the vicinity of thermocouple 1, and value decreases downstream. The amplitudes indicated in Table 2 are realized very seldom, since they are a superposition of many oscillations modes. For the data from United Kingdom, at a frequency 8 Hz the temperature pulsations on a wall do not exceed 5 K.

TABLE 2. PREDICTED PEAK-TO-PEAK TEMPERATURE DIFFERENCES

Participant	dT1	dT2	dT3	dT15	dT6	note
UK	86	64	38	6	21	fluid
	59	33	16	9.2	2.6	inner surface
India	~6	~9	~12	~15	~18	fluid
Japan (1996)	~30	~20				inner surface

In other works, (Table 3), liquid non-stationary flow and the temperature profile are calculated and thus periodical changes of liquid velocity and temperature in the vicinity of the pipe wall are detected. The frequency of these variations is less then 10 Hz. These pulsations are not concerned to a turbulence - their scale is very large - and are caused by the interaction of the small jet and the main flow in the whole volume of the pipe. The pulsations of fluid velocity and temperatures results downstreams and have a maximum in the region of thermocouples 2-15. The peak-to-peak of temperature pulsations induced on the inner surface of the pipe reaches 19-20 K in the vicinity of 3-15 thermocouples (Table 3).

TABLE 3. PREDICTED PEAK-TO-PEAK TEMPERATURE DIFFERENCES (INNER SKIN)

Participant	dT1	dT2	dT3	dT15	dT6	f, Hz
Korea				15		3,8
Russia	9	17	20	17	12.5	7-8
Italy	0.5	0.4	4			6,12
Japan (1997)	10.6	24	23.6	14	3.6	

In works, enumerated in Table 3 the analysis of the temperature pulsations, caused by a small-scale turbulence, was not carried. Summarizing, it is possible to say the following. In order to obtain a comprehensive picture of temperature fluctuations on the pipe wall, these two types of distribution should be summed. The result should be as follows: liquid temperature fluctuation span near the pipe wall is approximately constant along the wall, while the dominant frequency of this fluctuation decreases downstream.

3. BRIEF DESCRIPTION OF "TURBO-FLOW" CALCULATIONAL CODE

The two-dimensional calculational code TURBO-FLOW is developed in IPPE to provide a solution of the diverse technical problems in a short time. It is intended for simultaneous solving of several correlated non-stationary transport problems in a limited computational model. The computational model can consist of several diverse parts, interacting with each other. There are no limitations on geometry complexity of a computational model (within the limits of two-dimensional consideration). The list of transport problems, which can be solved, contains calculation of fluid current, calculation of a temperature field in fluid and rigid units, transport problems for concentration of substances, for components not mixing up with fluid etc. To solve any technical problem with the aid of the TURBO-FLOW code it is necessary to present it as a collection of transport problems in a continuum. The features of setting, explained below, are based on a wish to achieve minimum costs of time at realization of concrete calculations.

For the description of a fluid flow problem the equation of motion as conservation law of the scalar value - volumetric density of circulation is used. This equation is completely equivalent to the known vector ones of motion and does not contain any assumptions.

$$\tilde{v} \frac{d\tilde{\Omega}}{d\tau} + \int \mathbf{V} \cdot \tilde{\Omega} d\mathbf{S} = \frac{1}{\rho} \int d\mathbf{r} [\rho \mathbf{g} + \mathbf{f}] \quad (1)$$

where ρ - the fluid density, \mathbf{V} - the velocity vector, \mathbf{g} - the gravitational constant, \mathbf{f} - the volumic density of friction, \tilde{v} , \mathbf{S} and \mathbf{r} - are the integration volume, its surface and closed circuit limiting volume projection onto the solution plane, respectively. Square brackets imply depth averaging over the space free for flow. Definition of circulation:

$$\tilde{v} \tilde{\Omega} = \int d\mathbf{r} [\mathbf{V}] \quad (2)$$

Averaging of stream of circulation on a surface \mathbf{S} :

$$\mathbf{V} \tilde{\Omega} = \tilde{\mathbf{V}} \tilde{\Omega} \alpha, \alpha \geq 1 \quad (3)$$

A flow function F is used for a velocity vector determining. At presence of volumetric sources of flow rate a potential E is used. Such an approach ensures satisfying of mass conservation law automatically:

$$\rho \mathbf{V} = \mathbf{k} \times \nabla F + \nabla E \quad (4)$$

$$\int \rho \mathbf{V} d\mathbf{S} = q_m \quad (5)$$

The components of friction can be circumscribed in any known manner. At a small number of designed cells in a computational model the preferably hydraulic description is:

$$\mathbf{f} = A\rho|\mathbf{V}| \cdot \mathbf{V} / 2 \quad (6)$$

A - Coefficient of friction (1/m), k - At unit-length vector, normal to the solution plane.

The transport problems are formulated as conservation laws. For temperature:

$$v\rho C \frac{dT}{d\tau} + \int \rho C \cdot \mathbf{V} \cdot T d\mathbf{S} - \int \lambda_{eff} \nabla T d\mathbf{S} = q_v \quad (7)$$

For concentration of gas:

$$v\rho \frac{dX}{d\tau} + \int \rho \mathbf{V} \cdot X d\mathbf{S} = q_x v \quad (8)$$

The structure of right members of these equations - volumetric sources and drains - depends strongly on a concrete content of a problem. There can be terms of generation and condensation of a vapour in a right member being solved at calculation of vapour concentration. At calculation of concentration the vapour in a right member can be terms of generation (if T_w more T_s) and condensation a vapour (if $X > 0$ and $T < T_s$). T , T_w - temperature of fluid in a given point and temperature in another part of a computational model, where the heat exchanger, located in a thermal contact to fluid in the given point is circumscribed. The right member of the equation for temperature in a general view can be expressed as follows:

$$q = k(T_w - T) + q_v - q_x r + \dots \quad (9)$$

$$k, q_v, q_x, r$$

Heat transfer coefficient, independent volumetric heat sources, source of concentration X and conversion factor (heat of vapourization).

A field of velocity, which enters in the transport equation is not surely a field of velocity, which is determined by current of fluid. For example, in case of calculation of concentration of a gas, it is necessary to introduce a correction, which is determined separately. A density of fluid, entering in all transport equations and motion equations, is determined by the equation of state:

$$\rho = \rho(T, X, \dots) \quad (10)$$

Motion of units or components of a computational model may play part of one of transport problems. It is a problem of destruction of constructions.

All transport problems are being solved in an uniform stream of time. Each problem is connected, when its current time becomes minimum among all other. The calculational time step (independent for each problem) varies continuously during the solution by criteria, specified by the user and by ones based on the speed of functions variations on previous step. The criterium of reaching a fixed state is a significant increase of time step.

Time-related changes of space allocations of functions (density of circulation, flow function, the temperatures and etc.) are being determined under the implicit scheme of variable directions. When it is impossible to construct an implicit scheme, which is usual for sources and drains as (9), a procedure "of an intermediate layer", permitting one to increase calculational step on time, is used. It is important when calculating heat exchangers. For processes with variations of a field of velocity by external reasons (change of flow rate, increase of bubbles, falling of constructions etc.) special numerical procedures, calculating "allowed" changes of velocity, are used.

The geometry of a two-dimensional computational model is being set in a discrete area with rectangular cells. There can be given several interacting computational models and a type of their interaction (for example, two outlines of a heat exchanger) be defined. There can be impenetrable sites, sources of flow rate, heat etc. inside a model. The sizes on third coordinate of a computational model are being set for each cell individually.

Boundary conditions for a problem of current are condition of impenetrability on hard parts of boundary, specific allocation of one or two components of velocity on open boundaries (including functions in time). The feature of boundary conditions description for a hydraulic problem in the TURBO-FLOW code is, that the boundary nodes of hard sites of a model are considered "as the liquid, fixed by external forces in one or two directions", these nodes are being used in calculation process along with internal ones. Influence of boundaries to current is thus formed, resulting in a fact that speeds limitation on a boundary generates circulation, which then determines a field of speed. Boundary conditions for the transport problems are values of appropriate functions or their derivatives on all boundaries. All boundary conditions can vary during solution on its current results.

Discrete approximation of the equations does not contain any essential differences from ones traditionally used. These approximating satisfy the requirement of correct description of conservation laws in a discrete area. Therefore the streams of circulation, heat, etc. are being determined from numeric values taken in a point located above on current in each calculation cell. Disadvantage of such an approach is equivalent intermixing near to a calculation cell due to the substitution of a vector of speed by its components in the convective terms of the transport equations. To eliminate effects of numerical intermixing the procedure "A figure with right angles" for streamlines, separating streams with different temperatures, concentration and etc. is being applied.

The TURBO-FLOW code is intended for use on IBM PC or compatible, programming language is FORTRAN. Execution time of one time step 0.7-1.5 s on a 486DX2-66 computer.

After each step execution pictures of isolines of calculated functions, graphics on time and numerical information at will of the user are being output to the screen. Isoline pictures (up to 6 pieces) are being output either at once onto one screen or one by one in a large view. There is a possibility to record a sequence of screens (i.e. steps on time) into memory for consequent demonstrating - from 400 up to 1200 pictures in memory 1.44 Mb.

4. TERMOHYDRAULIC COMPUTATIONAL MODEL OF T-JUNCTION

Configurations for the computational model for calculation of fluid flow and one for calculation of a temperature field in fluid and the pipe wall are different.

A two-dimensional calculational region for calculation of flow contains two independent parts. These parts represent two mutually - perpendicular sections of space of the main pipe in a mixing area of jets. Each of these parts is intended for the analysis of one type of oscillations in the mixing area. The non-stationary fields of velocity, obtained for two types of oscillations are being summarized and the result is being used for temperature calculations of fluid and the wall of the main pipe.

It is necessary to make some explanation here. If the jet is oscillating in an unlimited space in two mutually - perpendicular directions, the arising movements of ambient fluid also lay in mutually - perpendicular directions. If the jet is oscillating near to a wall, the oscillation in any direction is causing a movement of ambient fluid along a wall. There are the oscillations of combinative frequencies. Therefore it is necessary to summarize oscillations of different types, if they occur near a wall.

The two-dimensional calculational area for the temperature calculation contains three interacting parts. One part is intended for the temperature calculation of fluid, other - for the temperature calculation on width of wall in different places. The temperatures, obtained for fluid, are being used as boundary conditions for temperature calculation of the wall.

4.1. Calculational grid

A two-dimensional calculational grid, containing all indicated parts for termohydraulic calculation, is shown on Fig. 1. The first part of a grid represents a "liquid pipe", the cross section of which makes a half of cross-section of the pipe, and the thickness of "wall" is equal 0.03 in. The "Liquid pipe" is cut along formive and is extended onto a plane as shown in Fig. 1. "Walls of liquid pipe" pass along a diameter of the main pipe and along a wall of the main pipe. On Fig. 1 boundaries between these parts of "liquid pipe" are shown by dashed lines. The right dashed line is intersecting with the axis of the small pipe. The small jet looks like a cylindrical obstacle to main stream at the right side from a dashed line, and as specific allocation of a vector of velocity on an inlet of a small jet in the main pipe at the left-hand side from a dashed line. This part of the grid is intended for the calculation of mean velocity of fluid and pulsations of velocity, which are caused by periodic change of the distance between the small jet and wall of the pipe. This part is intended for calculation of average temperatures and pulsations of temperature of fluid also. It consists of 1872 cells and occupies in a vertical direction the space: 1 in above the axis of the small pipe and 0.11 in below this axis.

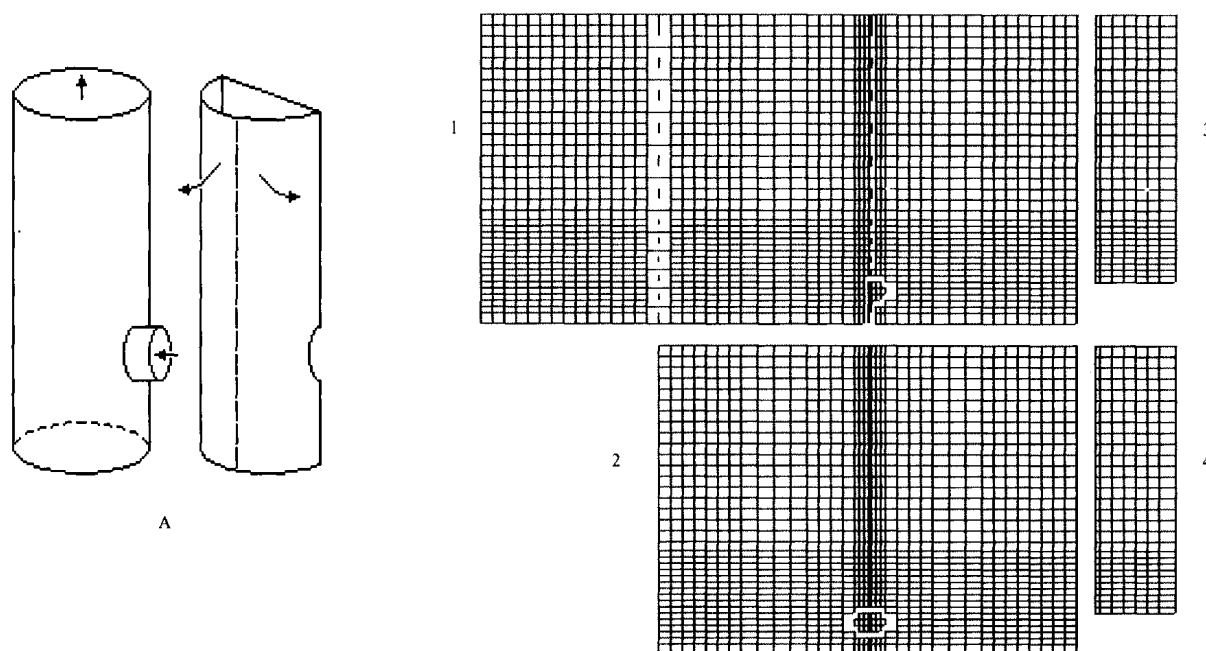


FIG. 1. The calculational grid..

A - part 1 of grid localization in space of main pipe,

1 - part of grid for calculation of velocity and temperatures of fluid, oscillations of a small jet in a radial direction,

2 - part of grid for calculation of oscillations of a small jet along a wall of the main pipe,

3, 4 - parts of a grid for calculation of temperature in a wall of the pipe.

The second part of the grid represents "liquid pipe" of the round form with thickness 0.03 m, located in the pipe along its wall. The small jet in this part of a grid looks as a cylindrical obstacle to main stream. Like the first part of a grid, the "Liquid pipe" is cut along formative and is extended on to a plane. However, its horizontal size is less then the circle of the main pipe. This is enough, preliminary calculations have shown, that the influence of a small jet to the main stream in such an analysis is localized near to the mixing area. The vertical size of the second part of the grid is the same, as of first part, number of cells makes 1332. This part of the grid is intended for calculation of velocity oscillations, caused by variations of the position of the small jet on a direction along a wall.

The third and fourth parts of the grid are intended for temperature calculation of the wall of the main pipeline and contain 203 cells each. The differences between them are, that for a third one (at the top of Fig. 1) temperature of fluid is being transferred from the first part of the grid from a dashed line over a small jet, and for the fourth part (at the bottom of Fig. 1) temperature is being transferred from a vertical line, which is located on a distance of 50 mm from a dashed line.

4.2. Boundary conditions and adopted coefficients of transfer

The boundary conditions for calculation of current of fluid are fixed and consist in the following. On low bounds of calculational grids a distribution allocation of a vertical component of velocity is given. The horizontal component of velocity is set to be equal to zero. For the first part of the grid, an irregular allocation of velocity is given - minimum is located about the mixing area of jets, the maximum is located on the opposite side of the main pipeline. Average velocity is 4.8 m/s, maximum velocity is 5.75 m/s, and minimum velocity is

3.8 m/s. Such allocation of velocity is determined by curving of the main pipe upstream from the place of streams merging. A uniform distribution of velocity of 3.8 m/s is given for the second part of the grid. On top bounds of both calculational grids the horizontal component of velocity is equal to zero, while the vertical component of velocity is not given a priori, it is being determined from calculation.

Periodic boundary conditions are given on side boundaries of the first part of the grid. Values obtained during calculation of functions (velocity, flow function, circulation, temperature) about the left boundary are being transferred onto the right boundary. Similarly, the values of function obtained about the right boundary are being transferred onto the left boundary. It is being executed for each time step. To support this algorithm, the calculational area contains additional cells outside of a line of a cut.

Conditions of impenetrability are given on side boundaries of the second part of a grid. An uniform profile of velocity for a small jet is given in the site connection of pipes. The value of velocity here - 2.27 m/s. The coefficient of friction has been calculated from the speed of the main stream and is adopted to be equal $A = 0.04$ (1/m).

The boundary conditions for calculation of a temperature field of fluid are fixed and consist in the following. A constant temperature $T = 340^{\circ}\text{C}$ is given on the down bound of the first calculational grid, a constant temperature $T = 430^{\circ}\text{C}$ is given in the location of an outlet of the small jet in the main stream. Coefficients of the equation (7) numerical values $\lambda_{eff} = 2200$ (W/m² °C), $C = 1283$ (J/kg °C), $\rho = 861$ (kg/m³).

The boundary conditions for a temperature field of a pipe wall calculation consist in the following. Heat transfer coefficient α and temperature of fluid are given on the internal surface of the pipe wall (the left boundary of the third and fourth parts of a grid on Fig. 1). The temperature of fluid on a boundary is being determined on each time step from time-variant temperature field of fluid. Adiabatic boundary conditions are given on all other boundaries of grids for calculation of temperature of the pipe wall. Numerical values of coefficients of the equation (7): $\lambda_{eff} = 19$ (W/m² °C), $\rho C = 4250$ (kJ/ m³ °C), $\alpha = 100000$ (W/m °C).

5. CALCULATION RESULTS

As a result of the calculations, a sequence of instantaneous flow patterns and temperature fields in fluid and pipe wall is obtained. The calculational time step was being varied and was equal 0.008-0.018 s. The calculated duration of the process from any initial state was 40 s. Time-Averaged values of velocity, temperature and other parameters were obtained by processing of instantaneous values with the aid of a mathematical filter (time constant is 0.6-3 s).

5.1. Flow characteristics

Instantaneous flow patterns for selected instants of a characteristic period are shown in Fig. 2. The mixing area of the main flow and the small jet is localized near the pipe wall. The cause is rather low velocity of the small jet in relation to the velocity of the main flow.

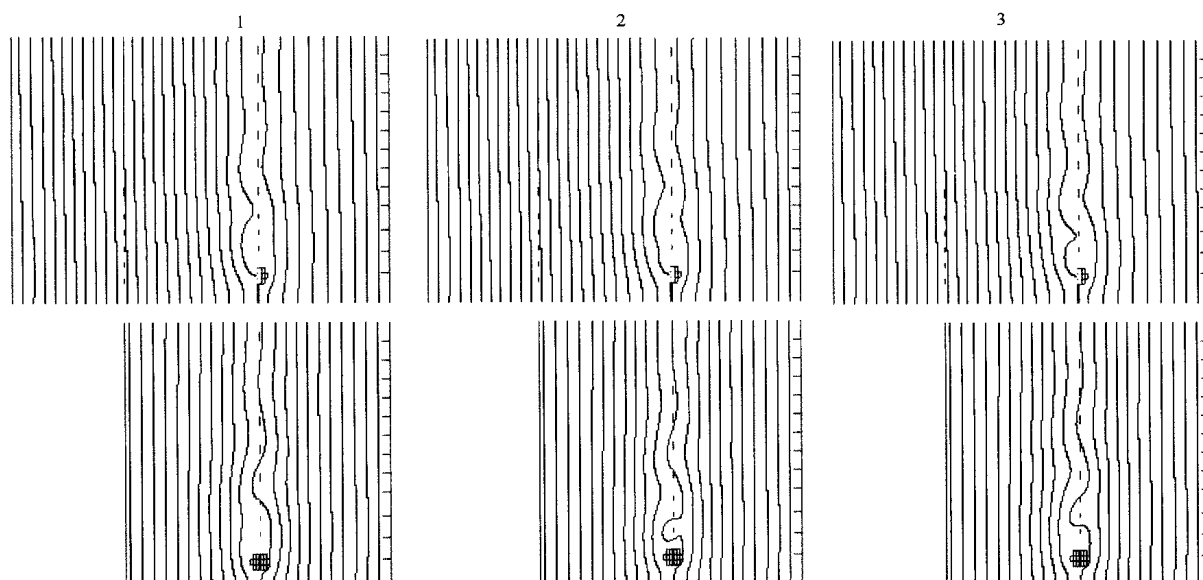


FIG. 2. Contour plots of flow function for consequent instants of an oscillation period..

The flow has a non-stationary periodic character in a mixing area of jets. In the remaining space of the pipe the flow is stable. The frequency of oscillations is 8.1 Hz for radial oscillations being calculated in part I of the model in Fig. 1. For azimuthal oscillations, which are being calculated in part 2 of the model, the frequency is equal 7.45 Hz. The oscillations character of a mixing area reminds known "Karman track" at streamlining of an obstacle. The obtained frequencies correspond to the size of the small jet (it is an "obstacle") and to the main flow velocity. The frequency of radial oscillations is more, than the frequency of azimuthal oscillations, since the size of "obstacle" in part 1 of the model is less than one in part 2 (Fig. 1).

The results of an instantaneous flow patterns processing are shown on Fig. 3.

- time-averaged flow pattern.
- a non-stationary part of flow - a difference between an instantaneous pattern and a mean on time flow pattern. It is shown here how oscillations of fluid velocity happen. These are a sequence of circulations, which rotate in different directions. The sequence as a whole moves on flow with a velocity of 0.7 local mean velocity of fluid.
- RMS of flow pulsations. This picture shows the localization of velocity pulsations area. The horizontal size of the area is 160-180 mm, the vertical size of the area is 600 mm.

5.2. Characteristics of mean temperatures and temperature pulsations

The two flow patterns (for part 1 and part 2 of the computational models) were summarized for each time step. The resulting field of velocity was used for fluid temperatures calculation. Instantaneous temperature fields of fluid are shown in Fig. 4.

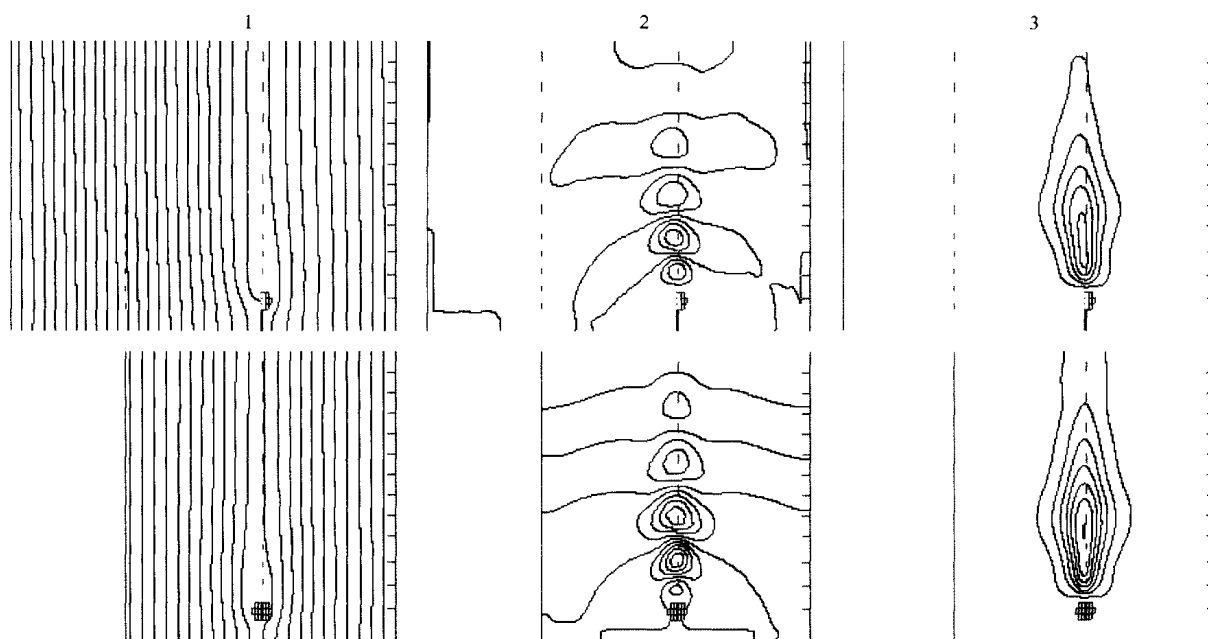


FIG. 3.

1 - contour plot of mean flow function (streamlines for mean flow),

2 - contour plot of flow function fluctuation (instantaneous value),

3 - contour plot of RMS of flow function fluctuation.

The step between lines for plots 2 and 3 is 10 times and 20 times less, than for plot 1.

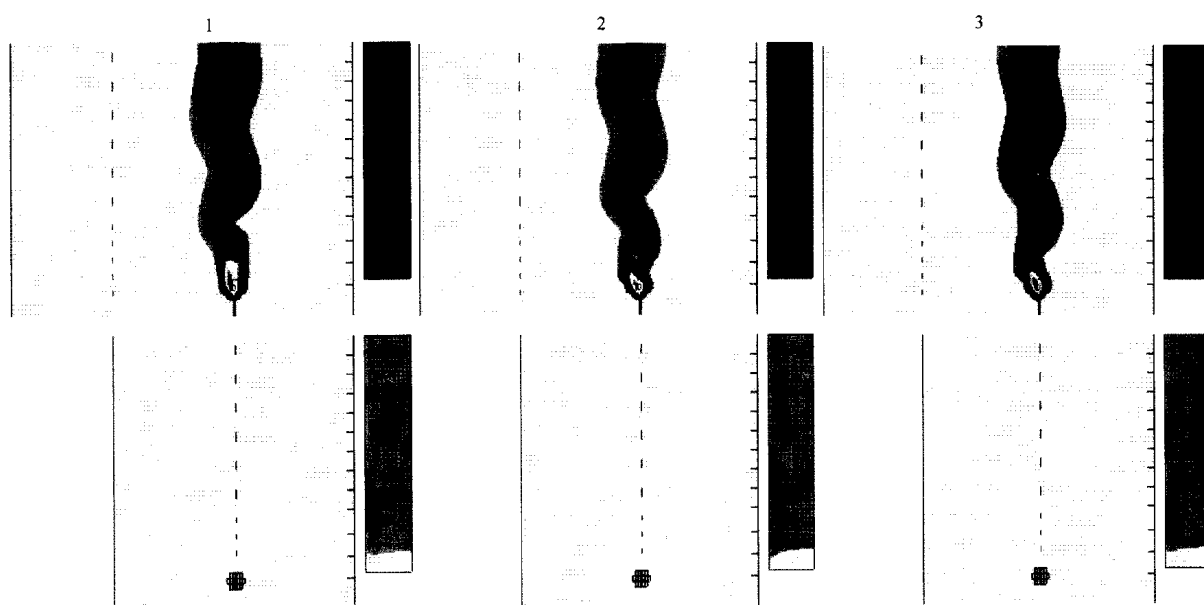


FIG. 4. 1 - Instantaneous pictures of a temperature field for consequent instants of an oscillation period..

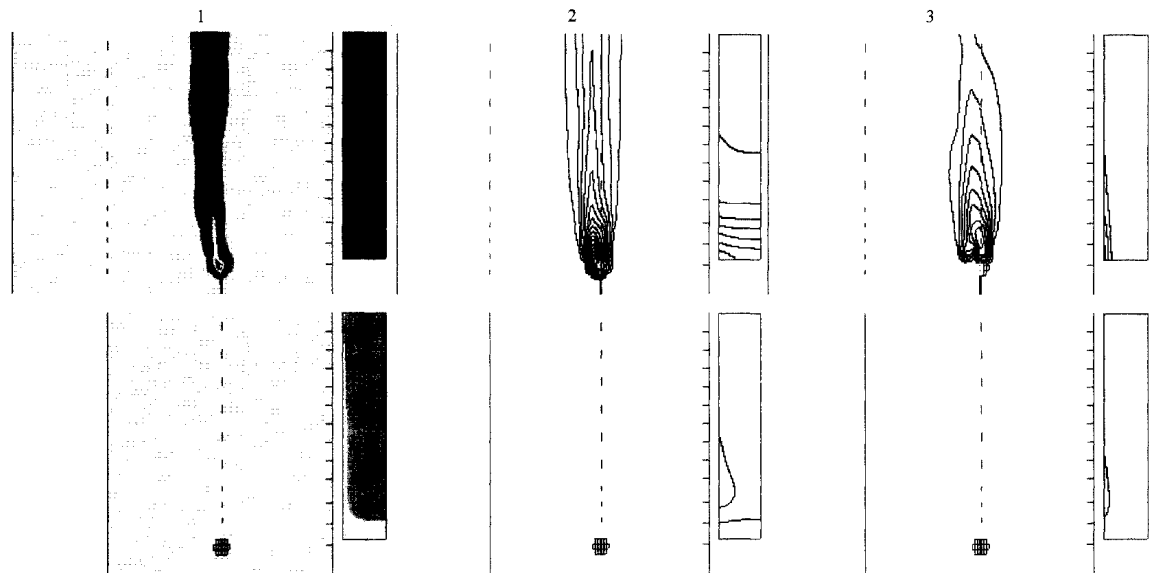


FIG. 5.

1 - instantaneous picture of a temperature field at a moment of oscillations minimum,
 2 - contour plot of mean temperature. Line are drawn every 5 K,
 3 - contour plot of RMS of temperature fluctuation.
 Line are drawn every 2.5 K.

TABLE 4. PREDICTED MEAN TEMPERATURES (°C)

termocouple	vertical distance from axis of small pipe, mm	horizontal distance from center line of small pipe is zero	horizontal distance from center line is 50 mm
1	80	377.6	343.7
2	160	367.5	348.3
3	250	359.4	348.9
15	360	356.1	348.3
6	620	354.2	347.6

The temperature field is similar to a wavy track of hot fluid near the pipe wall. This track moves in the flow direction being cooled gradually. The wavelength of the track and the velocity of its movement determine a frequency of local temperatures pulsations. This frequency is 7.77 Hz (a half-sum of radial and azimuthal flow oscillations frequencies). The width of the track determines an area of increased temperatures effect on the pipe wall. The width of the track varies periodically. The frequency of these variations is 0.325 Hz (half of radial and azimuthal flow oscillations frequencies difference). Maximum width of the track is shown in Fig. 4, and minimum width is shown in Fig. 5.

When the width of the track is maximal, there are the temperature pulsations with frequency of 7.77 Hz on an inner pipe wall, and the wall gets warm proportionally to the span of the pulsations. When the width of the track is minimal, the inner pipe wall is cooled up to the temperature of the main flow. Because of that there are low-frequency pulsations of temperature on an inner pipe wall. The low-frequency pulsations in a part of a pipe wall to the left from the small pipe and in one to the right from the small pipe differ in oscillations phase π .

An area of a pipe wall, which is subject to influence of mean temperature increase and to influence of temperature pulsations, is shown on Fig. 5 - a time-averaged field of temperatures and a RMS of temperature deviations. Values of mean temperatures of the pipe wall at thermocouple positions are given in Table 4. Because of adiabatic boundary conditions on an outer pipe wall the mean temperatures of sodium, ones of inner and outer walls are equal. We can note that mean temperatures have decreased by 5°C because of low-frequency pulsations (Table 1).

Time histories of temperature pulsations for fluid and the wall at thermocouple positions and at the welded seam are shown in Figs 6-11. The character of low-frequency temperature pulsations is determined by a horizontal distance to the small pipe. On a distance of 70 mm the pulsations have sinusoidal character. On a frequency of 7.77 Hz the peak-to-peak of temperature pulsations for an inner wall of the pipe is 28°C at the thermocouple 2 position, while on a frequency of 0.325 Hz it is 35°C in the same place. The temperature pulsations of high frequency do not penetrate into the thickness of a wall. At a depth of 2 mm in a wall there are only low-frequency pulsations of temperature with peak-to-peak of 5°C, while the peak-to-peak is 2.5°C at a depth of 3 mm.

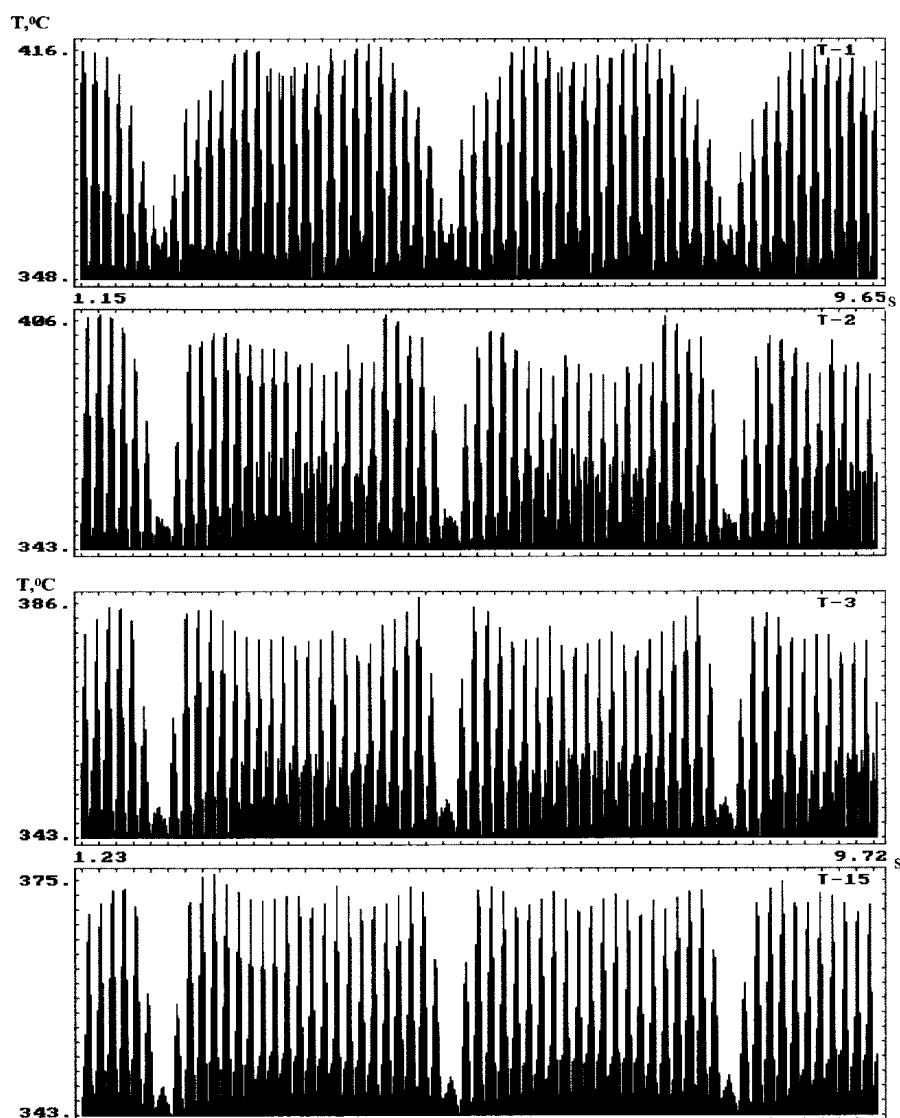


FIG. 6. Temperature history of sodium at thermocouples 1, 2,3 and 15 positions.

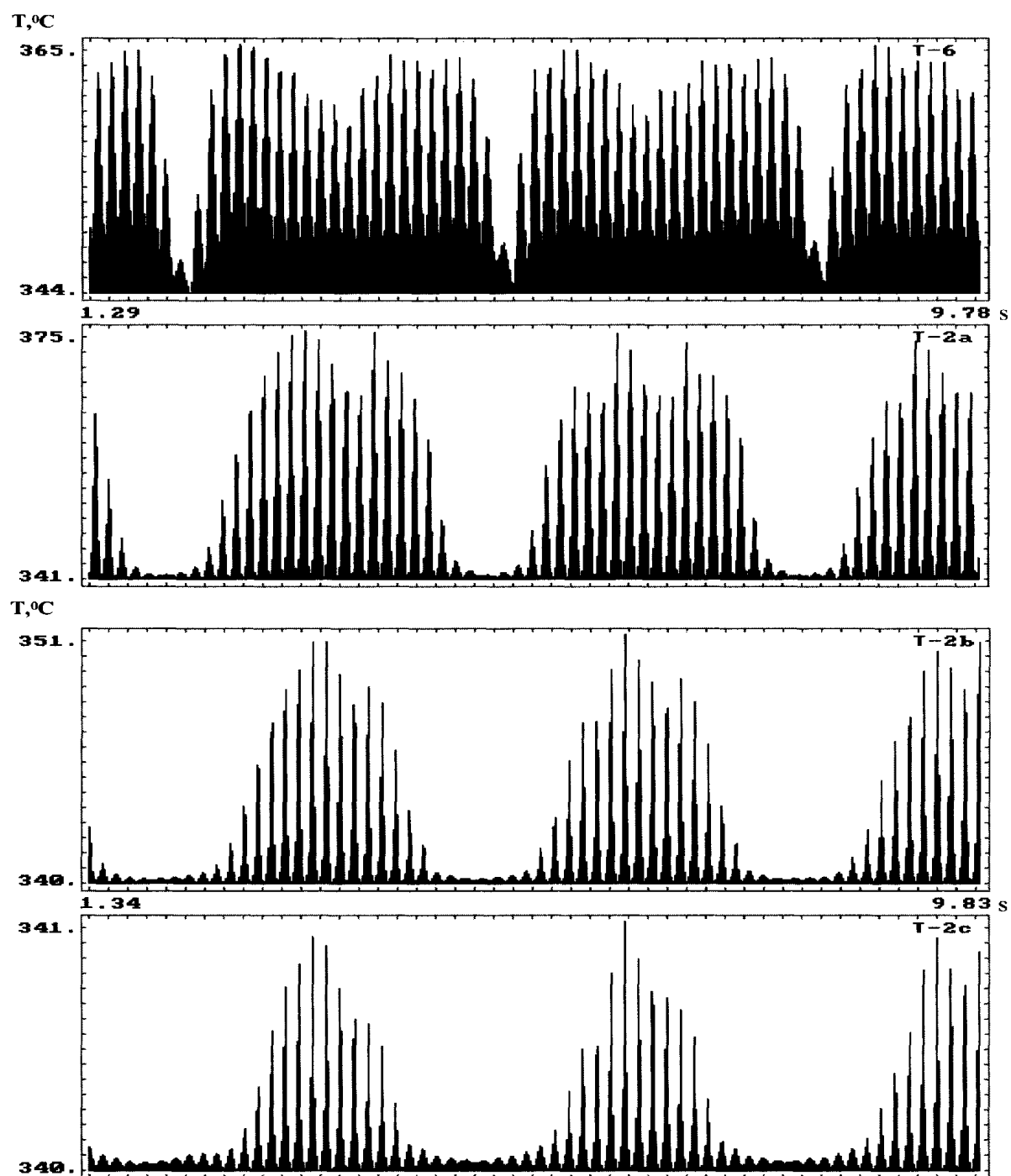


FIG. 7. Temperature history of sodium at thermocouples 6, 2 positions. The points 2a, 2h, 2c are located at a distance of 50, 75, 100 mm from an axis of the small pipe.

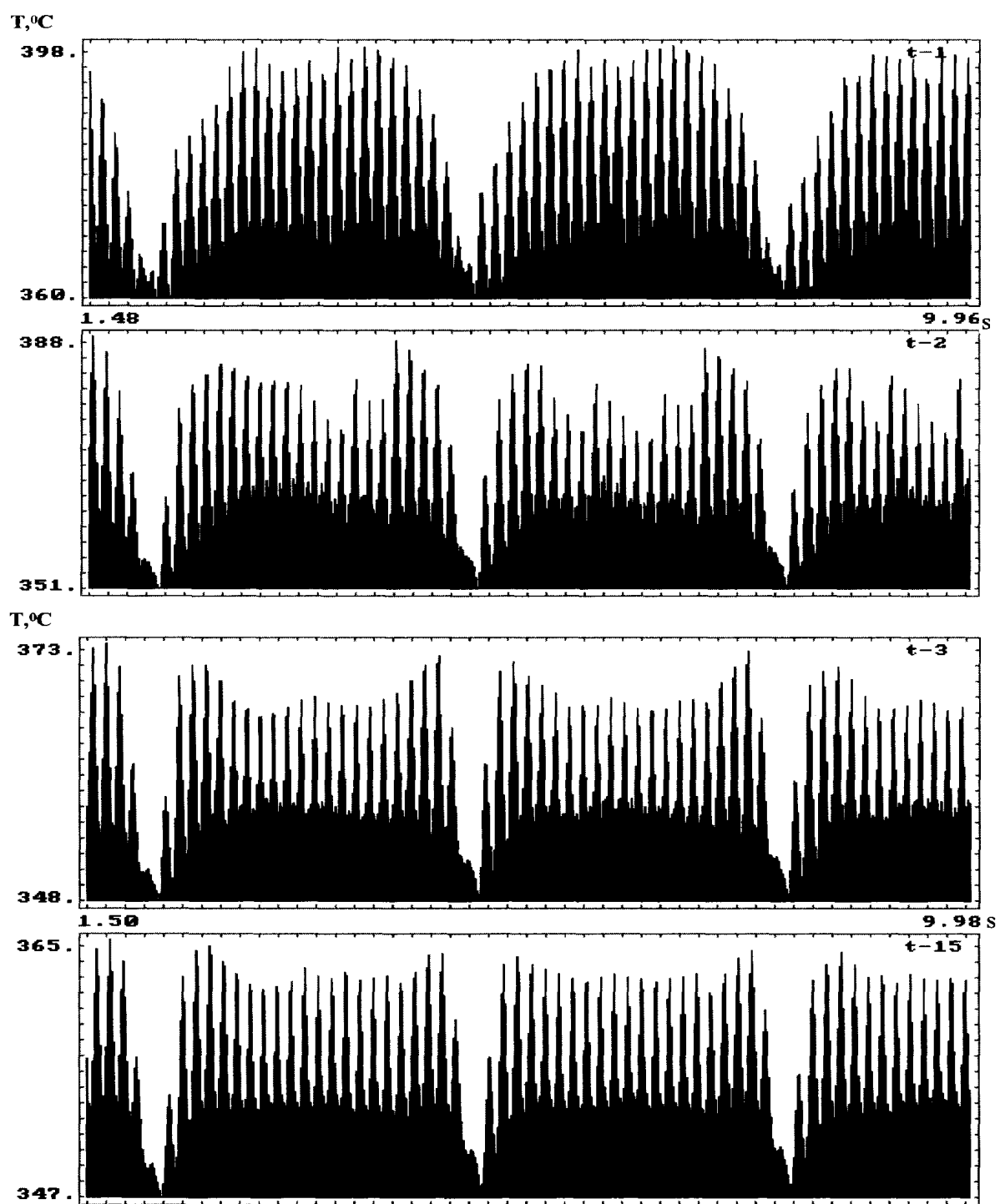


FIG. 8. Temperature history on the inner skin at thermocouples 1, 2, 3, and 15 positions.

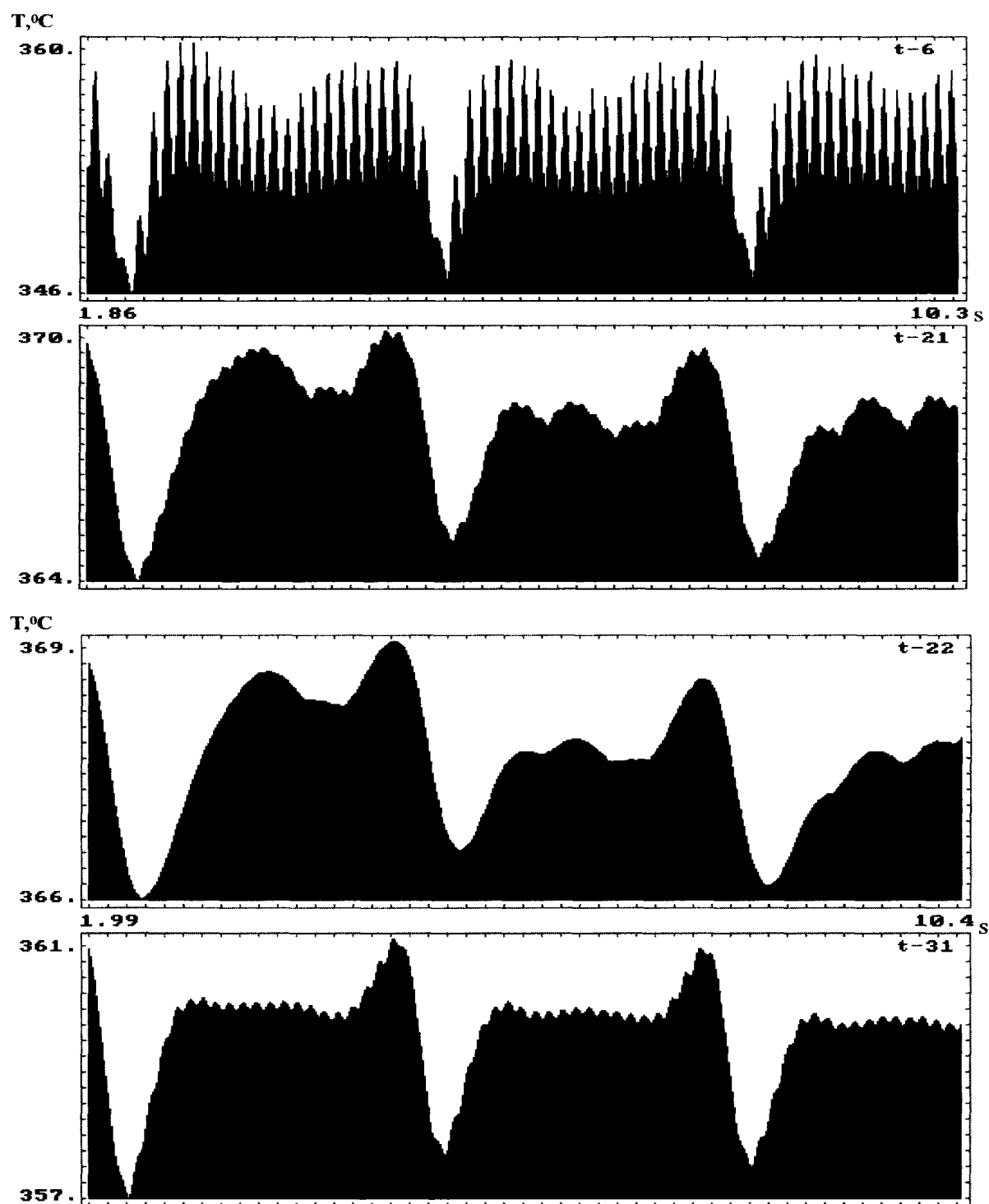


FIG. 9. Temperature history on the wall at thermocouples 6, 2,3 position. The points 21, 22, 31 are located at a distance of 2, 3, 2 mm from the pipe inner skin.

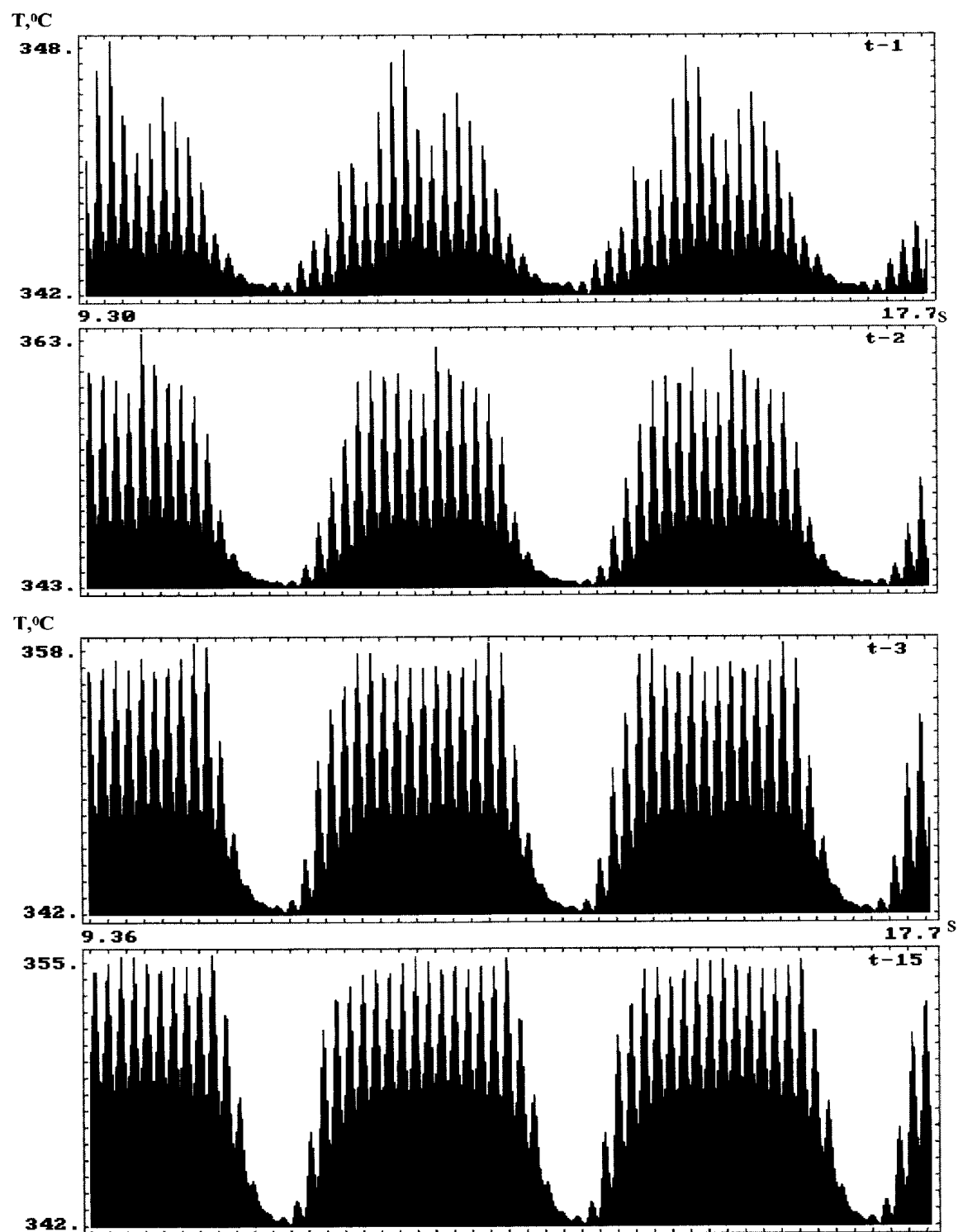


FIG. 10. Temperature history on the inner skin at thermocouples 1, 2, 3, and 15 position. All points are located at a distance of 50 mm from an axis of the small pipe.

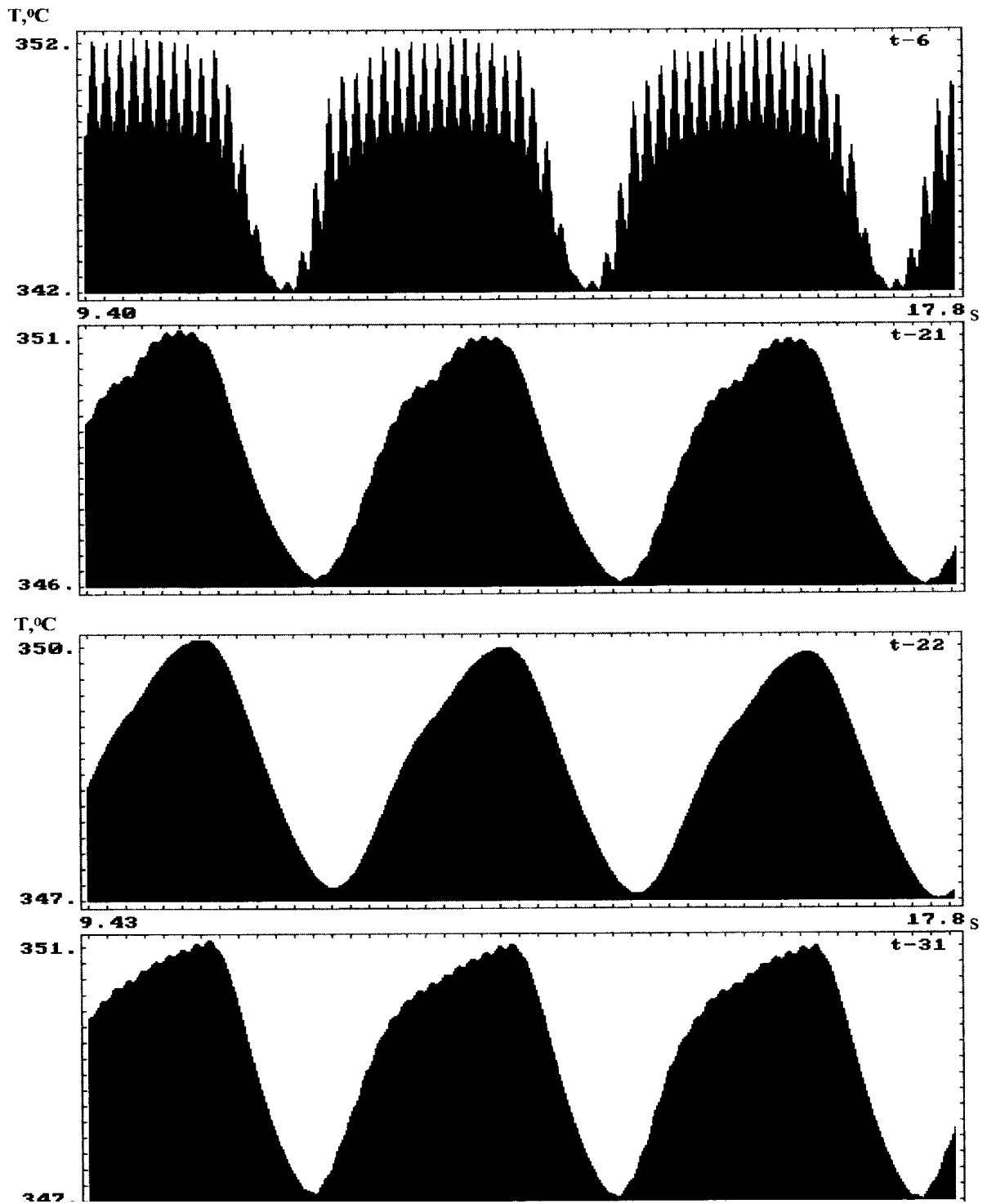


FIG. 11. Temperature history on the wall at thermocouples 6, 2,3 position. All points are located at a distance of 50 mm from an axis of the small pipe. The points 21, 22, 31 are located at a distance of 2, 3, 2 mm from the pipe inner skin.

6. CONCLUSIONS

It is possible to make the following conclusions from the results of available calculational and experimental data comparison. The mixing area is located near a pipe wall because of rather low velocity of the small jet. This area makes oscillations about an average position in different directions with distinct frequencies. Mean temperature state of a pipe wall and intensity of low-frequency, combinative oscillations of mixing area as well as temperatures of a wall depend considerably on a position of the small jet downstream from a merging place.

It is necessary for correct calculation of the mean characteristics to determine carefully boundary conditions at an entrance of the small jet. The best decision is to locate boundary of a computational model inside the small pipe. Authentic calculational results for non-stationary intermixing of liquid jets can be obtained by a prolonged calculation of the oscillatory process only. A time step calculational should be small enough to enable calculation of highest frequencies of the mixing area oscillation. The calculation duration should allow calculation of lowest, combinative frequencies of oscillations, so, it should be more, than the time of these frequencies establishment.

It is possible to recommend an increase of the small jet velocity up to the value of the main flow velocity for elimination of temperature pulsations in a pipe wall.

It is possible to make the following conclusions from results obtained in this work. It is developed a two-dimensional calculational termohydraulic model of the T-junction, permitting to perform numerous alternative calculations in a short time and to study consequences of various design variations. There is proposed an explanation of low-frequency pulsations of velocity and temperature appearance in a mixing streams area, located near to a wall.

Calculations of non-stationary periodic flow and temperature fields in fluid and a pipe wall for the T-junction of LMFR secondary circuit are carried out. The frequencies of oscillations of fluid in a mixing area are 8.1 and 7.45 Hz for radial and azimuthal oscillations respectively. The combinative frequencies are 7.77 and 0.325 Hz. At a frequency of 7.77 Hz the peak-to-peak temperature difference for an inner pipe skin is 28°C at thermocouple 2 position, at a frequency of 0.325 Hz it is 35°C in the same place. At a depth of 2 mm in a wall the peak-to-peak temperature difference decreases down to 5°C at a frequency of 0.325 Hz. High-frequency oscillations do not penetrate by this distance. It is necessary to notice, that the lowest frequencies are being calculated as a difference of the highest frequencies. Therefore the value accuracy of frequency is rough in a calculation, and the lowest frequencies may have no the fixed value in an experiment. It is necessary to use the most dangerous of predicted frequencies for termomechanical calculations.

THERMAL STRIPING BENCHMARK EXERCISE: THERMAL HYDRAULIC ANALYSIS OF THE PHENIX FAST REACTOR SECONDARY PIPEWORK T-JUNCTION

R. STAINSBY, D. MARTIN
AEA Technology plc
Risley, Warrington
Cheshire, United Kingdom

Abstract. A thermal hydraulic analysis of the T-junction which forms the basis of the Thermal Striping Benchmark Exercise has been carried out using the CFX4 CFD code together with an analytical boundary layer attenuation model. The mean momentum, temperature, turbulence and temperature variance fields were determined using CFX4 and the results were used to construct the spectra of the temperature fluctuations at the positions of the thermocouples. Application of a boundary layer attenuation model generated spectra at both the inside and outside surfaces of the pipe wall. These spectra were used to synthesise fluctuating temperature histories in the fluid and on both surfaces of the pipe wall at the thermocouples which showed significant temperature variances. Out of the 15 thermocouples, significant variances were found only at Thermocouples 1,2,3,6 and 15.

1. INTRODUCTION

This paper describes the thermal-hydraulic modelling, carried out by AEA Technology, of the T-junction which forms the basis of the IAEA (and the European Working Group on Codes and Standards) benchmark exercise on thermal striping.

The thermal hydraulic analysis was divided into three main tasks. The first task was to predict the flow, temperature, turbulence and temperature variance distributions using the CFX4 computational fluid dynamics (CFD) code. The second task was to use the predicted velocity, turbulence and variance fields to generate the spectra of the temperature fluctuations in the fluid adjacent to each thermocouple location. An attenuation model, which was based on a 1-dimensional transient conduction model, was applied to the fluid spectra to determine the spectra at both the inner and outer surfaces of the wall. The third task was to synthesise fluctuating temperature/time histories based on the information contained within the spectra and a computer program was written to do this. This program uses inverse fast Fourier transforms (FFT's) to perform the reverse of the operations that are required to obtain a spectrum from a random signal. The random nature of the temperature~time history is generated by substituting random phase angles into the inverse FFT's.

2. COMPUTATIONAL FLUID DYNAMICS MODEL

2.1. Overview of the model

A model of the T-junction was set up using AEA Technology's general purpose CFD code CFX4. CFX4 is based on a multi-block body-fitted finite volume discretisation scheme and solves transport equations for velocity, mass continuity, turbulence, enthalpy and for an arbitrary number of user-defined scalars.

Steady flow conditions were assumed to exist within the T-junction so a steady-state calculation was performed. As the two inlet flows were at different temperatures and, therefore, densities, the density field was allowed to vary with temperature and the resulting buoyancy forces were included in the model.

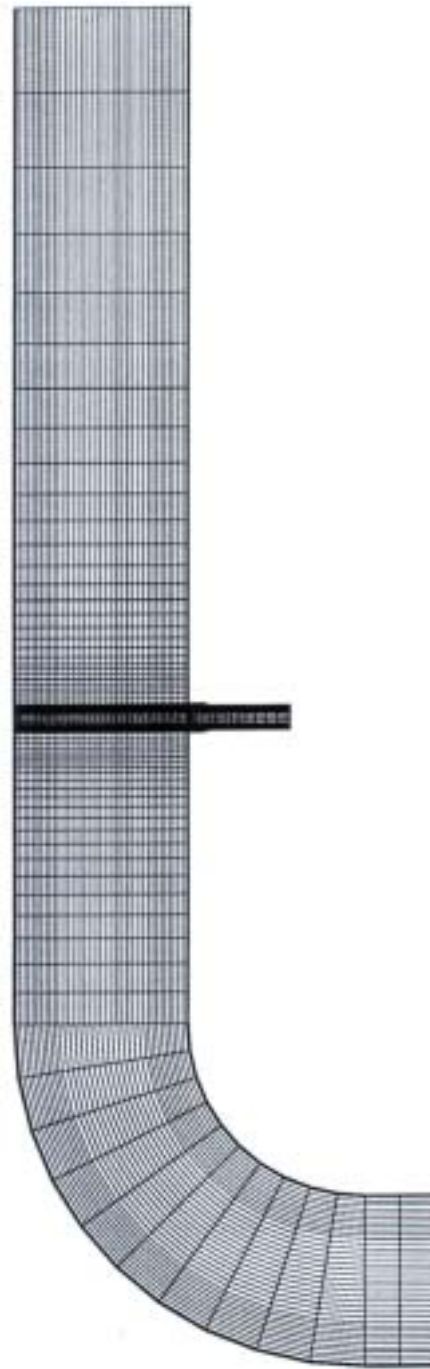


FIG. 1. Vertical section through the computational grid.

The normal use of CFX4 does not allow fluctuating temperatures to be calculated directly. To do so would require a large eddy simulation (LES) which, whilst technically feasible with CFX4, would be prohibitively expensive to run for 3-dimensional problems. Therefore, the approach adopted was to use an additional scalar transport equation to solve for the variance of the temperature fluctuations.

Previous experience of predicting the flow around bends has shown that the resolution of the secondary transverse flows is sensitive to the way in which the convection terms are discretised. Specifically, the false diffusion inherent in first order upwind and hybrid

schemes tends to lead to an under-prediction of the secondary velocities. Therefore, in this benchmark exercise, all of the transport equations have been discretised using the higher order upwind scheme (HUW) which is a non-diffusive second order scheme.

2.2. Computational grid

A computational grid was constructed which represented the fluid and the pipe walls within the T-Junction. The region covered by the grid extended from 0.4m upstream of the bend to 2.1m downstream of the centre-line of the T-junction and included 0.3m of the small branch pipe. The grid contained 102984 cells which were weighted to concentrate them in the mixing zone. Figure 1 shows a longitudinal section through the computational grid.

2.3. Temperature variance equation

The temperature variance equation is obtained by multiplying the transport equation for the instantaneous temperature fluctuations with the fluctuating temperature field. Time averaging the resulting equation leads to a transport equation for the variance of the temperature fluctuations. This variance is simply the mean square value of fluctuating temperature history. The variance equation derived in this way contains higher moment terms which must be expressed, or modelled, in terms of known quantities. The modelling applied leads to a “one-equation” variance model, so called because only one partial differential transport equation needs to be solved for the variance field if the velocity, turbulence and temperature fields are known.

The variance equation is;

$$\frac{\partial \rho \bar{\theta}^2}{\partial t} + \frac{\partial \rho U_j \bar{\theta}^2}{\partial x_j} = D_\theta + P_\theta - \rho \varepsilon_\theta$$

where the three terms on the RHS represent the diffusion, generation and dissipation of temperature fluctuations, the modelled forms of which are, respectively;

$$D_\theta = \frac{\partial}{\partial x_j} \left(\left(\frac{\mu_T}{\sigma_\theta} + \frac{\mu}{Pr} \right) \frac{\partial \bar{\theta}^2}{\partial x_j} \right); \quad P_\theta = 2 \frac{\mu_T}{\sigma_\theta} \left(\frac{\partial T}{\partial x_j} \right)^2; \quad \varepsilon_\theta = \frac{\bar{\theta}^2 \varepsilon R}{k}$$

where R is the ratio of the dynamic and thermal turbulent time scales and is assumed to be constant and to take the value of 2.

The assumption of a constant turbulent time scale ratio is only true when the structures of the momentum and temperature fields are identical. An alternative is to derive a transport equation for the dissipation of variance ε_θ giving rise to a two-equation variance model. However, as the dissipation equation itself contains unknown terms which have to be modelled, the decision was made to limit the variance model to a one-equation representation.

2.4. Boundary conditions

Inlet boundaries were defined to exist upstream of the bend in the main pipe and on the end of the stub which represented the branch pipe. At both of these inlets, fully developed

turbulent flow was assumed to exist with the normal velocity following a power law relationship of the form;

$$U = U_c(1 - r/R)^n$$

with the mean velocity and centre-line velocities related by;

$$\bar{U} = \frac{2U_c}{(n+1)(n+2)}$$

Values of n were chosen to suit the Reynolds numbers of the flows in the two pipes (Knudsen and Katz [1]), with n values of 1/10 and 1/7 being applied to the main and branch pipes respectively.

The inlet profiles for the turbulent kinetic energy k were obtained using mixing length hypothesis [2] from;

$$k = l_m^2 \left(\frac{\partial U}{\partial r} \right)^2$$

where the mixing length l_m was obtained from Nikuradse's equation;

$$\frac{l_m}{R} = 0.14 - 0.08 \left(\frac{r}{R} \right)^2 - 0.06 \left(\frac{r}{R} \right)^4$$

The inlet turbulence dissipation rate profile was given by;

$$\varepsilon = \frac{C_\mu^{3/4} k^{3/2}}{l_m} \quad ; \quad C_\mu = 0.09$$

The inlet temperature profiles were assumed to be uniform and the temperature variance at both inlets was assumed to be zero.

The outer surface of the pipe walls was assumed to be adiabatic. Whilst the technical specification [3] stated that the heat loss from the pipework was 130 W/m and, at the specified flow rate, this causes a temperature drop of only 1.3×10^{-4} °C/m. Therefore the assumption of adiabatic boundaries will have a negligible effect on the predicted temperatures in pipework which is only a few metres long.

2.5. Material properties

The physical properties of liquid sodium and the pipe walls used in the calculation were as follows:

Sodium

Density (kg/m ³)	870 - 0.2422 ($T - 613$) with T in Kelvin
Viscosity	31.49 mPa.s
Thermal conductivity	75.24 W/m/K
Specific heat capacity	1.296 kJ/kg/K

Pipe Walls (AISI 304 Stainless steel)

Thermal conductivity	20 W/m/K (Branch pipe) 18.8 W/m/K (Main pipe)
Density	7930 kg/m ³
Specific heat capacity	0.56 kJ/kg/K

The density of liquid sodium was allowed to vary with temperature so that buoyancy effects to be taken into account. In addition, the use of a variable density allowed the simultaneous prescription of the correct mass flows and the correct mean velocities at both of the inlet boundaries. All of the other physical properties were assumed to not vary with temperature except for a slight variation in the thermal conductivity of the walls where different, but constant, values were used for the branch and for the main pipe.

3. CONSTRUCTION OF SPECTRA

Following the method presented by Peniguel [4], a spectrum at a given location in the fluid is constructed using the mean values of U , k , ε , and variance obtained from the CFD solution. The shape of the spectrum is an empirical fit to experimental measurements and is attributed to Buffet and Tenchine [5]. In sodium, there exists four apparent frequency breaks at which the shape of the spectrum changes, and these are defined as;

$$f_1 = \frac{U}{2\pi} \left(\frac{\varepsilon}{k^{3/4}} \right)$$
$$f_2 = \frac{U}{2\pi} \left(\frac{\varepsilon}{\alpha^3} \right)^{1/4}$$
$$f_3 = \frac{U}{2\pi} \left(\frac{\varepsilon}{(v\alpha^2)} \right)^{1/4}$$
$$f_4 = \frac{U}{2\pi} \left(\frac{\varepsilon}{v^3} \right)^{1/4}$$

Over the frequency intervals between the above breaks, the power spectral density is defined by;

$$0 < f < f_1$$

$$E_\theta(f) = \frac{\bar{\theta}^2}{F(v, \alpha, k, \varepsilon)} \frac{2\pi k^{5/2}}{U \varepsilon^2}$$

$$f_1 < f < f_2$$

$$E_\theta(f) = \frac{\bar{\theta}^2}{F(v, \alpha, k, \varepsilon)} \varepsilon^{-1/3} \left(\frac{2\pi}{U} \right)^{-2/3} f^{-5/3}$$

$$f_2 < f < f_3$$

$$E_\theta(f) = \frac{\bar{\theta}^2}{F(v, \alpha, k, \varepsilon)} \alpha^{-1} \left(\frac{2\pi}{U} \right)^{-2} f^{-3}$$

$$f_3 < f < f_4$$

$$E_\theta(f) = \frac{\bar{\theta}^2}{F(v, \alpha, k, \varepsilon)} \alpha^{-3} \varepsilon^{2/3} \text{Pr}^{-2/3} \left(\frac{2\pi}{U} \right)^{-14/3} f^{-17/3}$$

where

$$F(\nu, \alpha, k, \varepsilon) = \frac{5}{2} - \frac{k}{\varepsilon} - \left(\frac{\text{Pr} \alpha}{\varepsilon} \right)^{1/2} \left(\frac{2}{7} + \frac{3}{14} \text{Pr}^{7/3} + \text{Pr}^{-1/2} \right)$$

These equations define a one-sided spectrum such that the variance is given by;

$$\bar{\theta}^2 = \int_0^\infty E_\theta(f) df$$

4. BOUNDARY LAYER ATTENUATION

The attenuation of temperature fluctuations on transmission through a boundary layer was modelled using Peniguel's conduction damping model. This model is a solution to the partial differential equations which represent the conjugate heat transfer problem of transient one-dimensional conduction across the boundary layer and through the pipe wall. Fourier transforms are used to transform the equations from time~distance space into frequency~distance space.

The edge of the conduction dominated part of the boundary layer is at a distance $y=\delta$ from the pipe wall (which is at $y=0$), and the outer surface of the pipe wall is at $y=-L$. The resulting transfer functions at the inner and outer surfaces of the pipe wall respectively are;

$$H_s(\omega, 0) = \frac{e^{\chi_\delta} (e^{\chi_L} + 1)}{\left((e^{2\chi_L} + 1) - [(1 + \sigma)e^{2\chi_L} + (1 - \sigma)](1 - e^{2\chi_\delta}) / 2 \right)}$$

and

$$H_s(\omega, -L) = \frac{2e^{\chi_\delta} e^{\chi_L}}{\left((e^{2\chi_L} + 1) - [(1 + \sigma)e^{2\chi_L} + (1 - \sigma)](1 - e^{2\chi_\delta}) / 2 \right)}$$

where

$$\chi_\delta = (1 + i)\delta \sqrt{\frac{\omega}{2\alpha_F}} ; \chi_L = (1 + i)L \sqrt{\frac{\omega}{2\alpha_S}}$$

and

$$\sigma = \frac{k_S}{k_F} \sqrt{\frac{\alpha_F}{\alpha_S}}$$

For a given frequency, the power spectral density at either surface of the pipe wall is constructed from the product of the corresponding transfer function and the power spectral density within the fluid. Thus, complete spectra are generated at both of the surfaces of the pipe wall by determining the transfer function at suitable increments of the full frequency range of the spectrum in the fluid. In practice however, to avoid numerical underflows and overflows, the maximum frequency that can be tolerated numerically is a few orders of magnitude less than the highest frequency in the fluid.

5. GENERATION OF A TIME SERIES FROM A SPECTRUM

The previous two sections detailed the construction of the spectra in the fluid and at the inner and outer surfaces of the pipe wall. This section details a technique by which

temperature~time histories can be synthesised which possess all of the properties contained within the given spectra. Because a temperature~time history is represented numerically by a finite number of samples separated by a constant time increment it is, more generally, referred to as a time series.

The technique used to generate a time series is effectively a reversal of the normal method of deriving a spectrum from a time series. Therefore, it is useful to present the method by which a spectrum is derived from a time series before presenting the reverse of the procedure.

5.1. Generation of a spectrum

This section gives the equations for generating a spectrum from a time series. This follows the method given by Newland [6]. The method starts from a discrete time series, i.e., a series of measurements at equally spaced time intervals and it is assumed that the time series has a mean value of zero. Using the Fast Fourier Transform (FFT) method this time series is transformed into a Fourier series, which is used to determine the spectrum. There are a few technical issues to consider, some of which will be mentioned in the description of the method and some which will be discussed later. The advantage of using the Fast Fourier Transform is that it is computationally efficient, this is a standard method, the details of which can be found in [6].

The method of generating a spectrum from a time series starts from a series of values, x_r , at equally spaced times.

$$x_r, \quad r = 0, 1, \dots, (N - 1)$$

There are N values of x_r which are spaced at intervals of ΔT , so the total time for the series is

$$T = N \Delta T$$

It is implicitly assumed that the time series represents values which are constant over the time interval ΔT and it is also assumed that the time series has zero mean.

The Fast Fourier Transform (FFT) method is used to determine the Fourier coefficients of this time series. There are N terms in the Fourier series, the same number as in the time series.

$$X_k = \frac{1}{N} \sum_{r=0}^{N-1} x_r e^{-i 2 \pi \frac{k r}{N}}, \quad k = 0, 1, \dots, (N - 1)$$

The FFT depends on N being a power of 2. It has been assumed that there are sufficient members of the time series for this to be so. If this is not so then the time series can be extended by the addition of zeros until there are the required number of terms. This modifies the equations slightly, and Newland [6] gives the details. It will be assumed that N is a power of 2 for simplicity.

The first stage in determining the spectrum is to obtain the discrete spectrum. The coefficients of the discrete spectrum are given from the Fourier coefficients by taking the

product of each Fourier coefficient, X_k , with its complex conjugate, X_k^* , and hence the spectral coefficients are real numbers;

$$S_k = X_k^* X_k$$

This represents a spectrum which only contains values at equally spaced frequencies, and is a result of using a discrete time series. The spectrum is usually assumed to be continuous and so the discrete spectrum is only an approximation to the desired one. The discrete time series is taken to be a sample of the actual time signal which is continuous and contains terms at all frequencies (maybe within a range). The spectrum for this time series should be a continuous function of the frequency. Newland [6] shows how a continuous spectrum can be derived from the values given by the above equation. This is achieved by using the following equation;

$$S(\omega_k) = \frac{T}{2\pi} S_k$$

where

$$\omega_k = \frac{2\pi k}{T} = k \Delta\omega$$

and $\Delta\omega$ is the spacing between the frequencies for the Fourier components. This continuous spectrum is known as the smoothed spectrum obtained from the discrete spectrum because it is usually a smoothed version of the actual spectrum, and so is usually an approximation.

The frequency spacing of the spectrum is related to the total time for the series;

$$\Delta\omega = \frac{2\pi}{T}$$

The frequency spacing decreases as the length of the time series increases, so increasing the length of the time series improves the accuracy of the spectrum provided that the number of terms increases.

The maximum frequency for the spectrum is given by;

$$\omega_m = \Delta\omega N = \frac{2\pi}{\Delta T}$$

which increases as the number of values in the time series increases, or the time interval decreases. The value given by the above equation is not the maximum frequency represented by the spectrum, which is less due to the problem known as aliasing. This problem arises from use of finite time series to generate a finite Fourier series and this is discussed by Newland[6]. The outcome is that the spectrum is only valid up to a frequency given by;

$$\omega_{\max} = \frac{\pi}{\Delta T}$$

which is half the maximum frequency defined previously. This is the Nyquist frequency. Beyond this frequency the spectrum repeats itself. The spectrum repeats itself with a period of

ω_{\max} . The maximum frequency depends on the time interval ΔT used in the time series, and this in turn depends on the length of the time series T and the number of terms N .

5.2. Generation of a time series

The method described in the previous sub-section is reversed to give a time series from a given spectrum. Newland [6] gives an outline of the method, a more detailed account is given here. The method starts from a continuous spectrum which is used to determine a discrete spectrum. This is used to determine Fourier coefficients from which, by using the Inverse Fast Fourier Transform (IFFT) method, a time series is derived.

The spectrum is assumed to consist of a continuous function, $S(\omega)$, of the angular frequency ω . This will be defined up to a maximum frequency ω_{\max} ;

$$S(\omega), \quad 0 \leq \omega \leq \omega_{\max}$$

This maximum frequency is the Nyquist frequency. It is half of the maximum frequency required for the Inverse Fast Fourier Transform (IFFT), as a result of the aliasing problem mentioned in the previous section. If the number of terms in the IFFT is limited to N , then the generated time series will have N terms and the time, T , for the length of the time series will be given by;

$$T = \frac{\pi N}{\omega_{\max}}$$

For a given spectrum increasing the number of terms increases the length of the time series. If a particular length is required for the time series then this specifies the number of terms required.

The coefficients of the discrete spectrum are determined from the continuous spectrum at equally spaced angular frequencies by;

$$S_k = S(\omega_k) \left(\frac{2\pi}{T} \right), \quad k = 0, 1, \dots, \frac{N}{2}$$

where

$$\omega_k = k \Delta \omega$$

and

$$\Delta \omega = \frac{2\pi}{T}$$

The Fourier coefficients, X_k , are required from the discrete spectrum. The values of the discrete spectrum are real but the Fourier coefficients are complex, so only the absolute values of the Fourier coefficients can be determined. These are given by;

$$|X_k| = S_k^{1/2}, \quad k = 0, 1, \dots, \frac{N}{2}$$

Note that because the spectrum is only defined up to the maximum frequency, ω_{\max} , which is half the maximum value required by the IFFT, only half of the Fourier coefficients are unique.

To generate a time series using the IFFT the Fourier coefficients must have an imaginary component. The imaginary component is the phase angle, whereas the absolute value of the Fourier coefficient gives the amplitude. The phase angle cannot be determined from the spectrum because this information is lost when deriving a spectrum from the Fourier coefficients. This means that the time series generated from a spectrum is not necessarily unique, a number of different time series can be generated from the same spectrum. The spectrum determines the frequencies and amplitudes present in the time series, but not the phases. As the information concerning phase angles is not given values have to be determined. The phase angles are obtained by generating random numbers from a uniform distribution between 0 and 2π . The Fourier coefficients are determined by;

$$X_k = |X_k| e^{i\theta_k}, \quad k=0,1,\dots,\frac{N}{2}$$

where θ_k is a random number. Note that, because the random phase angles cancel out when the Fourier coefficients are multiplied by their complex conjugates, the derived time series would give the correct discrete spectrum if the procedure is reversed.

To determine the time series the Fourier coefficients are required for values of k up to $N-1$ and the ones not given by the above equation can be determined from their complex conjugates (see Section 5.3);

$$X_k = X_{N-k}^*, \quad k = \frac{N}{2} + 1, \dots, N-1$$

When all of the Fourier coefficients are known the time series can be determined using the IFFT. This is represented by the equation;

$$x_r = \sum_{k=0}^{N-1} X_k e^{i 2\pi \frac{k r}{N}}, \quad r = 0, 1, \dots, N-1$$

The values of x_r give the required time series. The spacing between these values is given by;

$$\Delta T = \frac{\pi}{\omega_{\max}}$$

and the total time is;

$$T = \frac{\pi N}{\omega_{\max}} = N \Delta T$$

Therefore, for a given number of Fourier coefficients, the duration of the time series is limited by the maximum frequency represented by the spectrum, i.e., a spectrum which extends up to a high frequency will give rise to a time series of a short duration. In practice, to avoid the use of an excessive number of Fourier coefficients, reasonable durations for the time series can be

obtained by neglecting the portion of the spectrum which lies above a prescribed “cut-off” frequency (low-pass filtering). The selection of a suitable cut-off frequency depends on the shape of the spectrum and should be chosen such that the final truncated spectrum spans about five decades of the power spectral density.

5.3. Relationship between Fourier coefficients

The Fourier coefficients are obtained from a time series by the following discrete Fourier transform;

$$X_k = \frac{1}{N} \sum_{r=0}^{N-1} x_r e^{-i2\pi \frac{rk}{N}}, \quad k = 0, 1, \dots, \frac{N}{2}$$

and

$$X_{N-k} = \frac{1}{N} \sum_{r=0}^{N-1} x_r e^{-i2\pi \frac{r(N-k)}{N}}, \quad k = 1, 2, \dots, \frac{N}{2}$$

which give the values for X_k for k up to $N/2$. This can be rewritten as;

$$X_{N-k} = \frac{1}{N} \sum_{r=0}^{N-1} x_r e^{i2\pi \frac{rk}{N}} e^{-2\pi i}, \quad k = 1, 2, \dots, \frac{N}{2}$$

so

$$X_{N-k} = X_k^*$$

or

$$X_{N-k}^* = X_k$$

This demonstrates the relationship between the Fourier coefficients.

From the relationship between the Fourier coefficients a relationship between the spectral coefficients is found;

$$S_{N-k} = X_{N-k}^* X_{N-k} = X_k X_k^* = S_k, \quad k = 0, 1, \dots, \frac{N}{2} - 1$$

This is related to aliasing, and shows that the spectrum repeats itself.

6. RESULTS

6.1. Mean fields

The CFX4 model was set up as detailed in Section 2 and run to convergence. The solution converged well and it did not show signs of any transient instability. An initial run was performed with hybrid differencing, no variance equation and uniform inlet profiles. This initial solution provided the initial fields for the next run which retained hybrid differencing but introduced buoyancy, variance and non-uniform inlet velocity profiles. A final run using higher order differencing completed the solution. A total of 8000 iterations were performed across the different runs which required about 20 hours of CPU time on a Sun ULTRA 1 and about 140 Mbytes of memory.

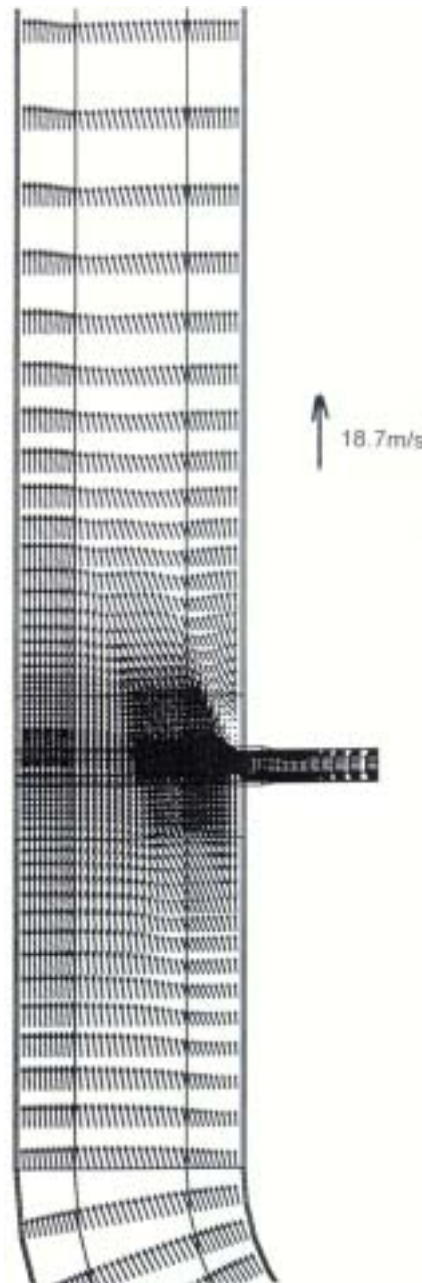


FIG. 2. Velocity vectors on the vertical symmetry plane.

The predicted velocity distribution on the vertical symmetry plane is shown in Figure 2. At first sight this velocity distribution looks quite surprising with the flow in the straight section of the main pipe continually directed towards the wall on the left (the opposite side to intersection with the branch pipe). Examination of the secondary flow distribution at the exit of the bend, Figure 3, shows a strong secondary flow field with the twin counter rotating vortices clearly shown. The transverse flow across the plane of the bend, which flows in the direction of increasing radius contains a peak transverse velocity of 1.3m/s. This strong transverse flow is very stable and persists in the straight pipe downstream of the intersection. Figure 4 shows the transverse velocity distribution at the intersection of the two pipes and this shows that the jet which issues from the branch adds to the existing right-to-left transverse flow generated by the bend. The combination of the jet momentum with that contained within the transverse flow is enough to detach the jet from the wall and deflect it deep into the main flow.

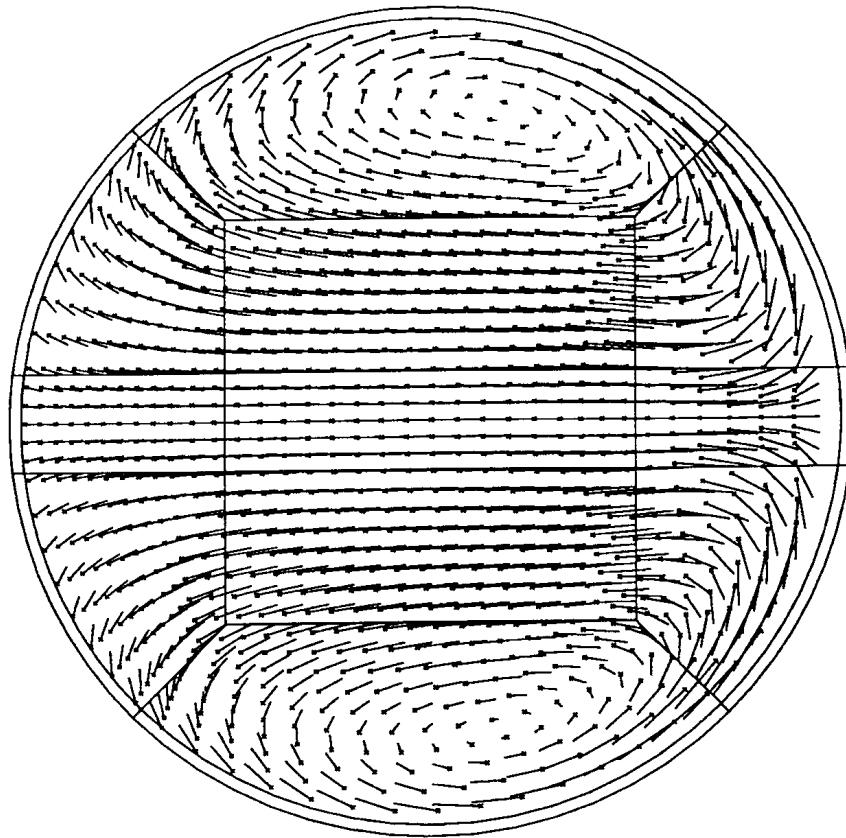


FIG. 3. Transverse velocity distribution at the exit of the bend.

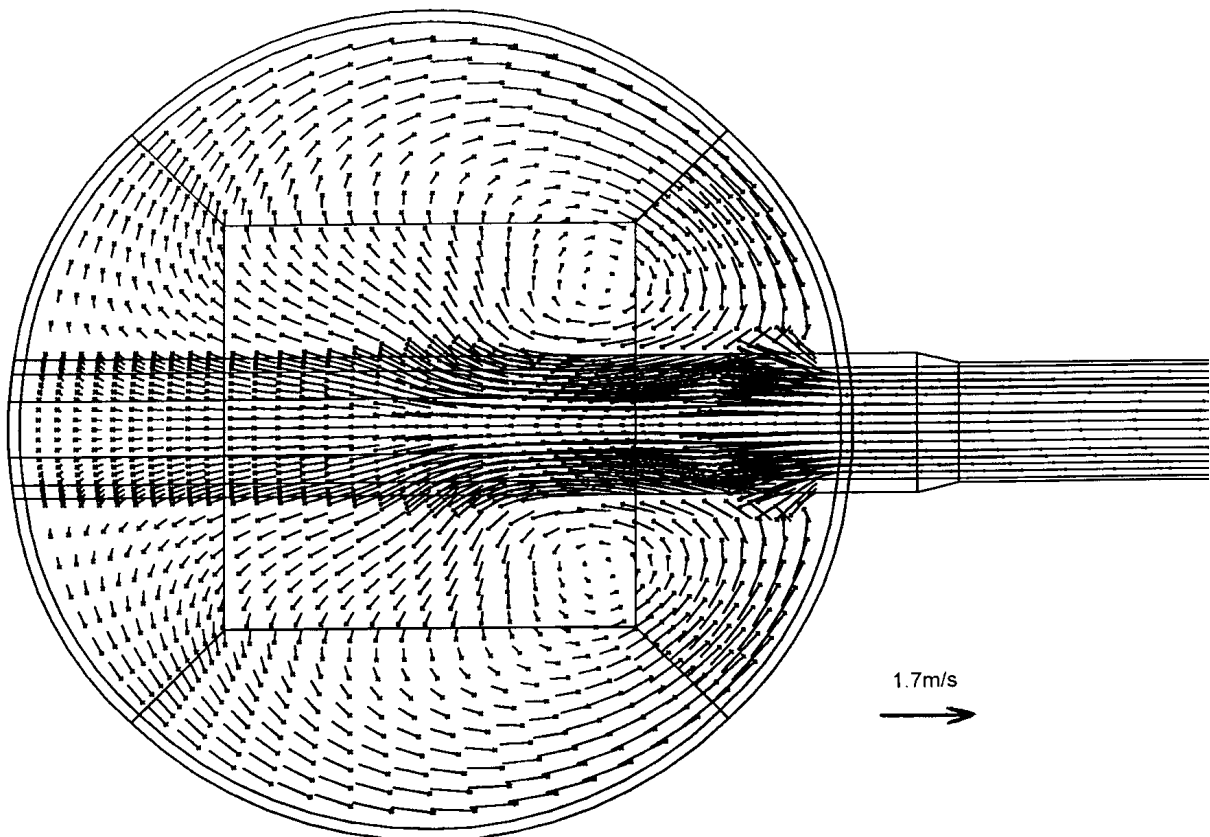


FIG. 4. Transverse velocity distribution at the intersection of the two pipes.

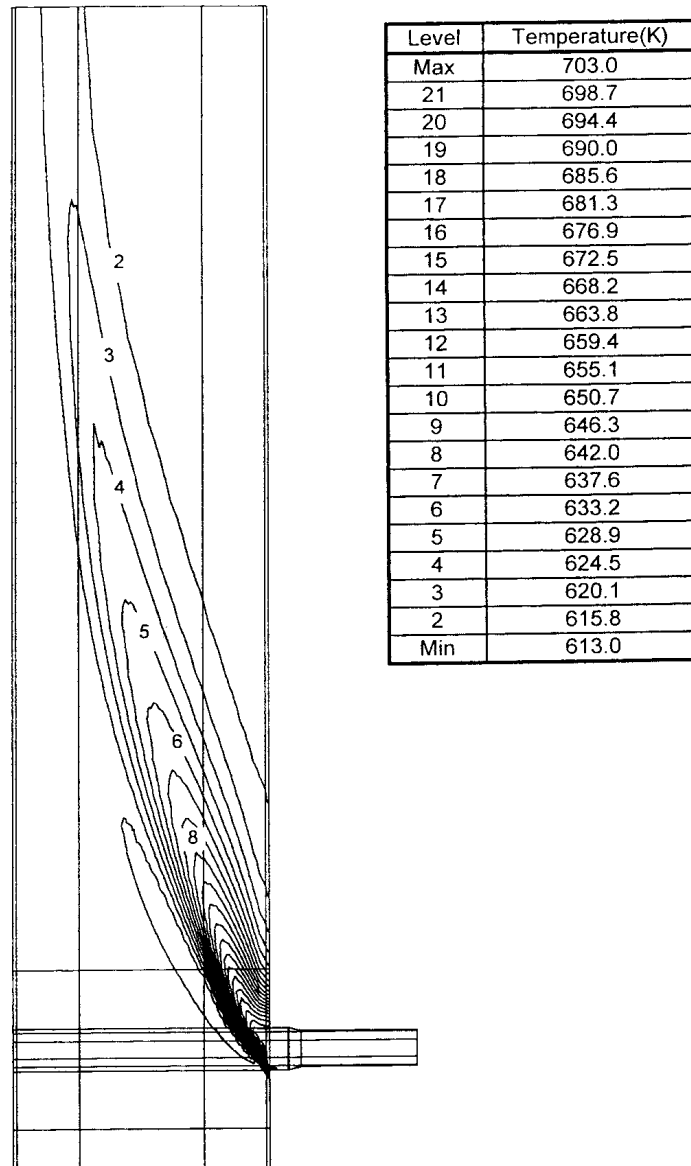


FIG. 5. Temperature distribution on the vertical symmetry plane.

The detachment of the jet from the wall results in the temperature distribution on the vertical symmetry plane shown in Figure 5. Figure 5 shows that the main pipe wall is influenced by the hot jet for only a short distance, about 8 branch diameters, downstream of the intersection. Hot fluid is convected across the centre-line of the main pipe so that after 23 branch diameters downstream of the intersection the plume is completely contained within the opposite half of the cross section of the main pipe. Predicted mean temperatures at the 15 thermocouple positions are shown in Table I.

Figure 6 shows the predicted distribution of the temperature variance plotted on the vertical symmetry plane. The overall shape of the variance plume closely follows that of the thermal plume except for close to the mouth of the branch where the peak variances around the edges of the jet rather than in the centre of the jet. This distribution is to be expected as the variance is generated by turbulence acting on the mean temperature gradients, with the maximum temperature gradients occurring around the periphery of the jet close to the mouth of the branch.

TABLE I. PREDICTED MEAN TEMPERATURES

Thermocouple	Outer Surface Temp. (K)	Inner Surface Temp. (K)	Fluid Temp.(K)
1	674.38	676.71	677.53
2	635.41	637.30	637.93
3	623.48	624.69	625.10
4	612.99	612.99	612.88
5	612.99	612.99	612.88
6	614.67	614.92	615.01
7	612.99	612.99	613.00
8	612.99	612.99	612.99
9	613.00	613.00	613.00
10	702.38	702.93	702.99
11	694.15	702.04	702.95
12	703.00	703.00	703.00
13	612.99	612.99	612.99
14	612.99	612.99	612.99
15	618.36	619.10	619.35

TABLE II. PREDICTED VELOCITY, TURBULENCE AND TEMPERATURE VARIANCE IN FLUID

Thermocouple	U (m/s)	k (m ² /s ³)	ϵ (m ² /s ³)	Temp. Variance (K ²)	δ (mm)
1	0.407	0.9904E-01	0.1987E+01	0.9176E+02	7.0
2	3.043	0.1192E+00	0.2620E+01	0.5636E+02	7.0
3	3.842	0.1084E+00	0.2269E+01	0.1885E+02	7.0
4	4.863	0.1270E+00	0.3337E+01	0.1000E-09	7.0
5	4.863	0.1270E+00	0.3337E+01	0.1000E-09	7.0
6	4.459	0.1155E+00	0.2497E+01	0.5000E+00	7.0
7	5.296	0.1478E+00	0.3613E+01	0.4959E-08	7.0
8	5.310	0.1480E+00	0.3623E+01	0.3120E-08	7.0
9	3.404	0.7840E-01	0.1397E+01	0.1099E-08	7.0
10	2.897	0.4672E-01	0.1925E+01	0.3676E-04	8.5
11	1.063	0.1458E-01	0.3361E+00	0.2442E-01	8.5
12	1.902	0.2650E-01	0.8215E+00	0.1193E-08	2.5
13	4.949	0.1362E+00	0.5138E+01	0.1000E-09	7.0
14	4.949	0.1362E+00	0.5137E+01	0.1000E-09	7.0
15	4.193	0.1102E-01	0.2329E+01	0.5899E+01	7.0

The variance in the fluid, the velocity and the turbulence quantities for the near-wall nodes and the distances of the nodes from the wall (δ) corresponding to the positions of the 15 thermocouples are shown in Table II.

Of the 15 thermocouple locations, significant levels of temperature variance were found only at Thermocouples 1, 2, 3, 15 and 6, all of which lie on the mid-line which runs through the intersection of the two pipes.

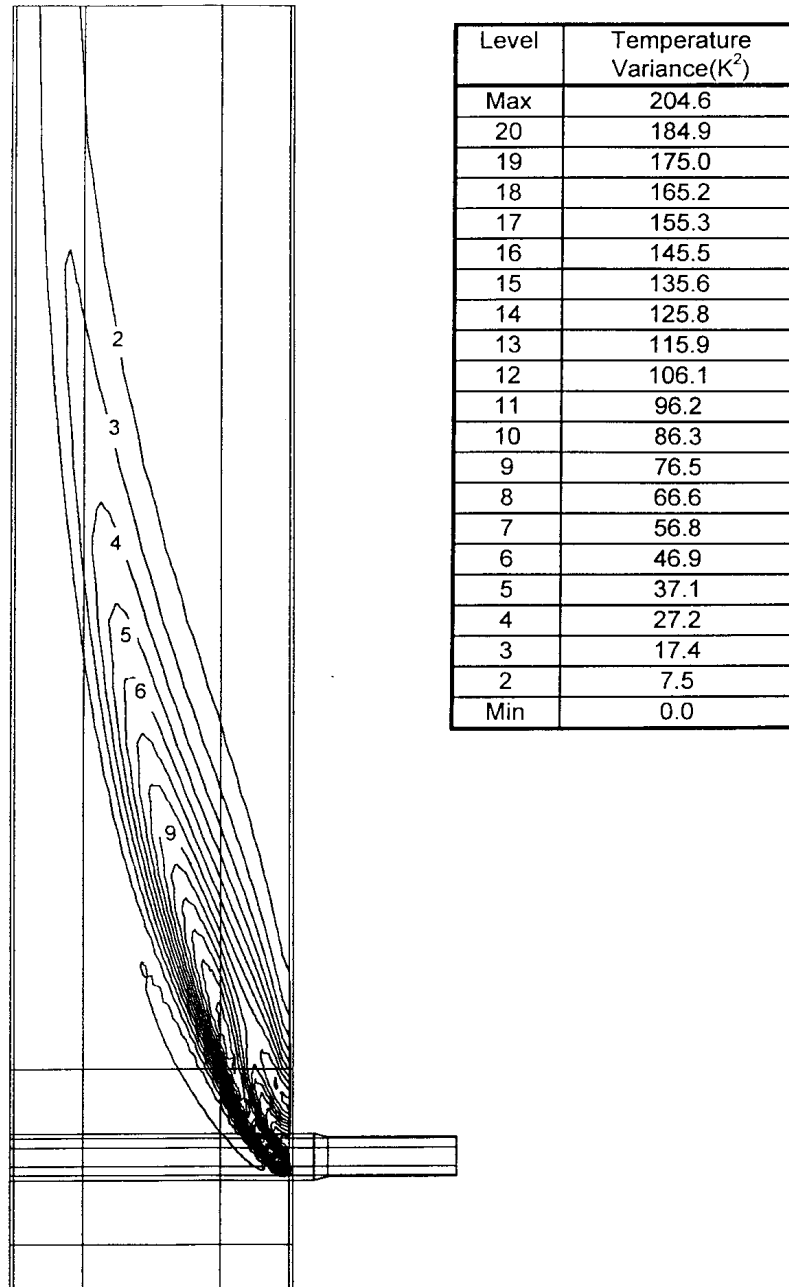


FIG. 6. Temperature variance distribution on the vertical symmetry plane.

6.2. Fluctuating temperature spectra

The spectra of the temperature fluctuations in the fluid have been constructed, for the locations of Thermocouples 1,2,3,6 and 15, using the equations given in Section 3 and the results presented in Table II. The boundary layer attenuation model presented given in Section 4 was used to determine the spectra at the inner and outer surfaces of the pipe wall at the locations of the same five thermocouples. The predicted fluid and pipe wall spectra at the location of Thermocouple 1 are shown in Figure 7.

Integration of the attenuated spectra at both surfaces of the pipe wall leads to the variances and these are compared with the variances in the fluid, predicted by CFX4, and presented in Table III.

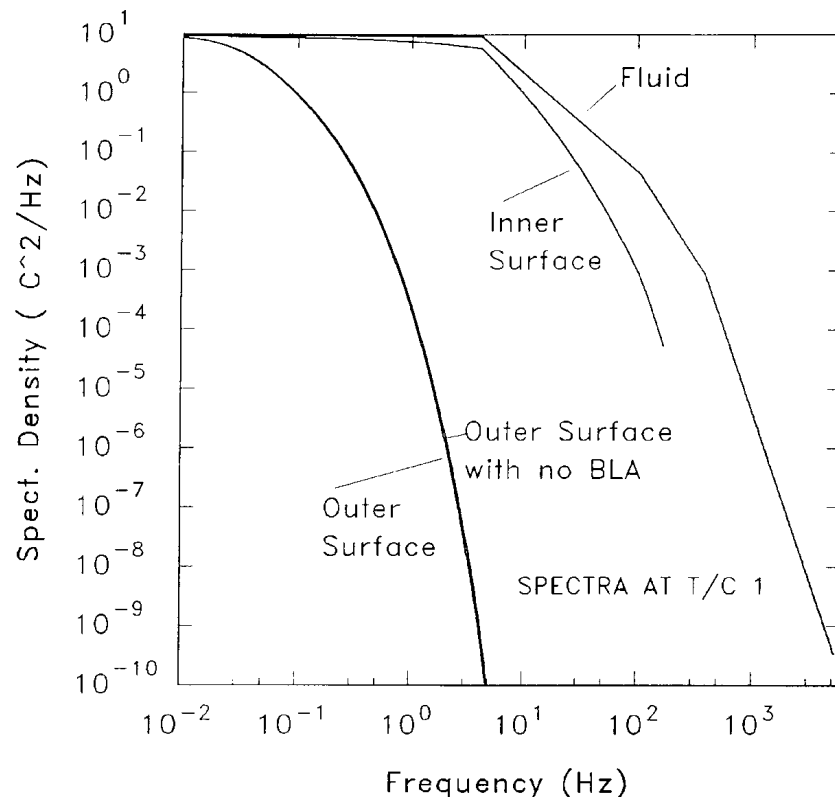


FIG. 7. Predicted spectra at Thermocouple 1.

TABLE III. PREDICTED VARIANCES IN THE FLUID AND ON THE INNER AND OUTER SURFACES OF THE PIPE WALL

T/C	Temp. variance in fluid (K^2)	Temp. variance on inner surface (K^2)	Temp. variance on outer surface (K^2)
1	91.76	18.676	0.1735
2	56.36	5.0449	0.0200
3	18.85	3.0587	0.0086
6	0.500	0.0837	2.08E-04
15	5.899	0.6889	2.12E-03

6.3. Fluctuating temperature histories

The predicted spectra were used to synthesise temperature fluctuation~time histories using the method detailed in Section 5.2 for the thermocouples at locations 1,2,3,6 and 15. In each of the histories the number of Fourier coefficients was limited to 2^{16} . Unfortunately, because the spectra in the fluid extend up to high frequencies, the resulting durations of the time series would generally be less than one second when 2^{16} Fourier coefficients are used. The fluid spectra were arbitrarily truncated at 1kHz which extended the duration of the resulting time series' to just under 33 seconds. Samples of these synthesised histories are shown in Figures 8 to 10 for the fluid and inner and outer surfaces of the wall respectively at the location of Thermocouple 1.

Temperature Fluctuation (K)

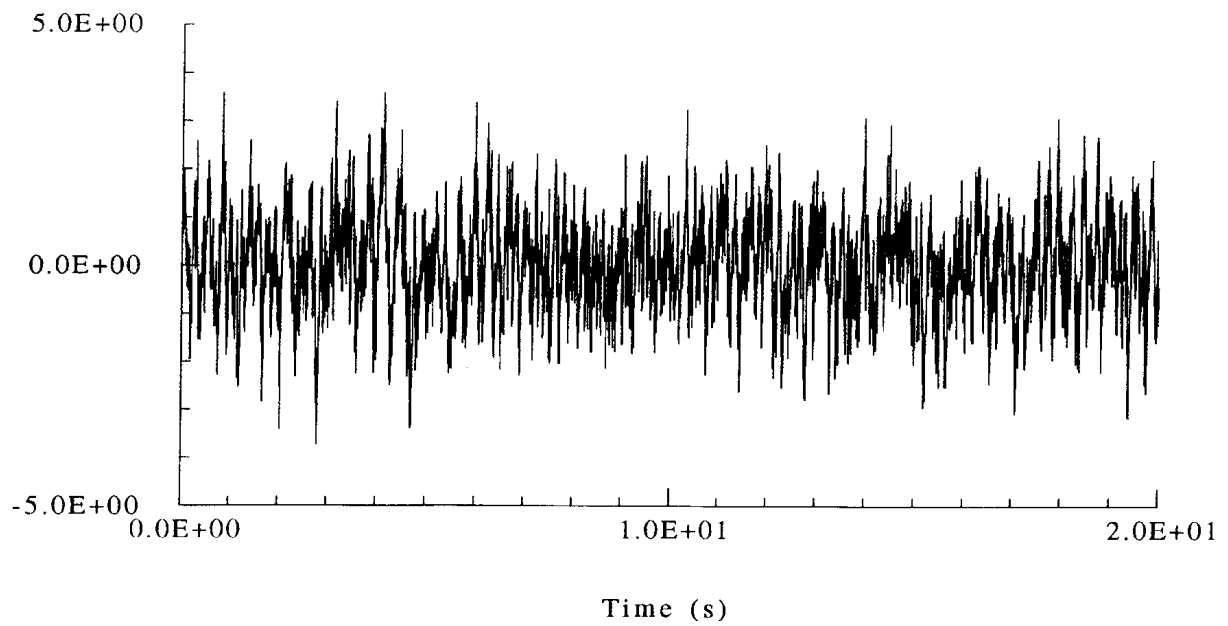


FIG. 8. Predicted fluctuating temperature history in the fluid at Thermocouple 1.

Temperature Fluctuation (K)

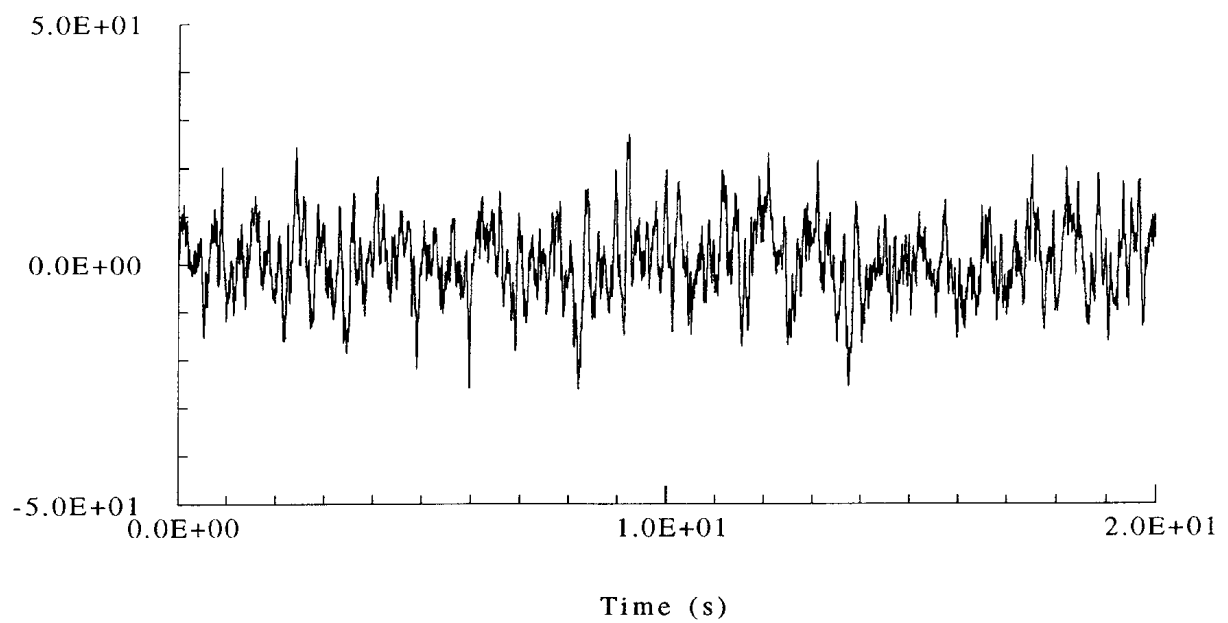


FIG. 9. Predicted fluctuating temperature history on the wall inner surface at Thermocouple 1.

Temperature Fluctuation (K)

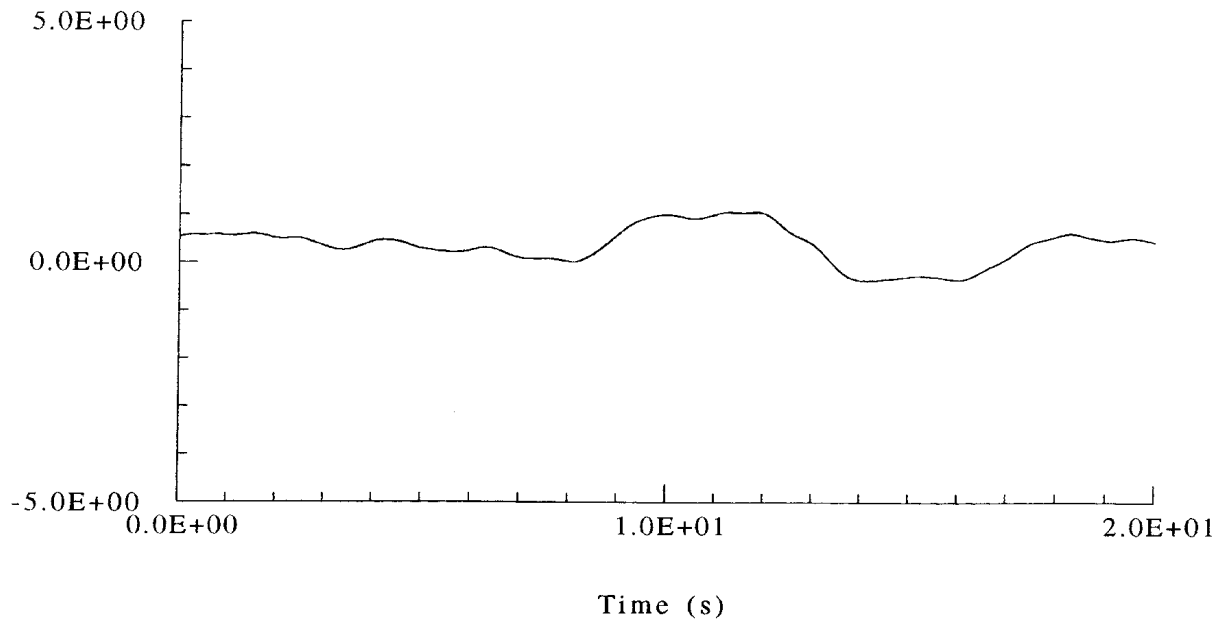


FIG. 10. Predicted fluctuating temperature history on the wall outer surface at Thermocouple 1.

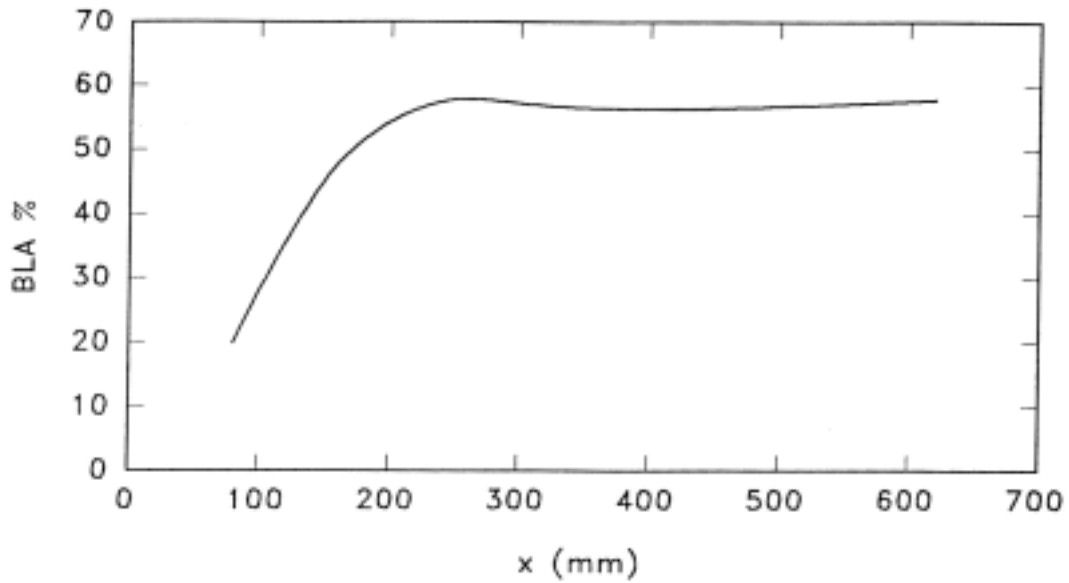


FIG. 11. Predicated boundary layer attenuation downstream of the intersection

Each temperature time history was post-processed to extract the maximum amplitudes and to check that the variance obtained by integration of the time series were close to those of the original spectra. The amount of boundary layer attenuation is normally expressed as the reduction in peak-to-peak temperature fluctuation between the wall and the fluid outside of the boundary layer expressed as a percentage of the fluid value. Table IV presents the peak-to-peak temperature fluctuations for the fluid and on the inner and outer surfaces of the pipe wall together with the reduction in temperature fluctuation across the boundary layer.

TABLE IV. PREDICTED PEAK-TO-PEAK TEMPERATURE DIFFERENCES AND PERCENTAGE BOUNDARY LAYER ATTENUATION

T/C	ΔT in fluid (K)	ΔT on inner surface (K)	BLA (%)	ΔT on outer surface (K)
1	86.48	59.33	19.82	3.52
2	64.17	33.47	47.83	1.01
3	37.74	15.92	57.81	0.50
6	6.138	2.596	56.44	0.08
15	21.09	9.189	57.71	0.28

The variation of the boundary layer attenuation downstream of the intersection is shown in Figure 11. Immediately downstream of the intersection, there is a separation of the boundary layer which minimises the boundary layer attenuation, which takes a value of about 20% at the location of Thermocouple 1. After the boundary layer is re-established, the boundary layer attenuation reaches a “fully developed” value of just under 58%.

7. DISCUSSION

The predicted temperature and variance distributions are strongly influenced by the secondary flow which is generated by the flow around the bend in the main pipe. This influence is characterised by the jet which emerges from the branch being “lifted” off the wall and deposited deep inside the main flow instead of remaining attached and flowing along the wall. In practice this effect will be strongly dependent on how closely the fabricated pipe bend and T-junction match the ideal symmetrical geometry of the CFX4 model. For instance, if the branch pipe does not lie in exactly the same plane as the bend in the main pipe, the jet will not be aligned with the transverse flow and the jet will not be lifted off the wall as strongly and would also be skewed to one side. Similarly if either of the flows into the modelled domain possessed initial swirl components, the symmetry of the flow would be lost and again the jet would not lift off as strongly and would again be skewed to one side.

If the bend was not present in the main pipe, one would normally expect the jet to remain attached to the pipe wall and for vortices to be formed by the main flow in the wake of the jet which would be shed in a periodic manner. The absence of both jet attachment and instabilities due to vortex shedding in the CFX4 calculation are attributed, therefore, to the stabilising influence of the secondary flow generated by the bend.

In summary, geometrical imperfections in the physical component and flow disturbances, particularly swirl, generated by fittings upstream of the modelled domain could have a strong influence on the predicted temperature and temperature fluctuation distributions. There is a need, therefore, to investigate the sensitivity of the predicted distribution to practical variations in the real geometry and to the condition of the inlet flows.

8. CONCLUSIONS

A thermal hydraulic analysis of the T junction which forms the basis of the thermal striping benchmark exercise has been carried out using the CFX4 CFD code together with an

analytical boundary layer attenuation model. The mean momentum, temperature, turbulence and temperature variance fields were determined using CFX4 and the results were used to construct the spectra of the temperature fluctuations at the positions of the thermocouples. Application of the boundary layer attenuation model generated spectra at both the inside and outside surfaces of the pipe wall. These spectra were used to synthesise fluctuating temperature histories in the fluid and on both surfaces of the pipe wall at the thermocouples which showed significant temperature variances (Thermocouples 1,2,3,6 and 15).

The CFX4 solution converged to give mean fields which did not display any transient behaviour. This solution showed temperature and variance plumes which become detached from the pipe wall owing to the influence of the secondary flow generated by the bend in the main pipe.

As the temperature and temperature fluctuation distributions are strongly dependent on the secondary flow distribution, it is judged that real effects, such as geometrical imperfections or inlet flow ill-conditioning, could disrupt the alignment of the jet and the secondary flow field and lead to significant differences between prediction and observed behaviour.

REFERENCES

- [1] KNUDSEN, J.G. and KATZ, D.L., Fluid Dynamics and Heat Transfer. McGraw-Hill, (1958) 153 pp.
- [2] LAUNDER, B.E. and SPALDING, D.B., Mathematical Models of Turbulence. Academic Press, London (1972) 26-37 pp.
- [3] GELINEAU, O. and SPERANDIO, M., Benchmark on a Tee Junction of LMFR Secondary Circuit Involving Thermal Striping Phenomena: Technical Specifications. Framatome Lyon (February 1996).
- [4] PENIGUEL, C., Predictions of Boundary Layer Attenuation Using a Conduction Damping Model in an Impinging Flow. Nuclear Electric Technology Division Report TD/STB/MEM/0147 (also TSSG/P(90)/130), (July 1991).
- [5] BUFFET, J.C. and TENCHINE, D., Transfer of Temperature Fluctuations Across Boundary Layers in Turbulent Liquid Metal Flows, ASME-PVPD Conference, Thermal Striping Paper 4, (1985).
- [6] NEWLAND, D.E., An Introduction to Random Vibrations and Spectral Analysis. Longman, (1984).

BENCHMARK ON TEE JUNCTION: FATIGUE DAMAGE ANALYSIS

M.W. J. LEWIS
AEA Technology pls,
United Kingdom

Abstract. This report presents the analysis of the effects of the estimated loading upon thermally induced fatigue cracking of the structures. It takes calculated temperature-time history and steady state stresses as its input information.

1. INTRODUCTION

The participants of the co-ordinated research project have requested that a benchmark be carried out to test the ability of analytical methods and national procedures to explain a physical problem caused by the mixing of two flows at different temperatures.

The problem has been encountered in the French PHENIX LMFBR in the secondary circuit. The tasks to be performed cover the following:

- Estimation of loadings inside the structures;
- Identification of damage modes induced by the loadings;
- Quantification of the damage effects, if any;
- Report the results of the analysis, including a description of and justification for the methods used.

2. DESCRIPTION OF BENCHMARK

A main pipe of ID 494 mm has sodium flowing at 340°C. After a horizontal pipe run, the pipe turns through 90° and the flow passes vertically upwards. In the vertical run, there is a tee junction with its axis horizontal. The exit diameter from the tee is 68 mm.

Sodium flows at a temperature of 430°C into the main pipe. Downstream of the tee junction is a circumferential butt weld in the main pipe (160 mm from the small pipe axis to the centreline of the weld). This weld is designated 1HI.

The material of construction is AISI 304 with the weld formed by plasma welding in two passes, the second pass using 16-8-2 filler wire. The weld remains in the "as welded" condition. The weld stands proud of the inner wall of the main pipe by about 1.3 mm. Its width is approximately 5 mm.

Time of operation of the circuit is approximately 90 000 hours. Information is provided on the mass flowrates, pressures and membrane stresses. Additionally, 15 thermocouples were mounted upon the external diameter of the main pipe. Measurements have given both mean and fluctuating temperatures for these thermocouples.

3. APPROACH TO THE PROBLEM

There are two questions to be answered. Firstly, do the methods and procedures explain the problems seen in service? And secondly, would the design methods and procedures avoid the problem if applied to the structures under consideration?

The approach for failure assessment is summarized below:

- Consider the source temperature difference in relation to the surface equibiaxial strains induced and the allowable strain range from high cycle fatigue endurance (avoidance of crack initiation);
- Consider the local fluid maximum temperature amplitude in relation to the surface equibiaxial strains induced and the allowable strain range from high cycle fatigue endurance (avoidance of crack initiation);
- Consider the local metal wall maximum temperature amplitude in relation to the surface equibiaxial strains induced and the allowable strain range from high cycle fatigue endurance (avoidance of crack initiation);
- Consider the local fluid temperature-time history and the potential for crack initiation within the plant lifetime (Miner's summation approach vs. actual fatigue curve);
- Consider the local metal wall temperature-time history and the potential for crack initiation within the plant lifetime (Miner's summation approach vs. actual fatigue curve);
- Consider the potential effects introduced by the circumferential weld in the main pipe in comparison to parent material.

The approach for design assessment is summarized below:

- Consider the source temperature difference in relation to the surface equibiaxial strains induced and the factored allowable strain range from high cycle fatigue endurance (avoidance of crack initiation);
- Consider the local fluid maximum temperature amplitude in relation to the surface equibiaxial strains induced and the factored allowable strain range from high cycle fatigue endurance (avoidance of crack initiation);
- Consider the local metal wall maximum temperature amplitude in relation to the surface equibiaxial strains induced and the factored allowable strain range from high cycle fatigue endurance (avoidance of crack initiation);
- Consider the local fluid temperature-time history and the potential for crack initiation within the plant lifetime (Miner's summation approach vs. design fatigue curve);
- Consider the local metal wall temperature-time history and the potential for crack initiation within the plant lifetime (Miner's summation approach vs design fatigue curve);
- Consider the potential effects introduced by the circumferential weld in the main pipe in comparison to parent material.

4. DESIGN METHODS FOR THERMAL STRIPING

4.1. History

Interim design procedures for the avoidance of thermal striping damage in AISI 316L(N) SPH were proposed in 1991 by CEA and AEA Technology [1,2,3]. The CEA proposals took into account the reduction in fatigue endurance at high cycles and low strain range resulting from the superposition of low cycle high strain ranges from operating cycles. The maximum allowable temperature amplitude for crack initiation at the end of component life at 550 K was 48 K for a low cycle fatigue usage factor of 0, reducing to 15 K for a LCFU factor of $> 0.5 \leq 0.8$.

The AEA Technology proposals were based upon allowing pre-existing defects of typically 100 μm to be extended to a depth of 500 μm at the end of component life, or avoidance of crack growth from defects by limiting thermal striping loadings to a level at which threshold stress intensity factor ranges are not exceeded. The maximum allowable temperature amplitude for avoidance of crack growth at 550 K was 48 K for a low cycle fatigue usage factor of 0, reducing to 24 K for a LCFU factor of $> 0.5 \leq 0.8$, assuming the threshold stress intensity factor range to be $4\text{Mpa}\sqrt{m}$. The equivalent Rankine strain range assuming biaxial restraint is related to the maximum temperature range by:

$$\Delta\varepsilon_s = \alpha \Delta\theta_p / (1-\nu)$$

The CEA proposals were examined in detail [4]. This work concluded that there is no necessity to apply high cycle endurance reduction factors to the design fatigue curve, as defects of the order of 50 μm are already accounted for in the high cycle end of the curve, and represent the level of damage applicable to a low cycle, high strain fatigue damage fraction of 1.

4.2. Avoidance of crack initiation

The design procedure proposed by AEA Technology is intended to ensure that no surface cracks will be generated in a nominally defect-free structure during its operational life [5]. It can be applied, therefore, only to a structure that meets the following criteria:

- In its initial condition, it has no significant surface imperfections (i.e. crack-like defects) or surface scratches deeper than 0.1 mm;
- It is not subject to significant creep-fatigue or thermal shock damage during its life;
- It is not subject to a corrosive environment its life (e.g. from the products of a sodium-water reaction) during its life.

The procedure assumes that the structure is immersed in a flow in which coolant from two different temperature sources is mixed. The first step is to assess whether the temperature difference between the two sources is sufficient to cause damage on the basis of the fatigue endurance limit for the material. If it is not, no further action has to be taken. If it is, the actual temperature fluctuations at the structure have to be assessed in order to determine the fatigue damage accumulation during the component lifetime. It is assumed that these fluctuations can be determined, for example, by measurements on a model using a fluid to simulate liquid sodium. The procedure has the following steps:

1. An experimental fatigue data curve for the material must be established. This is in the form of a relationship between the number of strain cycles to initiate cracks, and the amplitude of the cycles.
2. From this, a series of design-allowable fatigue curves (as a function of temperature) is deduced by reducing the strain amplitudes by a factor of 2 at the high cycle end, and by reducing the cycles to failure by a factor of 20 at the high strain end. The former factor is to allow for the effects of intra- and inter-cast variations in material properties, manufacturing damage, variations in surface finish, ageing, operational cycles and environmental damage which lead to surface crack-like defects up to 0.1 mm deep.
3. If the source temperature difference is then less than $\Delta\theta_p$, the value of $\Delta\theta$ corresponding to the strain endurance limit at 10^9 cycles, the structure is acceptable, in the sense that no defects will be initiated during its design life.
4. If the source temperature difference is greater than $\Delta\theta_p$, the actual temperature fluctuations at the structure have to be assessed. If the maximum temperature amplitudes are less than $\Delta\theta_p$ the structure is acceptable.
5. If the maximum temperature amplitudes are not less than this value, the cumulative damage caused by the fluctuations of amplitude greater than $\Delta\theta_p$ must be determined. This is carried out by a fatigue damage summation using Miner's method. It is assumed that the damage done by a single cycle of a certain amplitude is inversely proportional to the number of cycles of that amplitude which will cause failure, and that the damage done by successive cycles of different amplitudes can be summated. If the resulting total damage is less than 1, no initiation of defects will take place, and the structure is acceptable.

The AEA Technology design procedure based upon avoidance of crack initiation or crack initiation at the end of component life has been described [5]. The procedure takes into account the effects of other major operational cycles and transients. This procedure was accepted for use at the EC Structural Integrity Seminar held on 19-20 January 1993 within the Synthesis Report on Thermal Striping [6].

To be consistent with the definition of equivalent strain range used in RCC-MR (RB3227.9) for small temperature amplitudes enhancement of plasticity is negligible. The following equation relates thermal striping strain range to the temperature amplitude:

$$\Delta\epsilon_s = 2/3 (1+\nu) \lambda \alpha_i \Delta\theta_p / (1-\nu)$$

Where the component restraint condition is unknown or ill-defined, a temperature-to-strain conversion factor $\lambda = 1$ should be taken.

Table 4.1 gives the maximum allowable strain range for Type 316L(N)SPH steel for the avoidance of crack initiation. The strain range is taken from the fatigue curves recommended in [7] at 10^9 cycles.

For the temperature-to-strain conversion, the instantaneous coefficient of thermal expansion for Type 316L(N) is taken as:

$$\alpha_i = 16.10 \times 10^{-6} + 0.78 \times 10^{-8} T$$

Where the source temperature difference is greater than in Table 4.1, then the maximum local fluid temperature amplitude should be measured or calculated. If the fluid temperature amplitude is greater than in Table 4.1, then maximum local wall temperature amplitude must be measured or calculated.

TABLE 4.1. ALLOWABLE TEMPERATURE AMPLITUDES FOR AVOIDANCE OF CRACK INITIATION IN TYPE 316L(N) STEEL

Mean temperature °C	20	425	450	475	500	525	550	600
Strain range %	0.120	0.114	0.114	0.114	0.111	0.107	0.014	0.094
Allowable $\Delta\theta_p$ (K)	49.2	46.7	46.7	46.7	44.8	42.8	41.2	36.5

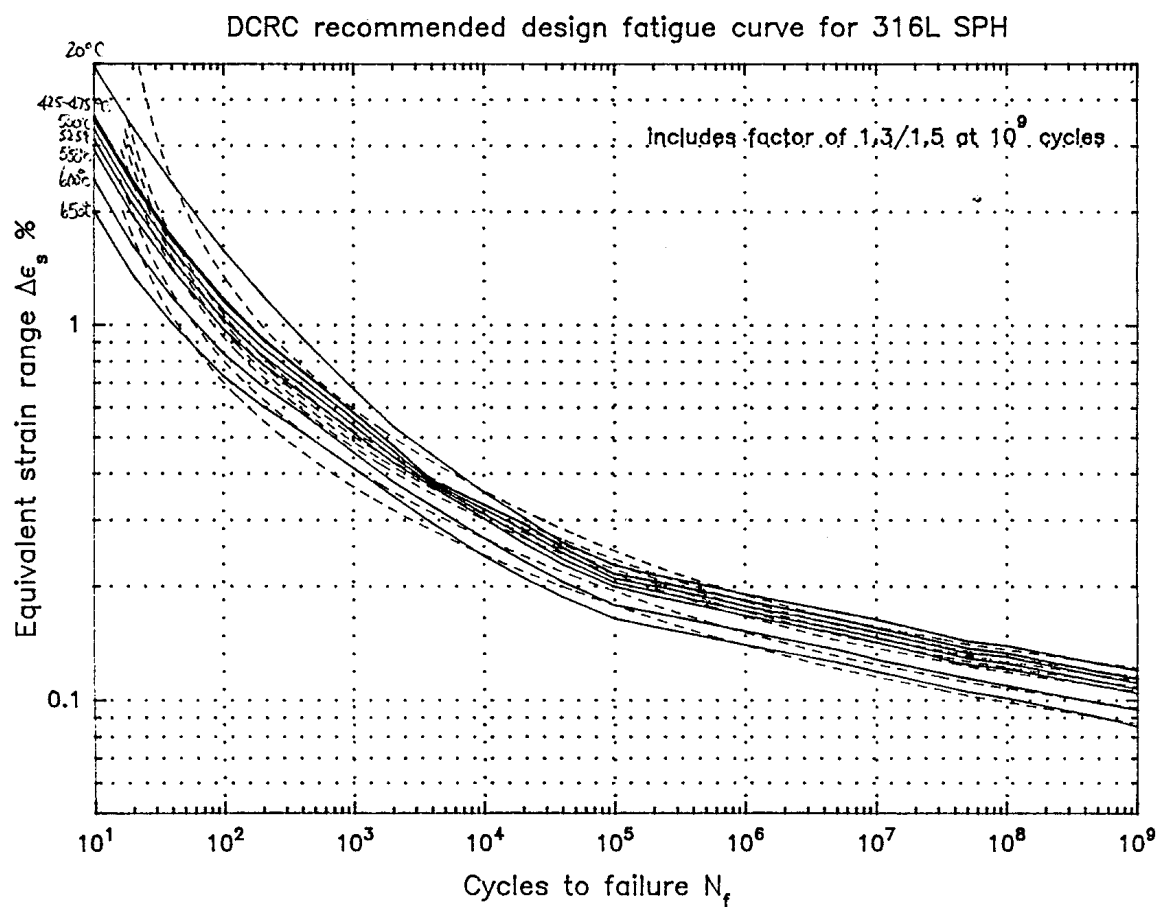


FIG. 1. Design fatigue curves for type 316L(N0 steel).

4.3. Crack initiation at end of component life

If the temperature amplitude is still greater than in Table 4.1, then a fatigue damage assessment is carried out from the actual temperature-time history (either local fluid or local wall histories). The history is analyzed using Rainflow cycle counting, from which the fatigue damage summation is determined according to Miner's law, that is:

$$V_s = \sum_{i=0}^n \frac{N_i}{N_f}$$

where N_f is the number of cycles to failure taken from the design fatigue curve [7]. The following equations give a close approximation to the fatigue curves for Type 316L(N):

$$\begin{aligned} 20^\circ\text{C} \quad \log_{10}(N_f) &= 1.0754 + 1.3349/\varepsilon - 0.1330/\varepsilon^2 + 0.0108/\varepsilon^3 \\ 425/450/475^\circ\text{C} \quad \log_{10}(N) &= 0.9065 + 1.2505/\varepsilon - 0.0987/\varepsilon^2 + 0.0071/\varepsilon^3 \end{aligned}$$

These design fatigue curves are shown in Fig 1.

Using a temperature-time history observed in the SUPERSOMITE facility [8], Table 4.2 gives maximum allowable temperature amplitudes for Type 316L(N) steel for a component life of 300 000 hours.

TABLE 4.2. ALLOWABLE TEMPERATURE AMPLITUDES FOR CRACK INITIATION IN TYPE 316L(N) STEEL AFTER 300 000 HOURS

Mean temperature °C	425	450	475	500	525	550	600	650
$\Delta\theta$ (K) Type 316L(N)	71-74	70-73	69-72	67-71	64-67	61-65	55-58	50-52

For a shorter exposure period of 6000 hours, the maximum allowable amplitude increases from 61-65 K to 84 K for a mean temperature of 550°C.

4.4. Ongoing developments

A factor of 2 has been applied to the base failure fatigue curve at the high cycle end to produce the design fatigue curves. For this design margin to be acceptable, the following criteria must be met:

1. The component will not be subjected to fault sodium conditions;
2. The surface finish must be less than 12.5 μm R_A ;
3. Surface scratches arising from manufacture and handling must not be deeper than 100 μm ;
4. Creep-fatigue and thermal shock damage must be limited to within the acceptable region of the creep-fatigue interaction diagram [7];
5. Other surface imperfections (crack-like defects) must not exceed 100 μm depth;
6. The component must not contain weldments.

The various factors contributing to the design margin of 2 on strain have been reviewed [9,10]. The work concluded the following individual and total fatigue strength reduction factors, summarized in Table 4.3.

It has been concluded that the reduction factor of 2 may be conservative for Type 316 steel with defects up to 100 μm [9]. However, for weldments the FSRF is likely to be higher than 2. The analysis applies to flush ground welds [9].

It has been concluded that a factor of 2 is possibly non-conservative for parent Type 316 steel, whilst the FSRF might be as high as 2.9 for weldments [10]. It is not stated whether the factors apply to flush ground or as-welded weldments [10].

TABLE 4.3. RECOMMENDED INDIVIDUAL AND TOTAL FATIGUE STRENGTH REDUCTION FACTORS (APPLIED TO MEAN PARENT FATIGUE DATA)

Factor	[9]	[10]
Cast-to-cast variation	1.2	1.5
Ageing	1.3	1.2
Rough surface finish > 5 μm CLA	1.2	1.2
Surface finish, mild environmental (high oxygen Na), ageing, manufacturing damage (scratches) leading to crack-like defects of the order of 20 to 50 μm	1.6* 1.9**	2.16*
Prior high strain cycling		1.3
Weld metal	1.5*	
Transverse welds	1.2	1.35
Weldments (including surface finish, mild environmental, ageing, manufacturing damage (scratches), manufacturing flaws up to 50 μm	1.8*	2.9*
Severe environmental damage (post sodium-water reaction)	?	
Short, sharp defects	100 μm 500 μm	1.7* 3.3*

* Total FSRF

** Total FSRF including cast variation

5. FAILURE ASSESSMENT METHODS FOR THERMAL STRIPING

5.1. Base fatigue curves

Figure 2 gives the base fatigue curves for Type 316L SPH steel at temperatures of typically 550°C. It can be seen that the DCPC design curve at high cycles is a factor of 2 lower than the base fatigue curve.

Figure 3 gives the best fit fatigue curve for AISI 304 at 425°C. The fatigue behaviour is slightly worse than for Type 316L SPH steel. Figure 4 gives the best fit fatigue curve for the weld joint at 425°C. This shows a lower endurance compared to AISI 304 parent material.

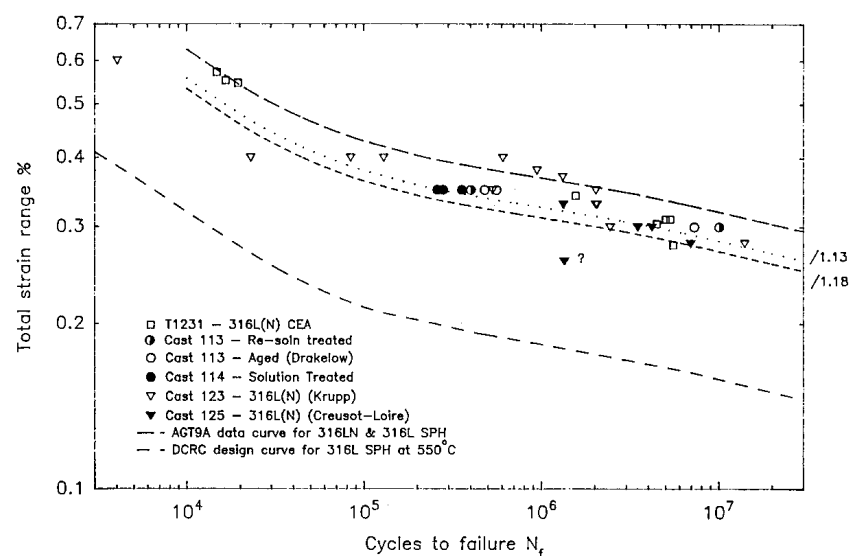


FIG. 2. Recommended fatigue curves for type 316L(N) steel.

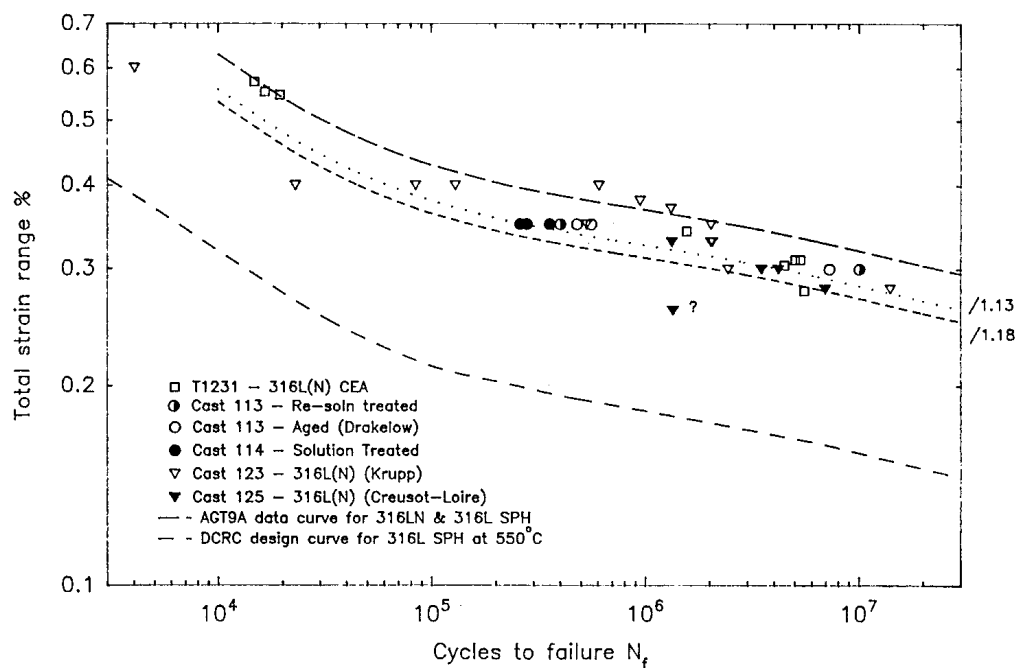


FIG. 3. Best fit fatigue curve for AISI 304 steel.

BEST FIT FATIGUE CURVE FOR WELD JOINT AT 425°C

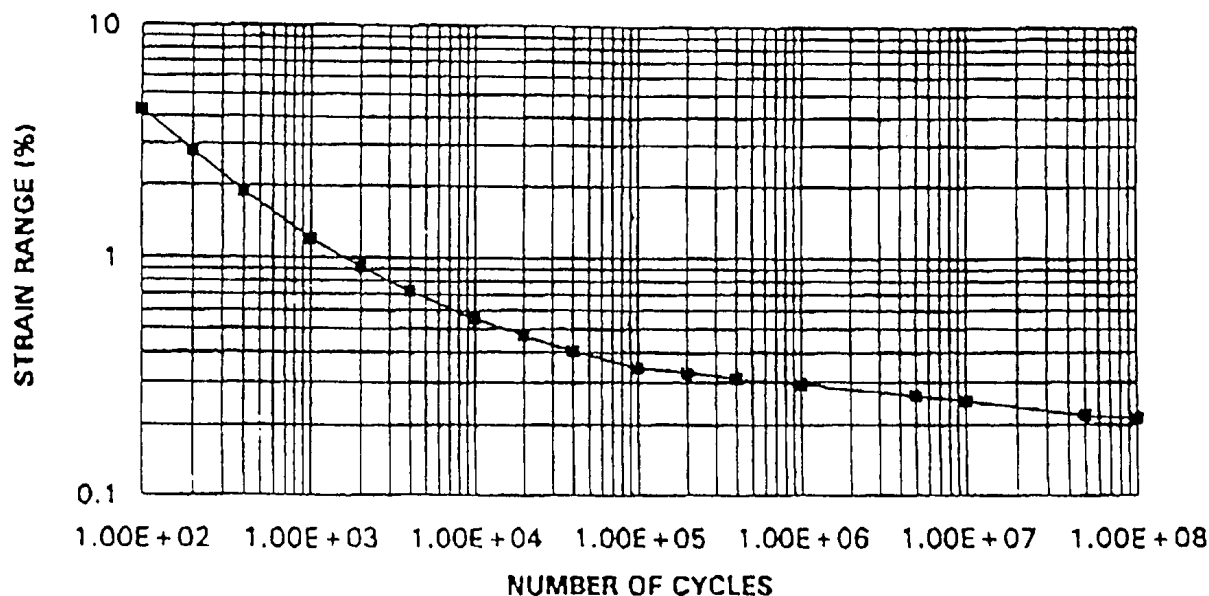


FIG. 4. Best fit fatigue curve for weld metal.

5.2. Fatigue strength reduction factors

In order to assess the plant failure, it is necessary to use the base fatigue curve, but factored in a certain manner such as to represent the material used in service. Thus factors for the following must be applied to the base fatigue curve:

—	Cast-to-cast variation	Factors for upper-lower bound and mean data;
—	Surface finish	Factor for actual inner wall condition (including weld);
—	Ageing	Factor to account for in-service deterioration;
—	Environmental effects	Exposure to high oxygen sodium;
—	Weldment	Factor to account for as-manufactured weld.

For cast-to-cast variations, it is proposed to use factors of 0.83, 1 and 1.2 to bound the range of possible cast behaviour.

For surface finish, it is proposed to use a factor of 1.2.

For ageing, it is proposed to use a factor of 1.2.

For environmental effects, it is proposed to use a factor of 1.1.

For weldments, it is proposed to use a factor of 1.25

Table 5.1 gives the corresponding total FSRF for the factors used above.

TABLE 5.1. FATIGUE STRENGTH REDUCTION FACTORS

Case	Description	Cast	Finish	Ageing	Environ	Weld	Total FSRF
P1	Parent material, upper bound fatigue properties	0.83	1.2	1.2	1.1	-	1.3
P2	Parent material, mean fatigue properties	1	1.2	1.2	1.1	-	1.6
P3	Parent material, lower bound fatigue properties	1.2	1.2	1.2	1.1	-	1.9
W1	Weld metal, upper bound fatigue properties	0.83	1.2	1.2	1.1	1.25	1.6
W2	Weld metal, mean fatigue properties	1	1.2	1.2	1.1	1.25	2.0
W3	Weld metal, lower bound fatigue properties	1.2	1.2	1.2	1.1	1.25	2.4

5.3. Failure assessment fatigue curve

Assuming a strain range of 0.258% at 10^9 cycles for AISI 304 parent material, the following table gives the allowable strain range for avoidance of crack initiation:

TABLE 5.2. ALLOWABLE STRAIN RANGE FOR AVOIDANCE OF CRACK INITIATION AT 425°C FOR AISI 304 AND WELD METAL

Case	P1	P2	P3	W1	W2	W3
Strain range %	0.195	0.163	0.136	0.156	0.130	0.109

6. GUMBEL ANALYSIS OF MAXIMUM TEMPERATURE AMPLITUDES

The computed temperature-time histories are very short in comparison to the component lifetime. A method for estimating the maximum temperature amplitude from short time samples has been developed which uses the Gumbel distribution. This approach has been developed as an extreme value distribution for the assessment of magnitudes of earthquake hazards [11]. The approach takes the form of derivation of the moments of the sample which are combined to give a prediction of the population maximum by taking the mean of the sample to which is added the sample variance multiplied by a factor.

This distribution takes the form:

$$G_v(\chi) = \exp \left[- \left(f_1 - f_2 \left(\frac{x-m}{\sigma} \right) \right)^{1/\tau} \right]$$

where $f_1 = \Gamma(1 + \tau)$ and $f_2 = \Gamma(1 + 2\tau) - f_1^2$ and Γ is the Gamma function. The m is the mean of the extremes, σ is the standard deviation and the predicted maximum is given by:

$$x_{\max} = m + \frac{f_1}{f_2} \sigma$$

Values of the parameters m , σ and τ are determined from the first, second and third moments obtained from the extreme values observed in a number of samples or time periods.

For several blocks of history (ideally more than 16), the Gumbel distribution parameters m_1 , m_2 , m_3 , r_s , and, τ_s are computed. These are related in the following manner:

$$m \approx m_1$$

$$\sigma \approx \sqrt{\frac{N}{N-1}} \sqrt{m_1 - m_2} / \left(1 - (0.1 + 2(0.4 - \tau_s)^2) / N \right)$$

$$r_s \approx \frac{\sqrt{N(N-1)} m_3 - 3m_2 m_1 + 2m_1^3}{N - 2(m_2 - m_1^2)^{3/2}} \left(1 + \frac{6}{N} \right)$$

and $\tau_s = 0$ when $r_s > 0.88$, $(0.282 - 0.317r_s)$ when $-0.69 \leq r_s \leq 0.88$ and 0.5 when $r_s < -0.69$.

Thus the maximum amplitude in infinite time period can be predicted from the maxima observed in discrete time periods.

It is also possible to predict the number of cycles from the Rainflow histogram obtained over a time period T to a longer time period T_o using the expression:

$$\lambda(\chi)T = \left(f_1 - f_2 \frac{(x-m(T))}{\sigma(T)} \right)^{1/\tau}$$

where m , σ and τ are parameters similar to those used in the Gumbel distribution. The number of cycles for time period T_o (i.e. the component lifetime) can be estimated from the transformations:

$$\sigma(T_o) = \sigma(T) \left(\frac{T}{T_o} \right)^\tau$$

$$m(T_o) = m(T) + \frac{f_1}{f_2} (\sigma(T) - \sigma(T_o))$$

assuming that the value of τ is the same for both distributions.

7. CRACK INITIATION ANALYSIS OF BENCHMARK

7.1. Material properties

The following mechanical and thermal properties have been assumed for parent AIST 304 and weld metal:

- Poisson's ratio 0.3
- Instantaneous coefficient of thermal expansion $18 \times 10^{-6}/^{\circ}\text{C}$

7.2. Allowable maximum temperature amplitudes

Using the equation:

$$\Delta\theta_p = 3/2 \Delta\epsilon_s (1-\nu) / [(1 + \nu) \lambda \alpha_i]$$

Table 7.1 gives the allowable temperature amplitudes for the cases considered: the temperature-to-strain conversion factor λ is assumed to be 1 for the component under consideration.

TABLE 7.1. ALLOWABLE MAXIMUM TEMPERATURE AMPLITUDES AT 425°C

Case	P1	P2	P3	W1	W2	W3
Allowable temperature amplitude K	87.7	73.1	60.9	70.2	58.5	48.7

The source temperature difference is 90 K, which is sufficient to cause crack initiation for both parent AISI 304 and weld metal if this fluctuation can be applied to the inner surface of the pipe.

For parent AISI 304 with mean fatigue properties and FSRF for surface finish only (ie material condition at the beginning of component life - no ageing, no environmental effects), crack initiation will be avoided since the allowable temperature amplitude is 96.5 K, above the source temperature difference.

For weld metal with mean fatigue properties and FSRF for surface finish only (i.e. material condition at the beginning of component life - no ageing, no environmental effects), crack initiation is possible, since the allowable temperature amplitude is 77.2 K, below the source temperature difference.

7.3. Local fluid and wall maximum temperature amplitudes

Since allowable temperature amplitudes for in-service material are less than the source temperature difference, the analysis must consider the local fluid and wall maximum temperature amplitudes [1]. Table 1.7.2 summarizes the maximum temperature amplitudes computed at the thermocouple positions indicated (together with mean temperature in brackets °C). This maximum amplitude is calculated from the difference between the maximum and minimum values in the data set. Note that material properties have been taken for 425°C mean temperature.

TABLE 7.2. LOCAL FLUID AND WALL MAXIMUM TEMPERATURE AMPLITUDES

	Position	Max fluid amplitude K	Max wall amplitude K
TC01A	80 mm downstream of tee, 0±5°	86.4	52.3
TC01	80 mm downstream of tee, 0°	74.7 (404)	59.9 (403)
TC02	160 mm downstream of tee, 0°	64.1 (365)	33.4 (366)
TC03	250 mm downstream of tee, 0°	37.7 (352)	15.9 (352)
TC15	380 mm downstream of tee, 0°	21.1 (346)	9.2 (346)
TC06	620 mm downstream of tee, 0°	6.1 (342)	2.6 (342)

Comparing these with the maximum allowable amplitudes for avoidance of crack initiation (Table 7.1), the following results are obtained:

TABLE 7.3. AVOIDANCE OF CRACK INITIATION OVER COMPONENT LIFE

Case	P1	P2	P3	W1	W2	W3
TC01A fluid	Yes (just)	No	No	-	-	-
TC01A wall	Yes	Yes	Yes			-
TC01 fluid	Yes	No	No	-	-	-
TC01 wall	Yes	Yes	Yes	-	-	-
TC02 fluid	Yes	Yes	No	Yes	No	No
TC02 wall	Yes	Yes	Yes	Yes	Yes	Yes
TC03 fluid	Yes	Yes	Yes	-	-	-
TC03 wall	Yes	Yes	Yes	-	-	-
TC15 fluid	Yes	Yes	Yes	-	-	-
TC15 wall	Yes	Yes	Yes	-	-	-
TC06 fluid	Yes	Yes	Yes	-	-	-
TC06 wall	Yes	Yes	Yes	-	-	-

Thus crack initiation will be avoided at all locations for parent material with wall temperature fluctuations. At thermocouples TC01 and TC01A, crack initiation is possible for Cases P2 and P3 (fluid fluctuations only). For thermocouple TC02, crack initiation is possible for Case P3 with parent material, whilst this will occur for Cases W2 and W3 (fluid fluctuations only) for weld metal.

7.4. Boundary layer attenuation

The flow predictions give maximum temperature amplitudes in the fluid (at a distance of 5 mm) and at the wall. The boundary layer attenuations (BLA) are calculated using the following equation:

$$BLA = 1 - \Delta T_w / \Delta T_f$$

where ΔT_w = the amplitude at the wall and ΔT_f = amplitude in the fluid.
Computed BLA values are given in Table 7.4:

TABLE 7.4. COMPUTED BOUNDARY LAYER ATTENUATION

	Position	Boundary layer attenuation %
TC01A	80 mm downstream of tee, $0\pm5^\circ$	39
TC01	80 mm downstream of tee, 0°	20
TC02	160 mm downstream of tee, 0°	48
TC03	250 mm downstream of tee, 0°	58
TC15	380 mm downstream of tee, 0°	56
TC06	620 mm downstream of tee, 0°	57

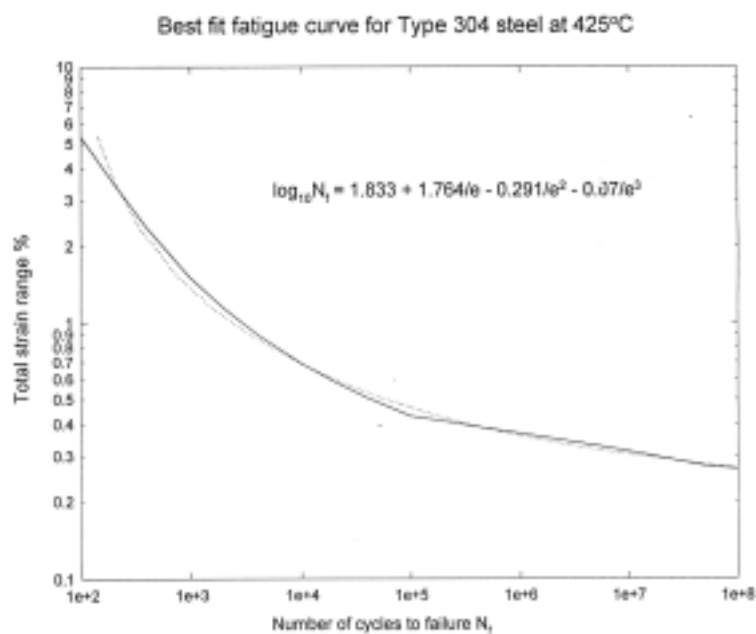


FIG. 5. Best fit fatigue curve for AISI 304 AT 425°C.

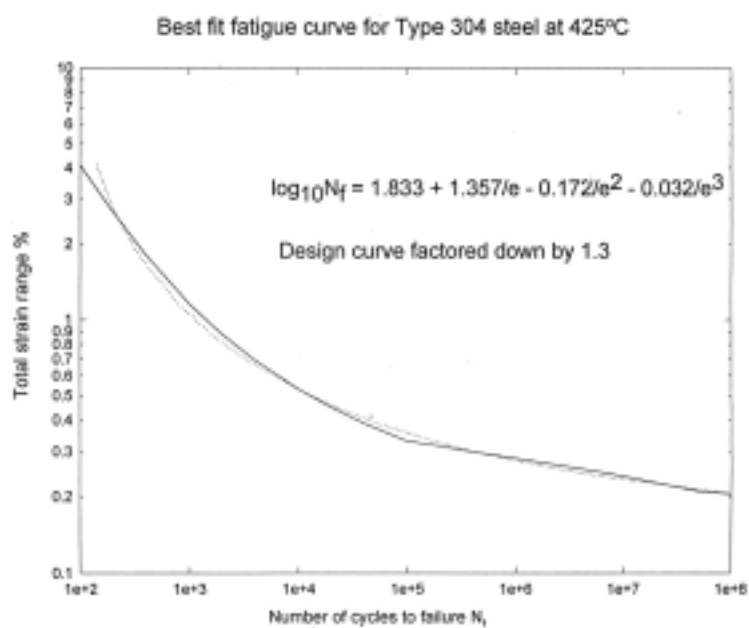


FIG. 6. Best fit fatigue curve for AISI 304 AT 425°C (case P1).

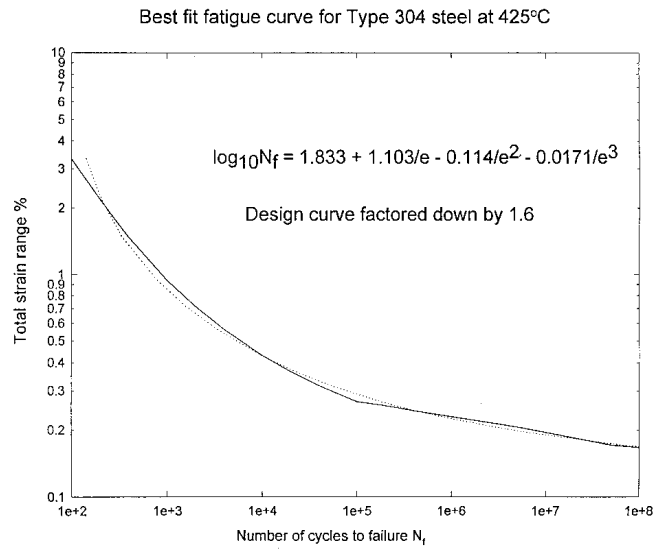


FIG. 7. Best fit fatigue curve for AISI 304 AT 425°C (case P2).

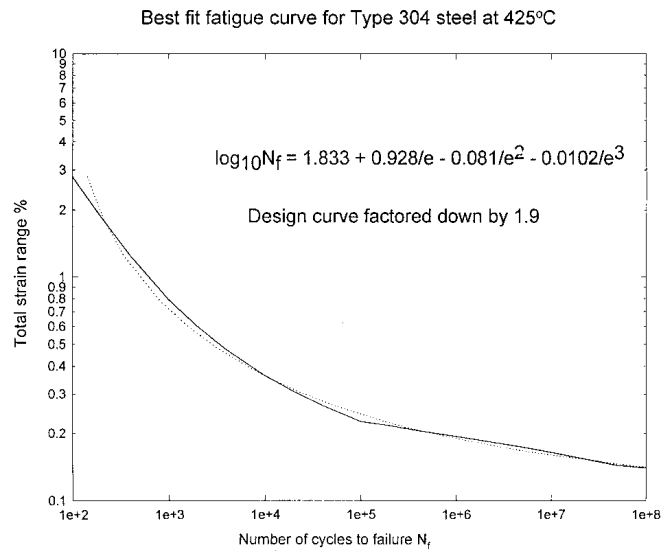


FIG. 8. Best fit fatigue curve for AISI 304 AT 425°C (case P3).

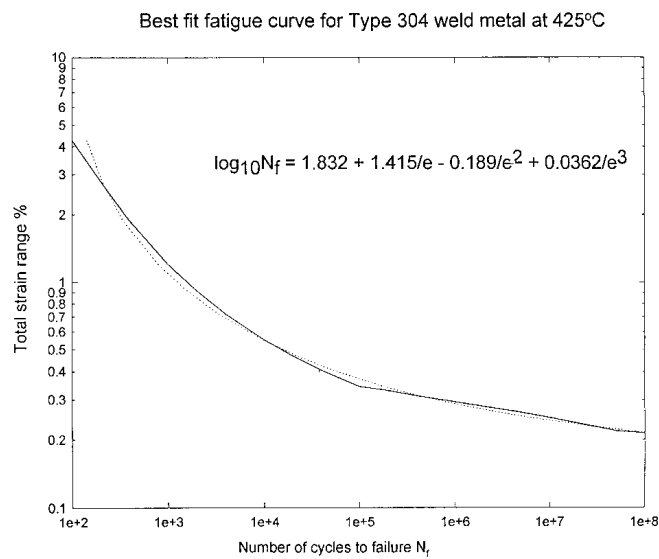


FIG. 9. Best fit fatigue curve for weld metal at 425°C.

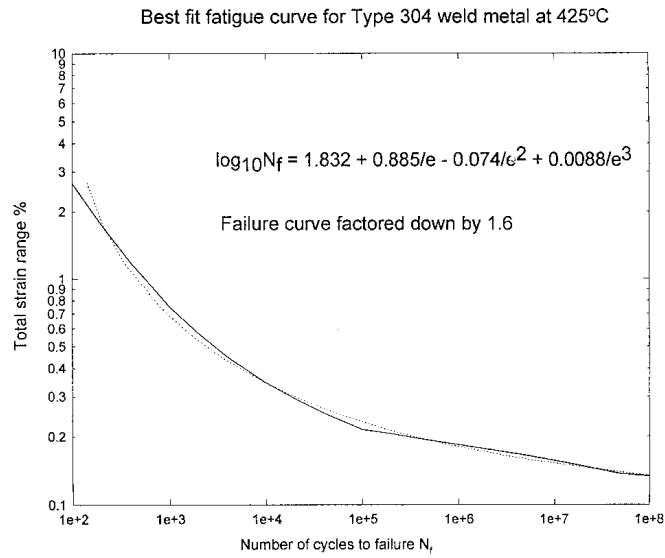


FIG. 10. Best fit fatigue curve for weld metal at 425°C (case W1).

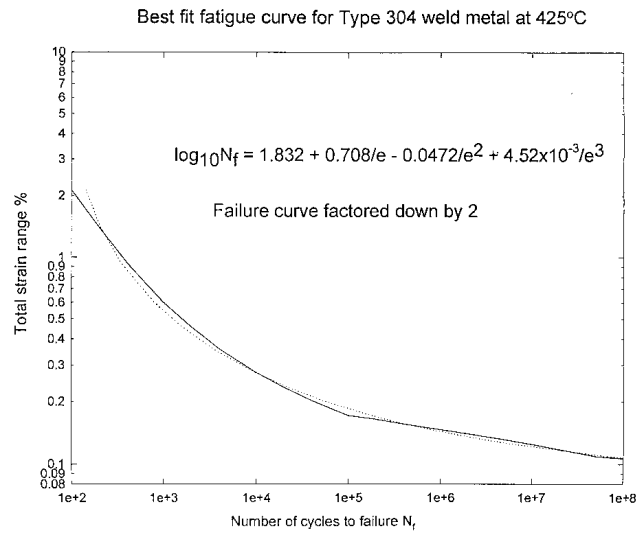


FIG. 11. Best fit fatigue curve for weld metal at 425°C (case W2).

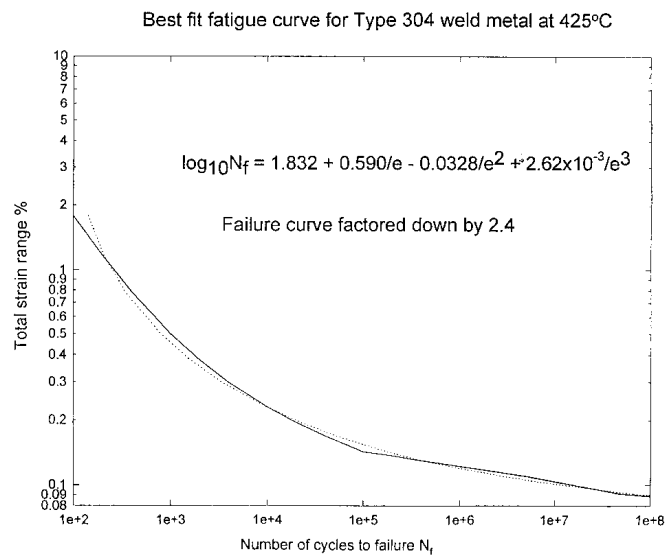


FIG. 12. Best fit fatigue curve for weld metal at 425°C (case W3).

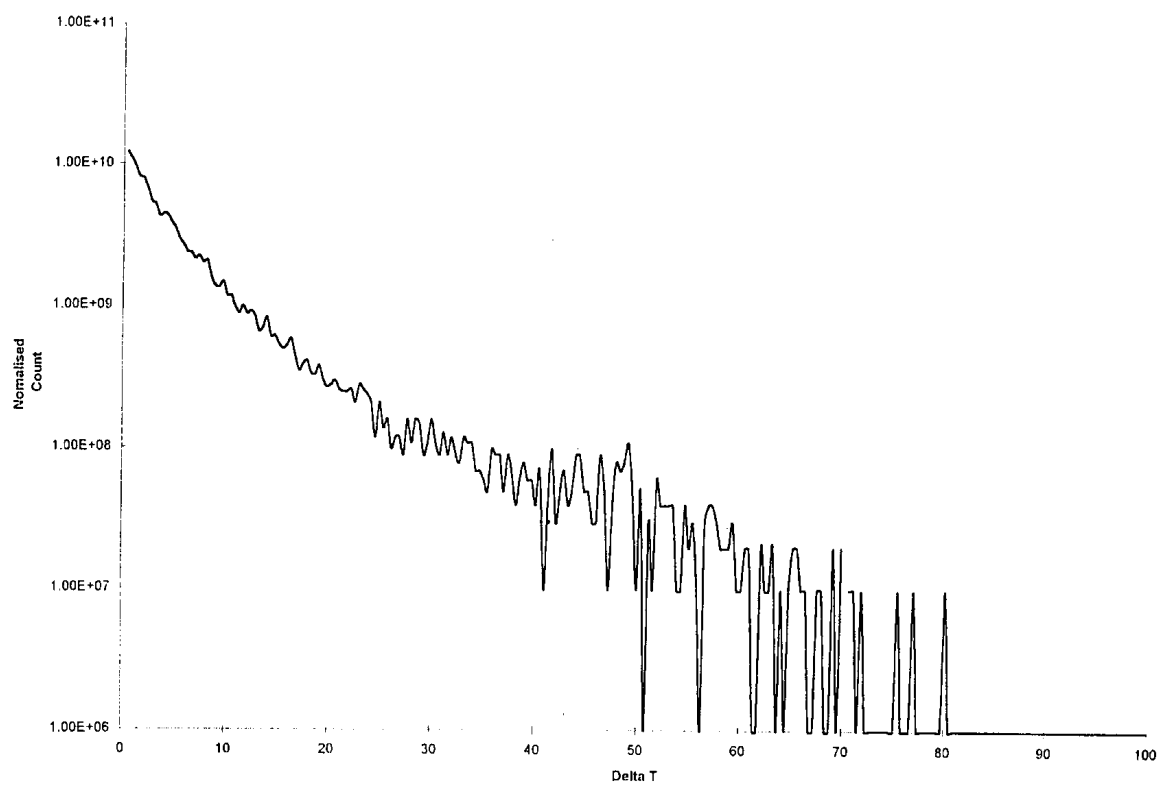


FIG. 13. Scaled rainflow histogram for TC1A fluid fluctuations.

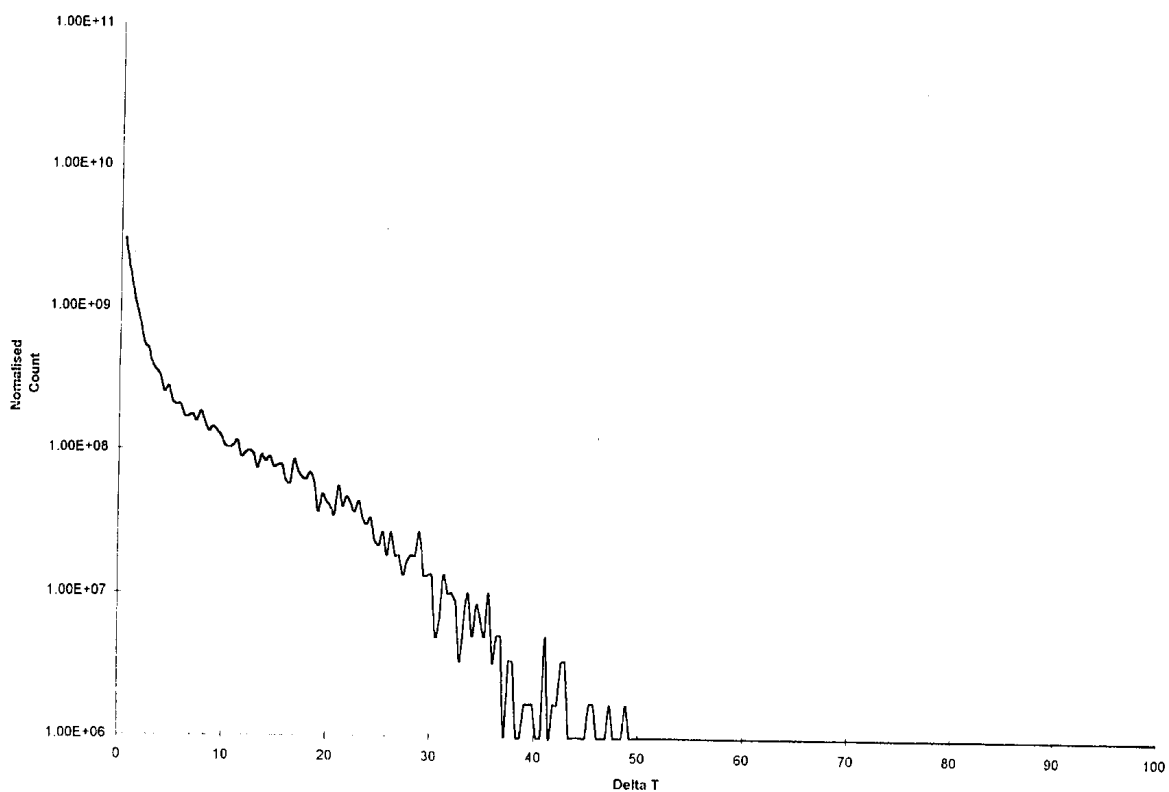


FIG. 14. Scaled rainflow histogram for TC1A wall fluctuations.

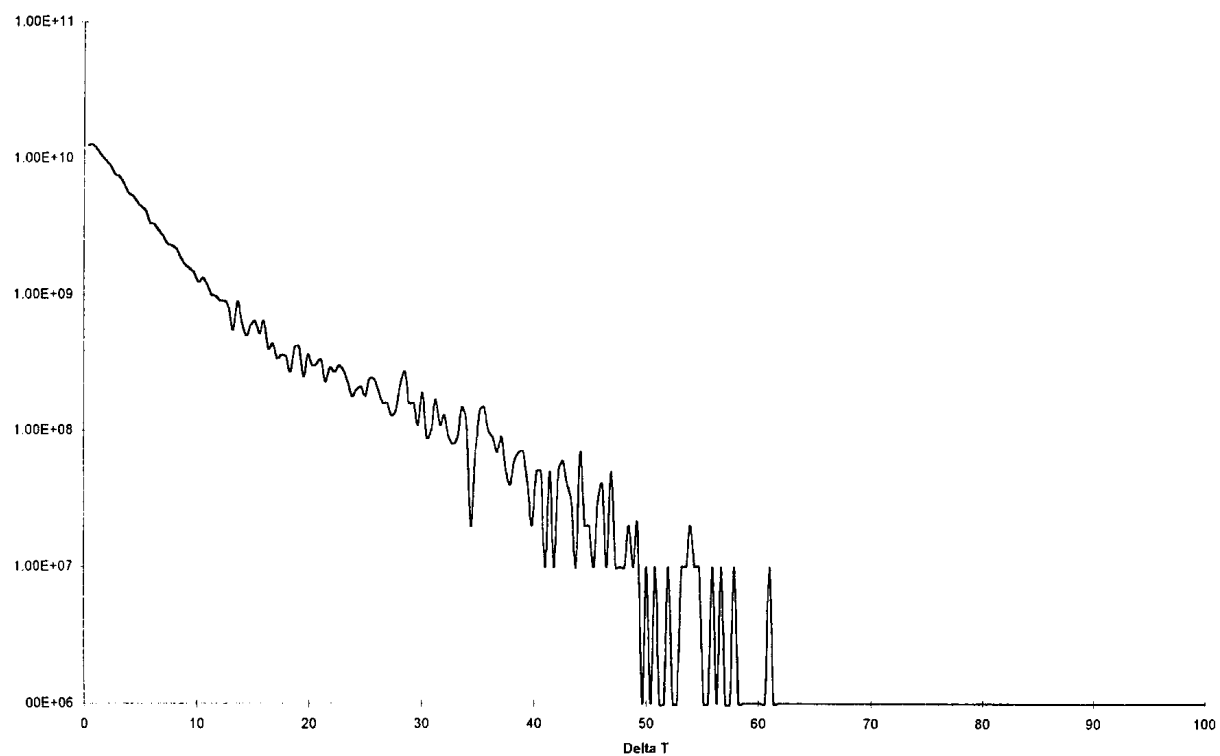


FIG. 15. Scaled rainflow histogram for TC2 fluid fluctuations.

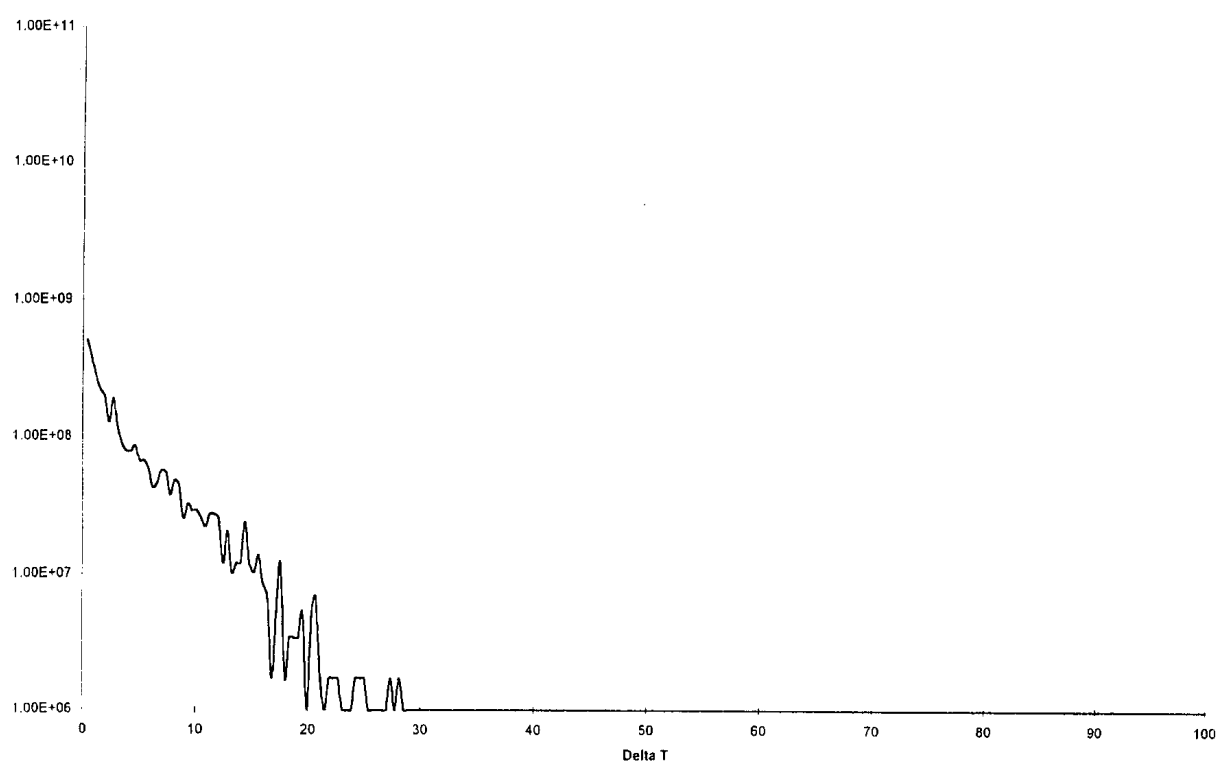


FIG. 16. Scaled rainflow histogram for TC2 wall fluctuations.

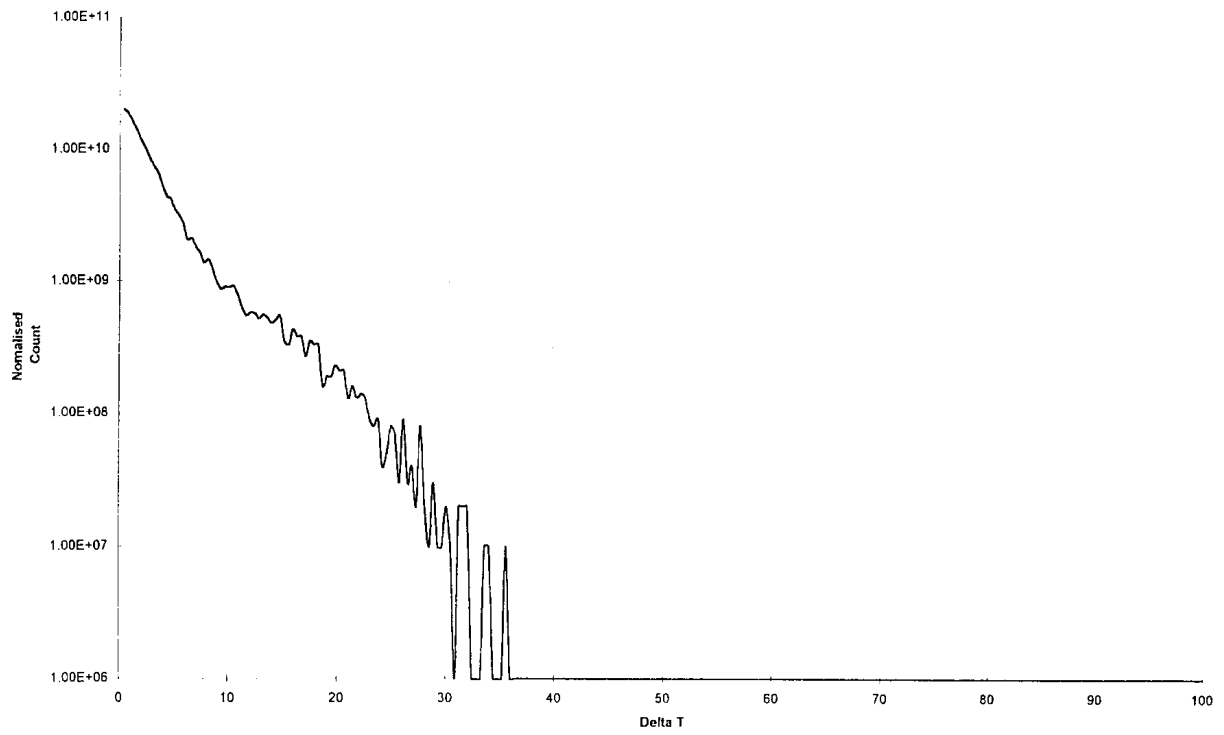


FIG. 17. Scaled rainflow histogram for TC3 fluid fluctuations.

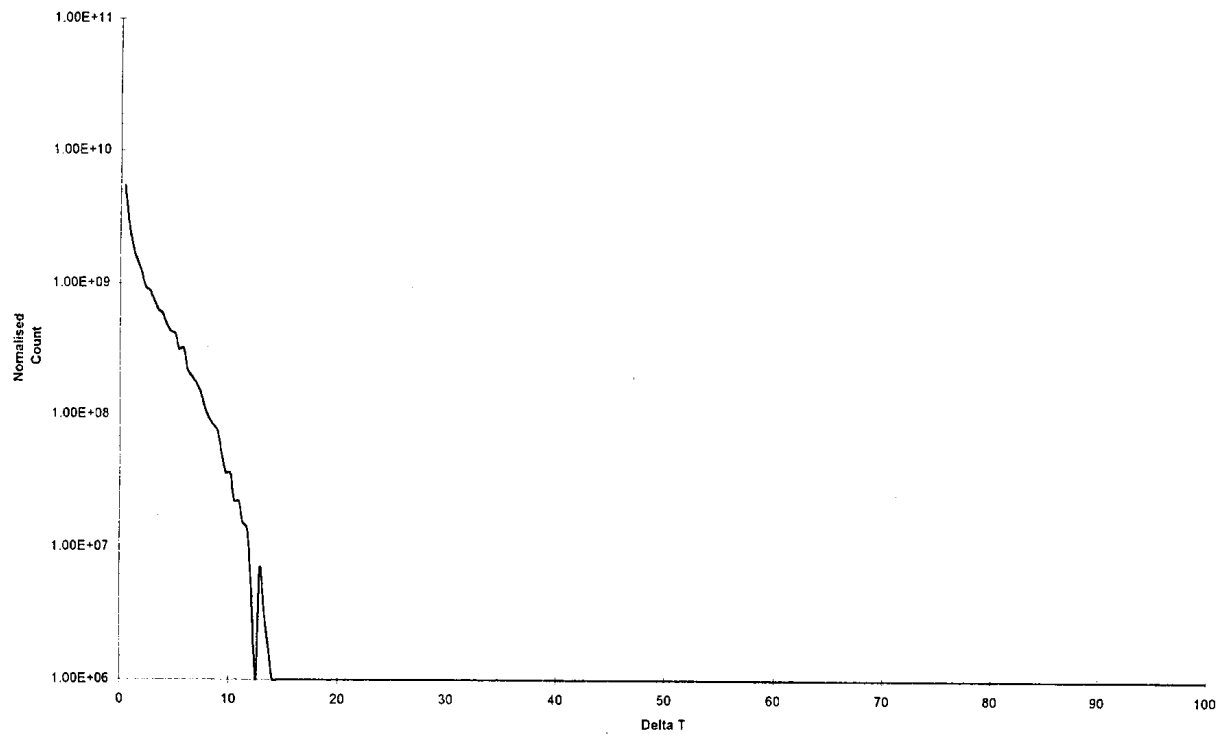


FIG. 18. Scaled rainflow histogram for TC3 wall fluctuations.

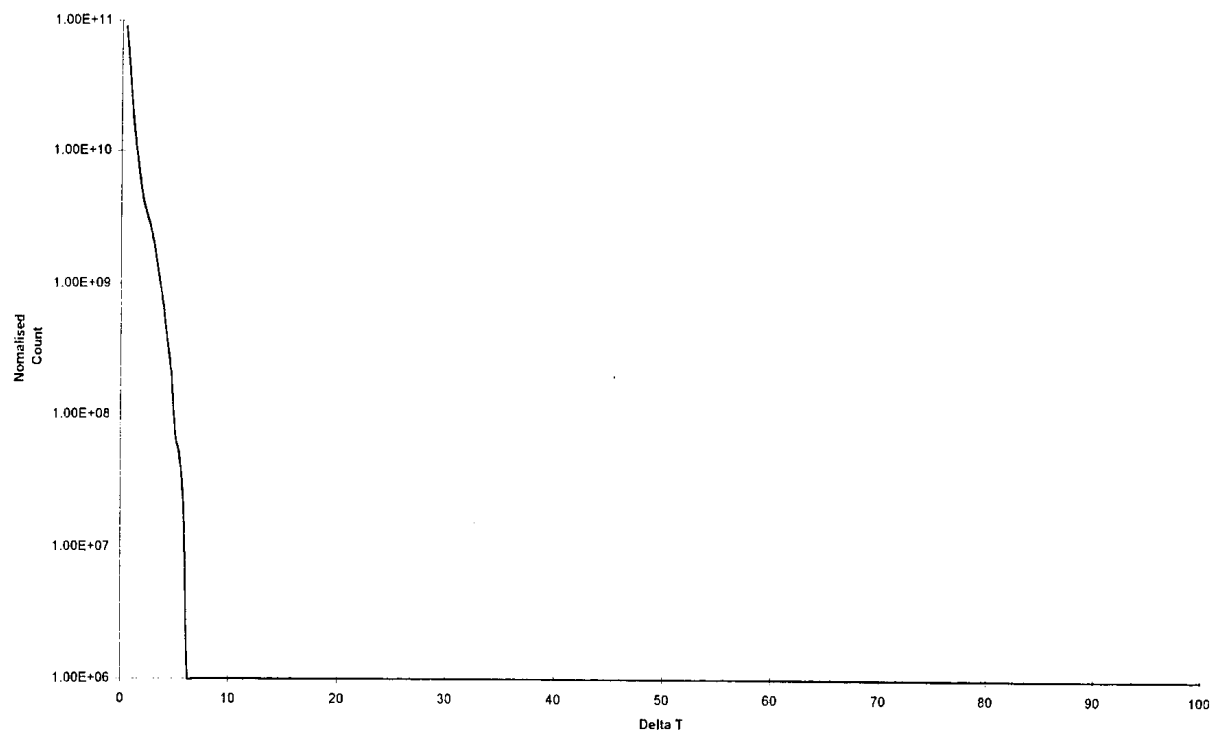


FIG. 19. Scaled rainflow histogram for TC6 fluid fluctuations.

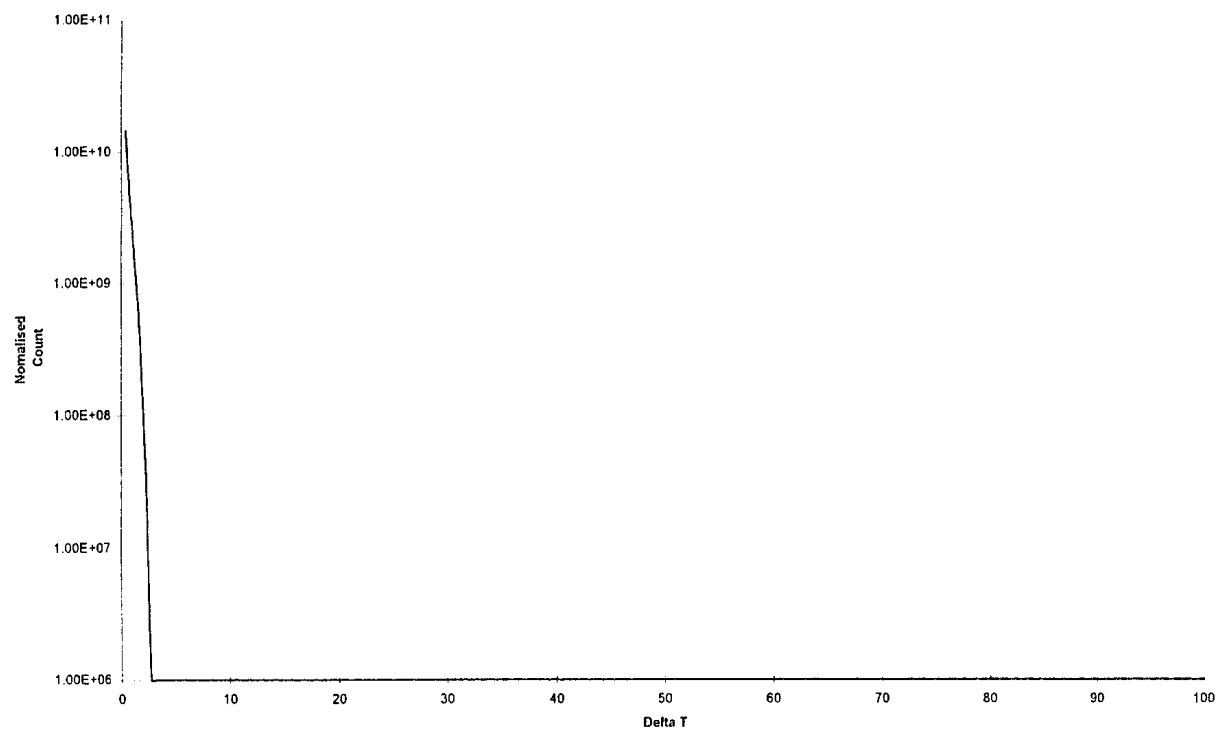


FIG. 20. Scaled rainflow histogram for TC6 wall fluctuations.

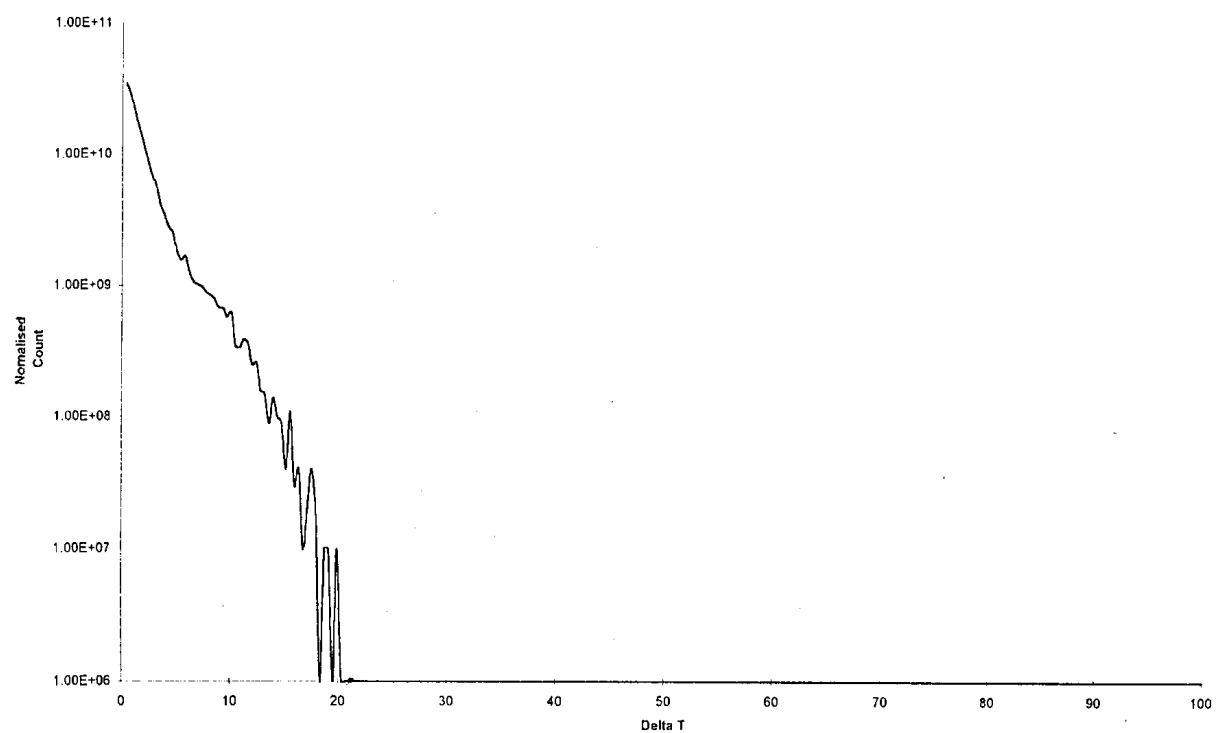


FIG. 21. Scaled rainflow histogram for TC15 fluid fluctuations.

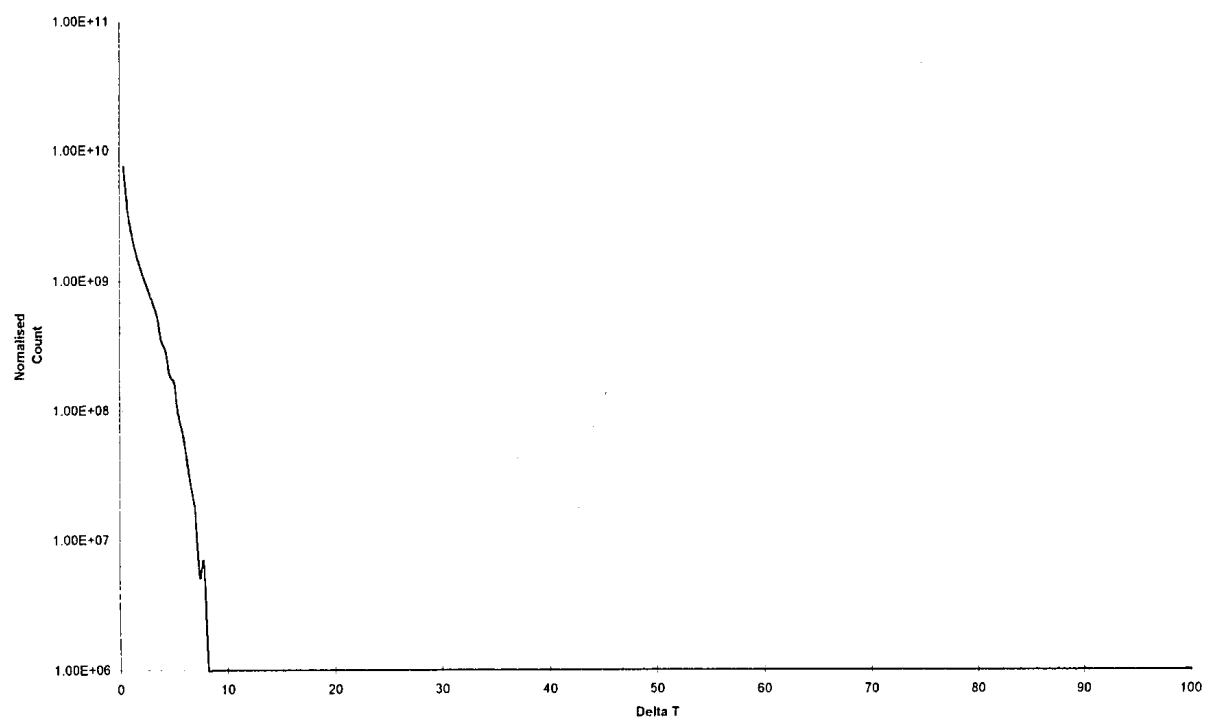


FIG. 22. Scaled rainflow histogram for TC15 wall fluctuations.

These values compare with BLA values of 60-70% in SUPERSOMITE, that is the degree of reduction of amplitude from the fluid to the wall is much smaller for the calculations performed on the mixing tee in PHENIX.

7.5. Fatigue damage summation

Best fit fatigue curves have been generated from the data supplied, for the failure data and for the failure data factored down by the values described above. These curves are shown in Figs 5-12, together with the coefficients for a relationship of the form:

$$\log_{10}N_f = A + B/\varepsilon + C/\varepsilon^2 + D/\varepsilon^3$$

These curves have been used to compute the Miner's summation from the Rainflow data generated by a computer program, which inputs the temperature-time history and cycle counts to give the total number of full temperature range cycles at amplitudes up to the maximum selected temperature of 100°C.

TABLE 7.5. PREDICTED MAXIMUM TEMPERATURE AMPLITUDES FOR FLUID THERMOCOUPLES

	TC1a	TC2	TC3	TC6	TC15
Max in data sample K	80.1	60.9	35.9	5.9	19.9
Gumbel factor m1	57.977	43.5242	25.9583	4.4128	14.6423
Gumbel factor m2	3426	1929	683.834	19.7148	217.4783
Gumbel factor m3	206452	87021	18276	89.1695	3725.2
Gumbel factor σ	9.07	6.616	3.5465	0.5516	1.9673
Gumbel factor r_s	0.4501	0.1201	0.2228	0.3605	0.1448
Gumbel factor τ_s	0.139	0.2439	0.2114	0.1677	0.2361
Gumbel predicted max K	113.2*	67.6	40.7	7.2	22.0

*Greater than source temperature difference

TABLE 7.6. PREDICTED MAXIMUM TEMPERATURE AMPLITUDES FOR WALL THERMOCOUPLES

	TC1a	TC2	TC3	TC6	TC15
Max in data sample K	48.8	28.1	13.7	2.3	7.8
Gumbel factor m1	33.887	3.54	10.6140	1.9470	6.2683
Gumbel factor m2	1167.26	73.6332	114.1477	3.8457	39.7754
Gumbel factor m3	40892	1546.64	1244.047	7.7011	255.5652
Gumbel factor σ	4.896	8.8028	1.371	0.2623	0.7814
Gumbel factor r_s	0.7190	2.0015	0.5197	0.0063	0.5907
Gumbel factor τ_s	0.0541	00.00	0.1173	0.28	0.0947
Gumbel predicted max	107.8*	N/A	20.4	2.8	13.1

*Greater than source temperature difference

TABLE 7.7. AVOIDANCE OF CRACK INITIATION OVER COMPONENT LIFE USING RAINFLOW MAXIMUM AMPLITUDES

Case	P1	P2	P3	W1	W2	W3
TC01A fluid	Yes	No	No	-	-	-
TC01A wall	Yes	Yes	Yes	-	-	-
TC02 fluid	Yes	Yes	No	Yes	No	No
TC02 wall	Yes	Yes	Yes	Yes	Yes	Yes

TABLE 7.8. AVOIDANCE OF CRACK INITIATION OVER COMPONENT LIFE USING INFINITE PERIOD MAXIMUM TEMPERATURE AMPLITUDES

Case	P1	P2	P3	W1	W2	W3
TC01A fluid	No	No	No	-	-	-
TC01A wall	No	Yes	Yes	-	-	-
TC02 fluid	Yes	Yes	No	Yes	No	No
TC02 wall	Yes	Yes	Yes	Yes	Yes	Yes

The resulting Rainflow histograms are shown in Figs 13-22, but scaled by a factor of the ratio of 90 000 hours to the sample length. These therefore represent an estimate of the numbers of cycles over the time to failure of the component. Histograms are given for both the fluid and wall temperature fluctuations. The largest temperature amplitude of 80.1 K is given in the fluid at thermocouple location TC01A.

Appendix 2 summarizes the results of the Miner's summation calculations. It can be seen that in only 2 cases for parent material at thermocouple TC01A (Cases P2 and P3) is crack initiation predicted in the component life of 90 000 hours using the fluid temperature amplitudes, whilst for weld metal a similar situation exists for fluid temperatures for cases W2 and W3 at thermocouple TC02.

In no instances is crack initiation predicted for wall temperature fluctuations. However, it must be recognized that the Rainflow cycle histogram for 90 000 hours has been estimated by scaling the histogram for the short time period of 32 to 190 s.

7.6. Maximum amplitude predictions

Tables 7.5 and 7.6 give the maximum temperature amplitudes seen in the computed histories (using Rainflow cycle counting), together with the maximum predicted amplitude in infinite time computed using the Gumbel analysis. This analysis uses the maximum amplitude observed in each of 64 blocks of data to predict the maximum value over an infinite period.

The maximum amplitudes are slightly different from those given in Table 7.2 because the highest and lowest temperatures do not necessarily form a single closed cycle.

Table 7.3 is revised in the light of the above results.

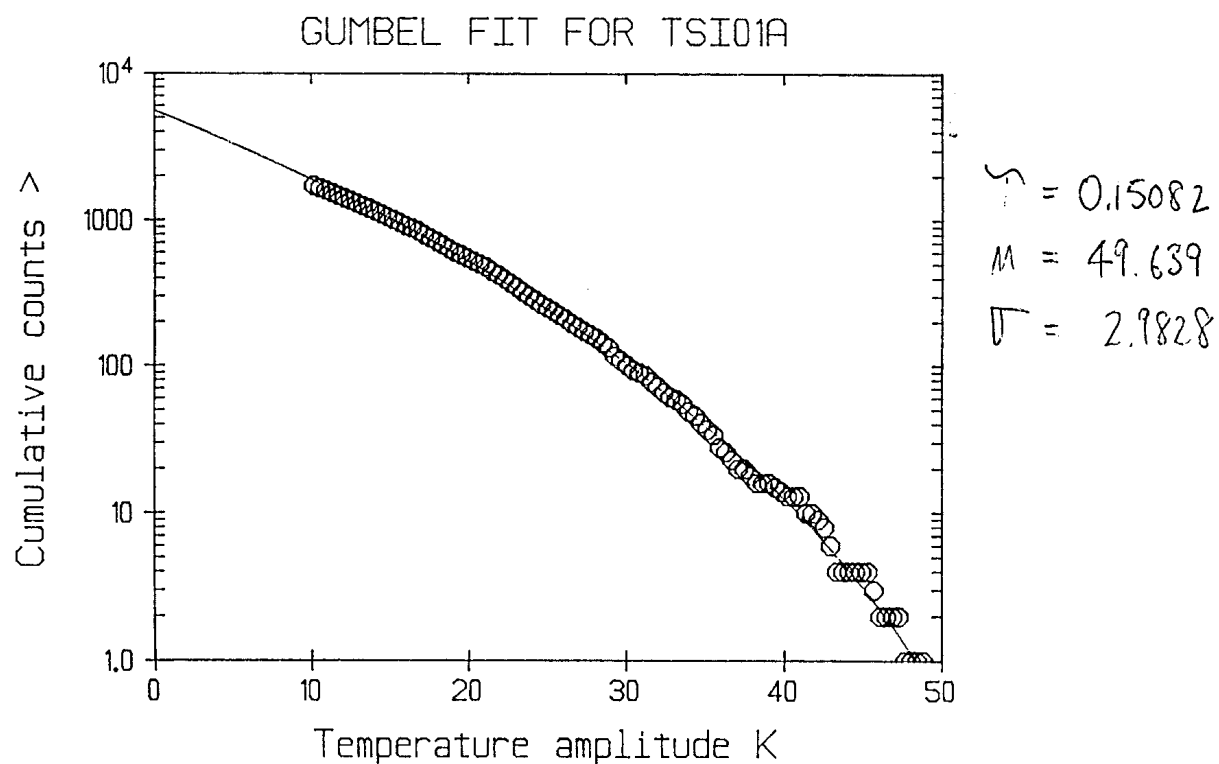


FIG. 23. Gumbel fit for TC1A wall fluctuations.

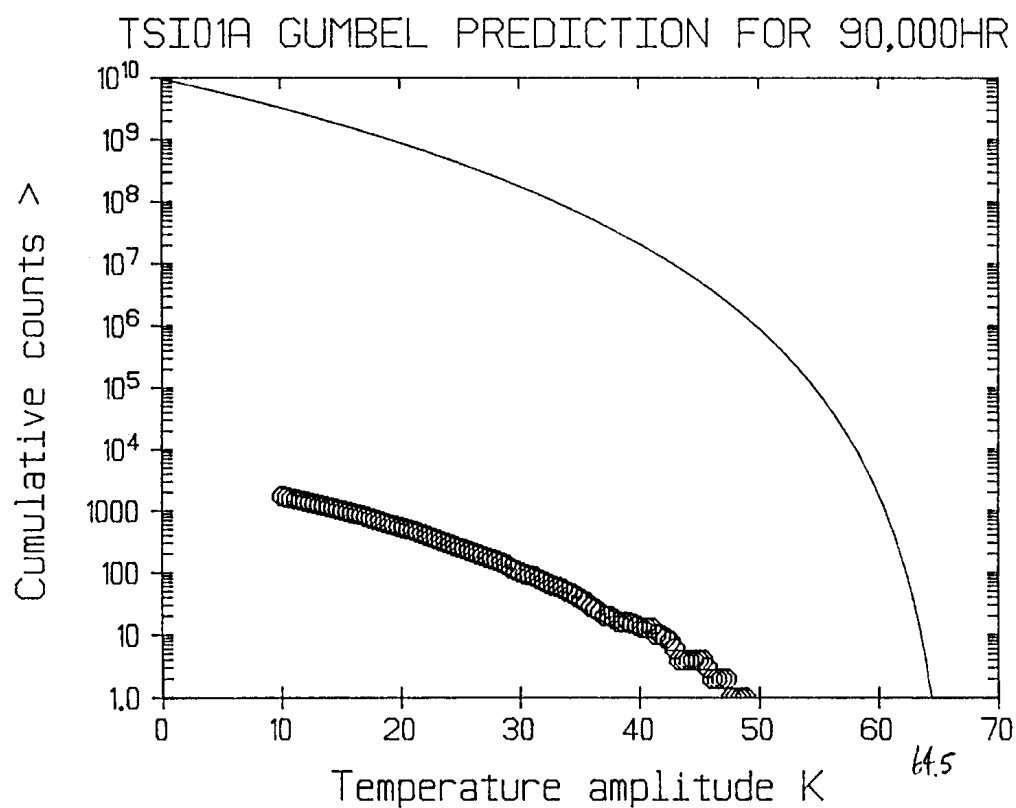


FIG. 24. Gumbel prediction for TC1A wall fluctuations.

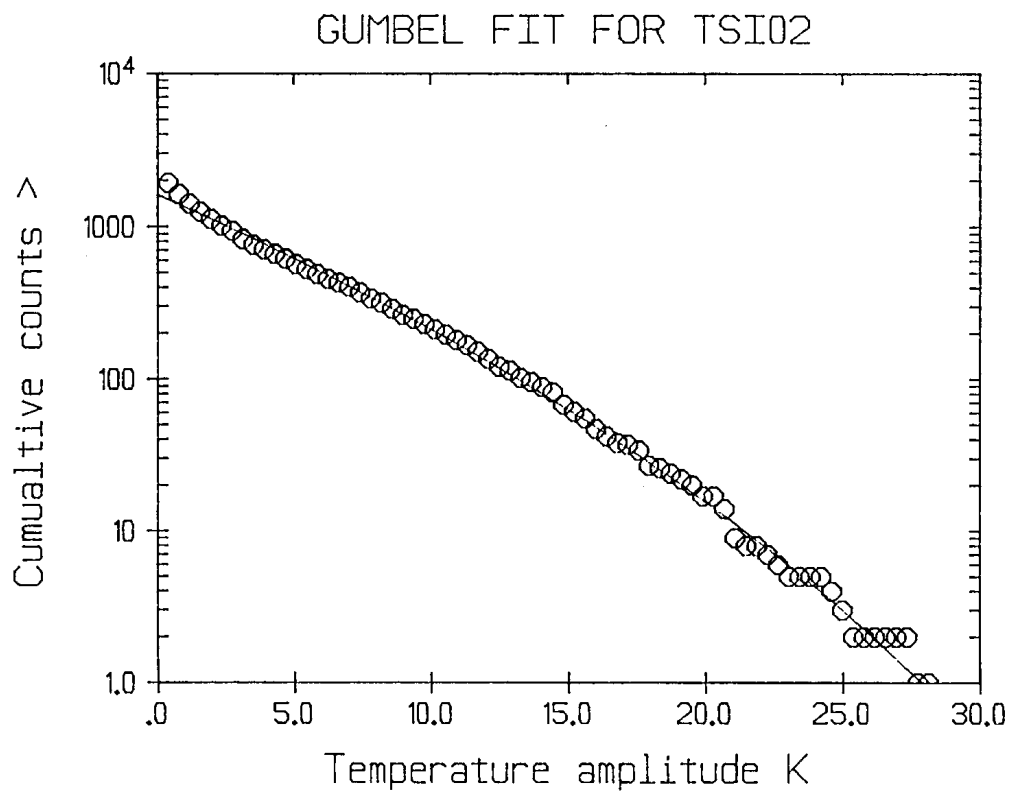


FIG. 25. Gumbel fit for TC2 wall fluctuations.

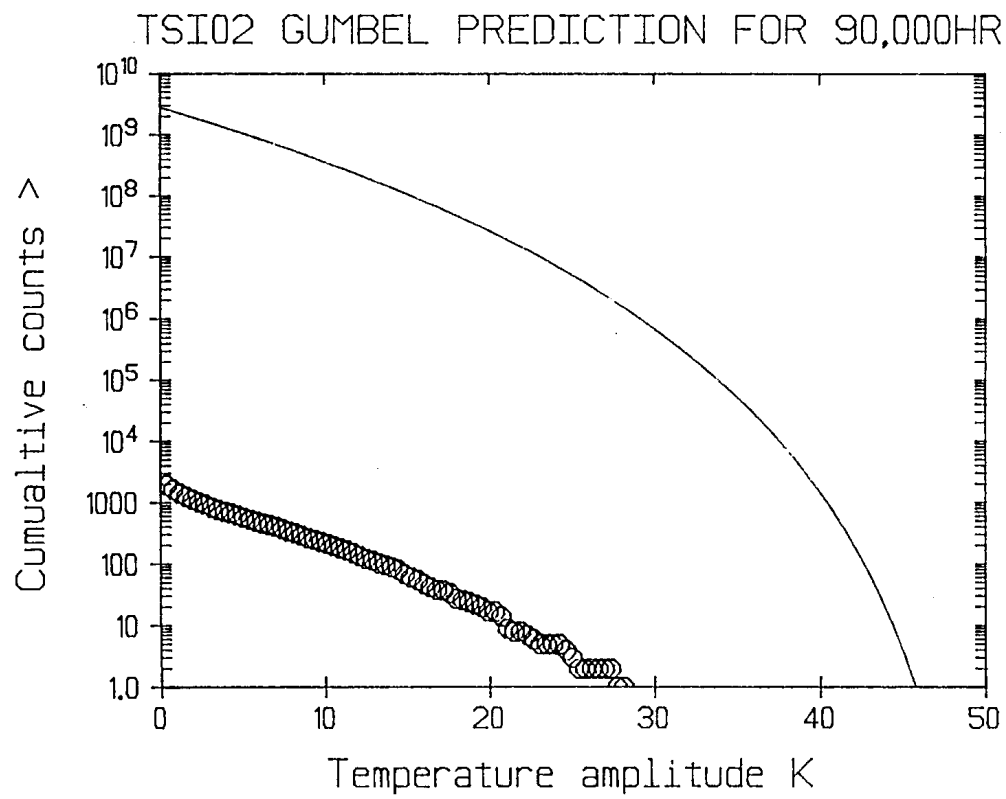


FIG. 26. Gumbel prediction for TC2 wall fluctuations.

7.7. Prediction of component lifetime Rainflow histograms

Using the method described in Section 6, Rainflow cycle histograms for the component lifetime of 90 000 hours have been estimated, in contrast to scaling those seen in short time periods of 32-190 s. These calculations have been carried out using a computer program MINSQ that uses a least squares method to estimate the Gumbel parameters.

Figures 23-26 present the results from the calculations. Rainflow cycle histograms have been computed for thermocouples TC1A and TC2 at the wall. These are shown in Figs 25 and 26 for comparison with Figs 14 and 16. The differences at the highest temperature amplitudes can be seen, since counts up to a maximum temperature amplitudes of 64.5 and 46 K are predicted for TC1A and TC2 respectively.

A Miner's summation has been performed using these computed Rainflow cycle histograms. Since for TC1A the maximum wall temperature amplitude of 64.5 K is less than maximum amplitude for cases P1 and P2, crack initiation in 90 000 hours is not predicted. For case P3, there are too few cycles above 60.9 K to initiate cracking.

A similar situation exists for TC2, since the maximum temperature amplitude of 46 K is less than the allowable for cases W1, W2 and W3.

Thus crack initiation is not predicted for either TC1A or TC2 using the computed wall temperature fluctuations.

8. DISCUSSION

Using the maximum temperature amplitudes from the computed short timescale temperature-time histories for the wall, crack initiation is not predicted at any location, including the weld. However, crack initiation is predicted at TC1A for fluid temperature fluctuations for Cases P2 and P3, and also at TC2 for Cases W2 and W3. Weld failure can therefore only be suggested if the wall temperature fluctuations are higher, perhaps due to the interaction of the inner weld bead (which stands proud into the flow) with the fluid flow.

The assessment method used shows the sensitivity of the results to several factors:

- The fatigue strength reduction factors actually appropriate for the material under consideration;
- The computed maximum temperature amplitude for a short time period;
- The method of estimation of maximum temperature amplitude in the component lifetime (or infinite time period);
- Maximum temperature amplitude calculated from Rainflow cycle counting (generally less than the max/min temperature difference);
- The scaling of Rainflow cycle counts in a short time period to represent those over the component lifetime.

The method of scaling Rainflow cycle counts using the Gumbel distribution is recommended in preference to direct scaling of the counts by the ratio of time periods. This method also seems to give a better prediction of maximum temperature amplitude in component lifetime, compared to the maximum predicted by Gumbel analysis using the

individual maxima in each of 64 blocks comprising the short time period temperature-time history.

9. CONCLUSIONS

1. Crack initiation in component lifetime is not predicted using wall temperature fluctuations;
2. Crack initiation is predicted at thermocouple TC1A for parent metal AISI 304 for Cases P2 and P3 using fluid temperature fluctuations;
3. Crack initiation is predicted at thermocouple TC2 for weld metal for Cases W2 and W3 using fluid temperature fluctuations.

10. RECOMMENDATIONS

A crack initiation assessment of the PHENIX pipe failure has been carried out using methods developed in the UK. Using the maximum temperature amplitudes from the computed short timescale temperature-time histories for the wall, crack initiation is not predicted at any location, including the weld. However, crack initiation is predicted at TC1A for fluid temperature fluctuations for Cases P2 and P3 (fatigue strength reduction factors of 1.6 and 1.9 respectively), and also at TC2 for Cases W2 and W3 (fatigue strength reduction factors of 2.0 and 2.4 respectively). Weld failure can therefore only be suggested if the wall temperature fluctuations are higher, perhaps due to the interaction of the inner weld bead (which stands proud into the flow) with the fluid flow.

The assessment method used shows the sensitivity of the results to several factors:

- The fatigue strength reduction factors actually appropriate for the material under consideration;
- The computed maximum temperature amplitude for a short time period;
- The method of estimation of maximum temperature amplitude in the component lifetime (or infinite time period);
- Maximum temperature amplitude calculated from Rainflow cycle counting (generally less than the max/min temperature difference
- The scaling of Rainflow cycle counts in a short time period to represent those over the component lifetime.

The method of scaling Rainflow cycle counts using the Gumbel distribution is recommended in preference to direct scaling of the counts by the ratio of time periods. This method also seems to give a better prediction of maximum temperature amplitude in component lifetime, compared to the maximum predicted by Gumbel analysis using the individual maxima in sub-blocks of the computed short time period temperature-time history.

The report concludes the following:

- Crack initiation in component lifetime is not predicted using wall temperature fluctuations;
- Crack initiation is predicted at thermocouple TC1A for parent metal AISI 304 for Cases P2 and P3 using fluid temperature fluctuations;

- Crack initiation is predicted at thermocouple TC2 for weld metal for Cases W2 and W3 using fluid temperature fluctuations.

It makes the recommendation: Consideration is given to the effect of the inner weld bead upon the magnitude of temperature fluctuations on the weld surface.

Consideration is given to the effect of the inner weld bead upon the magnitude of temperature fluctuations on the weld surface.

REFERENCES

- [1] STAINSBY, R., MARTIN, D., Thermal striping benchmark exercise thermal hydraulic analysis of the Phenix secondary paperwork T-junction, Report to the final Research Coordination Meeting on Harmonization and validation of fast reactor thermomechanical codes and relations using experimental data, Lyon, France, 20-24 April 1998.
- [2] RICHARDSON, T., Private communication.
- [3] LEWIS, M.W.J., BERGAMASCHI, Y., Interim design procedures for the avoidance of thermal striping damage in Fast Breeder Reactor components, paper E04/2 SMIRT 11 Transactions Vol E, Tokyo, Japan (1991).
- [4] LEWIS, M.W.J., Comments on CEA proposals for avoidance of crack initiation due to thermal striping, AGT-9B-92-56(UK), United Kingdom (1992).
- [5] LEWIS, M.W.J., Designing against thermal striping: a procedure based upon crack initiation for Type 316L(N) and mod 9Cr1Mo parent material, AGT-9B-92-65(UK), United Kingdom (1992).
- [6] LEWIS, M.W.J., Synthesis Report: Thermal Striping, AGT-9B-92-69(UK), United Kingdom (1992).
- [7] Compendium of DCR recommendations for EFR: 2nd edition up to March 1991, DCRC (1991).
- [8] LEWIS, M.W.J., SUPERSOMITE.
- [9] LEWIS, M.W.J., An examination of reduction factors applied to the high cycle fatigue behaviour of Type 316L(N) and 316L SPH steels, weldmetal and weldments, AEA Technology internal report (1992).
- [10] LEJEAIL, Y., The working out of a design rule in case of structures submitted to thermal striping, paper presented at Specialist's Meeting on "Correlation between material properties and thermohydraulics conditions in LMFRs", Aix-en-Provence, France, 22-24 November 1994.
- [11] ROSENHAUER, W., Methodological aspects encountered in the Lower Rhine Area seismic hazard analysis, "Seismicity and Seismic Risk in the Offshore North Sea Area" (p385) ed A.R. Pitsema and A. Gurbinar, D. Reidel Publishing Co 1983.

LIST OF PARTICIPANTS

International Atomic Energy Agency

J. Kupitz
A Rineiskii
A Stanculescu

FRAMATOME, Division NOVATOME, France

O. Gelineau,
M. Sperandio
J.P. Simoneau
J.M. Hamy

Cadarache Center, France

P.H.L. Roubin

Indira Gandhi Center for Atomic Research, India

P. Chellapandi
K. Velusamy,
A. Biswas
R. Rama
S. B. Bhoje
G. Vaidyanathan
S. C. Chetal

National Agency for New Technology, Italy

C. Caroli

Power Reactor and Nuclear Fuel Development Corporation, PNC, Japan

N. Kasahara
T. Muramatsu

Korea Atomic Energy Research Institute, Republic of Korea

Hyeong-Yeon Lee
Jong-Bum Kim
Bong Yoo

Korea Institute of Nuclear Safety, Republic of Korea

Yoo Youn-Won Park

Institute of Physics and Power Engineering, Russian Federation

S.I. Scherbakov
V.V. Yarovitsyn

OKB Mechanical Engineering, Russian Federation

P.N. Birbraer
A.I. Kiryushin
V.V. Zhukov
V.A. Sobolev
S.A. Soloviev

AEA Technology, United kingdom

M.W.J. Lewis

R. Stainsby

National Nuclear Corporation, United kingdom

D. Buckthorpe